Coronary Atherosclerosis

Imaging, biology and mechanics

Ayla Hoogendoorn

Coronary Atherosclerosis

Imaging, biology and mechanics

Ayla Hoogendoorn

ISBN: 978-94-6375-503-0

The research described in this PhD thesis has received funding from the European Research Council under the European Union's Seventh Framework Programme / ERC Grant Agreement nr. 310457.

Financial support for the printing of this thesis was kindly provided by:
Erasmus University Rotterdam, Infraredx, Inc., Cardialysis and Pie Medical Imaging

Financial support by the Dutch Heart Foundation for the publication of this thesis is gratefully acknowledged.

Coverdesign: Ayla Hoogendoorn and Astrid Moerman
Layout: Eduard Boxem, Persoonlijk Proefschrift
Printed: Ridderprint BV, Ridderkerk, the Netherlands

A digital version of this thesis is available at http://repub.eur.nl/

Coronary Atherosclerosis - Imaging, biology and mechanics

Coronaire atherosclerose - Beeldvorming, biologie en mechanica

Proefschrift

ter verkrijging van de graad van doctor aan de

Erasmus Universiteit Rotterdam

op gezag van de rector magnificus

Prof.dr. R.C.M.E. Engels

en volgens het besluit van het College voor Promoties.

De openbare verdediging zal plaatsvinden op

donderdag 19 september 2019 om 11.30 uur door

Ayla Hoogendoorn

geboren te Amsterdam

Erasmus University Rotterdam

Erasmus

PROMOTIECOMMISSIE

Promotoren
Prof.dr.ir. A.F.W. van der Steen
Prof.dr. D.J.G.M. Duncker

Overige leden
Prof.dr. F. Zijlstra
Prof.dr. M.J.A.P. Daemen
Dr. J.E. Roeters van Lennep

Copromotor
Dr. J.J. Wentzel

TABLE OF CONTENTS

CHAPTER 1

Introduction

Coronary artery disease: a global and personal burden

Coronary artery disease is a disease of the large muscular arteries of the heart (Figure 1.1) and is one of the most common cardiovascular diseases. Coronary artery disease is globally the leading cause of death and disability. Annually, over 110 million people suffer from coronary artery disease and there is an estimated, associated death of 8.9 million people[1]. In Europe alone, the yearly costs of coronary artery disease are estimated at 45 billion euros[2].

Well-known risk-factors for coronary artery disease are hypercholesterolemia, smoking, obesity, high blood pressure and diabetes. Progression of coronary artery disease can lead to narrowing (stenosis) of a coronary artery, which hampers blood supply to the cardiac muscle. When the blockage is partial and stable, patients can experience chest pain upon exercise, also called stable angina. In cases of more advanced coronary artery disease, acute blockage of the artery can lead to a myocardial infarction, also called an 'acute coronary syndrome'. When such a blockage is not resolved quickly, permanent damage to the heart muscle can result in a reduced cardiac contraction function, heart failure or death[3]. One of the main underlying causes of coronary artery disease is coronary atherosclerosis.

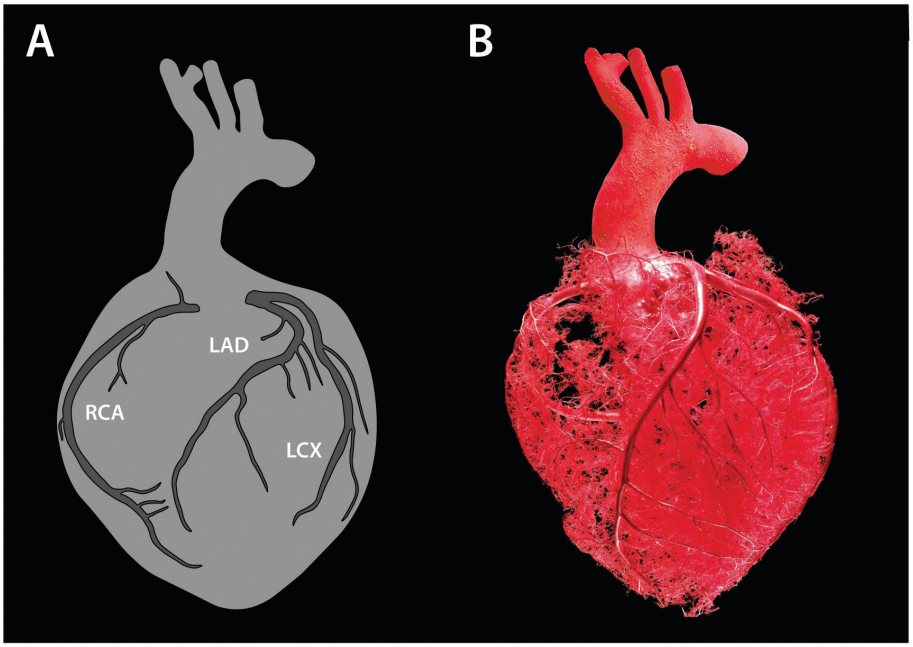

Figure 1.1: The cardiac circulatory system. A) The three main coronaries arteries of the heart: left anterior descending (LAD), left circumflex (LCX) and right coronary artery (RCA). **B)** The three coronary arteries branch off into the vast network of the cardiac microcirculation. Figure B: adjusted from Harshman[4].

The (natural) history of atherosclerosis

Already in 1575, Fallopius, one of the most important anatomists of the 16th century, described 'a condition in which arteries degenerate into bone'[5]. The term 'atheroma' was first introduced by Von Haller in 1755 who described an arterial pathology using the Greek term for 'a pocket containing gruel-like material'[5,6]. It was however not until 200 years later that the official term 'atherosclerosis' was adopted upon an initiative of Rabson[7]. Atherosclerosis is a complex, multifactorial disease of the larger muscular arteries and is initiated when the endothelial cells, aligning the inside of the artery, become dysfunctional. This dysfunctionality can be induced by (a combination of) traditional risk factors like smoking, ageing and hyperglycaemia[8], but also by low wall shear stress, a biomechanical force[9]. Endothelial cell dysfunction, which should actually be considered as cell activation, is characterised by a reduction of nitric oxide availability and an increased expression of inflammatory cell-attracting chemokines, cytokines and adhesion molecules[10]. Endothelial cell dysfunction also results in an increased permeability of the endothelial layer, whereby plasma-borne low-density lipoproteins can more easily intrude into the inner layer of the vessel wall, the intima. Once inside the arterial wall, these lipoproteins are oxidized, which in return leads to further activation of the endothelial cells[11].

The increased expression of adhesion molecules by the activated endothelial cells results in recruitment of inflammatory cells like monocytes. These monocytes migrate into the vessel wall, proliferate and turn into macrophages, which engulf the present oxidized lipoproteins. In time, these lipid-laden macrophages become foam cells and undergo cell death, thereby contributing to the formation of a necrotic core. Within this strong inflammatory environment, small calcifications and cholesterol crystals are formed[11].

Parallel to the vicious circle of increasing inflammation, the vascular smooth muscle cells that make up the media layer of the artery, are also activated. These activated smooth muscle cells migrate from the media into the intima, proliferate and will, together with the recruited inflammatory cells, produce extracellular matrix, further contributing to plaque growth[11].

In the initial phases of plaque growth, the artery compensates for the growth of the plaque by outward remodelling. This outward remodelling is however only sufficient until the plaque covers around 40% of the vessel area, after which, upon further growth, the plaque starts to protrude into the lumen[12]. Upon this growth process, a nutrient and oxygen shortage can arise in the centre of the plaque. This, together with inflammatory activity, triggers a process called 'angiogenesis' or 'neovascularisation' in which small blood vessels are formed in the adventitial layer, and grow into the plaque[13,14]. These

neo-vessels are underdeveloped and leaky, which can lead to haemorrhage inside the plaque, known to contribute to rapid plaque growth and destabilization[13–15].

In these more advanced atherosclerosis stages, smooth muscle cells and inflammatory cells form a fibrous cap over the highly inflamed, lipid-rich necrotic core, protecting the plaque from rupture. However, these same cells also produce enzymes like matrix-metalloproteinases which break down the fibrous tissue. Although this process is essential for smooth-muscle cell migration, it also leads to thinning of the supporting cap structure, increasing the vulnerability of the plaque to rupture[16]. When a plaque rupture occurs, the lipid-rich, highly inflamed content of the plaque is released into the bloodstream, which can lead to acute thrombus formation and subsequently a partial or complete blockage of the coronary artery. Besides plaque rupture, also plaque erosion (occurring on an intact plaque lacking an endothelial cell layer), and the presence of a calcified nodule have been pinpointed as triggers for thrombus formation[17].

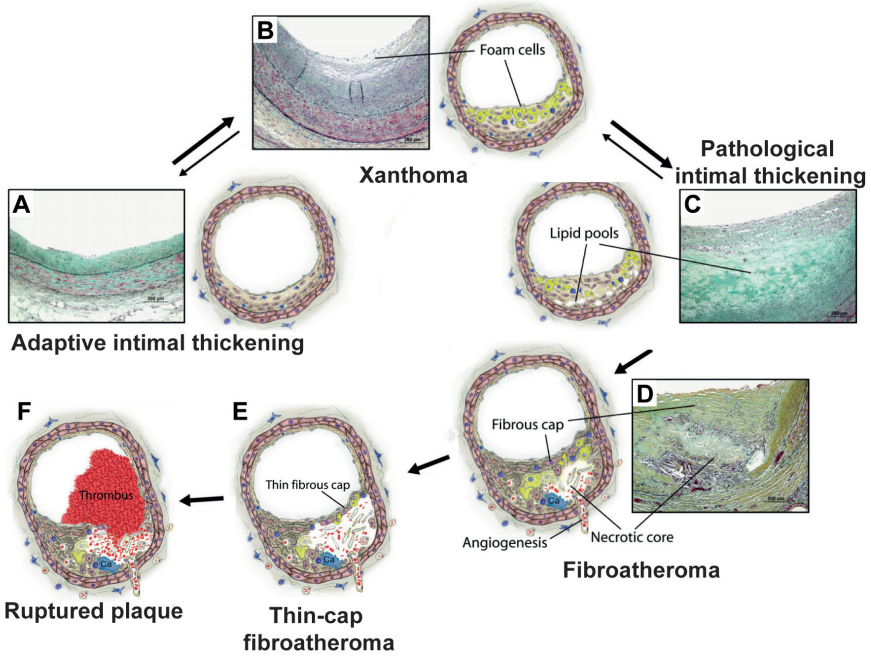

Figure 1.2: Classification of atherosclerotic plaque types with histological examples. A) Intimal thickening: mainly consisting out of smooth muscle cells. **B)** Intimal xanthoma: an accumulation of lipids, macrophages and foam cells. **C)** Pathological intimal thickening: presence of lipid pools, but no necrotic cores. **D)** Fibroatheroma: complex plaque with necrotic cores and a fibrous cap. Calcifications (Ca), cholesterol crystals and neovascularisation can be observed. **E)** Thin-cap fibroatheroma, a subcategory of the fibroatheroma: the most rupture-prone plaque type with a fibrous cap <65 µm. **F)** Ruptured plaque with overlying thrombus. All histological examples are a Movat's pentachrome staining. Adjusted from Bentzon et al. 2014[21].

Based on pathological evidence, all stages in atherosclerosis development have been described by the American Heart Association in an official classification scheme[18,19]. This scheme was later adjusted by Virmani et al.[20] (Figure 1.2). One of the plaque types that is of special interest with regard to acute coronary syndromes is the thin-cap fibroatheroma, a highly inflamed plaque with a large lipid-rich necrotic core and a thin, collagen-rich fibrous cap (Figure 1.2E). This is the plaque type that is most prone to rupture[20]. Although biological factors contribute to plaque destabilization, plaque rupture itself is a mechanical process. Mechanical forces act upon the plaque and the interaction between the plaque composition (i.e. plaque strength) and the mechanical stimuli determines whether the plaque will rupture or not, and thus how 'vulnerable' the plaque is. This process is more extensively described in Chapter 2.

It is also important to realize that histological classification of a plaque is a snap-shot in time, capturing the plaque composition only at one specific stage. The complex interaction between biological and mechanical stimuli leads to changes in plaque composition over a relatively short time frame. Furthermore, plaques do not always advance in one direction. Already in the 1980s, it was suggested that stable plaques do not only progress over time, but they can also undergo regression[22]. By only using histology, it is hard to capture this complex natural history of atherosclerotic plaques. Therefore, (invasive) imaging techniques are nowadays more frequently applied to detect changes in plaque size and composition over time, both to increase our understanding of disease pathophysiology, but also to guide clinical interventions (as further described under '1.4 Invasive imaging of coronary atherosclerosis').

All knowledge on atherosclerosis pathophysiology, as described above, is the result of decades of research. Unfortunately, it remains unclear what the exact circumstances are that determine in which individual patient, and where in the coronary system of that individual, plaques develop, progress, destabilize, rupture ánd cause an event. Two important challenges now lie in 1) further elucidating these exact conditions, and 2) finding biomarkers that enable selection of patients at risk.

The role of lipoproteins in atherosclerosis and their potential as a biomarker for event prediction

The physiological role of plasma lipoproteins is the transportation of water-insoluble cholesterol and lipids between the liver and the body's cells through blood. Lipoproteins have an outer shell consisting of phospholipids and cholesterol with embedded apolipoproteins. These apolipoproteins give the particle its functional identity. There are five types of plasma lipoproteins, classified according to their apolipoproteins and density: high-density lipoproteins (HDL); low-density lipoproteins (LDL); intermediate-

density lipoproteins (IDL); very-low-density lipoproteins (VLDL) and chylomicrons (also called 'ultra-low-density lipoproteins)[23]. As already mentioned in the previous section, uptake and oxidation of LDL particles in the vessel wall forms one of the main triggers for early atherosclerosis development[24].

The human LDL pathway in its physiological state acts to protect against atherosclerosis formation. The tight regulation of LDL receptor expression, and the high affinity of this receptor for LDL, enable the body to maintain the plasma LDL concentration below the threshold level for atherosclerosis development[25]. However, upon (pathological) elevation of plasma LDL levels, due to genetic mutations (familial hypercholesterolemia) or environmental factors like diet, LDL intrusion into the vessel wall increases at locations of endothelial cell dysfunction, which leads to early plaque formation[25].

Also the clinical guidelines reflect that LDL is considered as the major cholesterol transport particle responsible for the development of coronary artery disease[26]. Patients with a high risk of developing coronary artery disease (like patients with familial hypercholesterolemia), are receiving standard medical care to lower their (LDL) cholesterol levels[27]. Treatment includes high doses of statins and/or new, highly potent lipid-lowering drugs like PCSK9 inhibitors. Although high-intensity treatment is very effective in patients with a high (residual) risk of developing cardiovascular diseases, for patients with a low risk, this high-intensity treatment might not be necessary. Unfortunately, while for the patients as a group the cardiovascular disease risk can be predicted by age, sex, smoking and plasma levels of LDL-c and some known subtypes of LDL like Lp(a)[28], the risk of individual patients is hard to predict using these factors[29]. To improve patient risk stratification, but also to reduce costs related to overtreatment of low-risk patients, more accurate biomarkers are highly needed.

For a long time it has been known that LDL particles display a very heterogeneous phenotype with regard to size, density and molecular composition[30]. However, the biological function of many of these different particles remains unclear. One of the goals in future research is to further characterise and analyse the function of these LDL types, which might result in the discovery of new biomarkers that more reliably predict the individual risk of atherosclerotic disease development.

Invasive imaging of coronary atherosclerosis

Over the years, different imaging methods have been developed to detect coronary plaques for diagnosis and treatment purposes, but also to gain more insight in the natural disease process. X-ray based contrast angiography and the earliest invasive imaging studies mainly focussed on the lumen dimensions and on the size of the coronary plaques as a predictor for acute events[31]. However, of the culprit plaques

that are responsible for the initiation of an acute myocardial infarction, only 14% has a stenosis degree >70%[32]. Even more striking is the fact that 68% of these culprit lesions have a stenosis degree <50%[32,33]. These findings indicated that not only plaque size, but also plaque composition is of major importance for plaque risk-assessment. The development of high-resolution, invasive imaging techniques that enabled detection of different plaque components has therefore proven highly valuable[31].

The two most frequently used invasive, catheter-based imaging techniques are intravascular ultrasound (IVUS) and optical coherence tomography (OCT)[34]. IVUS is a technique that is based on measuring the reflection of sound waves. The high penetration depth of IVUS enables acquisition of detailed information on plaque size, and IVUS can reliably detect calcifications (Figure 1.3A-B). However, the technique also has limitations: the relatively low resolution (~200μm) does not allow analysis of smaller plaque components and cap thickness[34]. Furthermore, blockage of the signal by calcifications hampers plaque size measurements in calcified arteries[35] (Figure 1.3B). Moreover, IVUS cannot detect lipids. By the application of signal analysis techniques using the IVUS radio-frequency-signal, more information on tissue type could be added to the IVUS analysis. The most well-known application of this methodology is virtual-histology (VH-)IVUS[36]. Unfortunately, VH-IVUS is not widely applied in the clinic, partially due to limited histopathological validation[37].

The inability of IVUS to detect lipid-rich plaques has (partially) been overcome by the introduction of the combined near-infrared spectroscopy (NIRS)-IVUS catheter. The NIRS technique provides information on the probability of the presence of lipids inside atherosclerotic plaques, based on differences in absorption spectra of the various tissues. The technique has proven to be effective in detecting the plaques that contain a lipid-rich necrotic core, both in *ex vivo* samples as well as in *in vivo* clinical studies[38,39]. Furthermore, the ATHEROREMO, IBIS3[40] and LRP[41] studies showed that the NIRS-derived lipid-core burden index (LCBI), representing the percentage of artery containing lipid-rich plaques, is associated with an adverse cardiac outcome in coronary artery disease patients. The NIRS-IVUS catheter thus provides important information on both plaque size, as well as on some compositional features (Figure 1.3A-B). However, IVUS still lacks the resolution and imaging contrast for detecting all characteristics of vulnerable plaques[34].

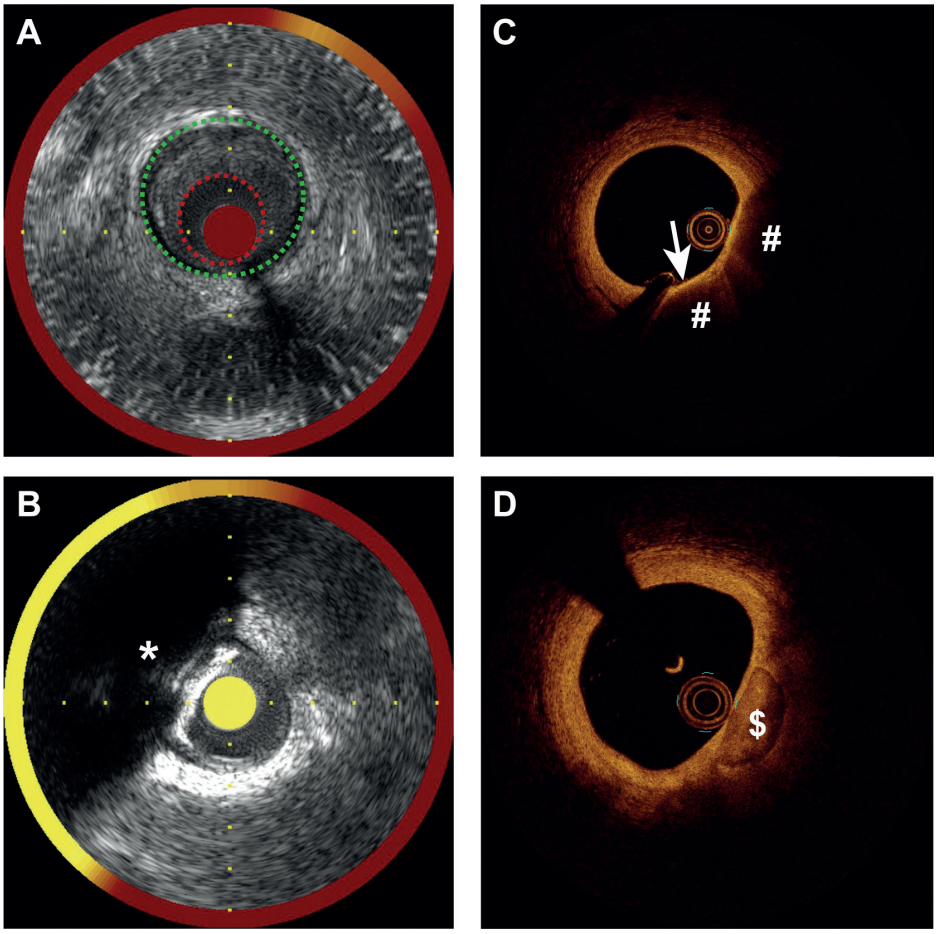

Figure 1.3: Example images of NIRS-IVUS and OCT. A-B) NIRS-IVUS images. The grey-scale background image is derived from IVUS. The red/yellow ring around the image is a visual representation of the probability of the presence of lipids derived from NIRS (yellow=high, red=low). **A)** Eccentric plaque in which lumen (red dotted line) and outer vessel wall boundaries (green dotted line) are indicated. **B)** Calcified plaque. The calcification results in a high intensity, bright signal with a sudden signal drop behind it (*), hampering detection of the outer vessel wall. **C-D)** OCT images. **C)** Left/top side of the artery: healthy vessel wall with a 3-layered appearance. Right/bottom side of artery: a lipid-pool (#) with overlying thin fibrous cap (arrow), indicative for a thin-cap fibroatheroma. **D)** Calcified plaque. The calcification can be seen as signal-poor heterogeneous regions with a clearly delineated border ($).

OCT is a light-based imaging technique that has a high resolution (~10µm), thereby enabling highly detailed analysis of plaque microstructures like cholesterol crystals and fibrous cap thickness (Figure 1.3C). Furthermore, in contrast to IVUS, OCT can detect lipids and, since light waves penetrate through calcifications, also the backside of the calcification can be visualized (Figure 1.3D)[34]. The main disadvantage of OCT is the limited penetration depth. This hampers plaque size quantification in case of large plaques. Furthermore, in parts of the coronaries with a large diameter like the left main coronary artery, the vessel wall can be partially or completely out-of-view[42].

Both OCT and IVUS have complementary advantages and limitations. By using a combination of both imaging techniques, one can obtain a detailed image of the size and structure of the plaque. Furthermore, the use of these catheters in serial imaging experiments enables detailed serial assessment of the changes in plaque size and composition. However, using multiple catheters is expensive, and increases patient burden and procedure length. Besides the development of integrated catheter systems, further research to image interpretation and development of automated detection software might help to extend the use of invasive imaging in procedure guidance and in patient risk-prediction.

Shear stress as a trigger for atherogenesis and atheroprogression

Atherosclerotic plaques develop at predilection sites in our arterial system, for example in the inner-curvature of the aortic arch and at bifurcations[43]. Although the development of atherosclerotic plaques is a complex biological process involving systemic risk factors, the frictional force 'shear stress' is an important determinant in the localization of plaque development[44]. Shear stress is a biomechanical force produced by the flow of blood over the endothelial cells and is dependent on the near-wall blood flow velocity gradient, vessel diameter and blood viscosity[45]. Different flow velocity profiles give rise to different shear stress levels (as further explained in Chapter 3). For example, at bifurcation regions or in curves, the peak velocity shifts towards the outer curve of the artery, giving rise to high shear stress regions in the outer curve and low shear stress regions in the inner curve. Due to the pulsatile nature of our blood flow, the absolute flow velocity and shear stress levels vary over the cardiac cycle. Therefore, time-averaged wall shear stress, the wall shear stress averaged over the cardiac cycle, is often used for quantification purposes (Table 1.1).

Atherosclerotic plaque development and shear stress are related since (changes in) shear stress can be 'sensed' by endothelial cells. Shear stress can influence vascular behaviour via mechanotransduction[52]. This process is particularly important since physiological variations in shear stress regulate vascular diameter. Higher shear stress is essential

Table 1.1 Overview of the (multidirectional) shear stress metrics

Shear stress metric	Description	References
Time-averaged wall shear stress (TAWSS)	Shear stress averaged over the cardiac cycle	46,47
Oscillatory shear index (OSI)	Ratio between back- and forward going shear stress	48
Relative residence time (RRT)	Relative time that a blood particle resides at a certain location at the vessel wall	49
Transverse wall shear stress (transWSS)	Shear stress vector along the wall, in perpendicular direction to the main flow direction	50
Cross-flow index (CFI)	The transWSS normalized for wall shear stress	51

for maintaining vascular homeostasis, and creates an atheroprotective environment. In regions with low wall shear stress, endothelial cells are activated and express pro-inflammatory chemokines, cytokines and adhesion molecules. This activated state is, as mentioned before, often called 'endothelial cell dysfunction' and underlies initial atherosclerosis development[9].

In order to further investigate the role of wall shear stress in atherogenesis, but also in plaque progression and destabilization, wall shear stress has to be assessed in a consistent and well-defined manner.

Computation of wall shear stress

The most precise method to compute wall shear stress is by using computational fluid dynamics (CFD). The data needed to perform CFD consist out of: 1) an accurate 3D geometry of the coronary lumen, 2) a measure of blood viscosity for which often a standard value is used, and 3) specific in- and outflow boundary conditions for the inlet and outlet of the artery.

The 3D reconstruction of the coronary lumen can be derived from imaging data. Most research groups[53–58] rely on the fusion of biplane X-ray angiography with either IVUS or OCT data to reconstruct the surface of the lumen, a method that was developed by Slager et al.[59]. This method was improved by van der Giessen et al.[60] who used CT-angiography instead of X-ray angiography to further advance the accuracy of the 3D geometry assessment.

In many studies, side branches are not taken into account in the 3D reconstruction. This is unfortunate, since side branch regions are prime locations for plaque development and are therefore highly interesting to assess the relationship between shear stress

and atherosclerosis. Furthermore, without taking the side branches into account, the amount of blood passing through a continuously narrowing artery is overestimated. This inherently leads an overestimation of the shear stress levels at the distal parts of the artery, hampering a reliable assessment of the relationship between shear stress and atherosclerosis development in these regions[61]. Some studies attempted to incorporate side branches based on biplane angiography[57,58]. One limitation of this method is that it is hard to assess the exact location of the bifurcation based on only two 2D images. The most accurate way to model the exact anatomy of the coronary side branches is again by using CT-angiography. Gijsen et al.[62] showed that it is feasible to combine IVUS and CT angiography imaging to get an accurate, and highly detailed 3D reconstruction of bifurcation regions.

Besides a detailed 3D geometry of the coronary artery, also the boundary conditions are important to obtain an accurate shear stress estimation. Blood flow velocity is one of the main determinants of shear stress, but is highly variable between individuals and also between arteries. Therefore, personalized and local flow velocity measurements are preferred. The most direct and accurate way to assess local flow velocity is by using catheter-based Doppler flow measurements[63,64].

The relation between wall shear stress and coronary atherosclerosis: evidence from in vitro, pre-clinical and clinical studies

The association between shear stress and endothelial dysfunction was first established in *in vitro* studies[65]. Subsequently, both pre-clinical and clinical serial imaging studies confirmed the role of time-averaged wall shear stress in the initiation, progression and destabilization of atherosclerotic plaques[48,57,66–71]. The role of wall shear stress is however complex and sometimes appears contradictive since both high and low time-averaged wall shear stress have been linked to plaque development[48,57,66–71]. When assessing the role of wall shear stress in plaque development, it is important to distinguish which stage of atherosclerosis is studied. As mentioned, in plaque initiation and early progression, the role of low time-averaged wall shear stress is well established. In more advanced disease stages, with high stenosis degrees, local increase of velocities and thus of wall shear stress, inevitably leads to colocalization of high wall shear stress and an advanced plaque phenotype. In these situations, high shear stress is a reflection of, and hence can be considered as a marker for, advanced, possibly vulnerable disease[72,73]. Although high wall shear stress also plays a direct causal role in plaque destabilization[74], the absolute force exerted by shear stress on the plaque is very small (in the order of 1 Pa). Therefore, larger forces like high tensile stress (~30,000 Pa) are more likely to be directly involved in the process of plaque rupture[74].

Time-averaged wall shear stress is the most commonly used wall shear stress parameter. However, this metric only describes shear stress in the main flow direction. Due to the pulsatile nature of our blood flow in combination with the 3D geometry of the artery, local changes in flow-velocity direction, and thus in shear stress, can occur. Therefore, in recent years, new shear stress metrics have been introduced to capture this multidirectional shear stress behaviour (Table 1.1). The influence of some individual multidirectional wall shear stress metrics on plaque development was pointed out in a few studies[48–50,75–77]. However, absolute wall shear stress levels are highly dependent on the used computation and imaging methodology (as described above). Therefore, a comprehensive study that assesses the influence of all (multidirectional) wall shear stress metrics is needed in order to compare the value of the individual metrics, both in plaque initiation and progression.

Helical blood flow as a potential atheroprotective factor

The curves and twists present in most arteries result in blood flow that describes a helical flow pattern. Helical flow is a combination of the rotational motion of the blood in the direction perpendicular to the main flow direction, and motion of the blood in the main flow direction (Figure 1.4). The existence of helical flow in our arterial system has been explained as a phenomenon that optimizes physiological blood transportation and stabilizes blood flow, thereby minimizing flow disturbance[78]. Reduction of this flow disturbance will minimize the exposure of the wall to low or multidirectional wall shear stress[79]. Hereby, helical flow could form an atheroprotective factor. Helical flow patterns have been observed in the aorta and in carotid, femoral, iliac, basilar and pulmonary arteries (see overview Table in Chapter 7). However, there is only scarce information present on the occurrence of helical flow in coronary arteries, and on how helical flow descriptors relate to the above-mentioned shear stress metrics in the coronaries. Also the direct relationship between helical flow and coronary atherosclerotic plaque development has so far not been investigated.

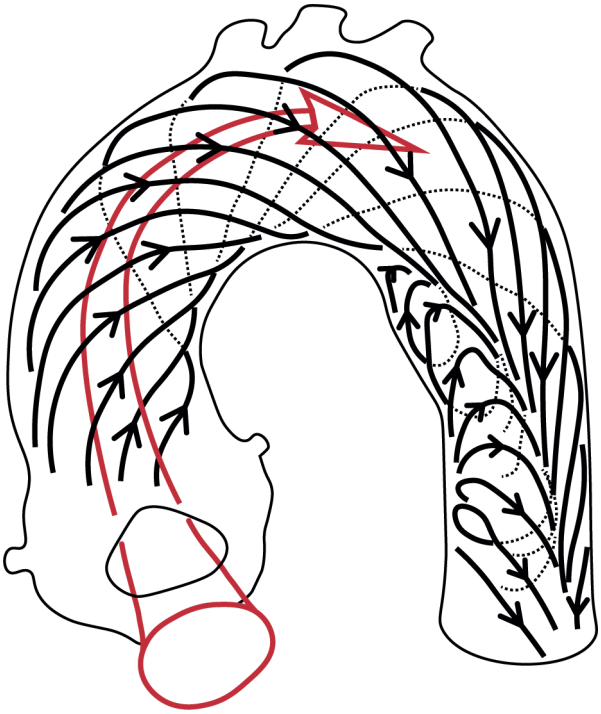

Figure 1.4: Helical flow in the aortic arch. While the main flow direction (red arrow) is following the curve of the artery, the blood flow is describing a helical flow pattern (black lines). Image inspired on Liu et al.[80].

THESIS AIM AND OUTLINE

This thesis is subdivided into three parts. These parts address different aspects of coronary atherosclerosis research, aimed to gain more insight in the development of coronary atherosclerosis and to assess the potential of new biomarkers that can be used to improve cardiovascular-related patient risk-prediction.

Part I:
Animal models of atherosclerosis

Animal models are highly valuable in atherosclerosis research, not only to study disease pathology, but also to test new pharmaceutics and imaging techniques. Many different animal models have been studied over the past years, but the quest for finding animal models that better mimic human disease is still ongoing. In the first part of this thesis, two studies are described that investigated the potential of existing atherosclerotic

animal models and that discussed the biomechanical aspects of atherosclerosis development in these models.

In **Chapter 2** of this thesis, an overview is given of animal models that present with atherosclerotic plaque rupture. While plaque rupture is seen as the ultimate proof of the presence of vulnerable plaques, plaque destabilization and rupture risk are greatly dependent on the biomechanical environment of the plaque. In this chapter we elaborate on the differences in (disease) biomechanics between humans and atherosclerotic animal models to improve the interpretation and clinical translation of the results derived from these models.

Chapter 3 a literature study is described on animal models in which the blood flow is surgically manipulated to induce the development of atherosclerosis. The influence of the different surgical manipulations on blood flow velocity and wall shear stress is discussed, and the resulting atherosclerosis development is described.

Part II:
Biomarkers of atherosclerosis

In the second part of this thesis, we investigated the potential of three biomarkers for atherosclerosis development and patient risk prediction. These biomarkers are circulating lipoproteins, wall shear stress and helical flow.

In **Chapter 4**, we describe an extensive characterisation of coronary atherosclerosis development in a porcine model of familial hypercholesterolemia. Serial, multimodality invasive imaging and histopathology were used to monitor the development, composition and location of coronary atherosclerotic plaques in these animals. Lipoprotein profiling was applied to investigate observed differences in atherosclerosis severity between animals. As a first proof-of-concept study, the findings derived from these pre-clinical lipoprotein analyses were tested in a small cohort of human homozygous familial hypercholesterolemia patients.

A second potential biomarker for vulnerable plaque development is described in **Chapter 5**. In this chapter, the porcine model from Chapter 4 was used to assess the role of five (multidirectional) wall shear stress metrics in coronary plaque development. Furthermore, the predictive values of these shear stress metrics for plaque growth, as well as for advanced plaque composition, were analysed.

In the study described in **Chapter 6** we investigated whether a relation between multidirectional wall shear stress and plaque development can also be found in humans with more advanced coronary atherosclerosis. In non-culprit arteries of patients with an

acute coronary syndrome, the individual and synergistic effects of (multidirectional) wall shear stress and plaque-lipid composition on advanced plaque growth were assessed.

Chapter 7 presents a study on the occurrence of helical flow in the coronary arteries using the data derived from the porcine model described in Chapter 4. The link between helical flow descriptors and (multidirectional) wall shear stress parameters is studied and the direct relation between helical flow and plaque development was assessed.

Part III:
Invasive imaging markers of atherosclerosis

In the last part of this thesis, two methods are presented that aid in improving the interpretation of invasive imaging for patient risk-assessment in the field of coronary atherosclerosis.

As described, the main limitation of OCT is the limited penetration depth, hampering the quantification of plaque burden in the case of large and/or lipid-rich plaques. However, plaque burden has proven to be an important predictive value for future cardiovascular events and is thus important to assess. Therefore, in **Chapter 8**, we present a study that aimed to assess the direct relation between the OCT-derived plaque free wall angle and the IVUS-derived plaque burden. Existence of this relation could help to overcome one of the limitations of the OCT catheter for assessment of plaque and patient risk.

Besides general plaque burden, also plaque composition has proven to be an important factor in determining future risk of plaque rupture. Both lipid-rich plaques (as detected by NIRS) and calcified arteries (detected by CT) have been associated with an increased event-risk. The introduction of the combined NIRS-IVUS catheter now enables the simultaneous, intravascular assessment of both plaque components. In **Chapter 9**, an observational study is described that assessed, in high detail, the colocalization of lipid-rich and calcified regions in coronary atherosclerotic plaques.

In **Chapter 10** the main findings of this thesis are summarized and placed in a clinical perspective. Furthermore, the potential implications of these findings for the future are discussed.

Part I

Animal models of atherosclerosis

CHAPTER 2

Animal models for plaque rupture: a biomechanical assessment

Kim van der Heiden*
Ayla Hoogendoorn*
Mat J. Daemen
Frank J.H. Gijsen

Based on:

'Animal models for plaque rupture: a biomechanical assessment',
Thrombosis and Haemostasis, 2016

*authors contributed equally

ABSTRACT

Rupture of atherosclerotic plaques is the main cause of acute cardiovascular events. Animal models of plaque rupture are rare but essential for testing new imaging modalities to enable diagnosis of the patient at risk. Moreover, they enable the design of new treatment strategies to prevent plaque rupture. Several animal models for the study of atherosclerosis are available. Plaque rupture in these models only occurs following severe surgical or pharmaceutical intervention. In the process of plaque rupture, composition, biology and mechanics each play a role, but the latter has been disregarded in many animal studies. The biomechanical environment for atherosclerotic plaques comprises of two parts, the pressure-induced stress distribution, mainly -but not exclusively- influenced by plaque composition, and the strength distribution throughout the plaque, largely determined by the inflammatory state. This environment differs considerably between humans and most animals, resulting in suboptimal conditions for plaque rupture. In this review we describe the role of the biomechanical environment in plaque rupture and assess this environment in animal models that present with plaque rupture.

INTRODUCTION

Atherosclerosis-induced clinical events like coronary heart disease, ischemic stroke and peripheral vascular disease are a result of arterial stenosis and/or thrombosis. The latter is caused by atherosclerotic plaque rupture (A), endothelial plaque erosion (B) or protruding calcified nodules (C)[81–83]. In man, only a subset of plaques with distinct morphological features is prone to rupture. These plaques were termed "vulnerable" in 1989 by Dr. James E. Muller[84]. Please note that the term *vulnerable* plaque is valid for all three plaque morphologies (A-C) that can cause arterial thrombosis[17]. In the past decades, the disease process has changed, not only by means of our medical interventions, e.g. use of statins, but also by changes in risk factors, e.g. increase in diabetic patients, increase in obesity and decrease in smoking[85]. Plaque rupture is still considered the main cause of cardiovascular events, but plaque erosion appears to be on the rise[85]. As animal models for plaque erosion and calcified nodules are currently lacking, we will focus on plaque rupture and will therefore only take into account the vulnerable plaque models that show events of rupture.

The burden of atherosclerotic disease in humans is traditionally estimated from the percentage of stenosis detected by coronary angiography or carotid CT, MRI or IVUS. However, these techniques fail to detect non-stenotic – possibly vulnerable - plaques as the degree of stenosis does not correlate to plaque vulnerability[33]. Patients without stenosis could still present with vulnerable atherosclerosis and consequently be at risk of cardiovascular events. In the 1990s, work by the groups of Dr. Virmani[86], Dr. Davies[87] and Dr. Falk[88] demonstrated that plaque composition correlates to plaque vulnerability, which eventually resulted in the publication of a consensus paper on vulnerable plaque terminology[89].

However, finding the vulnerable plaque in humans with current imaging techniques appears not to be the 'holy grail' to predict rupture-related future events. Different large clinical trials like the PROSPECT study[31] showed a very low future event rate in patients diagnosed with plaques characterized as vulnerable. One could state that not all vulnerable plaques rupture, or take it even further and state that most vulnerable plaques will never rupture. Moreover, even plaques characterized as stable did show some events of plaque rupture. This apparent contradiction in terminology can be explained in many cases by looking at the different biomechanical factors influencing plaque rupture. Both progression and regression of plaques is influenced by the whole organism environment which includes aspects like blood composition and blood pressure, but also genetics. All these processes can be described by three factors: the plaque composition, the underlying biological processes and the mechanics. All these factors have an individual effect on the plaque but also influence each other. This

complex interplay determines the development but also the fate of the plaque: further progression, regression or rupture.

During the past decade, a lot of research effort was put into development of new imaging modalities to detect specific plaque components in order to identify the patient at risk. Moreover, defining the biological and biomechanical mechanisms responsible for plaque destabilization and rupture would enable the development of new treatment strategies. Disease progression was studied in several longitudinal clinical studies, but these studies were limited by the fact that patients were already symptomatic upon study inclusion. Prospective cohort studies, like the Rotterdam ERGO study[90], provide insight into carotid plaque development and progression since the subjects are asymptomatic upon inclusion. However, imaging modalities to delineate plaque composition like nuclear or intravascular imaging, cannot be tested on these subjects. Therefore, we are restricted to post mortem or *ex vivo* imaging of diseased human arteries, accepting the major limitation of a cross sectional study and fully advanced disease state. To study the natural history of a plaque, test experimental imaging modalities and treatments, and gain mechanistic insight into plaque destabilization, we have to resort to animal models.

The use of the term 'vulnerable plaque' in humans[89] is however different from what is termed a vulnerable plaque in most animal models. While vulnerability in humans is related to a high risk of rupture, in animals, the term vulnerability is usually used only to refer to plaques with morphological characteristics of a vulnerable plaque, without actually resulting in plaque rupture. Moreover, animal models for vulnerable plaque pose a problem in the fact that all three factors i.e. the plaque composition, the biological processes and the mechanics, are different compared to the human setting. To promote plaque rupture in an animal model, all these parameters can potentially be altered to optimize the biomechanical conditions. In this review we will further discuss plaque composition in the context of biomechanics and rupture for both humans and appropriate animal models.

THE VULNERABLE PLAQUE CLASSIFICATION

The American Heart Association (AHA) classification, which was slightly adapted by Virmani et al., describes the histological composition of the different stages of human atherosclerotic plaques[91]. In short, the natural accumulation of smooth muscle cells (SMCs) in the intima i.e. adaptive intimal thickening is regarded as the first step in lesion formation. When foam cells are observed in these lesions, the lesions are called xanthoma or fatty streaks. The term pathological intimal thickening is used when,

besides SMCs and foam cells, extracellular lipids are present in the form of a lipid pool. Upon the introduction of inflammatory cells and necrosis, lesions have developed into fibroatheroma (FA; type IV lesion) which have a very low risk of rupture. These are highly cellular lesions with few lipids, a thick cap with abundant SMCs and collagen, little inflammation, and little necrosis/apoptosis. FAs can present with a thick fibrous cap or a thin cap (<65 µm in coronary plaques) overlying the necrotic core/lipid pool. The latter are termed thin cap fibroatheroma (TCFA) and are seen as the precursor lesions of plaque rupture.

It is important to realize that a classification based on composition/histology is a snapshot in time. During the natural history of atherosclerosis, plaques undergo compositional changes which are influenced by many different biological processes like inflammation and oxidative stress[92]. These biological processes can in turn be influenced by the composition of the plaque itself but also by changes in mechanically-induced signalling. Due to this complex interaction, plaques constantly change in composition and size and can change into a different plaque type in a relative short period of time[93]. Stable plaques can become more vulnerable over time, but vulnerable plaques can also stabilize[94]. During atherosclerosis development, plaques are exposed to changing mechanical conditions. These include not only the stresses inside the plaque but also the strength of the plaque itself. The fate (will the plaque rupture, progress or regress) of any given plaque at any given time point is determined by the mechanical forces acting upon the plaque. This means that every plaque has the potential to rupture, and could therefore be called 'vulnerable'. The likelihood of rupture however depends both on the composition as well as on the mechanical stimulus (Figure 2.1).

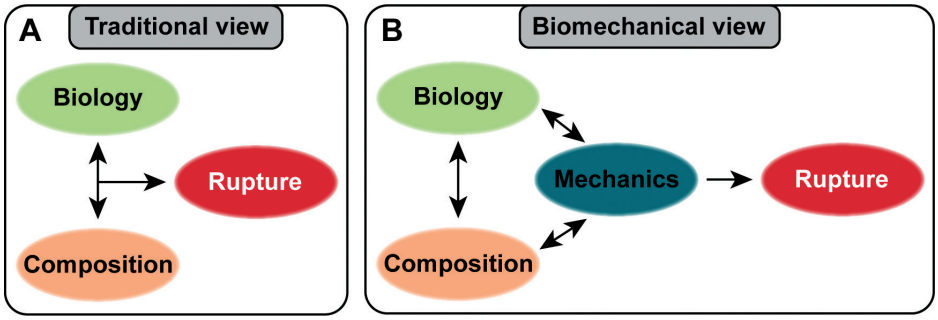

Figure 2.1: A) schematic overview of the traditional view of plaque composition, influenced by biological processes and vice versa, determining the risk of rupture. **B)** Biomechanical view of the processed that determine the risk of rupture. Note that especially the mechanics differ between humans and animals.

PLAQUE RUPTURE: A MECHANICAL PROCESS

Failure of a structure is a mechanical event in which the structure loses its integrity due to the forces it is exposed to. Failure, or rupture, occurs when the forces exceed a certain threshold value. From an engineering perspective, forces in a structure are often described using 'stress', while the threshold value is referred to as 'strength'. Irrespective of the rupture mechanism, the underlying paradigm is identical: cap rupture will occur if local stress exceeds local strength.

To understand and predict cap rupture, we therefore need to know the cap stress distribution and the strength of the cap. Almost all studies in human plaques focus on cap stress. This quantity is usually determined using a numerical technique called finite element analyses (FEA). This tool is a commonly used technique in various engineering disciplines and is applied to predict the mechanical behaviour of complex structures under various loading conditions. Applications of FEA range from optimizing airplane design to predicting mechanical heart valve failure. FEA requires three main input parameters, all of them relevant for the cap stress computations. First, the mechanical loading conditions are required. The main mechanical load for the cap is the intraluminal blood pressure. The second input parameter is the plaque geometry, including size and shape of the individual plaque components. Finally, the material properties of these components need to be described by a material model, which relates the forces to the resulting deformation of a material. Cap strength is much less intensively studied, and is mostly investigated in an experimental setting[95].

PLAQUE RUPTURE IN HUMAN PLAQUES

Many FEA studies investigated the impact of various geometrical risk factors on peak cap stress. In idealized geometries, cap thickness and necrotic core size were identified most influential [96,97]. The often-reported threshold for cap thickness of a vulnerable plaque is 65 µm. This threshold value was derived from morphometric analyses in 41 ruptured caps[86], in which 95% had a thickness smaller than 64 µm. The mean cap thickness was 23±19 µm, indicative of the large variation in that small sample. This is further corroborated by the study of Akyildiz et al.[98] in which they studied 77 intact human coronary plaques. The median cap thickness in that population was 190 µm, with 25% of the plaques having a cap thickness lower than 65 µm. In conclusion, there are caps thicker than 65 µm that did rupture, and there are many intact caps thinner than 65 µm. Thin caps and large necrotic cores lead to high peak cap stresses. In realistic geometries[98], this picture changes: cap thickness is still the most relevant parameter, but necrotic core size is less important, and lumen curvature and radius emerge as

independent predictors of peak stress. From these studies, it can be concluded that geometrical features of type IV plaques indeed are associated with elevated peak cap stress. However, there is also considerable variation, and not all type IV plaques will harbour caps with high peak cap stress, while some other –histologically stable- plaque types will have high peak cap stress.

The stresses in the plaque are also influenced by the mechanical properties of the plaque components. The properties of the plaque components can be described using material models. Most of the material models used in numerical studies are relatively simple[99,100] and characterize the property of a plaque component with a single value, the stiffness. The influence of the stiffness of the plaque components was investigated in several numerical studies. Especially the stiffness of the intima was shown to be important for peak cap stress[99]: stiffer intima properties will generally induce higher stress. Essentially the same holds for the residual stress: in the context of adequate quantification of absolute values for the peak cap stress, we need to establish the value of the residual stresses inside a plaque[101].

Cap strength is much less investigated. The most influential study used a combination of experimentally observed rupture locations and determined the peak stress at the rupture location. A threshold value was derived from that study[102], and this threshold value is used in almost all studies investigating rupture risk. A single threshold value is unlikely to be sufficient to determine rupture risk, since it was shown that cap strength shows quite some variation and is influenced by macrophages[95], collagen content[103], and possibly microcalcifications[104].The fact that plaque rupture occurs in human plaques reflects their biomechanical environment. This environment comprises of two parts, on the one hand pressure-induced stress distribution throughout the plaque and on the other hand the strength distribution throughout the plaque. Apparently, the conditions for human plaques are such that cap stress locally exceeds cap strength, leading to cap rupture. Although many uncertainties need to be dealt with, certain general statements can be made for the human situation. Histological plaque classification makes sense from a biomechanical perspective: plaques with a large lipid core, thin fibrous cap and complex shapes lead to high peak cap stresses[105]. The presence of macrophages and reduction of collagen content decrease cap strength. Together with elevated blood pressure, these plaques are at high **risk** of rupture. However, the true risk of rupture depends on the whole organism environment described by the interplay between plaque composition, biology and the mechanical environment (Figure 2.1), rendering a histologically-deemed stable plaque still at risk of rupture in a mechanically harmful environment. Conditions that can be mimicked –or exaggerated- in a lab setting, but how are these relevant biomechanical conditions for rupture in animal models?

THE MOUSE AS A MODEL FOR PLAQUE RUPTURE

The mouse has so far been the most often used model for vulnerable plaque due to its low costs, small size, fast plaque development and the many options available to induce genetic modifications. There are however some pronounced differences between mice and men regarding metabolism and physiology. Mice do not develop plaques naturally, but, in transgenics, plaque growth can be induced by different stimuli. Plaques in humans are more commonly located in the coronary arteries, carotid bifurcations, abdominal aorta, iliofemoral arteries, and carotid bifurcations, while atherosclerotic mice present plaques in the aorta, carotid bifurcation and brachiocephalic artery[106,107]. Furthermore, mice have a different LDL/HDL balance compared to humans[108]. Regarding plaque composition, murine plaques mainly consist of inflammatory components while these form only a very small part of the total plaque volume in humans[109]. Intraplaque haemorrhage (IPH), one of the driving factors of plaque destabilization in humans[15], is rarely reported in mice, just as the presence of luminal thrombi after an event. The latter could however be the result of a very fast clearance of the thrombus due to differences in the fibrinolytic system between mice and man[106,107].

Plaque rupture in mice: general biomechanical considerations

The prevalence of plaque rupture in mice was debated extensively[107,110–115]. Although some vulnerable plaque features can be copied in genetically and surgically manipulated mouse models, plaque rupture, according to the human definition, is rare. Apparently, the biomechanical environment for murine atherosclerotic plaques significantly differs from the human situation. The most striking difference between human and murine plaques is their size. Size does influence the mechanical environment significantly, and this is easily demonstrated using the well-known law of Laplace, which predicts the circumferential stress (σ) in a tube with wall thickness h and radius r loaded by a pressure p. It reads:

$$\sigma = (r/h) * p$$

This law is often used to predict average stress in a healthy arterial wall, and it demonstrates that the average stress in the wall of an artery with a radius of 2 mm and a wall thickness of 0.2 mm is identical to the average stress in an artery with a radius of 0.1 mm and a wall thickness of 0.01 mm. It also predicts that if the radius of the artery decreases and the wall thickness remains constant, the average stress in the wall would decrease accordingly. Translating this scaling law to atherosclerotic plaques, this implies that a 65 µm thick murine cap has much lower stresses than a human cap of similar thickness[116].

A second notable difference between human and murine plaques lies in their morphology. A comprehensive study[117] investigated plaque stresses in three different murine models, and concluded that morphology of plaques in the mouse models differed considerably from the human situation, leading to a different stress distribution inside the plaque. The murine plaques were often focally adhered to a relatively intact vessel wall. The mechanical load exerted by the intraluminal pressure is mainly carried by the media and adventitia, leading to elevated stresses in these structures. The soft lipid rich plaques deform along with the media and adventitia, leading to lower stresses, especially in the cap of the murine plaque.

The third difference between the biomechanical environment in human and murine plaques might be found in the differences in the material properties. Although experimental data are scarce[118,119], they seem to indicate that murine plaque components are generally softer, leading to lower plaque stresses[96,120].

No experimental data on cap strength in mice is available, although it has to be mentioned that calcifications, thought to reduce cap strength in human plaques[121] are not reported in murine plaque caps. Compared to the biomechanical studies on human plaques, the biomechanical environment in murine plaques is less well characterized and many issues need to be resolved. Not only plaque properties, but also murine cap strength should be investigated in detail. Keeping these uncertainties in mind, the smaller size, the morphological features and the softer plaque components all indicate that cap stresses in murine plaques are lower than in human plaques. The biomechanical environment of most murine plaques seems to be such that plaque rupture will not occur without –drastic- interventions.

To induce plaque rupture in mice, biological and/or mechanical stimuli that alter the biomechanical environment are required. The most applied stimuli include blood pressure elevation, changing local blood flow, increasing inflammation or a combination of these. Below we will describe these models and discuss the potential consequences of the applied stimuli in a biomechanical context.

Biomechanically suitable mouse models for plaque rupture

Some models do show clear signs of plaque rupture, as seen in humans, including luminal thrombi and erythrocytes in the cap cleft but they often use a combination of complex stimuli, which have an individual but also a combined effect on plaque biology and mechanics. Combination of cast (a perivascular device) placement around the carotid artery and p53 adenoviral overexpression to induce apoptosis spontaneously resulted in ‘cap breaks’ with extrusion of the plaque contents in 3 of 14 animals. Additional short

term administration of phenylephrine moderately increased the blood pressure but only resulted in luminal thrombosis and cap breakage in two different mice[122].

The main long-term effect of p53 on the biomechanical environment presumably acts through its effect on SMC apoptosis. The SMC is the main source of collagen production in atherosclerotic plaques. Increased SMC apoptosis can therefore be expected to decrease the total amount of collagen in the plaque, having two important effects on cap biomechanics. First, the overall stiffness of the plaque will decrease, generally leading to a minor decrease in cap stress[96]. Second, a decrease in collagen in the cap will decrease cap strength, and this effect can be expected to outweigh the first effect. The biomechanical environment is also changed due to administration of phenylephrine. This will increase the systolic blood pressure with approximately 15%, which will induce a similar relative increase in cap stress. This explains that the effect of such a minor pressure elevation through phenylephrine administration on the frequency of cap breakage is limited as well.

Of note, the effect of cast placement on the stresses in the plaque was never investigated. Manipulation of arteries through cast placement or ligations will inherently lead to changes in the biomechanical environment. Especially near the edges of cast and partial ligations, the 3D biomechanical stress environment will change drastically. The stiff structures surrounding the wall will prevent the artery to deform, leading to high strains, and therefore high stresses near the edges of the structure. If the cast or ligation induces a severe restriction, differences in luminal pressure between the upstream and downstream side will change the mechanical environment with higher stresses in the upstream region. Furthermore, the development of scar tissue potentially restricts the deformation of the arterial wall immediately upstream and downstream. In conclusion, the effect of cast placement or ligation is very complex, but is potentially important for plaque rupture. Especially near the edges of the cast, stress concentrations occur that are unlikely to be present in human plaques, potentially triggering unnatural failure mechanisms.

A different biological approach was used by Gough et al. (42) who induced molecular weakening of the cap by transfection of $ApoE^{-/-}$ mice with hematopoietic stem cells overexpressing matrix metalloproteinase (MMP) 9[123]. Proven signs of rupture in the form of cap breaks in the shoulder region were observed in almost half of the mice. The main biomechanical effect of overexpression of MMP9 is on cap strength: since it was demonstrated that collagen content is related to cap strength, degradation of this component reduces cap strength and therefore enhance the risk of cap rupture. The overexpression of MMP9 potentially has another important biomechanical effect: if the collagen in the media and adventitia is degraded, the overall stiffness of these two

layers will also decrease. The overall change in deformation could lead to increased deformation in the cap, inducing elevated peak cap stress.

Another study combined a cast and a short term LPS administration together with phenylephrine treatment and cold[124]. In around 30% of the mice they found cap disruption with luminal thrombus and cap breakage with core extrusion. Administration of LPS increases the inflammatory state in general. It was shown that LPS leads to an increase in Th17 cells, which through IL17 induces SMC apoptosis. This potentially decreases collagen content in the plaque, with previously discussed consequences. Phenylephrine will maximize the metabolic state of the heart, leading to increased heart rates and blood pressure. Exposing the animals to cold will increase microvascular resistance, potentially leading to a significantly larger increase in blood pressure, and therefore cap stress, compared to phenylephrine alone. However, no experimental data are available to confirm this.

Some models have used less complex methods to induce plaque rupture. Mice with a partial ligation of the carotid artery and renal artery to induce hypertension[125], formed plaques containing high numbers of macrophages, high MMP activity and there were signs of collagen breakdown and decreased actin content. More importantly, half of the mice showed rupture with luminal thrombi and IPH. The induced hypertension leads to a chronic increase in blood pressure of approximately 40%. This pressure increase exceeds the effect of phenylephrine, leading to a larger increase in peak cap stress. However, this relatively mild increase in the mechanical loading of the plaque alone cannot explain the high prevalence of plaque rupture in these mice. Chronic hypertension might influence biomechanical environment in several other ways. First, the observed increased plaque size leads to a redistribution of the mechanical load, inducing lower stresses in the cap of the plaque. On the other hand, one can argue that, although the plaque is larger, increased blood pressure leads to increased strain inside the plaque, inducing IPH [126]. This is potentially related to the increased inflammatory state of the plaque, which in turn could lead to the reported increased MMP levels in the plaques of these mice. This might induce local weakening of the cap, overruling the overall decrease in cap stress due to increased plaque size.

Clear events of plaque rupture and possible rupture-related events like buried caps[127] were observed in a new mouse model developed by Chen *et al.*[128]. Besides a large necrotic core and thin cap, the lesions proximal to the tandem ligation presented with high numbers of buried caps, ruptured fibrous caps and luminal thrombosis. The prevalence of rupture for the most proximal lesion most probably springs from a combined effect. First, plaque composition in the upstream lesion favours high cap stresses most. Second, the luminal pressures that the plaques are exposed to are

highest for the proximal lesion. Especially the two, highly stenotic, lesions can induce a significant pressure drop leading to large differences in the mechanical loading conditions for the lesions.

Another recent model targeted vessel wall stiffness by putting an ApoE$^{-/-}$/Fibrillin-1$^{-/-}$ double knockout mice on a high fat diet. These mice present with reduced levels of elastin in their vessel walls and consequently stiffer vessels[129]. On a high fat diet these mice developed large plaques with multiple features of vulnerability around the aortic valves, brachiocephalic artery and aorta. The plaques contained low levels of collagen and SMCs, large necrotic cores, macrophage infiltration, numerous buried caps and over half of the mice showed events of acute plaque rupture[129,130]. Uniquely, a high number of mice showed ruptured coronary plaques with thrombi and events of myocardial and cerebral infarction leading to sudden death[130]. The biomechanical effect of knocking out Fibrillin-1$^{-/-}$ most likely is determined by its effect on elastin. The loss of elastin leads to a larger vessel area, even if affected by atherosclerosis. Assuming plaque morphology and blood pressure are unchanged, this would result in exposure of the cap to increased strain levels, and therefore higher stress.

Very recently, a new mouse model was introduced with an inducible adeno-virus mediated gain-of-function mutation in the PCSK9 gene[131]. Induction of this mutation in ApoE$^{-/-}$ mice resulted in hypercholesterolemia and early plaque growth double as extensive as compared to control ApoE$^{-/-}$ mice. Although no further long-term studies have been published so far on advanced atherosclerotic plaque development in this model, these results are promising.

RABBITS AS A MODEL FOR PLAQUE RUPTURE

Another animal often used for vulnerable plaque and plaque rupture research, is the rabbit. The larger size might make rabbits into a preferred model over mice from a biomechanical point of view. In rabbits, atherosclerosis can be induced in the aorta by a high fat diet often in combination with induced endothelial dysfunction or injury[132–136]. It then takes several months before plaques develop, which are small in size, mainly contain lipids and are lacking many of the compositional vulnerable plaque features seen in humans. Rupture can however be induced by a severe, non-physiological and biomechanical relevant stimulus like injection of Russel's viper venom (acute coagulation) plus histamine which directly affects coagulation, endothelial cell attachment and vasoconstriction[137,138] or injection of liquid nitrogen which leads to acute endothelial cell damage[139].

In rabbits with inheritable hyperlipidaemia (WHHL rabbits) large, stable plaques develop in the aorta and coronary arteries (reviewed by Fan et al.[140]). However, a mutant colony of the WHHL, termed the myocardial infarction prone WHHL rabbit (WHHLMI), presents with vulnerable-type coronary plaques displaying a large lipid core, thin fibrous cap, accumulation of macrophages and even intraplaque haemorrhage at an age of 20 months (reviewed by Shiomi and Fan[141]). Plaque rupture was, however, never observed and the observed myocardial infarctions were attributed to stenosed plaques or vasospasm. Despite the fact that the mechanical environment appears more optimal in rabbits compared to mice due to the larger size of the plaques, rupture only occurs after severe stimuli which potentially induce different failure modes in the plaques. The main underlying cause seems to lie in the plaque composition. Although very frequently labelled as 'vulnerable', subtle differences between human and rabbit plaques render them much less rupture prone. Heterogeneity within the plaque, an important source of stress peaks, is generally absent. Moreover, the plaques are predominantly lipid rich, and the cap covering the core does not contain stiff collagen fibres. This implies that the mechanical stresses inside the plaque will be low, and from that perspective, it is not surprising that cap rupture in rabbits was not observed.

PIGS AS A MODEL FOR PLAQUE RUPTURE

Since size and composition matter considerably, larger animal models should be considered for investigating plaque rupture. Primate studies have been performed in the early years but lost focus after growing ethical concern. With regard to its size, anatomy and physiology, the pig now is the number one choice to mimic the human atherosclerotic disease process. From a biological point of view, pigs more closely resemble human metabolism with a comparable LDL/HDL balance due to their omnivorous nature[142]. However, the lack of genetically modified pigs is a limiting factor. Pigs do develop atherosclerosis naturally but, as in humans, it takes a very long time, which is a complicating factor in animal research. To increase the speed of plaque formation, the lipid balance is shifted by feeding a high fat diet. The anatomical positions at which plaques develop and the cardiovascular hemodynamic of humans and pigs are very similar. In contrast to smaller animal models, this model allows for the study of coronary atherosclerosis and can be used for intravascular imaging. The almost optimal biomechanical conditions should allow the development of a vulnerable plaque with potential to rupture. Plaque rupture is unfortunately still a rare phenomenon in pig models.

On a high fat diet, large plaques with vulnerable, human like features develop in normal swine, which takes up to two years[143]. Early models, including the naturally

hypercholesterolemic Rapacz pig[144,145], showed plaques with extensive vulnerable characteristics, including stenotic, complex lesions with necrotic core, fibrous cap, calcifications, inflammation, neovascularization, and IPH. This redirected the main focus of new models towards speeding up the process of vulnerable plaque development. Thim et al.[146] developed a new crossbred of the original Rapacz pig[144]. On a high fat diet, these pigs (n=10) spontaneously developed large plaques in the coronary arteries within half a year, with many features of human plaque vulnerability, including IPH and neovascularization, but no plaque rupture.

In normocholesterolemic pigs, a combination of interventions has been applied to accelerate the process of vulnerable plaque formation. The combination of high fat diet and diabetes was used in multiple studies[56,147–149] and resulted in large, advanced plaques in the coronary arteries, aorta and iliac arteries within half a year. Gerrity et al.[147] used pigs on high fat diet and induced diabetes to study plaque formation. The observed plaques displayed acellular necrotic cores, fibrous cap, medial thinning, IPH and calcifications and were often almost totally occlusive but plaque rupture was not observed. Similar results were obtained in smaller pig studies but none of these showed events of plaque rupture either[56,148,149]. From a biomechanical point of view, plaque rupture is expected to occur more frequently in the diabetic pig models since –on first sight- morphological plaque features and loading conditions resemble the human situation. Closer inspection of plaque composition reveals subtle, but biomechanically relevant differences between plaque composition in diabetic pigs and human. First, the necrotic core is described as 'relatively acellular'[147]. The accompanying histological data reveal plaques with extracellular lipid, but no discernible cholesterol crystals or cell debris. This seems to be indicative of an immature necrotic core. Compared to a true necrotic core, the immature necrotic core contains more cellular components, and they will account for a higher stiffness. This will reduce deformation of the cap, and therefore lower cap stress values will be present in these models. Furthermore, the cap covering the region with extracellular lipids appears to be rather thick [150]. Finally, the absence of a necrotic core will also reduce the inflammatory state of the cap, leading to increased cap strength. The combined effect of these observations, together with the limited number of vulnerable plaques included in most of the studies, might explain the lack of plaque ruptures observed in diabetic pig models.

Multiple studies[151–153] showed the effectiveness of partial carotid ligation in combination with a high fat diet. Large plaques with vulnerable characteristics like a necrotic core, calcium, IPH and thin fibrous cap were seen proximal to the stenosis in the carotid arteries[151,152]. Strikingly, adding diabetes as an additional risk factor, did not result in more vulnerable plaques[154].The only pig model that did show frequent signs of rupture in the form of cap rupture and luminal thrombus formation was developed by Jiang

et al.[153]. At 12 weeks after surgery these pigs displayed large, rupture prone plaques with neovascularization and IPH which were characterized up to AHA stage VI. As an additional sign of rupture even distal emboli were found in the rete mirable at the basis of the skull. The effect of ligation on the biomechanical environment in pigs will share features with the previously discussed effects in mouse models employing a cast or a ligation. In short, the ligation could prevent the artery to deform, leading to high strains and concomitant high stresses. The 70% stenosis created by ligation in the study by Jiang et al. [153] could affect the luminal pressure resulting in higher stresses in the upstream region, where most of the advanced plaques were seen. Note that the stress concentrations that occur are unlikely to be present in human plaques, potentially triggering unnatural failure mechanisms. The fact that rupture **is** observed in this ligation model but not in the other pig models, suggests a potential role for artery deformation and/or luminal pressure in plaque rupture in pigs. The use of relatively young animals, which still have elastic arteries that are capable of deformation, preventing a rise in luminal pressure, could therefore explain the lack of rupture in the other pig studies.

Recently, a new pig model with a mutation in the PCSK9 gene was developed by the group of Falk et al. (Al-Mashhadi, 2013). The first study with this model (n=13) showed promising results, but the most advanced plaques were characterized as FA and did not show signs of a vulnerable plaque type. In a new study design, hypertension was added as an additional risk factor by performing suprarenal aortic banding. The observed FAs appear to develop faster, but final study results have not been published so far[155].

CONCLUDING REMARKS

An optimal animal model to study plaque rupture is currently non-existent. Size, morphology and material properties of mice all result in lower cap stresses compared to human, thus prohibiting plaque rupture. Without drastic intervention, mouse and rabbit models do not demonstrate plaque rupture. Some of the intervention models that do show rupture have potential. Of these, manipulation of the biological processes with the possibility of vascular adaptation is preferred over models that create different cap failure modes by restricting vascular adaptation, e.g. ligation and cast placement. From a biomechanical perspective, plaque composition in rabbits differs too much from human plaques to be relevant for rupture studies. The pig model most resembles the human biomechanical environment ánd plaque morphology. The lack of rupture could be due to subtle differences in plaque composition, limited number of vulnerable plaques, or animal age, and requires more research. Induction of rupture in pigs should preferably focus on increasing stress, by reducing cap thickness, or reducing strength, by

manipulating the inflammatory status. We conclude that despite differences between animal models of atherosclerosis and the human disease process, animal models are still useful and necessary to study separate mechanistic disease processes.

CHAPTER 3

Animal models of surgically manipulated flow velocity to study shear stress-induced atherosclerosis

Leah C. Winkel
Ayla Hoogendoorn
Ruoyu Xing
Jolanda J. Wentzel
Kim van der Heiden

Based on:

'Animal models of surgically manipulated flow velocity to study shear stress-induced atherosclerosis', *Atherosclerosis*, 2015

ABSTRACT

Atherosclerosis is a chronic inflammatory disease of the arterial tree that develops at predisposed sites, coinciding with locations that are exposed to low or oscillating shear stress. Manipulating flow velocity, and concomitantly shear stress, has proven adequate to promote endothelial activation and subsequent plaque formation in animals. In this article, we will give an overview of the animal models that have been designed to study the causal relationship between shear stress and atherosclerosis by surgically manipulating blood flow velocity profiles. These surgically manipulated models include arteriovenous fistulas, vascular grafts, arterial ligation, and perivascular devices. We review these models of manipulated blood flow velocity from an engineering and biological perspective, focussing on the shear stress profiles they induce and the vascular pathology that is observed.

INTRODUCTION

Atherosclerotic plaque development occurs preferentially at geometrically predisposed areas, like the inner curvature of the aortic arch and at arterial branch points. This site-specific development occurs despite the fact that the entire vasculature is exposed to systemic risk factors like hypertension and hypercholesterolemia[58,156]. The specific plaque localization is caused by the local differences in blood flow velocities, and thus the shear stress, to which the vessel wall is exposed to. Besides blood flow-induced shear stress, the vessel wall is also exposed to wall strain. Shear stress is the frictional force generated by the blood flow on the vessel wall, parallel to the endothelium, while wall strain is generated by the blood pressure, perpendicular to the endothelium. Both forces play a role in either plaque initiation and/or development, but shear stress was most often correlated to atherogenesis[45,156,157]. This review focuses on the animal models in which the blood flow velocities, and thereby shear stress, have been manipulated in order to study its causal relation with atherosclerosis.

The SI-unit of shear stress is Pascal (Pa), which is equal to N/m^2 or 10 dynes/cm^2. Shear stress at the vascular wall, wall shear stress (WSS), can be calculated by combining data on flow velocity, blood viscosity and vessel geometry using advanced modelling techniques, and is usually averaged over the cardiac cycle. The most commonly used mathematical technique to calculate shear stress is computational fluid dynamics (CFD). Different blood flow velocity patterns in the vasculature give rise to diverse average WSS levels (Box 1) varying over the whole vasculature and between species. These WSS levels can range from 3-14 Pa in mice, 1-16 Pa in rabbits and 1-2 Pa in humans[158].

The correlation between atherosclerotic plaque localization and different blood flow velocity patterns is caused by the response of endothelial cells (ECs) to alterations in shear stress. ECs react via mechano-transduction by changing gene regulation and, subsequently, cell phenotype. The process of mechano-sensing and -transduction has been extensively studied and reviewed elsewhere[65,159–161]. It includes mechanical deformation and activation of cytoskeletal elements, primary cilia, the glycocalyx, the VE-cadherin/PECAM-1/VEGFR2 complex, integrins, ion channels, and G-protein coupled receptors[65,159–161]. The mechanical signal is subsequently converted into a biochemical signal. When exposed to a high unidirectional laminar shear stress, ECs are quiescent and align into the direction of the blood flow[45,162]. They express an anti-inflammatory and anti-oxidant gene profile controlled by a concerted action of the shear stress-responsive transcription factors of which Krüppel-like factor 2 (KLF2) and nuclear factor (erythroid-derived 2) -like 2 (Nrf2) are the most important[163–168]. An important function of KLF2 is regulating vascular tone via regulation of endothelin-1

(ET-1), a vasoconstrictor[168,169], and endothelial nitric oxide synthase (eNOS), producing the vasodilator nitric oxide (NO).

At regions of low or oscillatory shear stress, the endothelium is activated and shows a pro-inflammatory transcription profile. This pro-inflammatory profile is mainly regulated by activation of NF-kB and its transcriptional targets, resulting in expression of adhesion molecules, a decrease in NO, and a higher permeability to plasma macromolecules, which results in a dysfunctional endothelium that is prone to atherosclerotic plaque initiation[65,170,171].

The different cellular adhesion molecules expressed by the dysfunctional endothelium facilitate adhesion and migration of monocytes and lymphocytes[172,173] into the sub-endothelial layer. There, monocytes differentiate into macrophages, which will take up oxidized low density lipoprotein (oxLDL) and transform into foam cells[174]. These foam cells produce high levels of pro-inflammatory cytokines, chemokines, and growth factors, which attract more inflammatory cells and induce smooth muscle cell (SMC) proliferation and migration into the intima. This results in plaque growth. Initially, plaque growth will not affect lumen diameter due to compensatory outward remodeling[175]. Shear stress remains low and will therefore continue to activate pro-inflammatory pathways, including pathways related to extracellular matrix degradation (reviewed by Wentzel et al.[46]). This process in turn promotes further compensatory outward remodeling[53,66,93,175]. When outward remodelling is not sufficient anymore to avoid lumen protrusion of the growing plaque, the shear stress levels at the plaque will change[176].

During atherosclerosis development, plaques can develop into a stable plaque or a vulnerable plaque. While most atherosclerotic plaques are stable, some develop into a vulnerable or rupture prone plaque[20]. The American Heart Association (AHA) classification[19,20] describes the characteristics of the different stages of human atherosclerotic plaques. The vulnerable or rupture-prone plaques (AHA class IV, V and VI) often show an eccentric phenotype and are defined by a large, lipid-rich necrotic core, a thin fibrous cap infiltrated by inflammatory cells, and outward vascular remodeling[89]. Other common characteristics of human plaque vulnerability are intraplaque haemorrhage, neovascularization, and calcification[19,20,177–181].

Atherosclerotic plaque formation in humans is slow and spans over a period of decades. Furthermore, harvesting plaque tissue from humans is not straight forward, and thus molecular mechanisms involved in the generation and destabilization of plaques can be difficult to investigate. Therefore, several animal models for atherosclerotic plaque development including mouse, rat, rabbit, pig and primate are used. To initiate the atherosclerotic process in these animal models, risk factors like a high cholesterol

level and inflammation are genetically or experimentally induced. Shear stress can be surgically manipulated in these animal models in order to study the causal relationship between shear stress and atherosclerosis initiation and progression. This surgical manipulation can also be used to accelerate the atherosclerotic process. Here we review these surgically manipulated flow models from an engineering and biological perspective.

Box 1.

Blood flow velocity patterns and shear stress

Flow velocity patterns and the concomitant shear stress profiles, depend on the velocity profile itself, blood viscosity, lumen diameter and vessel geometry. A simplified schematic depiction of the different laminar flow and shear stress profiles is shown in Figure 3.1. The different flow routes a blood particle can follow are depicted by the streamlines. Blood flow is laminar in most cases, which means the blood flows in parallel layers, without intersecting. WSS is represented by the slope of the parabolic velocity profile depicted in Figure 3.1A. In case of a stenosis, caused by for example a plaque, flow remains laminar but can separate distal from the stenosis, forming recirculating flow layers near the wall, resulting in low and/or retrograde shear stress at the wall (Figure 3.1B). At a curvature, secondary flow can occur, meaning that flow is moving perpendicular to the flow direction (Figure 3.1C transverse section). This is still considered laminar flow as parallel flow layers are present. The peak velocity shifts to the outer curvature of the vessel, resulting in a higher shear stress at the outer curvature compared to the inner curvature (Figure 3.1C). At bifurcations, secondary flow is present similar to flow patterns seen at curvatures, resulting in particle movement parallel and perpendicular to the vessel wall (Figure 3.1D). This is not to be confused with the term turbulent flow. With turbulent flow, particles do not flow in parallel layers but intersect, and show unpredictable multi-directional, multi-velocity streamlines. Turbulent flow is uncommon but can occur occasionally in the human descending aorta, behind the aortic valve leaflets during peak systole, in large arteries distal to a very severe stenosis and in aneurysms[182–184]. Figure 3.1 summarizes the different flow velocity patterns at one point in time. However, due to cardiac contractions, flow in the arterial system is pulsatile and therefore flow velocities, and the time averaged wall shear stress, may differ in magnitude and direction.

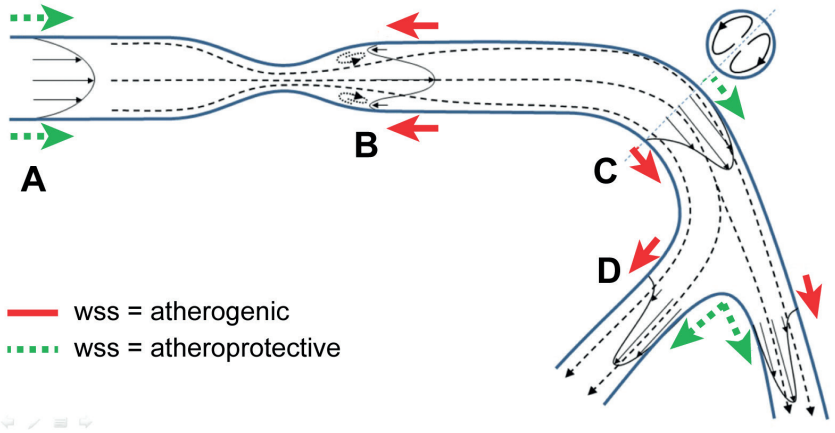

Figure 3.1: A schematic depiction of the different laminar flow and shear stress profiles.

FLOW VELOCITY MANIPULATED MODELS

Arteriovenous fistula models

The arteriovenous (AV) fistula model is one of the first animal models in which surgery was used to manipulate the flow velocities in order to study the correlation between shear stress and atherosclerosis[185]. For the creation of an AV-fistula, an artery is connected directly, end-to-side, to a neighbouring vein, thereby bypassing the distal arterial and venous vascular beds (Figure 3.2A). The AV-fistula is originally developed as a form of permanent vascular access for haemodialysis patients by inducing venous maturation. However, the development of venous neointimal hyperplasia often led to fistula failure. This observation triggered a series of studies with this model on vascular remodelling and maturation of the venous segment, and a few studies on plaque development.

Flow measurements and shear stress calculations in mice demonstrated that creation of an AV fistula resulted in elevated blood flow levels, and concomitantly shear stress, in the arterial segment.

The venous segment showed endothelial dysfunction, which was indicated by an upregulation of shear stress responsive pro-inflammatory genes and proteins. Furthermore, significant lumen narrowing occurred as a result of intimal hyperplasia with infiltrating macrophages and SMCs[186,187]. Flow velocities and shear stress changes in the venous segment were not reported. The hemodynamic at the site where the artery connects to the vein is so complex, it is not possible to predict what happens at that site without local measurements.

Similar results for blood flow and shear stress levels were obtained in in a dog and rabbit model, where flow velocities and shear stress in the arterial segment were also elevated, which led to vasodilation and eventually outward remodelling as a compensatory process to control the shear stress levels[185,188]. Furthermore, the group of Zarins[188] showed in rabbits that temporal reduction of shear stress in the arterial segment by short term closure of the fistula triggered the formation of neointimal hyperplasia with SMC infiltration in this segment. In rabbits, arterial segments that remained exposed to high shear stress showed no intimal hyperplasia[189–192]. In summary, the AV fistula model demonstrated a correlation between elevated shear stress and arterial remodelling in multiple animal models[193–197].

Vascular grafts

Bypass graft surgery with venous grafts is often used to treat atherosclerotic occlusive disease in patients. However, graft failure due to intimal hyperplasia and plaque formation often occurs. Animal models of vascular grafts were created to study the pathophysiology of atherosclerosis in coronary artery bypass grafts. These models involve surgical removal of a vessel segment, either artery or vein, which is then transplanted into, for instance, the carotid or coronary artery[198,199] (Figure 3.2B).

In mice, the vein graft resulted in early intimal cell-loss and vessel wall degeneration, which was followed by immune cell infiltration, intimal hyperplasia, matrix protein accumulation and an increase in SMC numbers[198]. In hypercholesterolemic pigs, vein grafts implanted in carotid arteries were obstructed by atherosclerotic plaques with lipid-rich necrotic cores and immune cell infiltration[200]. EC dysfunction and plaque formation were probably triggered by a combination of several factors. These factors include the surgically-induced vessel damage, hypoxia, and presumably hemodynamic factors. As no hemodynamic measurements were performed in this model, it is speculated that the introduction of a larger diameter vein in a smaller diameter artery resulted in a lower flow velocity in the graft, and thus lower shear stress, than in the native artery.

Ligation models

Another animal model used to study the role of shear stress in atherogenesis is the ligation model. The first ligation model described was developed by Wexler and Saroff[201] in the early 70's and was used to induce brain ischemia in rats by completely ligating the carotid artery, causing cessation of blood flow. When a correlation between reduced blood flow and intimal hyperplasia became evident[202–204], Kumar and Lindner[205] used the ligation model to study atherosclerosis in carotid arteries of mice. Others have

since altered the model of Kumar and Lindner to study atherosclerosis, by ligating different arteries e.g., the external or internal carotid artery, by varying the location of the ligature on the same artery, and by varying the degree of stenosis and the number of ligations. These different ligation models were used to address different research questions and are discussed below.

Complete ligation of the carotid artery

The Kumar and Lindner[205] model described a complete ligation of the common carotid artery in mice, resulting in complete cessation of blood flow distal to the ligation (Figure 3.2C). Because the artery was still subject to arterial blood pressure, pressure pulsation proximal to the ligation and extremely low and oscillatory shear stress were assumed, although, flow measurements were never performed[205]. Plaque development and thrombus formation occurred just proximal to the ligation[205]. A great number of studies in mice using the complete ligation of the carotid artery based their technique on the Kumar and Lindner model. This model was applied to accelerate plaque formation and to study molecular mechanisms involving endothelial activation, leukocyte recruitment and neointimal hyperplasia[206,207]. This model has also been used to study new imaging techniques and new drug treatments in mice[208–210].

Application of the complete ligation model in hyperlipidaemic mice induced rapid formation of lipid rich plaques with high macrophage content proximal to the ligation[211–214]. Furthermore, when these mice were treated with angiotensin II, a vulnerable plaque phenotype developed[215].

Plaque rupture was induced in mice by combining the complete ligation, which led to plaque formation, with subsequent placement of a non-constrictive cast around the area of the common carotid where plaque developed. Lipid rich plaques developed just proximal of the ligation and subsequently, after cast placement, plaque rupture, intraplaque haemorrhage and thrombus formation occurred [216,217]. As no hemodynamic studies were performed in this model, we speculate that completely ligating the artery causes a cessation of blood flow and probably results in very low shear stress, as mentioned above. Placement of a non-constrictive cast around an already developed plaque will probably not change the local shear stress unless very large changes in the vessel trajectory are introduced. Even in that case, shear stress will not be large enough to induce rupture itself. Since it is not expected that the presumably local decrease in plaque distensibility caused plaque rupture, the most plausible explanation for plaque rupture after cast placement is the additional local inflammation presumably causing plaque weakening[218].

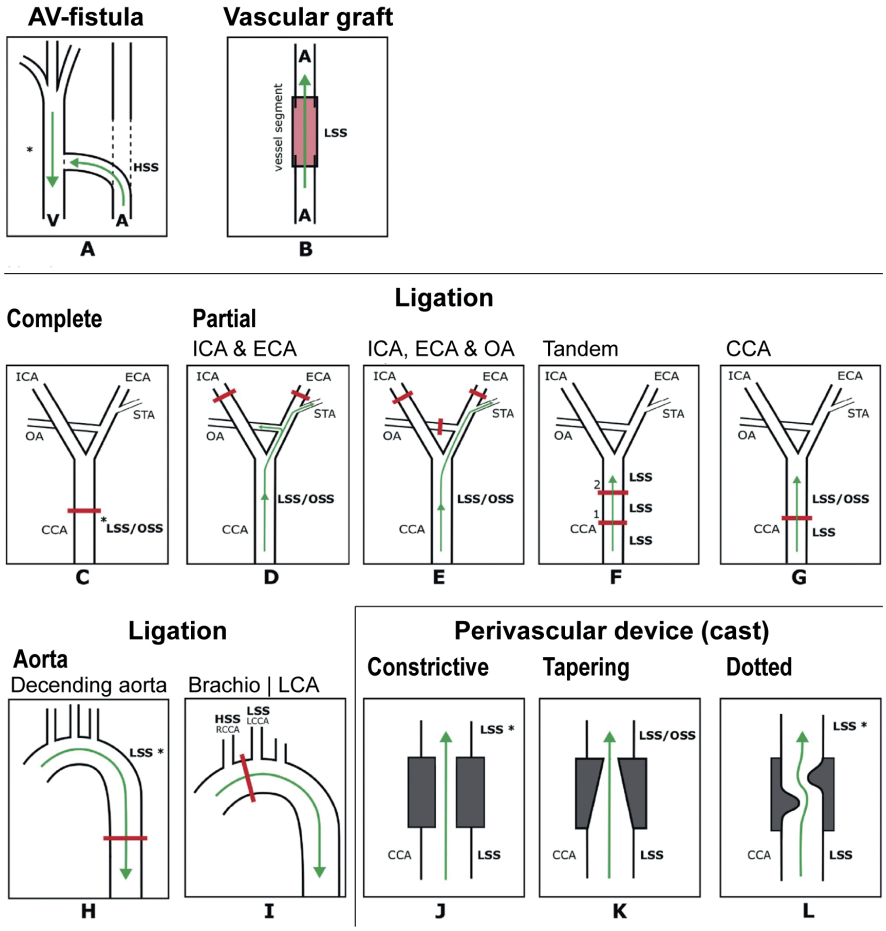

Figure 3.2: A schematic overview of all the flow alteration models described in this review and the measured or speculated shear stress levels. A) shows the AV-fistula model where an artery is attached to a vein (adapted from Castier et al.[186]). *At the site where the artery connects to the vein it is not possible to postulate what happens to the shear stress levels as the haemodynamics at this site are too complex. **B)** shows the vascular graft model in which a vessel segment is transplanted onto an artery (adapted from Zou et al.[198]). **C-I)** shows the ligation models. **C)** the complete ligation model in which the right common carotid artery (RCA) is completely tied off with cessation of flow as a result. The flow velocities and shear stress levels proximal to the ligation would be extremely low due to still existing variations of blood pressure and compliance of the artery. **D-G)** shows the partial ligation models (adapted from Nam et al.[221]). **D)** the internal carotid artery (ICA) and external carotid artery (ECA) are completely tied off. **E)** the ECA, ICA and the occipital artery (OA) are completely tied off leaving blood flow only through the superior thyroid artery (STA). **F)** in the tandem stenosis model, the RCA has two partially constrictive ligations placed in succession between the right subclavian artery (RSA) and the bifurcation. **G)** the RCA is partially tied off. **H-I)** show the aortic constriction models (adapted from Tropea et al.[223]). **H)** shows the partial ligation of the descending aorta. *Shear stress levels proximal to

continuation legend Figure 3.2: the ligation would be low, but depends on cardiac compensation. **I)** shows the partial ligation between the brachiocephalic artery (RCCA) and the left common carotid artery (LCCA) and the resulting shear stress levels. **J-L)** show the perivascular devices with a constrictive cast in **J**, a tapered cast in **K** and a dotted cast in **L** (adapted from von der Thüssen et al.[224], Cheng et al.[225] and Kivelä et al.[226]). *The shear stress levels in **J** would depend on the degree of constriction.

Partial ligation of the carotid artery

Cessation of blood flow induced by complete ligation generates a non-physiological flow condition and, therefore, does not reflect the *in vivo* situation. A more physiologically relevant model would generate a reduction in flow. Accordingly, a partial ligation model was developed to study the effect of altered and reduced blood flow velocities and shear stress on atherogenesis. This flow reduction can be achieved via different methods. Ligation of one or more of the arteries distal to the bifurcation of the common carotid artery, resulting in reduced blood flow through the common carotid artery[219–222] (Figure 3.2D-E). Another approach involves ligation using a spacer, in the form of a needle or a rod, to reduce lumen diameter of the common carotid artery or aorta, and thereby decreasing blood flow through this artery[128,151] (Figure 3.2F-I).

In the 80's, researchers ligated the left external carotid artery of rabbits to study the vascular response to altered blood flow in the common carotid artery[227]. Later, in the 90's, a model was developed in rats where both the right internal and the right external carotid artery were ligated, leaving blood flow through the ascending pharyngeal and the superior thyroid artery[219,220] (Figure 3.2D). Changes in shear stress were estimated using velocity measurements obtained with a transit-time flowmeter and vessel diameter was measured using a ruler under a dissecting microscope[219,220].This model has also been used in rats and mice to study the effect of shear stress on endothelial activation and neointimal hyperplasia[228–231]. Recently, Nam et al.[221] modified the above described ligation model by additionally ligating the occipital artery (OA) in mice, leaving blood flow through the superior thyroid artery only (Figure 3.2E). In this model, the effect on shear stress was extensively studied by performing CFD calculations using the geometry of the ligated carotid artery, which was determined by high-resolution ultrasound. The results showed a reduction in flow velocity during systole and reversal of flow direction during diastole. These changes in flow velocities resulted in low and oscillatory shear stress[221]. Large complex lipid rich plaques developed along the whole ligated artery proximal to the ligation sites, containing cholesterol clefts and intraplaque neovessels. This model has been used to study novel mechano-sensitive genes, and plaque formation in mice[232–235].

Plaque rupture has not been reported in the above described partial ligation models and extra stimuli are needed to induce rupture. For instance, ligating the renal artery

in addition to ligating the common carotid artery, in mice, increased the systolic blood pressure but lowered blood flow velocities in the carotid artery. Vulnerable plaques developed proximal to the ligation in the carotid artery. These plaques were characterized by a necrotic core, intraplaque haemorrhage and plaque rupture with lumen thrombus[125].

Recently, Chen et al.[128] developed a new partial ligation model to generate rupture prone vulnerable plaques in mice without an extra stimulus. A surgical procedure was developed, placing two partial ligations around the right carotid artery using a spacer to create a tandem stenosis (Figure 3.3F). Based on idealized computer-generated vessel geometry models and CFD calculations, they predicted that this approach would generate both low shear stress and high wall strain, thereby increasing the probability for plaque rupture. The *in vivo* flow measurements using ultrasound showed a 65% flow reduction. An unstable plaque developed between the proximal ligation and the origin of the right carotid artery from the brachiocephalic trunk. Rupture of the fibrous cap was described, along with intra plaque haemorrhage, intraluminal thrombosis and the presence of neovascularization. Stable plaques developed between the two ligations, and between the second ligation and the bifurcation[128].

Several groups attempted to create a model of surgically-induced plaque instability in pigs. As pigs have a physiology similar to humans, pig models develop plaques which have human-like characteristics[145,147]. Ishii et al.[151] partially ligated one of the common carotid arteries by using a spacer to create a stenosis (Figure 3.2G). Advanced plaques characterized by calcification, intraplaque haemorrhage and necrosis were located proximal to the ligation [151–154]. Hemodynamic measurements have yet to be performed in this model, but flow velocities are expected to be reduced upstream of the stenosis (Box 1).

Aortic constriction

Aortic constriction creates a pressure drop along the aorta which results in hypertension proximal to the constriction. To study hypertension-related atherogenesis or vascular remodelling in the aorta and carotid arteries, several models of aortic constriction were developed[236,237]. One model alters blood flow by creating a stenosis in the aorta by tightening a synthetic band around the descending aorta midway between the origin of the left subclavian artery and the diaphragm (Figure 3.2H). In rabbit and primate models, an increase in blood pressure in the aorta proximal to the band was measured while distal to the band blood pressure remained at baseline level[223,238–241]. Plaques developed at both sides of the constriction with differences in composition. Distal of the constriction, lumen stenosis and plaque area were less significant than lumen stenosis

and plaque area proximal of the constriction[238,241]. In the proximal plaque, foam cells were more abundant, and an increased expression of VCAM-1 and elevated levels of macrophage infiltration were observed[223,238]. Based on the measured pressure gradient, one could expect reduced flow velocities in this aortic constriction model (Box 1), but without flow measurements it is unknown what the amount of cardiac compensation is.

In a different aortic constriction model, in mice, the aorta was partially ligated between the origins of the brachiocephalic artery and left carotid artery using a suture[237] (Figure 3.2I). Flow velocity measurements at different time points in both right and left carotid arteries were performed using ultrasound showing an increase in blood flow and WSS in the right carotid artery and a decrease in the left carotid artery. This corresponded with vascular remodelling and increased media thickening in the right carotid artery while no change in vessel morphology was observed in the left carotid artery.

Perivascular devices

Another model to study the influence of specific flow velocity and shear stress patterns on the development of atherosclerosis uses perivascular devices (Figure 3.2J-K). These perivascular devices were mainly applied in mice. However, some studies used pig and rabbit models of atherosclerosis, which enabled the use of specific (intravascular) imaging techniques also used in the clinic.

Different perivascular constrictive devices were developed including a constrictive[224] and a tapered cast[225]. Recently, a dotted cast was also constructed and tested in rabbits[226]. These perivascular devices alter blood flow velocity profiles and concomitantly shear stress in distinct regions of the artery, enabling analysis of the effect of specific shear stress profiles on atherogenesis.

Constrictive cast model

The first cast model that focused on shear stress as a trigger for the development of atherosclerosis was developed by Von der Thüsen et al.[224], who designed a mildly constrictive cast inducing approximately a 30% luminal stenosis in a mouse common carotid artery (Figure 3.2J). Ultrasound blood flow and lumen diameter measurements were performed in mice directly after cast implantation. These measurements showed a decreased blood velocity and subsequently decreased shear stress levels in the proximal region of the cast compared to the baseline situation[242]. The alterations in shear stress lead to rapid formation of site-controlled atherosclerosis[224].

The effect of changes in shear stress on the development of an atherosclerotic plaque in the proximal region of the constrictive cast was analysed in multiple mouse studies[243–247]. The general phenotype of the plaques, induced by the use of a constrictive

cast, was relatively stable. Most studies showed plaques with low lipid, high SMC and high collagen content. However, levels of, for example, collagen and SMCs, varied between the studies. This was presumably due to the large variation in secondary study parameters like age, sex and diet. Strikingly, most studies also observed high macrophage content, which is often associated with plaque vulnerability. Interestingly, $LDLR^{-/-}$ mice developed smaller plaques[248] with more stable plaque characteristics in the proximal region[122] compared to the plaques in $ApoE^{-/-}$mice after cast placement.

In this cast model, plaque rupture is seldom observed in mice and can only be induced by adding an extra stimulus, like triggering of the immune system[249] or inducing apoptosis[122,250].

The first application of a cast in mini pigs was by the group of Falk[251]. An important advantage of this pig model is the more human-like plaques that these pigs develop and the spontaneous plaque rupture that can occur after cast placement, without the need of an extra stimulus. However, a disadvantage of the pig model is the lengthy duration of plaque development. In this model shear stress was assessed by MRI and CFD at the end of the experiment, when plaques had already developed. At this time of plaque development, shear stress in the cast region was elevated, while distal to the cast shear stress was oscillatory and lower than the area proximal to the cast, where it remained at baseline level. Plaque development varied extensively between animals, ranging from no plaque development at all, to thrombus formation and occlusion, mainly in the distal area. It is unclear why cast experiments in mice have been more consistent while the same technique induces such a wide range of plaque phenotypes in pigs.

Tapered cast model

Decreased shear stress, as induced by the constrictive cast, is an important trigger for atherosclerotic plaque formation. Besides low shear stress, also oscillatory shear stress patterns were indicated as a factor involved in plaque initiation and progression[252]. To compare the effect of low shear stress versus low, oscillatory shear stress on atherogenesis, Cheng et al.[225] developed a tapered cast (Figure 3.2K). Shear stress-induced by the tapered cast in the mouse carotid artery was calculated using CFD and the vessel geometry of the manipulated artery was obtained from histological images to create a 3D model of the vessel[225]. The tapered cast model induced low shear stress proximal to the cast, like the constrictive cast model. However, due to its tapered geometry, a shear stress gradient is present in the cast area, and flow separation causing low, oscillatory shear stress was observed distal to the cast. This cast model enabled the study of the causative role of both shear stress patterns on plaque development in one vessel segment at the moment of placement, avoiding inter-animal and inter-vessel variations. This is in contrast to the constrictive cast in pigs described above, where

shear stress was reported to be low and oscillatory after plaque development. In the tapered cast model, corresponding with the shear stress profiles, plaques developed both proximal and distal to the cast. Plaques in the proximal region had a higher lipid content, equal or higher macrophage content and lower collagen and smooth muscle cell levels compared to plaques that developed in the distal region[253–260]. Other characteristics of human plaque vulnerability, like the presence of micro-calcifications and iron and zinc deposits in the intimal layer were also observed in low shear stress region of mouse carotid arteries[261]. These plaque characteristics are rarely observed in other models applied in mice.

In conclusion, the different flow velocity patterns in this model induced the development of both stable and unstable atherosclerotic plaques.

Dotted cast

Beside the commonly applied cast models described above, Kivelä et al.[226] recently developed a 'dotted cast' with two non-symmetrically placed cushions inside (Figure 3.2L). This cast was developed to mimic eccentric plaque formation seen in the human situation, instead of the concentric plaque formation usually seen in other cast models. Implantation of the cast around one of the carotid and femoral arteries in New Zealand White rabbits reduced flow velocities, which were measured by ultrasound. Inside the dotted cast, high levels of shear stress can be expected on the apex of the cushions. Flow velocities returned to initial velocity levels after eccentric plaques developed. These plaques exhibited low numbers of macrophages and high smooth muscle cell levels, indicative for a stable plaque phenotype, although the lipid levels were not analysed.

Aortic Regurgitation

Haemodynamics was extensively studied in a model of diastolic retrograde flow in the aorta of mice. In this model, the aortic valve leaflets of mice were punctured to study the pathogenesis of atherosclerosis[262,263]. The model significantly alters blood flow patterns throughout the aorta, inducing extensive atherosclerotic plaque formation along the descending thoracic and abdominal aorta. Shear stress simulations, using CFD based on an ideal geometry, were performed and extensive analysis was done. Shear stress levels were reduced by 50% at a distinct pattern along the aortic arch, and plaque formation co-localized with these sites of low shear stress[263]. Although plaque formation was observed, further plaque characterization was not described (Table 3.1).

Table 3.1: Animal models of different surgically manipulated flow velocities.

Model flow manipulation	Flow velocity and shear stress profiles	Reported vessel pathology	Animal species	Remarks
AV-fistula	• High flow velocity, high WSS	• Endothelial activation[187] • Neointimal hyperplasia[185,188–191,193–197]	• Mice • Mice, rat, rabbit, pig, primate, dog	• Atherosclerotic plaque development only specific for AV-fistula
Vascular graft	• Low flow velocity assumed	• Neointimal hyperplasia[198,199] • Plaque; lipid rich, necrotic core[200]	• Mice • Pig	• Atherosclerotic plaque development only specific for vascular graft • Vascular grafts are exposed to non-physiological high pressure, and thus additional exposure to high strain
Ligation				
Complete CCA	• No flow (extremely low and oscillatory WSS assumed)	• Endothelial activation[206] • Neointimal hyperplasia[207] • Plaque; lipid rich, high macrophage content, intraplaque hemorrhage[205,211–215]	• Mice	• Atherosclerosis development due to complete cessation of blood flow, non-physiological flow condition
CCA & cast	• Low flow velocity and oscillatory WSS assumed	• Plaque; intra plaque haemorrhage, plaque rupture, lumen thrombus[216,217]	• Mice	• Development of plaque rupture
Partial				
ICA & ECA	• Low flow velocity, oscillatory WSS	• Endothelial activation[228] • Neointimal hyperplasia[229–231]	• Mice	• No surgery induced vessel damage at site of plaque development

Table 3.1: Continued

Model flow manipulation	Flow velocity and shear stress profiles	Reported vessel pathology	Animal species	Remarks
ICA, ECA & OA	• Low flow velocity, oscillatory WSS	• Plaque; lipid rich, neovascularization, cholesterol clefts[221,232–235]	• Mice	• No surgery induced vessel damage at site of plaque development • Haemodynamics studied by CFD • Large, diffuse plaques
CCA & renal artery	• Low flow velocity, oscillatory WSS	• Plaque; necrotic core, plaque rupture, lumen thrombus[125]	• Mice	• Development plaque rupture
Tandem CCA	• Low flow velocity, oscillatory WSS	• Plaque; disruption fibrous cap, intraplaque haemorrhage, lumen thrombus[128]	• Mice	• Large area of artery containing plaque
CCA	• Low flow velocity, oscillatory WSS	• Plaque; necrosis core, calcification, intraplaque hemorrhage[151–154]	• Pig	• Development plaque rupture
Aortic constriction	• RCCA: increased flow velocity & WSS • LCCA: decreased flow velocity & WSS • Aorta: low WSS	• Endothelial activation[236,237,264] • Neointimal hyperplasia[223,238,241]	• Mice, primate • Primate, rabbit	• No surgery induced vessel damage at site of plaque development • Large area with plaques
Perivascular device				
Constrictive cast CCA	• Low flow velocity, oscillatory WSS	• Plaque; low lipid, high SMC, high collagen content, high macrophage content, thrombus formation, plaque rupture[122,243–247,249,250] • Thrombusformation[251]	• Mice • Pigs	• Large variation in plaque phenotype in the same model • Local effect of cast on wall strain and wall motion due to pulsation

Table 3.1: Continued

Model flow manipulation	Flow velocity and shear stress profiles	Reported vessel pathology	Animal species	Remarks
Tapered cast CCA	• Low, high, low & oscillatory flow velocity and WSS	• Plaque; high lipid content, higher macrophage content, lower collagen and SMC content [225,253,254,257–261] • Micro-calcifications[261]	• Mice	• Creates two types of shear stress profiles and subsequently both "stable" and "unstable" plaque in one artery segment. • Effect of cast locally on wall strain and wall motion due to pulsation
Dotted cast CCA	• Low, high, low & oscillatory flow velocity and WSS	• Plaque; low numbers of macrophage and high SMC content[226]	• Rabbit	• Development eccentric plaques • Local effect of cast on wall strain and motion
Aortic regurgitation	• Low flow velocity, oscillatory WSS	• Plaque development, but composition not reported[262,263]	• Mice	• No surgery induced vessel damage at site of plaque development • Haemodynamics extensively studied

DISCUSSION

In this review we gave an overview of animal models in which blood flow velocities were surgically altered in specific areas of the vasculature enabling the study to the causative role of shear stress in atherosclerotic plaque formation. In these studies, different terminology for flow velocity and shear stress patterns is used, leading to confusion. Therefore, we defined the biomechanically correct terminology in Box 1/Figure 3.1, which depicts the most common flow phenomena that occur in the vasculature.

Many studies used the described models to accelerate or to control the induction of atherogenesis, but did not focus on the shear stress level that was generated. Consequently, solid analysis of the surgically-induced alterations in the haemodynamics was not often performed. It is important to realize that differences in vessel geometry or flow velocity can have a big effect on the outcome of shear stress calculations, and thus, can vary considerably between individual animals. Extrapolating data from previous studies is therefore less useful and it is recommended to perform CFD calculations for each individual animal. Because absolute values of shear stress differ between animals and change over time, it is better to portray relative differences in shear stress levels locally, e.g. proximal, inside, or distal to a cast. Another important point is the often-disregarded contribution of other biomechanical forces to plaque development that might be affected by surgical manipulation e.g. the effect of ligation or cast placement on wall strain is often ignored. Therefore, the reported effects might not be fully attributable to shear stress.

All the models we described have advantages and limitations. Choosing which model to use depends on the research question at hand. Each model generates different flow velocity and shear stress profiles at different locations, and even develops different plaque phenotypes.

According to our insights, the best mouse model to study low shear stress induced endothelial dysfunction would be the partial ligation model in which the ICA, ECA, or OA are ligated (Figure 3.2D and E). The advantage of the model is that the whole carotid artery is exposed to low or low oscillatory shear stress yielding enough tissue for molecular and array studies. Furthermore, the location and size of the arteries allows measurements of the flow and geometry, so that shear stress can be assessed by CFD. Because the ligations are placed away from the site of interest, the influence of surgery induced vessel damage on inflammation is avoided.

To study the effect of different shear stress profiles, low shear stress, high shear stress and low oscillatory shear stress in the same artery, ruling out inter animal variation, the tapered cast model would be the best suitable mouse model (Figure 3.2K). Both

endothelial dysfunction as well as plaque formation can be studied in relation to the different shear stress profiles. Since two different plaque phenotypes were observed in relation to the two different shear stress profiles, one with characteristics of a stable plaque and one with some features of human plaque vulnerability, this would be the model of choice when studying the comparison of those two plaque phenotypes. However, a disadvantage is the extensive area of vessel damage along the length of the cast and the inhibition of pulse pressure-induced arterial strain and outward remodelling due to the rigid cast. If the main interest of the research is vulnerable plaque development and rupture, the tandem stenosis model (Figure 3.2F) seems the most suitable. The combination of low shear stress and high wall strain creates several types of plaques, of which certain plaques show some features of human plaque vulnerability. However, the predicted shear stress profiles are based on idealized vessel geometry and are not yet validated *in vivo*. Furthermore, as the plaques develop at the sites of the ligation, there will always be some surgery induced vessel damage.

CONCLUSION

The use of animal models in which blood flow velocities and shear stress are surgically manipulated enables the study of shear stress-induced biological mechanisms of atherogenesis in a complex *in vivo* setting. The partial ligation model is most suited for studies on the relationship between low shear stress and (molecular markers of) endothelial dysfunction, whereas the tandem stenosis model and tapered cast model can be used to study the role of shear stress in advanced plaque formation including features of plaque vulnerability. Not only do these models provide novel insights into the pathogenesis of atherosclerosis, it also enables the testing of new imaging techniques and drug treatments, which could later be used in the clinic

ACKNOWLEDGEMENTS

The authors thank Hans Schuurbiers for developing the figures, and Frank Gijsen and Jelle Schrauwen for critically reading the manuscript.

Part II

Biomarkers of atherosclerosis

CHAPTER 4

A familial hypercholesterolemia pig model for advanced coronary atherosclerosis - variation in disease severity related to a distinct LDL profile

Ayla Hoogendoorn
Sandra den Hoedt
Eline M. J. Hartman
Ilona Krabbendam – Peters
Maaike te Lintel Hekkert
Leonie van der Zee – van Vark
Kim van Gaalen
Karen Th. Witberg
Kristien Dorst
Jurgen M. R. Ligthart
Ludovic Drouet
Kim Van der Heiden
Jeanine Roeters van Lennep
Antonius F.W. van der Steen
Dirk J. Duncker
Monique T. Mulder
Jolanda J. Wentzel

Based on:

'A familial hypercholesterolemia pig model for advanced coronary atherosclerosis - variation in disease severity related to a distinct LDL profile', *in rebuttal for ATVB*

ABSTRACT

Objective

In an adult porcine model of familial hypercholesterolemia (FH), coronary plaque development was characterized. To elucidate the underlying mechanisms of the observed inter-individual variation in disease severity, detailed lipoprotein profiles were determined.

Approach and results

FH pigs (3 years old, homozygous *LDLR* R84C mutation) received a high-fat diet for 12 months. Coronary atherosclerosis development was monitored using serial invasive imaging and histology. A pronounced difference was observed between mildly-diseased pigs (MDs) which exclusively developed early lesions (maximal plaque burden 25% (23%-34%)) (n=5) and advanced-diseased pigs (ADs) (n=5) which developed human-like, lumen intruding plaques (maximal plaque burden 69% (57%-77%)) with large necrotic cores, intra-plaque haemorrhage and calcifications. ADs and MDs displayed no differences in conventional risk factors. Additional plasma lipoprotein-profiling by size-exclusion chromatography (SEC) revealed two different LDL subtypes: 'regular' and 'larger' LDL. Cholesterol, S1P, ceramide and sphingomyelin levels were determined in these LDL-subfractions using standard laboratory techniques and HPLC-MS/MS respectively. 'Regular' LDL of ADs contained relatively more cholesterol (LDL-C) ('regular'/'larger' LDL-C ratio 1.7 (1.3-1.9) vs. 0.8 (0.6-0.9); (p=0.008)) and sphingomyelins than MDs, while 'larger' LDL contained more S1P and ceramides. 'Larger' and 'regular' LDL was also found in plasma of three hoFH patients with varying LDL-C ratios.

Conclusions

In our adult FH pig model, inter-individual differences in atherosclerotic disease severity were directly related to the distribution of cholesterol and sphingolipids over a distinct LDL profile with 'regular' and 'larger' LDL. A similar LDL profile was detected in hoFH patients.

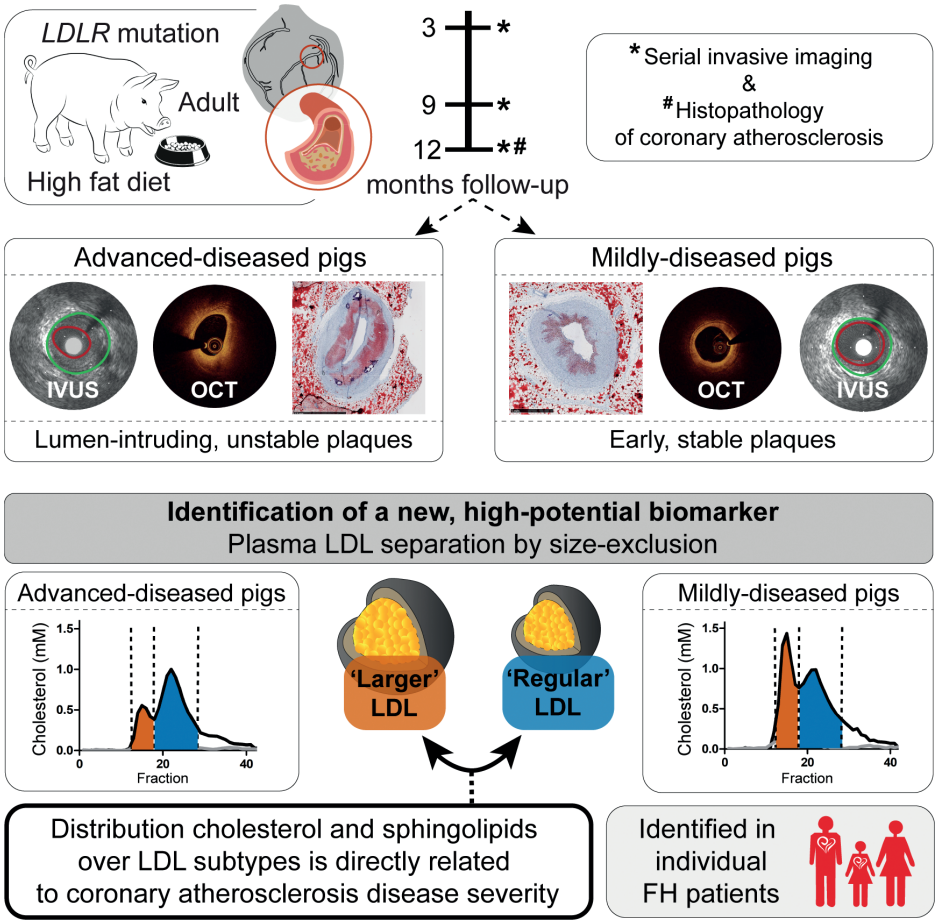
LDLR mutation
Adult
High fat diet
3
9
12
*
*
*#
months follow-up
*Serial invasive imaging
&
#Histopathology
of coronary atherosclerosis
Advanced-diseased pigs
IVUS
OCT
Lumen-intruding, unstable plaques
Mildly-diseased pigs
OCT
IVUS
Early, stable plaques
Identification of a new, high-potential biomarker
Plasma LDL separation by size-exclusion
Advanced-diseased pigs
Cholesterol (mM)
Fraction
'Larger' LDL
'Regular' LDL
Mildly-diseased pigs
Cholesterol (mM)
Fraction
Distribution cholesterol and sphingolipids over LDL subtypes is directly related to coronary atherosclerosis disease severity
Identified in individual FH patients

INTRODUCTION

Coronary atherosclerotic plaque destabilization and rupture is one of the most important causes of acute coronary events and sudden death[89,265,266]. Therefore, risk-assessment of atherosclerotic plaques prior to the occurrence of an acute coronary event is an important focus of coronary artery disease (CAD) research. Herein, *in vivo* studies with serial imaging and histopathological analyses are essential to understand the mechanisms and causative factors of plaque growth and destabilization. Unfortunately, natural history studies in humans are limited by the long time-frame of disease development, by the small number of longitudinal (invasive) imaging time points, and by the very limited possibility to collect tissue. This urges the need for a pre-clinical animal model that presents with human-like coronary artery disease.

Because of their comparable coronary size, anatomy and diet, pigs are currently the animal model that most closely resembles the human disease pathophysiology and that is most suitable for testing new imaging methods[106,267,268]. Atherosclerosis development in pig models is often stimulated by a combination of high fat diet (HFD)[269] and/or diabetes[56,66,93,147,270–272]. Some of the most successful porcine models for non-surgical induced atherosclerosis carry mutations in genes that regulate the lipid metabolism, like in the *LDLR*[150,273] or *PCSK9*[274] genes. These mutations are similar to those found in patients with familial hypercholesterolemia (FH) and result in high plasma cholesterol levels[275]. On an HFD, these FH pig models do develop (coronary) atherosclerotic disease, but, like in most other pig models, plaque progression is often modest and does not reach human-like advanced disease stages with symptomatic plaques, especially in the coronary arteries.

Previous studies with atherosclerotic pig models assessed plaque development exclusively in young, growing animals. For humans, it is known that lipid profiles, blood pressure, arterial mechanics and inflammatory status are very different between adolescents and older people[276–278], while these are factors with a major impact on atherosclerotic disease development. Hence, these factors may also affect atherosclerosis development in young pigs. Therefore, we refined a previously described and promising *LDLR* mutation mini-pig model[150] by using adult animals from the start of the study. Furthermore, in contrast to earlier studies, we followed these animals for up to one year after the start of an HFD and monitored natural atherosclerotic plaque development and composition in the coronary arteries using multiple invasive imaging techniques and histology. We provide a detailed analysis on plaque size, localization and composition at three time points during the follow-up period on HFD as a road-map for future studies with this promising pig model. To unravel the underlying mechanisms contributing to the observed inter-individual variation in coronary atherosclerotic

plaque development that is observed similarly in human FH patients[279], we deployed a detailed plasma lipoprotein analysis.

MATERIAL AND METHODS

FBM pig model and plaque imaging

The animal study protocol was approved by the local animal ethics committee (DEC EMC3318 (109-14-10)), and the study was performed according to the National Institutes of Health guide for the Care and Use of Laboratory animals[280]. Familial Hypercholesterolemia Bretonchelles Meishan minipigs homozygous for the *LDLR* R84C mutation (n=11, castrated male) as described before by Thim *et al.* 2010[150] were fed a normal laboratory diet (102243/60, Sanders Ouest, Etrelles, France) until the start of the study. At the age of 34±3 months, an HFD (10% lard and 0.75% cholesterol, The National Institute of Agronomic Research, France) was started. Plaque development in the coronary arteries was monitored by performing invasive imaging of the left anterior descending (LAD), the left circumflex (LCX) and the right coronary artery (RCA) using intravascular ultrasound (IVUS) and optical coherence tomography (OCT). The imaging protocol was performed at 3 time points (3 (T_1), 9 (T_2) and 10-12 (T_3) months on HFD) to assess (changes in) plaque size and composition.

The day before the imaging procedure, the pigs were fasted and were given an oral loading dose of 300mg carbasalate calcium. On the day of the procedure, the animals were sedated with a mix of Xylazine (2.25mg/kg, 20 mg/ml) and Zoletil 100 (tiletamine/zolazepam) (6mg/kg, 100 mg/ml) injected intramuscularly, anesthetized with sodium thiopental (4mg/kg, 50mg/ml) administered via an ear vein, intubated and ventilated with oxygen (25-30% v/v) and nitrogen (75-80% v/v) to maintain blood gases within the physiological range. Anaesthesia was maintained by isoflurane inhalation (1–2.5% v/v).

Via a carotid sheath, arterial blood samples were collected, and 250mg acetylsalicylic acid and 10,000 units of heparin were administered to prevent blood clotting. Heparin administration was repeated every hour in a dose of 5,000 units. Subsequently, a guiding catheter (Mach 1, 8F, various types, Boston Scientific, Marlborough, MA, USA) was advanced through the carotid sheath into the ostium of either one of the three main coronary arteries under angiographic guidance to perform a series of imaging procedures. Before imaging, isosorbide mononitrate (0.04mg/kg, 1mg/ml) was administered via the guiding catheter to induce epicardial coronary vasodilation. Starting position of all imaging catheters was registered by serial monoplane angiography under at least 2 angles. First, an optical coherence tomography (OCT) catheter (Dragonfly Optis Imaging Catheter, St, Jude Medical, St. Paul, MN, USA) was

advanced into the artery as distal as possible up to a maximal depth of 75mm. A pullback of 75 mm (36 mm/s) was performed under a constant contrast (Visipaque 320, GE Healthcare, Buckinghamshire, U.K.) flush rate of 4 mL/s (Medrad Injection System, Bayer HealthCare LLC, Whippany, NJ, USA). Subsequently, an intravascular ultrasound (IVUS) catheter (TVC Insight Coronary Imaging Catheter, InfraRedX, Burlington, MA, USA) was positioned at the same anatomical location as the OCT catheter and a pullback (0.5 mm/s) was performed. During the IVUS pullback, the heart rate was closely monitored and registered for later use in IVUS triggering.

During the imaging procedure at the first time point, one of the pigs died due to an acute cardiac tamponade and was excluded from the study. Furthermore, fast plaque development in two other pigs led to cardiovascular complications and subsequent early sacrifice shortly after T_2. Of these two latter pigs, the data of T_1 and T_2 were used for analysis. After the final imaging time point, the pigs were sacrificed and the coronary arteries were collected for histology.

Coronary histology

Coronary tissue was sampled every 3 mm and used for histological (Haematoxylin and Eosin (HE), Resorcin-Fuchsin or Miller (collagen and elastin), Oil-red-O (ORO) (lipids) and Martius, Scarlet and Blue (MSB) (fibrin)) and immunohistochemical stainings (CD68 (macrophages), CD31 (endothelial cells)). For the analysis, histological slides taken every 3mm were classified according to the revised AHA classification[20] as no plaque (NP), intimal thickening (IT), intimal xanthoma (IX), pathological intimal thickening (PIT) and fibrous cap atheroma (FA). The presence of a necrotic core in the latter plaque type was identified as a lipid-rich region, scarce in nuclei and fibrous tissue with an overlaying fibrous cap[20]. The presence of intraplaque haemorrhage was assessed on both HE and MSB stained sections as bright pink (HE) and red (MSB) stained areas. Neovascularisation in the plaque area could be detected using CD31 staining. The presence of calcifications was assessed on the Oil-red-O staining and calcifications were subdivided in micro (spotty appearance, <10µm/<5% of plaque area[281]) or macrocalcifications. Quantification of lipids, macrophages or necrotic core size was performed by manual or semi-automatic delineation of the lumen, media, outer wall and the respective plaque component on all histological slides using BioPix IQ software (BioPix AB, version 3.4.0). To compare the plaque types found in the proximal versus the distal regions of the coronary arteries, the first half of the excised artery (up to 14 (LAD), 9 (LCX) and 16 (RCA) 3mm-blocks) were regarded as proximal and the other half distal. These numbers were determined based on a median split of the total number of blocks of the individual arteries. Furthermore, a 3mm region was marked as ‘around a

side branch' when a side branch was present in at least one of the slices derived from that respective block.

Invasive image analysis

Analysis of IVUS and OCT data was performed using QCU-CMS software (version 4.69, Leiden University Medical Centre, LKEB, Division of Image Processing). Before analysis, IVUS pullbacks were ECG-triggered by selecting the frame that was recorded 6 frames before the R-peak by in-house developed software. Hereby differences in lumen size were removed that were induced by movement of the catheter or because of cardiac contraction. These ECG-gated IVUS images were analysed approximately every 0.5 mm by semi-automatic delineation (with manual correction) to assess lumen and outer wall dimensions. Based on these contours, total vessel area (VA), lumen area (LA) and plaque area (PA=VA-LA) (mm^2) were quantified. Plaque burden (PB) was calculated as PA/VA*100%. For final analysis, data were averaged over 3mm in longitudinal direction to reduce the influence of manual drawing errors and to reduce statistical dependence amongst the data points. The plaque size was also assessed by classifying the maximal intima-media thickness (IMT) per 3mm-segment into 4 grades (<0.5mm, 0.5-0.7mm, 0.7-1.0mm and >1.0mm) according to the method of Chatzizisis et al.[66]. The percentage of the segments occupied by the respective grade was quantified per artery and averaged over all arteries.

For the OCT analysis, frames with a poor flush were excluded. Lumen contours were automatically segmented every millimetre (1 out of 5 frames). Subsequently, OCT frames were analysed according to consensus standards[42] and were identified as fibrous plaque, lipid-rich plaque or a fibrous cap atheroma (FCA) in pullbacks that showed at least one frame with visible plaque. Angles for individual plaque components were drawn manually. Fibrous plaques were defined as homogeneous, signal-rich intimal thickening with an IMT>0.5mm. Lipid-rich plaques were defined as displaying an inhomogeneous, fading signal combined with an absent 3-layered structure. Lipid-pools were identified when a signal-low region with a diffuse border was present with an overlying signal-rich layer: the fibrous cap. Minimal, maximal and average fibrous cap thickness were determined automatically by the QCU-CMS software. Plaque classification per frame was based on the most severe classification in that respective frame: fibrous, lipid-rich or fibrous-cap atheroma (FCA). The latter classification was given when a lipid-pool was present in the plaque.

Plasma analysis pigs

At the start of every imaging procedure, blood samples were drawn from the carotid sheath into EDTA and clotting tubes. Blood tubes were spun at 1460 g for 10 minutes (Thermo scientific Heraeus centrifuge 3 S-R) to isolate the plasma and serum, which was stored at -80°C. Standard plasma analysis was performed on fresh plasma by the internal clinical chemistry department to determine leucocyte count and levels of total cholesterol, low-density lipoprotein (LDL) and high-density lipoprotein (HDL).

Patient data

EDTA plasma was collected from three homozygous *LDLR* mutation FH (hoFH) patients who were treated at the Erasmus MC, The Netherlands. All patients provided written informed consent and the collection of blood was approved by the Medical Ethical Committee of the Erasmus MC (MEC 2012-309). Human pool plasma, used as a reference, was a mixture of plasma of approximately 100 non-FH patients that was residual material remaining after diagnostic analyses from the department of clinical chemistry. No informed consent was needed for the use of this residual material.

Lipoprotein profiling

EDTA plasma and serum collected from the pigs at T_1 was used to perform lipoprotein profiling by density-gradient ultracentrifugation (DGUC)[282–285] and size-exclusion chromatography (fast-protein liquid chromatography (FPLC)). For the latter analysis, the FPLC profile was obtained from 200 µl plasma. Plasma was added to a Tricorn Superose200 10-300 GL column and a Tricorn Superdex 6 10-300 GL column with a flow rate of 0.5 ml/min. FPLC-fractions of 0.5 mL were collected. Cholesterol and triglyceride levels were determined in all gradient or elution fractions using standard laboratory methods as previously described[284–286]. Sphingolipid (ceramides (Cer), sphingosine-1-phosphate (S1P) and sphingomyelin (SM)) content of the total plasma, and of the individual LDL fractions, was measured using high-pressure liquid chromatography mass-spectrometry analyses (HPLC-MS/MS). For analysis, the total cholesterol (FPLC and DGUC), S1P (FPLC), ceramide (FPLC) and sphingomyelin (FPLC) levels in the LDL fractions were assessed by calculating the area under the curve (AUC). Sphingolipid levels were expressed relative to the total cholesterol levels in the respective lipoprotein pools. Also the Cer(d18:1/16:0)/Cer(d18:1/24:0), Cer(d18:1/18:0)/Cer(d18:1/24:0) and Cer(d18:1/24:1)/Cer(d18:1/24:0) ratios were assessed within the LDL fractions[287].

To identify different LDL subpopulations, the lipoproteins from pig plasma samples and from the hoFH patient plasma samples were first separated on density by DGUC. From

these density gradients, the LDL fractions were isolated and subsequently separated on size by FPLC.

Statistics

IBM SPSS Statistics (version 21.0) software was used for statistical analysis. Non-normal distributed data are presented as median (range) and statistical difference was determined with the Mann-Whitney U test. Normally distributed data are shown as mean±standard deviation (SD) and significance was determined using an unpaired student's t-test, a repeated measures ANOVA with post-hoc testing (Bonferroni) or a paired student's t-test. Difference in the frequency distribution of different plaque categories was tested using a Chi-square test or a Fisher's exact test. Absolute values subtracted from imaging and histological data were averaged per artery. For categorical multiple group comparison, z-scores >1.96 were regarded significant. For all other tests $p<0.05$ was regarded to indicate statistical significance.

RESULTS

General model characteristics

The weight of the pigs remained constant during the follow up period at 86 kg (60-104 kg). After 3 months of HFD, a significant increase in total cholesterol (from 1.9 mM (1.8-2.2 mM) to 10.4 mM (8.9-22.3 mM)), LDL-cholesterol (LDL-C) (from 1.5 mM (1.4-1.8 mM) to 8.8 mM (6.7-23.3 mM)) and HDL-cholesterol (HDL-C) levels (from 0.3 mM (0.2-0.3 mM) to 2.9 mM (2.1-4.9 mM)) was observed compared the levels before HFD ($p<0.05$).

Advanced and mildly-diseased pigs: general characteristics and *in vivo* IVUS measurements of plaque size and plaque growth

Five of the 10 pigs displayed development of large, lumen intruding plaques in the coronary arteries (maximal plaque burden 69% (57%-77%)) (advanced-diseased pigs (ADs)) while the other 5 pigs showed limited plaque development (maximal plaque burden 25% (23%-34%)) (mildly-diseased pigs (MDs)) (Figure 4.1A). Since the difference in plaque development between both groups was so pronounced, all subsequent results are presented separately for the MDs and the ADs.

In the ADs, plaque area (PA) was markedly larger and lumen area (LA) was smaller compared to the MDs ($p<0.05$) (Figure 4.1B and C). The ADs demonstrated significant increase in PA (Figure 4.1B) and decrease in LA (Figure 4.1C) at T_2 and T_3 compared to T_1 ($p<0.05$). In the MDs, plaque growth (Figure 4.1B) was limited but still significant

(p<0.05), while the LA (Figure 4.1C) showed a slight increase from T_1 to T_2 (p<0.05) and a decrease at T_3 (p<0.05).

At the last time point, on average 21% of the analysed segments of the ADs was occupied by plaques with a maximal intima-media thickness (IMT) >1.0mm while in the MDs none of the segments demonstrated plaques with this IMT grade (Figure 4.1D).

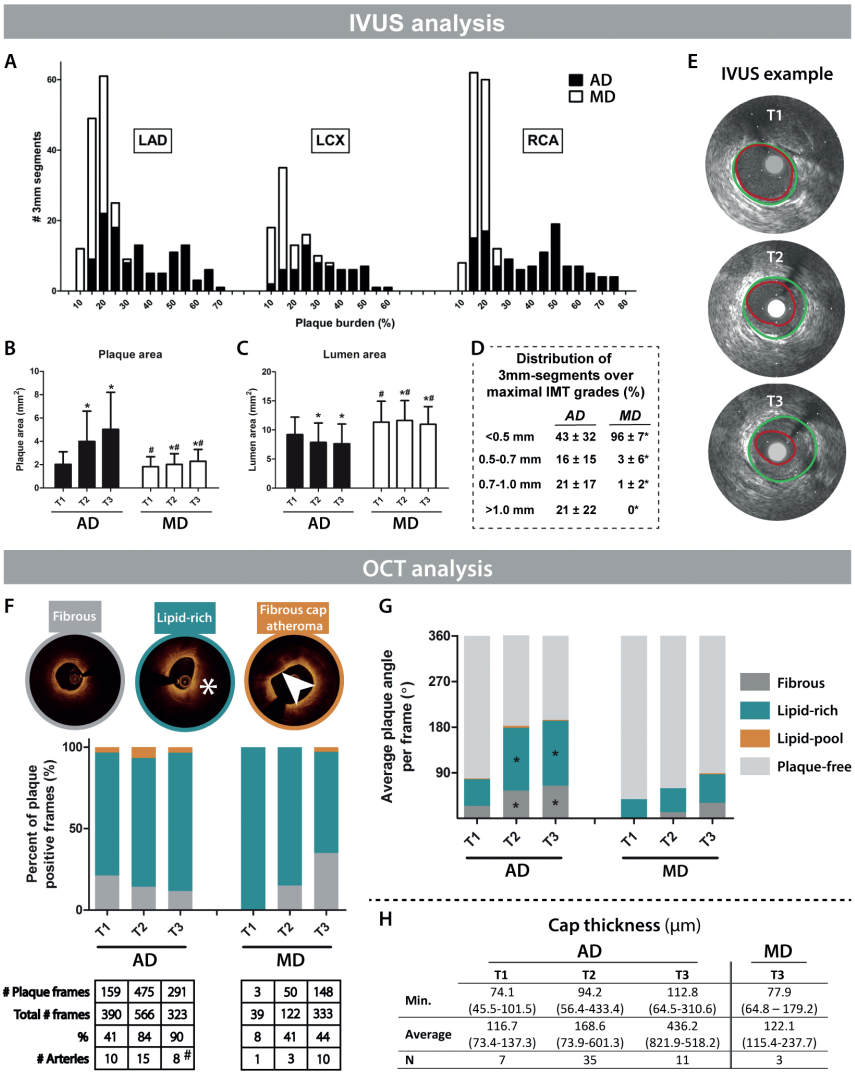

Figure 4.1: ***In vivo*** **IVUS and OCT analysis of coronary plaque development. IVUS analysis (A-E)**:

Figure 4.1: Continued: **A)** Stacked histogram of the number of 3mm segments (y-axis) with a corresponding PB (%) at the last imaging time point (x-axis) of the advanced-diseased pigs (ADs) (black bars) and mildly-diseased pigs (MDs) (white bars) in the LAD, LCX and RCA. **B-C)** Change of plaque area (PA) (mm^2) (**B**) and lumen area (LA) (**C**) between T_1-T_3 (mean±SD). *p<0.05 compared to T_1. #p<0.05 between MDs and ADs at the corresponding time point. **D)** Average percentage (±SD) of the number of 3mm segments per artery that displayed one of the maximal intima-media thickness (IMT) grades at the last imaging time point. *p<0.05 compared to FRs. **E)** Example IVUS images of plaque growth between T_1-T_3 at one location in an AD pig. Vessel wall (green) and lumen border (red) are indicated. **OCT analysis (F-H)**: **F)** Average percentage of a fibrous, lipid-rich (*) or fibrous-cap atheroma (FCA; arrowhead points out lipid-pool with overlying fibrous cap) of all plaque positive frames for T_1-T_3. The total number of plaque positive frames and arteries is depicted under the figure. #Note that at T_3, data of 2 highly atherosclerotic AD pigs are missing due to early sacrifice after T_2. **G)** The average angle of fibrous plaque, lipid-rich plaque or lipid-pool per frame at T_1-T_3. **H)** Median (range) cap thickness values derived from the frames presenting with a lipid-pool (i.e. FCA). The minimal (Min.) and average thickness, and the number of fibrous caps are displayed.

Plaque classification by OCT

The percentage of OCT frames that presented with plaque increased over time in both the MD and AD pigs (Figure 4.1F). The large majority of the OCT-detected plaques presented as lipid-rich and this distribution did not change over time (Figure 4.1F). OCT-observed fibrous cap atheroma (FCA) were rare. In ADs, OCT-FCA occurrence increased between T_1 and T_2 from 4.4% (7 frames) to 7.4% (35 frames) of the total number of frames with plaque (p=0.001) and tended to decrease again at T_3 to 3.8% (11 frames) (p=0.07) (Figure 4.1F). This latter observation is explained by the loss of 2/5 AD pigs before T_3 which demonstrated the majority of OCT-FCAs (57%) at T_2. In the MDs, OCT-FCA were only observed at T_3 in 2.0% (3 frames) of the total number of frames with plaque. In a more detailed analysis, the ADs displayed an increase in the average total plaque angle between T_1 and T_2 which could mainly be attributed to the increase in both fibrous and lipid-rich angles (p<0.05) (Figure 4.1G). Furthermore, there was a small, but non-significant increase in the lipid-pool angle. Between T_2 and T_3, both the average plaque angle and the composition remained constant in the ADs which can again be explained by the loss of 2 AD pigs with the most advanced plaques at T_2. The MDs displayed a small, but non-significant increase in average plaque angle and no significant changes in plaque composition were observed (Figure 4.1G). Cap thickness was determined in OCT-FCAs (Figure 4.1H) and in the ADs respectively 2 (T_1), 3 (T_2) and 1 (T_3) frames presented with a thin-fibrous cap (<65 µm). In the MDs, one frame with a thin-fibrous cap atheroma was observed and only at T_3.

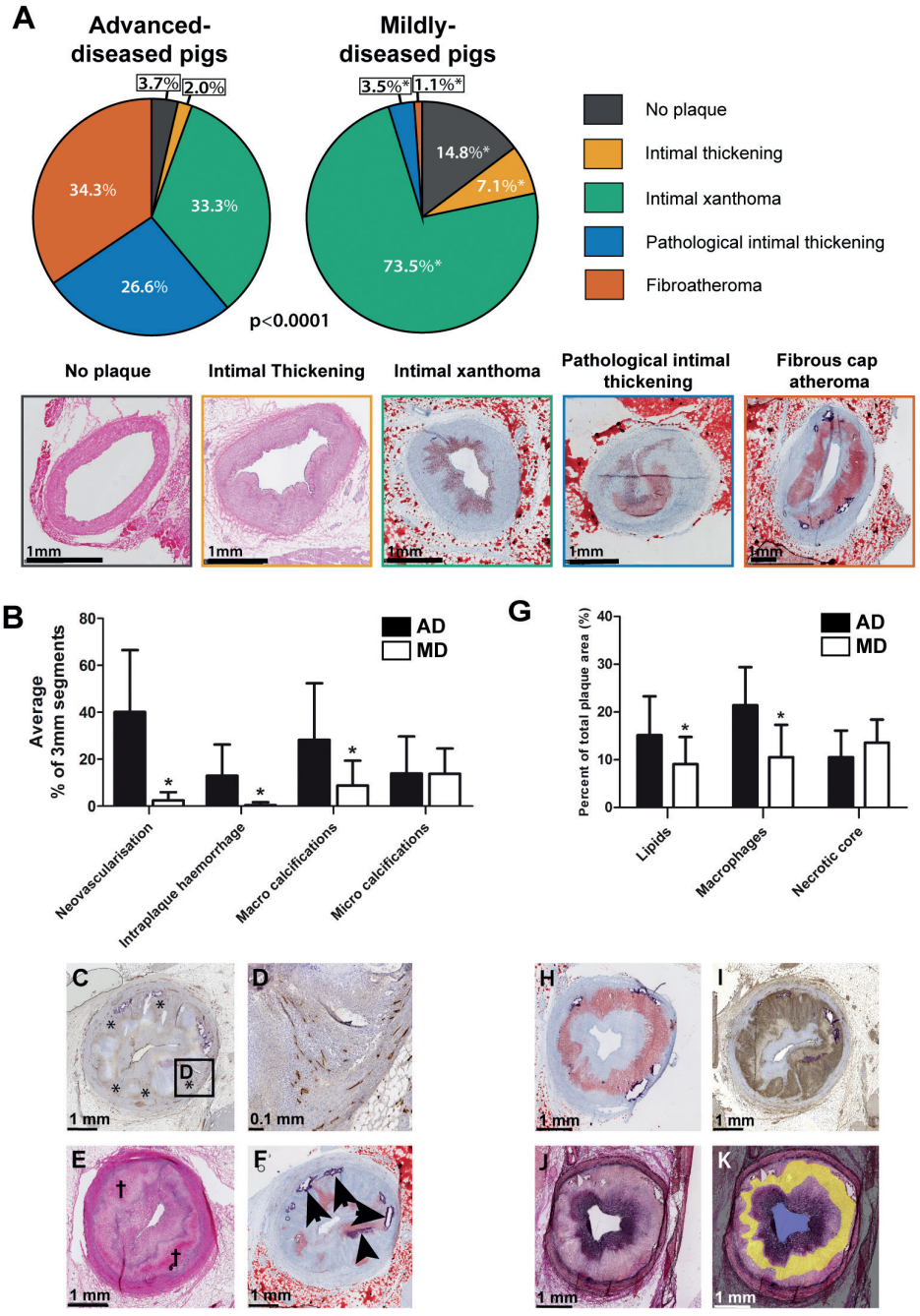

Figure 4.2: Histological quantification of coronary plaque classification and components.

Figure 4.2: Continued: **A)** Quantification of the frequency of occurrence of the different plaque types. Data are presented as a percentage of the total number of segments, separately for the mildly-diseased pigs (MDs) (283 3mm-segments) and advanced-diseased pigs (AD) pigs (297 3mm-segments). *z-score>1.96 compared to ADs. Bottom of the figure: example images of the respective plaque types: 'no plaque' and 'intimal thickening': HE-staining; other plaque types: Oil-red-O staining (red = lipids, purple = calcifications). **B)** Mean (±SD) percentage of 3mm segments per artery that contained the respective plaque component in ADs (black bars) and MDs (white bars). *p<0.05. **C-F** histological examples of the plaque components quantified in the bar graph. **C**) Neovascularisation (*, CD31-staining: brown), **D)** Magnification of C). **E)** Intraplaque haemorrhage (†, HE-staining). **F)** Lipids (Oil-red-O staining: red), microcalcifications (arrowhead) and macrocalcifications (arrows). **G)** Mean (±SD) area percentage per artery of the respective plaque component in ADs (black bars) and MDs (white bars) in segments positive for that plaque component. *p<0.05 compared to ADs. **H-K)** Example images of: **H)** lipids (Oil-red-O staining (red)); **I)** macrophages (CD68 staining (brown)); **J)** collagen (Miller staining (purple)). The Miller staining was used to delineate the necrotic core (indicated in yellow in **K)**).

Histological characterization of the coronary atherosclerotic plaques

Plaque classification and localization

In total, 580 coronary 3 mm segments were analysed by histology: 297 segments from ADs and 283 segments from MDs, with on average 19±6 segments per artery. In the ADs, the presence of a healthy vessel wall or a vessel wall with intimal thickening was rare, while intimal xanthoma, pathological intimal thickening and FCA were each present in approximately one third of all analysed segments (Figure 4.2A). For the MDs, intimal xanthoma was the most frequently observed plaque type, covering 73.5% of the segments. The frequency of the various plaque classes differed significantly between the ADs and MDs (X^2=211.0, p<0.0001) (Figure 4.2A).

The PA of each respective plaque type did not differ between AD and MD pigs (Table 4.1), while the intima/media ratio for segments with PIT was significantly higher in the AD than the MD pigs.

In the ADs, the anatomical distribution of the various plaque types differed significantly over the coronary arteries with a higher frequency of FCAs in the proximal part of the arteries compared to the distal part (χ^2=39.6, p<0.0001). In contrast, the plaque type distribution in the MDs was more homogenous (Figure 4.3A). Mainly for the MDs, the presence of a side branch coincided with a trend towards a more advanced plaque type (Figure 4.3B). In comparison with the LAD and RCA, the LCX presented with more early-stage plaques which was most apparent in the MDs (Figure 4.3C).

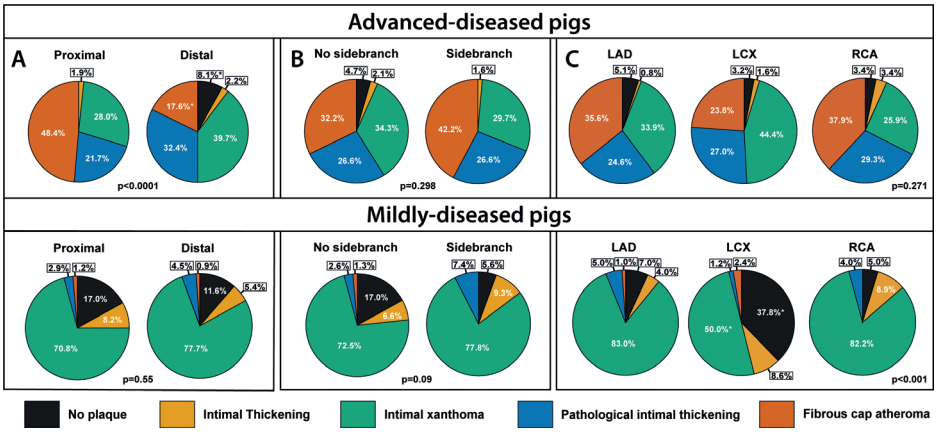

Figure 4.3: Association between the anatomical location in the coronary artery and the histological plaque classification. Distribution of plaque in regions **A)** proximal versus the distal, **B)** Side branch (SB) versus no SB, **C)** LAD versus LCX versus RCA. The data are split on advanced diseased pigs (top figures) and mildly diseased pigs (bottom figures). P-values indicate overall significance. *z-score>1.96 for that respective plaque type compared to the other plaque types.

Quantification of plaque components

Neovascularization, intra-plaque haemorrhage and macro-calcifications were frequently observed in the ADs and were rare in the MDs ($p<0.05$), while micro-calcifications were equally present (Figure 4.2B-F). Furthermore, coronary segments obtained from the ADs contained a significantly larger area percentage of lipids and macrophages compared to the MDs (Figure 4.2G-I) when the component was present. In necrotic core positive segments, the necrotic core area percentage did not differ (Figure 4.2G, J, K), but necrotic cores were much more frequently present in plaques from ADs (102 segments, 34%) compared to MDs (3 segments, 1%).

Table 4.1: Plaque area and intima-media ratio for every plaque type as determined by histology

	Advanced-diseased pigs				Mildly-diseased pigs			
	IT	*IX*	*PIT*	*FCA*	*IT*	*IX*	*PIT*	*FCA*
PA (mm^2)	0.90±1.12	0.92±0.60	2.09±0.90	4.23±1.38	0.69±0.55	0.75±0.34	1.78±0.65	3.38±2.25†
IMR	0.63±0.68	0.69±0.35	1.78±0.48	2.56±0.70	0.35±0.23	0.54±0.36	1.06±0.38*	1.48±0.74†

PA=plaque area, IMR=intima/media ratio, IT=intimal thickening, IX=intimal xanthoma, PIT=pathological intimal thickening, FCA= fibrous cap atheroma. *$p<0.05$ compared to the same plaque type of the advanced-diseased pigs. †FCA in mildly-diseased pigs: n=3, no statistics performed on this category.

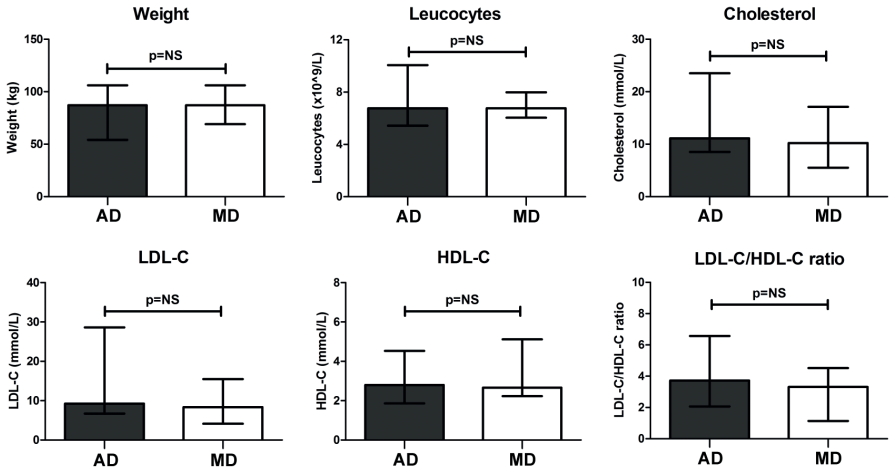

Figure 4.4: Weight, inflammation and cholesterol levels in advanced diseased and mildly diseased pigs. Weight, leucocyte count, total cholesterol, high-density lipoprotein cholesterol (HDL-C), low-density lipoprotein cholesterol (LDL-C) levels, and the LDL-C/HDL-C ratio. Data are from the advanced diseased pigs (AD) and mildly diseased pigs (MD) in the period on high fat diet. Data are presented as median (range).

Lipoprotein profiling of the advanced and mildly-diseased pigs

The ADs and MDs carried the same *LDLR* mutation, were fed the same amount of HFD and displayed no differences in conventional risk factors such as weight, total cholesterol levels, leucocyte count (inflammation), LCL-C, HDL-C and the ratio of LDL-C/HDL-C (Figure 4.4). In order to increase understanding of the large differences in coronary plaque development between the MD and AD pigs, detailed lipoprotein profiling was performed.

Detection of 'regular' LDL and 'larger' LDL

Separation of the plasma lipoproteins by density (DGUC) showed high LDL-C levels and relatively low HDL-C and VLDL-C levels (Figure 4.5) in all pigs. AD and MD pigs demonstrated no significant differences in total LDL-C in DGUC (area under the curve: 7.1 (4.5 – 18.1) vs. 7.1 (5.1 – 10.3)) (Figure 4.5). Separation of the plasma lipoproteins by size (FPLC) however revealed a marked difference in distribution of cholesterol over the lipoproteins between AD and MD pigs which was most pronounced in the fractions expected to contain LDL-C and VLDL-C (Figure 4.6A and Figure 4.5). While cholesterol was detected at both the LDL and VLDL location in the FPLC fractions, the lipoproteins at the VLDL location did not contain triglycerides (Figure 4.5).

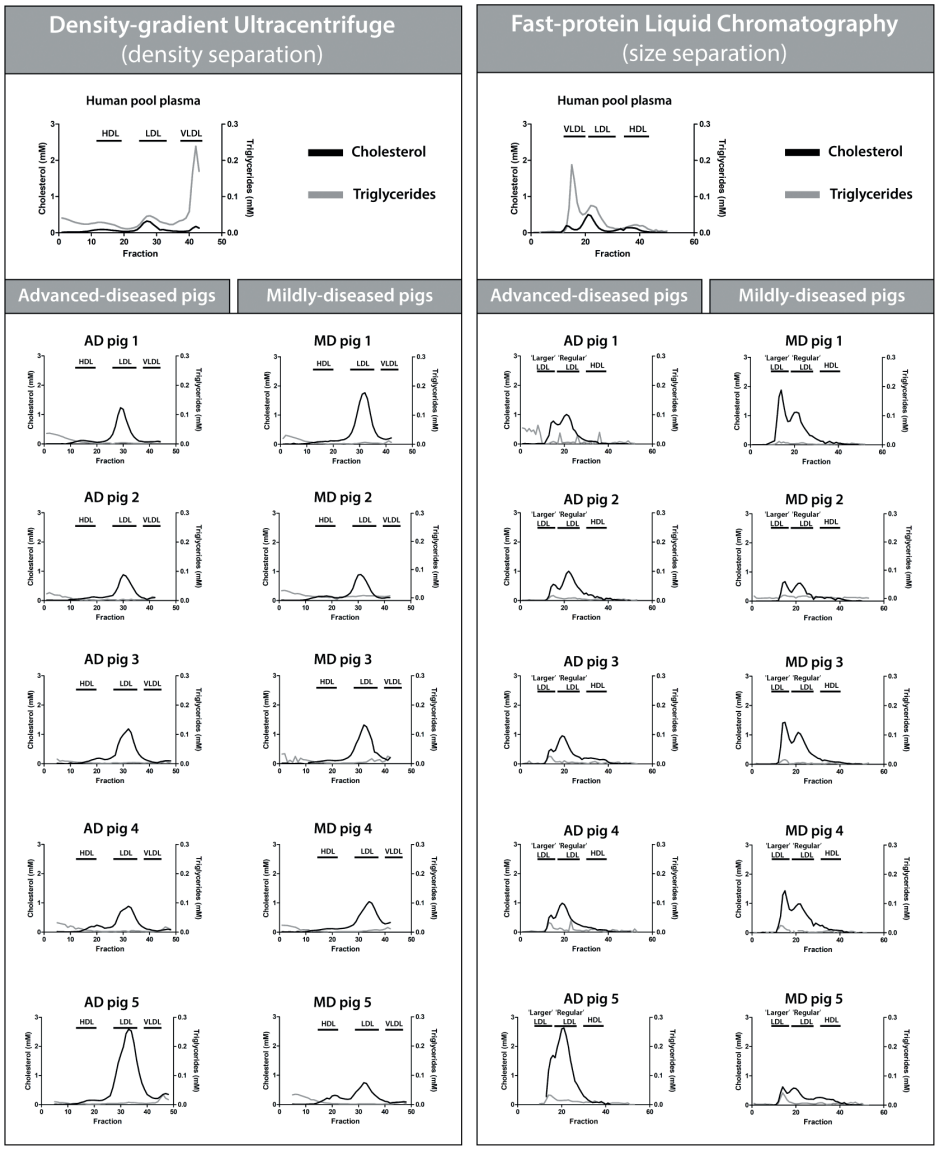

Figure 4.5: Overview of the DGUC (density separation) and FPLC-derived (size separation) lipoprotein profiles from all pigs. The two top graphs demonstrate example profiles from human pool plasma for comparison. The other graphs indicate the DGUC and FPLC profiles for all individual advanced diseased pigs (ADs) and mildly diseased pigs (MDs). Both cholesterol levels (black line) and triglyceride levels (grey line) are indicated.

Since VLDL is characterized by high levels of triglycerides (as for example observed in human pool plasma, Figure 4.5), the almost absent triglycerides at the VLDL location suggest that the observed larger lipoprotein subpopulation is highly unlikely to be VLDL. In line with this, the DGUC profiles showed hardly any cholesterol in the fractions in the VLDL-density range (Figure 4.5). To further elucidate the origin of the larger-sized lipoproteins, we isolated the DGUC LDL fractions and subsequently separated these fractions on size by FPLC. This analysis excluded the presence of VLDL and revealed the presence of LDL within the size-range of 'regular' LDL, but also of LDL within the size-range of VLDL (Figure 4.6B). Based on these data we will from now on call the specific lipoprotein subclass with the density of LDL, but the size of VLDL: 'larger' LDL.

In the AD pigs, the 'regular'/'larger' LDL-C ratio was significantly and consistently higher than in MD pigs (Table 4.2).

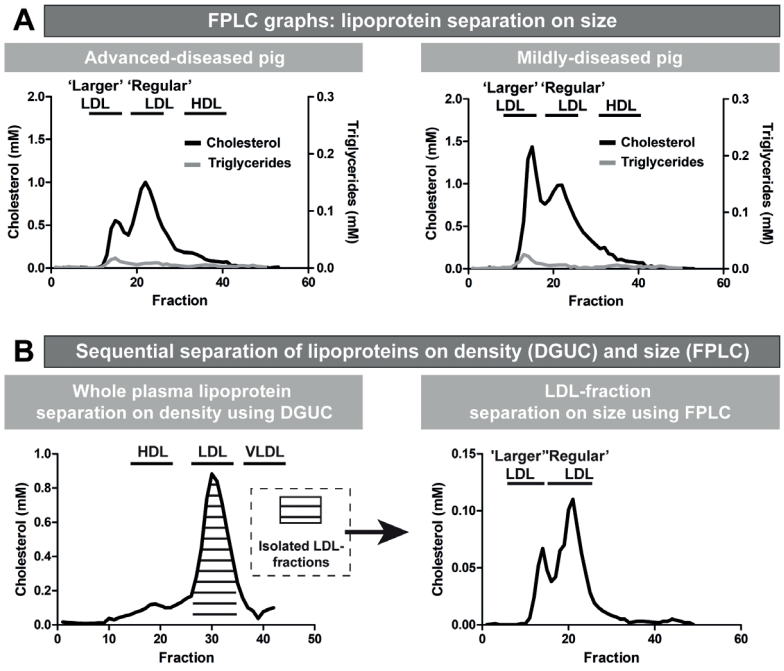

Figure 4.6: Distinct lipoprotein profile with 'larger' and 'regular' LDL associated with coronary atherosclerosis disease severity. A) Representative FPLC profiles of one advanced-diseased pig (AD) and one mildly-diseased pig. Both the cholesterol levels (black line) and the triglyceride levels (grey line) are indicated. 'Larger' LDL has the same size as VLDL. **B)** Sequential separation of lipoproteins using DGUC and FPLC (graph of one example AD pig). Lipoproteins were separated on density using DGUC. Subsequently, the pooled LDL fractions were subjected to FPLC revealing the presence of 'regular' LDL and 'larger' LDL.

Sphingolipid content of 'regular' and 'larger' LDL

Next, the sphingolipid content of the 2 LDL subclasses was determined and expressed relative to the cholesterol concentration. In the ADs, the Cer(d18:1/18:0) content of the 'larger' LDL was significantly higher than in MDs (Table 4.3). Furthermore, the 'regular'/'larger' LDL ratios of S1P(d18:1), Cer(d18:1/16:0) and Cer(d18:1/18:0) were significantly lower in the ADs than in the MDs. Cer(d18:1/14:0) showed a similar trend (Table 4.3). These results indicate relatively higher S1P and long-chain ceramide levels in 'larger' LDL and/or lower levels in 'regular' LDL of the AD pigs compared to the MD pigs. Moreover, compared to the MDs, a lower ratio of Cer(d18:1/16:0)/Cer(d18:1/24:0) (p=0.10) and Cer(d18:1/18:0)/Cer(d18:1/24:0) (p=0.03) was observed in 'regular' over 'larger' LDL in ADs (Table 4.4). This indicated that in the ADs, 'larger' LDL contained relatively more long-chain ceramides (Cer(d18:1/16:0) and Cer(d18:1/18:0)) and/or less very long-chain ceramides (Cer(d18:1/24:0)) compared to 'regular' LDL, whereas in MDs there were relatively less long-chain ceramides in relation to very-long-chain ceramides. No differences were found in the Cer(d18:1/24:1)/Cer(d18:1/24:0) ratio in 'regular' over 'larger' LDL (Table 4.4) between ADs and MDs.

With regard to the sphingomyelins, the SM(d18:1/16:0) and SM(d18:1/18:0) content was higher in 'larger' LDL of ADs than of MDs. In 'regular' LDL, the difference was even more pronounced with 2 to 3-fold higher SM(d18:1/16:0), SM(d18:1/18:0), SM(d18:1/18:1), SM(d18:1/20:0), SM(d18:1/24:0) and total SM levels in ADs compared to MDs (Table 4.5). Accordingly, also the 'regular'/'larger' LDL ratios of these respective SMs were significantly higher in the AD pigs than in the MD pigs (Table 4.5).

Table 4.2: Cholesterol content of 'regular' and 'larger' LDL

	Advanced-diseased pigs	Mildly-diseased pigs	p-value
Cholesterol 'regular' LDL	6.3 (6.1 – 17.7)	7.3 (3.6 – 7.7)	1
Cholesterol 'larger' LDL	1.9 (1.3 – 5.3)	5.0 (2.3 – 7.3)	0.22
Ratio cholesterol 'regular'/'larger' LDL	3.3 (2.5 – 4.7)	1.5 (1.1 – 1.8)	***0.008***

Data presented as median (range) of the area under the curve. Significant values are indicated as italic and bold.

Table 4.3: S1P and Ceramide content of 'regular' and 'larger' LDL

	Advanced-diseased pigs	Mildly-diseased pigs	p-value
S1P(d18:1) total plasma ($x10^{-5}$)	12.4 (3.7 – 16.7)*	14.4 (7.7 – 17.4)	0.84
S1P(d18:1) 'regular' LDL ($x10^{-5}$)	2.7 (1.7 – 13.0)*	4.7 (1.3 – 6.4)	0.42
S1P(d18:1) 'larger' LDL ($x10^{-5}$)	4.7 (2.9 – 17.2)*	3.6 (1.4 – 7.9)	0.56
S1P(d18:1) 'regular'/'larger' LDL	0.6 (0.5 – 0.8)*	0.9 (0.8 – 1.3)	***0.016***
Cer(d18:1/14:0) total plasma ($x10^{-5}$)	0.9 (0.4 – 1.2)	0.7 (0.4 – 1.1)	1
Cer(d18:1/14:0) 'regular' LDL ($x10^{-5}$)	0.6 (0.4 – 1.0)	0.6 (0.3 – 1.1)	1
Cer(d18:1/14:0) 'larger' LDL ($x10^{-5}$)	1.1 (0.9 – 1.6)	0.6 (0.4 – 1.5)	0.42
Cer(d18:1/14:0) 'regular'/'larger' LDL ratio	0.6 (0.4 – 0.8)	0.8 (0.7 – 0.9)	0.06
Cer(d18:1/16:0) total plasma ($x10^{-5}$)	7.3 (3.4 – 11.1)	6.9 (3.7 – 9.3)	0.69
Cer(d18:1/16:0) 'regular' LDL ($x10^{-5}$)	13.3 (4.7 – 14.7))	9.2 (5.2 – 12.6)	0.55
Cer(d18:1/16:0) 'larger' LDL ($x10^{-5}$)	19.7 (7.9 – 21.6)	11.9 (6.3 – 13.0)	0.31
Cer(d18:1/16:0) 'regular'/'larger' LDL ratio	0.7 (0.6 – 0.7)	0.8 (0.8 – 1.1)	***0.008***
Cer(d18:1/18:0) total plasma ($x10^{-5}$)	2.4 (1.2 – 3.8)	1.7 (1.4 – 2.6)	0.55
Cer(d18:1/18:0) 'regular' LDL ($x10^{-5}$)	5.3 (2.2 – 7.8)	3.0 (2.6 – 6.7)	0.69
Cer(d18:1/18:0) 'larger' LDL ($x10^{-5}$)	7.9 (4.0 – 11.8)	3.8 (2.8 – 4.4)	***0.032***
Cer(d18:1/18:0) 'regular'/'larger' LDL ratio	0.6 (0.5 – 0.7)	1.0 (0.7 – 1.5)	***0.008***
Cer(d18:1/20:0) total plasma ($x10^{-5}$)	8.9 (3.6 – 14.8)	7.2 (6.5 – 14.7)	0.84
Cer(d18:1/20:0) 'regular' LDL ($x10^{-5}$)	5.0 (2.0 – 5.9)	3.5 (2.7 – 6.6)	0.55
Cer(d18:1/20:0) 'larger' LDL ($x10^{-5}$)	6.1 (2.8 – 8.9)	5.3 (3.7 – 7.0)	0.55
Cer(d18:1/20:0) 'regular'/'larger' LDL ratio	0.8 (0.7 – 0.9)	0.7 (0.6 – 0.9)	0.69
Cer(d18:1/22:0) total plasma ($x10^{-5}$)	20.9 (9.7 – 38.7)	18.3 (13.8 – 36.4)	1
Cer(d18:1/22:0) 'regular' LDL ($x10^{-5}$)	8.2 (3.8 – 11.9)	6.0 (4.8 – 12.1)	0.55
Cer(d18:1/22:0) 'larger' LDL ($x10^{-5}$)	13.5 (5.9 – 17.2)	9.6 (6.5 – 13.9)	0.55

Table 4.3: Continued

	Advanced-diseased pigs	Mildly-diseased pigs	p-value
Cer(d18:1/22:0) 'regular'/'larger' LDL ratio	0.7 (0.6 – 0.9)	0.7 (0.6 – 0.9)	1
Cer(d18:1/24:0) total plasma ($x10^{-5}$)	20.8 (11.8 – 35.3)	17.1 (12.8 – 32.8)	1
Cer(d18:1/24:0) 'regular' LDL ($x10^{-5}$)	11.1 (7.7 – 11.9)	8.3 (6.1 – 13.2)	0.31
Cer(d18:1/24:0) 'larger' LDL ($x10^{-5}$)	16.3 (12.4 – 18.8)	13.5 (9.8 – 15.9)	0.15
Cer(d18:1/24:0) 'regular'/'larger' LDL ratio	0.62 (0.5 – 0.8)	0.62 (0.6 – 0.9)	0.69
Cer(d18:1/24:1) total plasma ($x10^{-5}$)	19.9 (11.3 – 24.9)	16.5 (12.8 – 32.3)	1
Cer(d18:1/24:1) 'regular' LDL ($x10^{-5}$)	10.8 (6.3 – 12.7)	7.6 (6.7 – 13.4)	0.69
Cer(d18:1/24:1) 'larger' LDL ($x10^{-5}$)	14.9 (8.4 – 16.3)	12.6 (8.5 – 14.7)	0.22
Cer(d18:1/24:1) 'regular'/'larger' LDL ratio	0.7 (0.7 – 0.8)	0.7 (0.6 – 1.0)	1
Cer Total total plasma ($x10^{-5}$)	80.4 (41.5 – 120.7)	66.8 (52.7 – 128.8)	0.84
Cer Total 'regular' LDL ($x10^{-5}$)	54.2 (27.6 – 58.8)	38.7 (29.9 – 62.7)	0.55
Cer Total 'larger' LDL ($x10^{-5}$)	77.6 (43.3 – 85.3)	58.1 (38.6 – 65.0)	0.10
Cer Total 'regular'/'larger' LDL ratio	0.7 (0.6 – 0.8)	0.8 (0.7 – 1.0)	0.22

All sphingolipid data were expressed relative to the cholesterol concentration in total plasma or the respective LDL peak. Data are presented as median (range) of the area under the curve. *Data of 1 pig are missing. Significant values are indicated as italic and bold.

Table 4.4: Sphingolipid-ratios in 'regular' and 'larger' LDL

	Advanced-diseased pigs	Mildly-diseased pigs	p-value
Cer(d18:1/16:0)/Cer(d18:1/24:0) total plasma ($x10^{-5}$)	0.3 (0.2 – 0.7)	0.3 (0.3 – 0.4)	0.84
Cer(d18:1/16:0)/Cer(d18:1/24:0) 'regular' LDL ($x10^{-5}$)	1.1 (0.6 – 1.5)	1.0 (0.7 – 1.5)	0.84
Cer(d18:1/16:0)/Cer(d18:1/24:0) 'larger' LDL ($x10^{-5}$)	1.1 (0.6 – 1.5)	0.8 (0.6 – 0.3)	0.84
Cer(d18:1/16:0)/Cer(d18:1/24:0) 'regular'/'larger' LDL ratio	1.0 (0.8 – 1.3)	1.2 (1.2 – 1.3)	0.10

Table 4.4: Continued

	Advanced-diseased pigs	Mildly-diseased pigs	p-value
Cer(d18:1/18:0)/Cer(d18:1/24:0) total plasma ($x10^{-5}$)	0.1 (0.1 – 0.2)	0.1 (0.1 – 0.1)	0.84
Cer(d18:1/18:0)/Cer(d18:1/24:0) 'regular' LDL ($x10^{-5}$)	0.4 (0.2 – 0.8)	0.4 (0.3 – 1.1)	0.55
Cer(d18:1/18:0)/Cer(d18:1/24:0) 'larger' LDL ($x10^{-5}$)	0.5 (0.2 – 0.7)	0.3 (0.2 – 0.4)	0.15
Cer(d18:1/18:0)/Cer(d18:1/24:0) 'regular'/'larger' LDL ratio	0.9 (0.8 – 1.3)	1.3 (1.2 – 2.5)	***0.032***
Cer(d18:1/24:1)/Cer(d18:1/24:0) total plasma ($x10^{-5}$)	1.0 (0.6 – 1.2)	1.0 (1.0 – 1.1)	0.55
Cer(d18:1/24:1)/Cer(d18:1/24:0) 'regular' LDL ($x10^{-5}$)	1.0 (0.8 – 1.1)	1.0 (0.8 – 1.2)	0.69
Cer(d18:1/24:1)/Cer(d18:1/24:0) 'larger' LDL ($x10^{-5}$)	0.9 (0.7 – 1.1)	0.9 (0.8 – 1.1)	0.69
Cer(d18:1/24:1)/Cer(d18:1/24:0) 'regular'/'larger' LDL ratio	1.2 (1.0 – 1.3)	1.1 (1.0 – 1.2)	0.69

All sphingolipid data were expressed relative to the cholesterol concentration in total plasma or the respective peak. Data are presented as median (range). Significant values are indicated as italic and bold.

Table 4.5: Sphingomyelin content of 'regular' and 'larger' LDL

	Advanced-diseased pigs	Mildly-diseased pigs	p-value
SM(d18:1/16:0) total plasma ($x10^{-3}$)	17.0 (8.0 – 17.4)	13.4 (11.4 – 22.6)	0.55
SM(d18:1/16:0) 'regular' LDL ($x10^{-3}$)	85.1 (62.7 – 134.0)	33.5 (25.4 – 46.3)	***0.008***
SM(d18:1/16:0) 'larger' LDL ($x10^{-3}$)	36.9 (34.9 – 41.6)	25.8 (22.3 – 35.1)	***0.032***
SM(d18:1/16:0) 'regular'/'larger' LDL	2.3 (1.8 – 3.4)	1.2 (1.1 – 1.3)	***0.008***
SM(d18:1/18:0) total plasma ($x10^{-3}$)	2.9 (1.2 – 3.0)	2.6 (1.7 – 3.9)	0.55
SM(d18:1/18:0) 'regular' LDL ($x10^{-3}$)	11.8 (9.2 – 25.4)	5.3 (3.5 – 6.7)	***0.008***
SM(d18:1/18:0) 'larger' LDL ($x10^{-3}$)	5.5 (4.5 – 7.0)	4.3 (3.0 – 5.1)	***0.032***
SM(d18:1/18:0) 'regular'/'larger' LDL ratio	2.4 (1.8 – 3.6)	1.2 (1.1 – 1.3)	***0.008***
SM(d18:1/18:1) total plasma ($x10^{-3}$)	0.6 (0.3 – 0.7)	0.4 (0.3 – 0.9)	0.55
SM(d18:1/18:1) 'regular' LDL ($x10^{-3}$)	2.4 (1.7 – 4.0)	0.9 (0.6 – 1.4)	***0.008***

Table 4.5: Continued

	Advanced-diseased pigs	Mildly-diseased pigs	p-value
SM(d18:1/18:1) 'larger' LDL ($x10^{-3}$)	1.0 (0.9 – 1.2)	0.7 (0.5 – 1.0)	0.095
SM(d18:1/18:1) 'regular'/'larger' LDL ratio	2.5 (1.8 – 3.9)	1.2 (1.1 – 1.4)	***0.008***
SM(d18:1/20:0) total plasma ($x10^{-3}$)	3.9 (1.5 – 4.2)	4.3 (2.6 – 5.7)	0.31
SM(d18:1/20:0) 'regular' LDL ($x10^{-3}$)	11.5 (8.1 – 18.2)	5.0 (3.5 – 7.8)	***0.008***
SM(d18:1/20:0) 'larger' LDL ($x10^{-3}$)	5.0 (4.4 – 5.7)	4.5 (3.0 - 5.5)	0.31
SM(d18:1/20:0) 'regular'/'larger' LDL ratio	2.0 (1.9 – 3.4)	1.2 (11 – 1.4)	***0.008***
SM(d18:1/22:0) total plasma ($x10^{-3}$)	6.3 (4.4 – 7.5)	6.4 (5.0 – 9.0)	0.55
SM(d18:1/22:0) 'regular' LDL ($x10^{-3}$)	17.0 (10.6 – 24.6)	6.8 (4.8 – 44.3)	0.151
SM(d18:1/22:0) 'larger' LDL ($x10^{-3}$)	5.3 (4.8 – 7.6)	5.6 (4.2 – 6.4)	0.548
SM(d18:1/22:0) 'regular'/'larger' LDL ratio	2.7 (2.1 – 3.5)	1.3 (1.0 – 6.7)	0.151
SM(d18:1/24:0) total plasma ($x10^{-3}$)	3.3 (2.7 – 4.7)	3.7 (2.8 – 4.9)	0.31
SM(d18:1/24:0) 'regular' LDL ($x10^{-3}$)	7.3 (4.6 – 11.4)	2.2 (1.6 – 3.5)	***0.008***
SM(d18:1/24:0) 'larger' LDL ($x10^{-3}$)	2.5 (1.8 – 2.8)	2.0 (1.5 – 2.7)	0.310
SM(d18:1/24:0) 'regular'/'larger' LDL ratio	2.6 (2.1 – 4.3)	1.2 (0.8 – 1.3)	***0.008***
SM(d18:1/24:1) total plasma ($x10^{-3}$)	14.6 (13.6 – 20.1)	16.5 (12.3 – 21.4)	0.69
SM(d18:1/24:1) 'regular' LDL ($x10^{-3}$)	38.6 (26.9 – 69.5)	15.0 (10.2 – 45.7)	0.310
SM(d18:1/24:1) 'larger' LDL ($x10^{-3}$)	12.9 (11.4 – 17.0)	12.1 (9.4 – 14.4)	0.095
SM(d18:1/24:1) 'regular'/'larger' LDL ratio	2.4 (2.1 – 4.1)	1.2 (1.0 – 3.3)	0.095
SM Total total plasma ($x10^{-3}$)	46.5 (36.5 – 56.4)	47.2 (36.1 – 68.3)	0.84
SM Total 'regular' LDL ($x10^{-3}$)	156.7 (128.0 – 287.0)	69.9 (49.7 – 92.4)	***0.008***
SM Total 'larger' LDL ($x10^{-3}$)	72.4 (65.2 – 80.7)	54.9 (44.4 – 69.7)	0.095
SM Total 'regular'/'larger' LDL ratio	2.4 (1.9 – 3.6)	1.2 (1.1 – 1.3)	***0.008***

All sphingolipid data were expressed relative to the cholesterol concentration in total plasma or the respective LDL peak. Data are presented as median (range) of the area under the curve. Significant values are indicated as italic and bold.

LDL profile in homozygous FH patients

Clinical characteristics of the 3 hoFH patients, all carrying *LDLR* mutations, are described in Table 4.6. Isolation of LDL by DGUC and subsequent separation of the isolated LDL fractions by FPLC revealed the presence of 'regular' and 'larger' LDL in the plasma of all three hoFH patients. The LDL profiles of Patient 2 and 3 were similar to the LDL profiles of the ADs with higher 'regular' LDL-C levels compared to 'larger' LDL-C levels while Patient 1 displayed an LDL-C profile similar to MDs (Figure 4.7).

Table 4.6: Homozygous FH patient characteristics

	Patient 1	**Patient 2**	**Patient 3**
Age (years)	23	31	28
Sex (m/f)	m	m	m
BMI	27.2	23.0	18.7
Hypertension	no	no	no
Diabetes	no	no	no
Smoker	no	former	no
Statines	yes	yes	yes
Ezetimibe	yes	yes	yes
Other lipid lowering medication	Lomitapide	Lomitapide	Lomitapide
FH mutation	LDLR Null/null G352D, exon8/ 2417insG, exon 17	LDLR Null/null 1685delACT, exon 11/ 1685delACT, exon 11	LDLR Null/null 4.4Kb dupl, exon 12/ 2.5Kb del exon 7 and 8
Highest cholesterol (mmol/L)	23.6	17.2	20.6
Cholesterol (mmol/L)	16.0	2.8	15.1
LDL (mmol/L)	14.5	1.7	14.6
HDL (mmol/L)	0.9	1.1	1.2
Triglycerides (mmol/L)	1.6	0.3	0.4

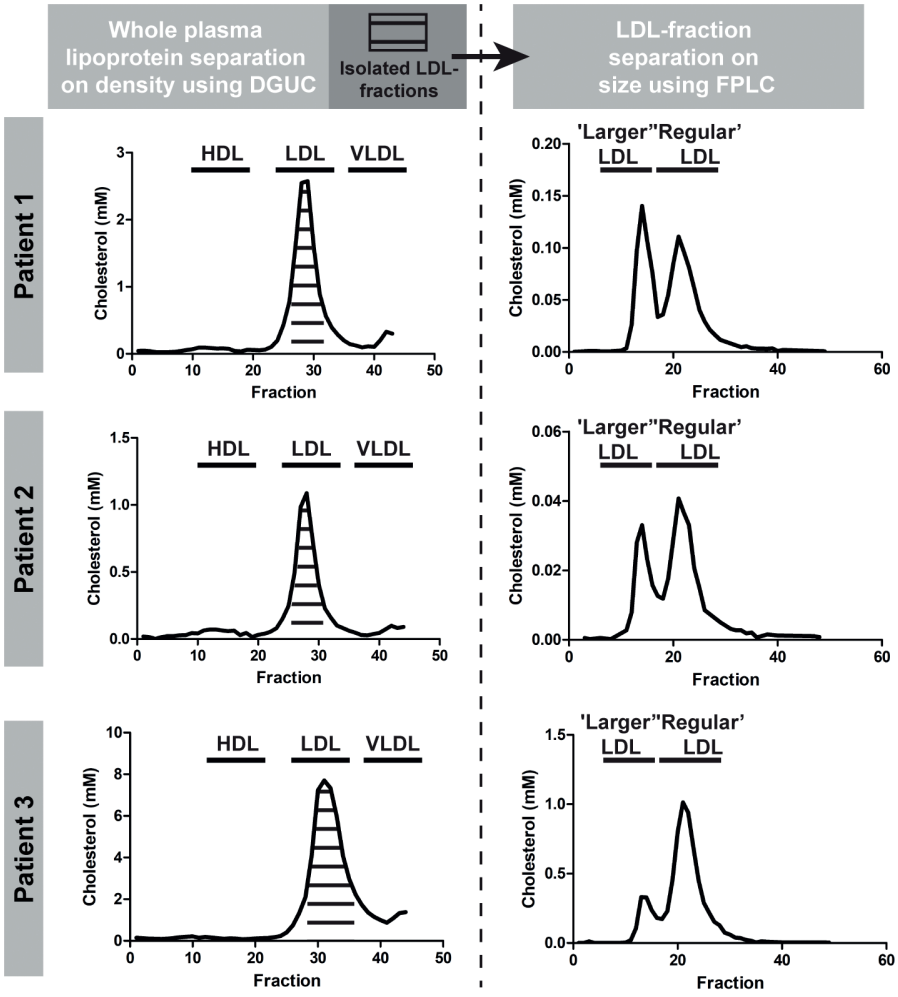

Figure 4.7: LDL profiles of three homozygous FH patients. Lipoproteins were separated on density using DGUC. Subsequently, the pooled LDL fractions were subjected to FPLC revealing the presence of 'regular' LDL and 'larger' LDL in hoFH patients.

DISCUSSION

Our main findings were that: 1) on a HFD, plaques in all hoFH pigs progressed significantly, but we could distinguish mildly-diseased pigs (MDs) and advanced-diseased pigs (ADs), despite the presence of the same homozygous *LDLR* R84C mutation and similar cholesterol, LDL-C, HDL-C and inflammatory levels; 2) the plaques of the MDs progressed to a stage of intimal xanthoma while in the ADs, large, advanced plaques with vulnerable characteristics including lipid-rich necrotic cores, calcifications, neovascularization and intraplaque haemorrhage were frequently observed; 3) separation of plasma lipoproteins based on size revealed a distinct LDL profile which differed significantly between ADs and MDs. This LDL profile contained both 'regular' LDL and lipoproteins with the density of LDL and the size of VLDL, i.e. 'larger' LDL; 4) the distribution of cholesterol and sphingolipids over 'regular' and 'larger' LDL shortly after the start of the HFD could significantly and consistently be linked to the severity of subsequent coronary atherosclerosis development; 5) the distinct LDL profile with 'larger' and 'regular' LDL was also observed in plasma of homozygous FH patients.

Coronary atherosclerosis development: comparison with other pig models

Although the MD pigs in our study did develop early plaques with a growth rate consistent to humans (on average 0.05 mm^2/month vs. 0.02mm^2/month[57]), pigs that develop more advanced, unstable plaques are most useful for cardiovascular studies. Therefore, we compared the results from the AD pigs with data from previously published studies on pig models of non-surgically induced coronary atherosclerosis development (Table 4.7).

Coronary plaque size

In comparison with all other porcine models of diet- or genetically-induced hypercholesterolemia with or without diabetes, our AD pigs present with one of the largest histological plaque sizes (Table 4.7). Only the HFD-diabetes pig model described by Patel et al.[270] presented with on average larger plaque areas (5.0 vs. 8.2 mm^2). Differences in tissue processing and the lack of perfusion fixation in many studies, including ours, however hampers a direct comparison, especially with the results of three studies which do use this tissue processing technique[150,273,288].

Although the lack of perfusion fixation of the histological samples could lead to overestimation of the plaque size, invasive imaging confirmed the presence of large plaques in our animals where 21% of the artery was occupied by plaques with a maxIMT>1.0 mm.

Table 4.7: Overview porcine studies of natural coronary atherosclerosis development with histological analysis

Reference	Breed	Sex	Age at start study (weeks)	Max. FU time (weeks)	Induction of atherosclerosis	Plaque size (PA unless otherwise indicated)	IMR	Plaque classification (% coverage of artery)
Prescott 1991[145]	Rapacz	Unknown	Mature	234	None	Occlusive	-	FCA
Neeb 2010[269]	Ossabaw (O) Yucatan (Y)	Male	Unknown	40	HFD	-	-	-
Thim 2010[150]	FBM minipig	Castrated male	39	18	HFD	NP/IT/IX: 0.28mm²* PIT: 0.93 mm²* FCA: 2.53 mm²*	NP/IT/IX: 0.19* PIT: 0.42* FCA: 1.26*	-
Al-Mashhadi 2013[274]	Yucatan PCSK9 mutation	Male(m) and female(f)	Unknown	46	HFD	Male: 0.29 mm²*† Female: 0.25 mm²*†	-	NP: 0%* IX: 0%(m) / 25%(f)* PIT: 100%(m) / 25%(f)* FCA: 0%(m) / 50%(f)*
Davis et al. 2014[273]	Yucatan LDLR$^{-/-}$	Female and castrated male	22	6	HFD	0.2 mm²	-	-

Table 4.7: Continued

Reference	Breed	Sex	Age at start study (weeks)	Max. FU time (weeks)	Induction of atherosclerosis	Plaque size (PA unless otherwise indicated)	IMR	Plaque classification (% coverage of artery)
Pedrigi et al. 2015[75]	Yucatan PCSK9 mutation	Female	Unknown	34	HFD	0.2 mm^2	-	NP:41% IT: 30% IX: 5% PIT: 24%
Poulsen et al. 2016[288]	FBM minipig	Castrated female	29	38	HFD	Average maximal PA*: 1.8 mm^2	-	NP: 11% IX: 60% PIT: 18% FCA:11%
Shim et al. 2017[289]	Yucatan $ApoE^{-/-}$	Unknown	8	44	HFD	Average maximal PA*†: 0.15 mm^2	-	IX: 75%*† PIT: 25%*†
Badin 2018[290]	Ossabaw	Female	130 (young) or 458 (old)	48	HFD	-	Average: 0.3 (young)†; 0.8 (old)†	-
Tharp 2019[291]	Rapacz	Castrated male	60	26	HFD	-	-	-
Hoogendoorn 2019	**FBM minipig**	**Castrated male**	**147**	**52**	**HFD**	**IT: 0.9 mm^2†§ IX: 0.9 mm^2†§ PIT: 2.1 mm^2†§ FCA: 4.2 mm^2†§ Average: 2.0 ^{m}m2**	**IT: 0.6†§ IX: 0.7†§ PIT: 1.8†§ FCA: 2.6†§ Average: 1.4**	**NP: 4%†§ IT: 2%†§ IX: 33%†§ PIT: 27%†§ FCA: 34%†§**

Table 4.7: Continued

Reference	Breed	Sex	Age at start study (weeks)	Max. FU time (weeks)	Induction of atherosclerosis	Plaque size (PA unless otherwise indicated)	IMR	Plaque classification (% coverage of artery)
Gerrity 2001[147]	Yorkshire	Male	8-12	48	HFD or HFD + diabetes	Stenosis degree: 86%†	-	-
Chatzizisis 200[86]6	Yorkshire	Male	Unknown	30	HFD + diabetes	-	Average: 0.55 – 1.3*†	IT: 18.3%* IX/PIT: 39.4%* FCA:42.3%*
Koskinas 2010/2013[67,93]	Yorkshire	Male	12-14	36	HFD + diabetes	Average: 1.6 – 2.7 mm^2*†	-	IT: 6%* IX/PIT: 25%* FCA: 69%*
Patel 201[327]0	Yorkshire	Male	Unknown	39	HFD + diabetes	-	-	No plaque: 13% IT/IX: 22% PIT: 22% FCA: 43%
Ludvigsen 2015[271]	Göttingen	Castrated male	11	43	HFD + diabetes	0.27 mm^2†	0.23†	IX: 33% PIT: 33% FCA: 33%
Ditzhuijzen 2016[272]	Yorkshire/ Landrace	Male	11	65	HFD or HFD + diabetes	-	-	IT - FCA

Plaque size and classification are based on histological data. Data based on imaging are mentioned in the text if the manuscript. Majority of the numbers are estimated from graphs. HFD=high fat diet, NP=no plaque, IT=intimal thickening, IX=intimal xanthoma, PIT=pathological intimal thickening, FCA=fibrous cap atheroma, IMR=intima-media ratio. *Only of the largest lesions, †Tissue not pressure fixed, ‡ Of all lesions, not of the whole artery, §Only of the advanced-diseased pigs. ||No imaging results reported on spontaneous plaque development.

Furthermore, IVUS-derived plaque burden is a measure that is often applied in the clinic to quantify disease burden, but is unfortunately rarely reported by other porcine model studies. Badin et al.[290] and Tharp et al.[291] observed average plaque burdens of 38% and 50% respectively. We demonstrated a maximal plaque burden of 77% in the ADs, indicating the presence of lumen intruding, clinically relevant plaques[12].

Coronary plaque composition

Monitoring changes in plaque composition in animal models by serial invasive imaging is vital to assess the development stage, plaque stability and similarity to human plaques. Our OCT imaging data showed a clear increase of coronary atherosclerosis over time. The large majority of the plaques presented as lipid-rich already from the first time point, whereas lipid-pools, i.e. FCAs, were rare, even at the last imaging time point. This observation is in large contrast to our histological data and might be the result of the main drawback of OCT: the inability to image beyond lipid-rich tissue[42]. According to our histological analysis, one-third of the plaques in the ADs presented as FCAs with lipid-rich necrotic cores. The majority of these FCAs were thick-cap FCAs and lipid-rich tissue, present between the lumen and the lipid-pool, could shield the lipid-pool from detection by OCT, leading to an underestimation of FCA presence by OCT.

The histologically-detected advanced plaque types PIT and FCAs were observed more frequently in the ADs from our study compared to many other models described in literature[67,75,93,271,272,274,288,292], except for the HFD-diabetes model by Patel et al.[270] (Table 4.7), confirming that the advanced disease stage observed in our model is very rare.

Besides a generally advanced plaque type, ADs displayed important features of unstable plaques[20]. Several of the previously studied porcine models also present with plaques that display necrotic cores, calcifications and neovascularisation[93,145,147,272,274,292], although quantification is often not reported. While some papers also report the occurrence of IPH[145,147,150,274], the AD pigs in this study present widespread IPH, known to be an important indicator of fast plaque growth and destabilization[15].

While the MD pigs displayed more diffuse disease development, AD pigs developed the largest and most advanced plaques mainly in the proximal coronary regions. This latter observation very well matches the coronary atherosclerosis growth patterns observed in humans[293].

Taken together, the AD pigs of the adult FBM minipig model from this study develop some of the most advanced plaques so far described in literature and this model is not complicated by the introduction of extra risk-factors like diabetes[270]. The development of the large plaques with unstable, human-like features as observed in the AD pigs is likely associated with the advanced age of the animals. Unlike almost all previous studies (Table

4.7), we used adult pigs instead of juveniles for our experiments since, as mentioned in the introduction, ageing is known to enhance atherosclerosis development both in pigs[290] and in humans[276–278]. The extensive characterization of coronary atherosclerosis development in this model forms a road-map for future pathophysiological or imaging studies with this highly relevant model. Selection of the ADs on forehand by using the described lipoprotein profiling would further accommodate this. Future studies will have to provide more information on sex-dependent differences and a possible genetic basis and heredity of the observed inter-individual differences in disease development.

The distribution of cholesterol and sphingolipids over low-density lipoprotein subclasses is directly linked to the severity of subsequent coronary atherosclerosis development

Although inter-individual variation in coronary artery disease development has been previously observed in FH patients[279] as well as in other animal models of FH, such a pronounced difference in disease development as observed in our pig model has, to the best of our knowledge, not been reported. Conventional risk factors such as total cholesterol, LDL-C and inflammatory markers could not distinguish AD from MD pigs. Detailed lipoprotein analysis, performed to elucidate possible underlying mechanisms, however revealed an LDL profile with 'regular' and 'larger' LDL in FH pigs on an HFD that was distinctly different between MD and AD pigs.

LDL is an established and important initiator and promotor of atherosclerosis and remains the primary target of prevention of CAD[294]. Not only the concentration of circulating LDL determines the risk of CAD, also differences in size, density and composition can influence its atherogenicity[295]. In this study, the observed LDL-C profile with 'regular' and 'larger' LDL distinguished AD from MD pigs in all cases. Since this LDL-profile was already present early in the study, before the start of major plaque development, there could be a causal relation with the severity of coronary atherosclerosis development. Although the 'larger' LDL particles were similar in size to VLDL, we considered these particles to be LDL because of the very low triglyceride levels after size separation and the very low levels of VLDL-C after density gradient ultracentrifugation. Lipoproteins with the density of LDL and size of VLDL have been observed previously in atherosclerotic tissue homogenates[296] and in plasma of HFD-fed pigs with an LDLR-mutation[150] (same breed used in this study) and with an PCSK9-mutation[274]. However, this 'larger' LDL has not been linked to disease severity before.

Beside cholesterol, also the distribution of sphingolipids over 'larger' and 'regular' LDL was significantly different between AD and MD pigs which could indicate a difference in LDL functionality. For S1P, the 'regular'/'larger' LDL ratio was higher in ADs than in MDs, and while the long-chain ceramide content was relatively higher in 'larger' LDL of

the ADs compared to the MDs, the long-chain sphingomyelin (SM) content was higher in 'regular' LDL of the AD pigs. Sphingolipids, like SMs, S1P and ceramides, are a large group of structurally and functionally diverse lipids that are found in lipoproteins where they preserve structure and play a role in functionality of the lipoproteins. *In vitro* studies have shown that SM contained in LDL can undergo hydrolysis by sphingomyelinases, leading to increased LDL-ceramide levels, which in turn promotes LDL aggregation[297–299] and fusion[299]. Aggregated/fused LDL can infiltrate into the vessel wall via enhanced binding to proteoglycans[298,299]. Accordingly, LDL in atherosclerotic plaques contains markedly higher levels of ceramide compared to LDL in plasma or in the healthy vessel wall[298,300]. High levels of LDL-derived ceramides and sphingomyelins in the vessel wall can induce apoptosis[301], foam cell formation[297,298] or increase plaque inflammation[302]. Higher LDL-ceramide and sphingomyelin levels may thus contribute to the enhanced atherosclerosis development in AD pigs.

The 'larger' LDL observed in our FH pigs may consist of aggregated LDL as Öörni et al.[299] showed that the aggregation/fusion of ceramide-rich LDL can give rise to two LDL subclasses upon separation by size-exclusion. This hypothesis is in line with the high SM levels observed in 'regular' LDL of the ADs, which could make this LDL subtype more prone to aggregation. However, MD pigs presented with the highest 'larger' LDL-C levels which contained relatively low ceramide levels, rendering aggregation unlikely.

The 'larger' LDL of the AD and MD pigs differs in long-chain, but not in very long-chain ceramides, suggesting that besides ceramide concentration, also ceramide chain-length influences the atherogenicity. Accordingly, Hartmann et al.[303] reported that an increase in long-chain over very-long chain ceramides can enhance cell proliferation and apoptosis.

Since these different LDL fractions can only be identified using FPLC instead of the more commonly applied DGUC technique, a recommendation for future studies would be to characterize the components of the lipoprotein fractions also based on FPLC.

Clinical relevance

Multiple clinical studies associated plasma-levels of ceramides and sphingomyelins with coronary artery disease development[304], vulnerable plaque composition[305] and with future major adverse cardiovascular events[287,305,306]. Furthermore, higher ratios of Cer(d18:1/16:0)/Cer(d18:1/24:0) and Cer(d18:1/18:0)/Cer(d18:1/24:0) have been pinpointed as predictors for cardiovascular death[287,305]. Based on the plasma levels of ceramides and SMs, we could not distinguish AD from MD pigs, possibly by a lack of power. When we however assessed the ceramide ratios in the two LDL subclasses, these were directly related to disease severity. These data suggest that assessment of

the cholesterol and sphingolipid distribution over the two LDL subclasses is a highly potent and possibly even stronger biomarker for individual risk assessment of coronary atherosclerosis development than LDL-C and sphingolipid levels in plasma. Future studies are necessary to further elucidate the exact composition and biological function of 'larger' LDL, and of the importance of the 'regular'-/'larger' LDL balance.

An interesting observation is the occurrence of the distinct LDL profile with 'regular' and 'larger' LDL in the plasma of three homozygous FH patients in whom the LDL-C ratios displayed pronounced differences between the patients. Cardiovascular disease severity is highly variable in FH patients and currently, no existing biomarker can reliably predict cardiovascular disease development in individual FH patients[307]. The distinct LDL profile discovered in this study forms a promising biomarker for individual FH patients and even a potential drug target. A clinical study with a larger cohort of homozygous and heterozygous FH patients, specifically also including women, will have to show the value of this LDL profile as a biomarker and/or as a risk-factor for cardiovascular disease. It also needs to be determined whether this distinct LDL profile is also present in other dyslipidemia patients, and whether lipid-lowering medication like statins influence this LDL profile.

LIMITATIONS

The sample size in this study was relatively small. The division of the group of pigs with regard to disease severity was unforeseen and resulted in a low number of animals with advanced disease, but it also enabled the discovery of a new, high-potential biomarker for atherosclerosis development. Despite the low number of animals in both groups, this potential biomarker still came out as a significant predictor. Furthermore, while histology was important for determining the plaque composition at a detailed level, the lack of perfusion fixation of the coronary histological samples hampered accurate quantification of plaque size. Besides, the low number of patients did not allow for a study to the relation with clinical outcome, but this first exploratory study did establish the first proof of the presence of a potential new biomarker for CAD.

CONCLUSION

The adult, hoFH FBM pig model is a large animal model in which half of the pigs allows for assessment of early plaque development while the other half demonstrates development of advanced coronary atherosclerotic plaques when fed an HFD. This latter group of advanced-diseased pigs presented with widespread development of

large, lumen intruding plaques with extensive unstable, human-like features. These features render these pigs very suitable for testing and validating new interventions and (invasive) imaging techniques. Besides, we identified a distinct low-density lipoprotein profile in which a detailed component analysis revealed that the distribution of cholesterol and sphingolipids over 'larger' and 'regular' LDL was directly associated with the severity of coronary atherosclerosis development. Despite the low number of pigs, these measurements were highly significantly different between both groups of pigs, indicating the power and potential of this biomarker. Since this LDL profile was already present before the start of major plaque development, there may be a causal relation. This novel biomarker is highly useful to select advanced-diseased pigs early in the study. Moreover, since we also detected this specific LDL profile in human homozygous FH patients, this specific LDL profile has a great potential to function as a biomarker to select those individual (FH) patients at the highest risk of developing cardiovascular disease or to become a treatment target.

ACKNOWLEDGMENTS

We gratefully acknowledge Dennis Akkermans and Vincent Vaes for their help with animal caretaking and for their support during the experimental procedures. We would also like to thank Claire Bal Dit Sollier for her support in arranging the animal logistics, Frank Leijten for the genotyping of the pigs and Adrie Verhoeven for critically reviewing the manuscript.

CHAPTER 5

Multidirectional wall shear stress promotes advanced coronary plaque development – comparing five shear stress metrics

Ayla Hoogendoorn
Annette M. Kok
Eline M.J. Hartman
Giuseppe de Nisco
Lorena Casadonte
Claudio Chiastra,
Adriaan Coenen
Suze-Anne Korteland
Kim Van der Heiden
Frank J. H. Gijsen
Dirk J. Duncker
Antonius F.W. van der Steen
Jolanda J. Wentzel

Based on:

'Multidirectional wall shear stress promotes advanced coronary plaque development – comparing five shear stress metrics', *in rebuttal for Cardiovascular Research*

ABSTRACT

Aims

Atherosclerotic plaque development has been associated with wall shear stress (WSS). However, the multidirectionality of blood flow, and thus of WSS, is rarely taken into account. The purpose of this study was to comprehensively compare five metrics that describe (multidirectional) WSS behaviour and assess how WSS multidirectionality affects coronary plaque initiation and progression.

Methods and results

Adult familial hypercholesterolemic pigs (n=10) that were fed a high-fat diet, underwent imaging of the three main coronary arteries at three time points (3 (T_1), 9 (T_2) and 10-12 (T_3) months). A 3D-geometry of the arterial lumen, in combination with local flow velocity measurements, was used to calculate WSS at T_1 and T_2. For analysis, arteries were divided into 3mm/45° sectors (n=3648). Changes in wall thickness, and final plaque composition were assessed with near-infrared spectroscopy-intravascular ultrasound (NIRS-IVUS) and optical coherence tomography (OCT) imaging, and histology. Both in pigs with advanced and mild disease, the highest plaque progression rate was exclusively found at low TAWSS or high multidirectional WSS regions at both T_1 and T_2. However, the eventually largest plaque growth was located in regions with initial low time-averaged WSS or high multidirectional WSS, that, over time, became exposed to high time-averaged WSS or low multidirectional WSS at T_2. Besides plaque size, also the presence of vulnerable plaque components at the last time point was related to low and multidirectional WSS. Almost all WSS metrics had good predictive values for the development of plaque (47-50%), and for advanced fibrous cap atheroma development (59-61%).

Conclusions

This study demonstrates that low and multidirectional WSS promote both initiation and progression of coronary atherosclerotic plaques. The high predictive values of the multidirectional WSS metrics for fibrous cap atheroma development indicate their potential as an additional clinical marker for vulnerable disease.

INTRODUCTION

Ischemic coronary artery disease (CAD), caused by destabilization and subsequent rupture of atherosclerotic plaques, is predicted to remain the leading cause of death[308]. Although the complex process of plaque development is incompletely understood, wall shear stress (WSS) is known to play a key role. WSS is a biomechanical metric that describes the frictional force between blood flow and the endothelial cells covering the arterial wall. Both pre-clinical and clinical studies showed an intricate role of WSS in (advanced) plaque development, since both low and high WSS have been associated with plaque growth and destabilization[48,57,66–71]. To further elucidate the role of WSS in coronary atherosclerosis, longitudinal imaging studies are crucial. Moreover, since most studies only use time-averaged WSS (TAWSS) as a descriptor of disturbed blood flow, the multidirectionality of blood flow, induced by its pulsatile nature in combination with the 3D geometry, is not taken into account. Therefore, in recent years, new WSS metrics have been developed to capture this multidirectional flow behaviour: the oscillatory shear index (OSI), relative residence time (RRT), transverse WSS (transWSS) and its normalized version: the cross-flow index (CFI) (Table 5.1). The role of TAWSS, RRT and OSI was demonstrated in a number of studies[48–50,75,77,309]. However, transWSS and CFI have not been investigated before in a longitudinal imaging study with histopathology. Since patient studies do not allow for multiple invasive imaging procedures and the collection of coronary tissue, we employed a highly relevant porcine model of familial hypercholesterolemia[150] to study the effect of multidirectional WSS on plaque development. By using adult, full grown pigs, we excluded the influence of growth-related changes in the geometry of the coronaries, important for serial assessment of WSS and plaque size. Serial, multimodality invasive imaging, combined with a detailed histological analysis enabled us to comprehensively compare five different (multidirectional) WSS metrics to assess how multidirectional WSS affects both plaque initiation and progression.

Table 5.1: Overview of the (multidirectional) shear stress metrics

Shear stress metric	Description	References
Time-averaged wall shear stress (TAWSS)	Shear stress averaged over the cardiac cycle	46,47
Oscillatory shear index (OSI)	Ratio between back- and forward going shear stress	48
Relative residence time (RRT)	Relative time that a blood particle resides at a certain location at the vessel wall	49
Transverse wall shear stress (transWSS)	Shear stress vector along the wall, in perpendicular direction to the main flow direction	50
Cross-flow index (CFI)	The transWSS normalized for the wall shear stress	51

METHODS

A detailed description of the surgery protocol, blood and tissue processing, and of histological and imaging analysis is provided in Chapter 4.

Animal model, invasive imaging procedure, and histology analysis

The animal protocol was approved by the local animal ethics committee of the Erasmus MC (DEC EMC109-14-10) and the study was performed according to the National Institutes of Health guide for the care and use of Laboratory animals[280]. At the age of 34±3 months, familial-hypercholesterolemic Bretonchelles Meishan (FBM) pigs[150] (n=10, castrated males) were put on a high-fat diet (10% lard and 0.75% cholesterol, the National Institute of Agronomic Research, France) that was given in restricted amounts to maintain a constant weight. At three months of high-fat diet (T_1), the 3D geometry of the coronary arteries was assessed by CT angiography (CTA). Subsequently, an invasive imaging procedure was conducted in which near-infrared spectroscopy - intravascular ultrasound (NIRS-IVUS), and optical coherence tomography (OCT) imaging were used to assess the coronary plaque size and composition in all three main coronary arteries (i.e., left anterior descending (LAD), left circumflex (LCX) and right coronary artery (RCA)). Furthermore, invasive local Doppler-derived flow velocity measurements were obtained at multiple locations in the coronaries using a ComboWire (Volcano, Corporation, Rancho Cardova, USA). This imaging procedure was repeated at 9 (T_2) and 10-12 months (T_3) for all pigs. At the last imaging time point, animals were sacrificed by an overdose of pentobarbital followed by exsanguination by removal of the heart. The coronary arteries were collected from the heart and used for histological analysis according to the methods described in Chapter 4. In short, all 3-mm coronary segments

were classified according to the adjusted AHA classification[20] (i.e., no plaque, intimal thickening (IT), intimal xanthoma (IX), pathological intimal thickening (PIT) and fibrous cap atheroma (FCA)). Furthermore, the lipid, macrophage and necrotic core content of each segment was quantified.

OCT analysis

OCT analysis was performed using QCU-CMS software (version 4.69, LKEB, Division of Image Processing, Leiden University Medical Centre, Leiden, The Netherlands) and plaque composition was assessed every millimetre (1 out of every 5 frames) according to the OCT analysis consensus standards[42]. Lumen contours were delineated semi-automatically. Fibrous tissue, lipid-rich tissue or lipid-pools were indicated manually by drawing angles from the lumen centre. Fibrous tissue was indicated when a plaque (WT >0.5mm), presenting as homogeneous and low-attenuation signal with the 3-layered structure still visible was present. A plaque region with an inhomogeneous, slowly attenuating signal and an invisible 3-layered wall structure was classified as lipid-rich. A lipid-pool angle was indicated as a region with a sudden drop in signal with a diffuse border and an overlying signal rich cap structure. Each frame was classified according to its most advanced component as fibrous, lipid-rich or fibrous cap atheroma (FCA). The latter classification was given when a lipid pool was present.

IVUS analysis

Before analysis, the IVUS pullbacks were gated by selecting the frames that were located 6 frames before the R-peak in the ECG signal using in-house developed software. Hereby, changes in lumen size caused by movement of the catheter or by the contraction of the heart were removed. Analysis of the gated IVUS pullbacks was performed using QCU-CMS software. In every gated IVUS frame, vessel wall and lumen borders were delineated semi-automatically. Interobserver variability was assessed for the manual segmentation of the plaque area. For this analysis, two independent expert observers (AH and EH) both segmented a total of 1192 IVUS frames derived from multiple different pullbacks of different disease stages. The average intraclass correlation coefficient was high: 0.927 (0.805-0.976).

Wall shear stress calculations

Geometrical model construction

For the 3D reconstruction of the coronary arteries at T_1 and T_2, the CTA scan was reconstructed over a 300 ms time window at diastole to ensure maximal filling of the coronary arteries, including all side branches. Semi-automatic CTA segmentation[310] was

performed in Mevislab (Bremen, Germany) whereby the centreline of the coronary artery was determined. The IVUS images were longitudinally and circumferentially registered to the CTA using the location of side branches. Subsequently, the IVUS lumen and wall contours of T_1 and T_2 were placed at the corresponding location on the centreline. The side branches and the proximal and distal ends of the artery outside of the IVUS region were segmented on CTA. These CTA contours were scaled to match the IVUS lumen contours of the main artery to account for incomplete filling of the artery or for the blooming effect of the contrast in the CTA. The IVUS contours of T_1 and T_2 (main artery and thus region-of-interest) and CTA contours (proximal and distal section outside the IVUS region and the side branches) were fused to reconstruct a 3D geometry of the luminal surface of the whole coronary artery at T_1 and T_2 (Figure 5.1A). The wall thickness (WT) was computed by calculating the distance between the vessel wall and lumen contours.

Boundary conditions

For computational fluid dynamics (CFD), information on the inflow and flow distribution through the side branches is required. The flow was derived from intravascular Doppler-derived velocity measurements (Figure 5.1A). Quality of these measurements was assessed by an experienced committee (AH, AK, EH, FG, JW) and only reliable measurements were used to determine the velocity rate. The most proximal good flow measurement was used for a time-dependent velocity waveform that was imposed on the inlet of the artery. Flow distribution was determined based on velocity measurements in the segments between side branches. For regions where no (reliable) flow measurements were available, the Huo-Kassab diameter-based scaling law[311] was applied to determine the flow distribution between the main branch and the side branch. Furthermore, the vessel lumen was considered as rigid and subjected to no-slip boundary condition. Blood was assumed to behave as shear-thinning fluid and was modelled according to the Carreau model[312].

Meshing and computational fluid dynamics solution procedure

Each 3D geometry of the lumen at T_1 and T_2 was converted to a tetrahedral mesh in ICEM CFD (v.17.1, ANSYS Inc., Canonsburg, PA, USA) which was used for CFD simulations. The mesh size was determined by a mesh independence study (errors <1% of shear stress were allowed), resulting in a typical element size of 0.05 mm. Unsteady CFD simulations were performed using Fluent (v.17.1, ANSYS Inc.). The solution procedure was carried out following previously described methods[313].

Post processing: matching OCT, NIRS and histology data to WSS

To assess the association between T_1 or T_2 WSS levels and subsequent plaque growth (ΔWT/month), all IVUS and WSS data of T_2 and T_3 were matched to the T_1 IVUS pullback. This enabled us to study the relation of ΔWT/month T_1-T_2 and WSS at T_1; and the relation of ΔWT/month T_2-T_3 and WSS at T_2. The match was performed both longitudinally and circumferentially based on the location of side branches. For the relation between T_1 WSS levels and plaque composition, OCT and NIRS-IVUS data at T_{last} were matched to the T_1 IVUS pullback according to the same methods as for the WT analysis, to allow a direct coupling to the 3D lumen geometry and thus to the WSS data.

To match the histology data with WSS at T_1, the histological 3mm-segments were matched on the IVUS pullback taken at T_{last}, which could subsequently be matched to IVUS data of T_1 and thus to WSS at T_1. Matching was performed in longitudinal direction and was based on the location of side branches and typical plaque components like calcifications. Between the matching points, the histology blocks were linearly distributed.

Table 5.2: Overview average WSS levels for each tertile of the respective WSS metrics

TAWSS (Pa)	T_1			T_2		
	Low	Mid	High	Low	Mid	High
AD	0.62±0.21	0.85±0.29	1.20±0.57	0.55±0.28$^{\#}$	0.86±0.49	1.32±0.90†
MD	0.70±0.27	0.93±0.40	1.29±0.70	0.48±0.15$^{\#}$	0.60±0.21*†	0.79±0.36*†

OSI (x10^{-3}) (-)	T_1			T_2		
	Low	Mid	High	Low	Mid	High
AD	0.52±0.73	2.71±3.54	15.26±23.66	1.06±1.87†	3.65±4.78†	25.60±52.03†
MD	0.79±1.33	2.88±4.07	12.35±22.60	8.03±14.16†	13.75±15.47*†	30.76±24.84†

RRT (Pa^{-1})	T_1			T_2		
	Low	Mid	High	Low	Mid	High
AD	1.04±0.43	1.37±0.47	1.94±0.69	1.06±0.48	1.55±0.65†	2.73±2.97†
MD	1.03±0.51	1.31±0.55	1.75±0.80	1.63±0.79*†	1.99±0.81*†	2.51±0.90†

CFI (x10^{-2}) (-)	T_1			T_2		
	Low	Mid	High	Low	Mid	High
AD	3.31±2.22	7.11±3.79	13.93±7.25	2.87±2.03†	6.62±3.85†	14.91±9.68†
MD	3.50±2.24	6.98±3.55	13.84±7.69	4.38±2.21*†	8.79±3.51*†	16.36±7.15†

Table 5.2: Continued

transWSS ($x10^{-2}$) (Pa)	T_1			T_2		
	Low	Mid	High	Low	Mid	High
AD	2.32±1.97	4.55±3.34	8.14±5.66	1.70±1.37†	3.53±2.47†	6.99±4.81†
MD	2.22±1.40	4.50±2.61	8.82±5.51	1.57±1.09†	3.31±2.07†	6.40±3.99†

AD= advanced-diseased pigs; MD=mildly-diseased pigs. *p<0.05 compared to AD. †p<0.05 compared to T_1

Analysis of WSS, WT and plaque composition data

For analysis, all arteries were divided into 3 mm segments of 45° (sectors) (Figure 5.1B). For each individual artery, the WSS metrics at T_1 and T_2 were divided into artery-specific tertiles (low, mid and high) (Table 5.2).

IVUS data of T_2 and T_3 were matched based on anatomical landmarks to the IVUS-data at T_1 to assess, at each location, changes in plaque size (i.e. plaque growth). All data on plaque growth ($\Delta WT\ T_1 \rightarrow T_2 = WT\text{-}T_2 - WT\text{-}T_1$; $\Delta WT\ T_2 \rightarrow T_3 = WT\text{-}T_3 - WT\text{-}T_2$) were expressed as ΔWT per month on high-fat diet between the respective time points. The used matching method enabled projection of T_2 WSS on the T_1 WSS maps, whereby permitting assessment of locations with sustained low WSS or sustained high WSS. Locations were classified as 'sustained' when the WSS remained either 'low' or 'high' at both T_1 and T_2.

To assess the relation between OCT and NIRS-derived plaque composition and WSS, sectors regarded as 'positive' on OCT (fibrous or lipid-rich) or on NIRS (a 'high probability' (>60%)) were selected. This selection method for NIRS positive sectors is the same analysis method used for standard determination of the lipid-core burden index (LCBI), but applied to sector level instead of total-vessel level. The percentage of all OCT or NIRS-positive sectors that was exposed to low, mid and high WSS was assessed.

Since the matching between histology and IVUS was not performed in circumferential direction, the WSS data of each matched 3-mm segment was averaged circumferentially.

Statistics

IBM SPSS Statistics (version 24.0) software was used for statistical analysis. Normally distributed data are shown as mean±standard deviation (SD) and statistical difference was determined with a repeated measures ANOVA with Bonferroni post-hoc testing. Statistical differences in frequency distributions were assessed using a Chi-square test. Non-normally distributed data are presented as median (inter-quartile range (IQR)) and statistical difference was determined with a Mann-Whitney U test. Statistical analysis of the WSS data was performed using a linear mixed effects model, with WSS (low, mid, high), as fixed factor and the individual vessel as random factor, adjusting for cholesterol levels. The Bonferroni correction was applied to adjust for multiple comparisons between the WSS tertiles. For comparison of the WSS effect on plaque progression between T_1-T_2 and T_2-T_3, time was added as a repeated measure factor to this same model. In all figures that display the association between plaque size or composition and the five WSS-metrics, the estimated means and standard errors derived from these models is displayed. $p<0.05$ was regarded as significant.

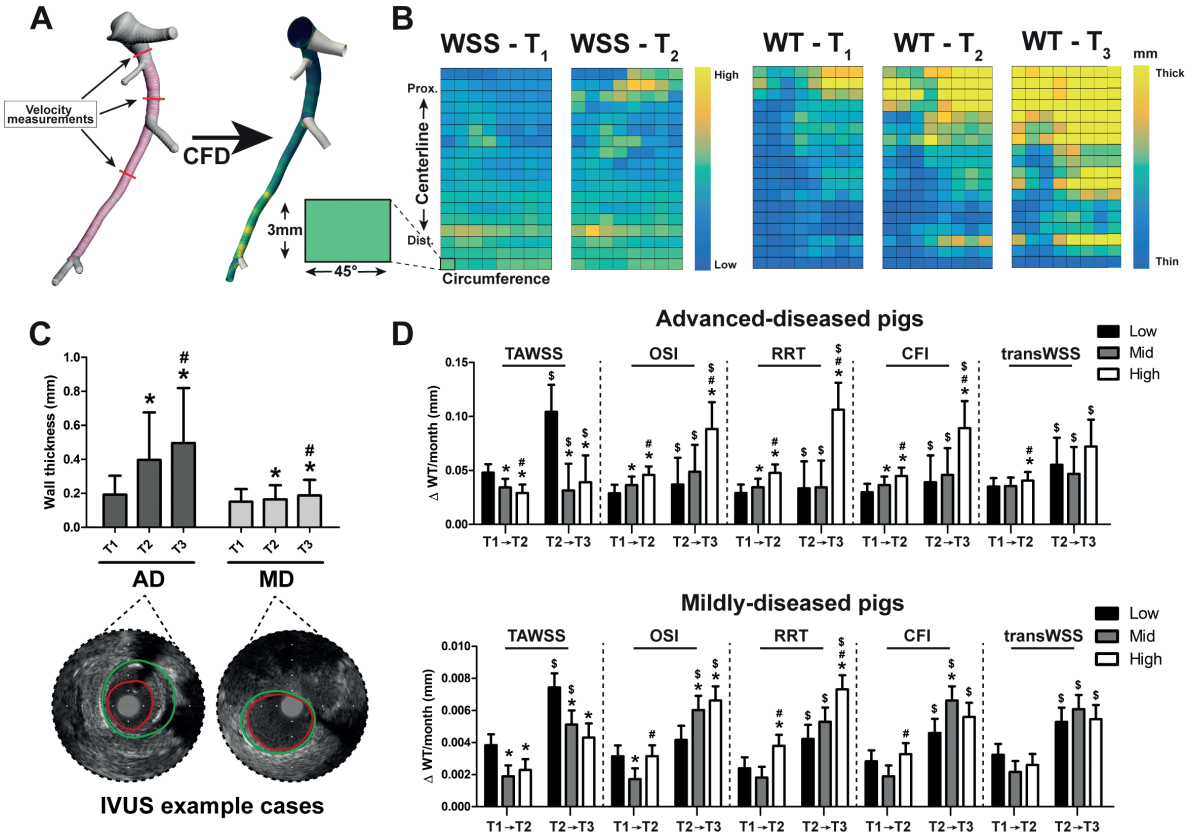

Figure 5.1: Methodology of wall shear stress (WSS) calculation and analysis, and the relation between local (multidirectional) WSS levels and the subsequent plaque growth rate in both plaque initiation and progression.

Figure 5.1: Continued: **A**) IVUS (pink) and CT (white) contours were fused to reconstruct the grey lumen surface. This surface, together with local flow measurements, was used as input for computational fluid dynamics, resulting in local WSS values (yellow=high; blue=low). **B)** From the 3D reconstructions, a 2D map of the WSS levels at T_1 and T_2, and of the wall thickness (WT, T_1-T_3) was created. For the analysis, the artery was divided in 3mm/45° sectors. **C)** The mean (±SD) WT at T_1-T_3 in advanced-diseased (AD) (n=1893 sectors at T_1 and T_2 and n=1240 sectors at T_3) and mildly-diseased (MD) (n=1755 sectors) pigs with two representative IVUS frames from T_3 (red contour=lumen; green contour=vessel wall). *p<0.05 compared to T1, $^{\#}$p<0.05 compared to T_2 (statistics: two-way repeated-measures anova with Bonferroni post hoc). **D)** The effect of low/mid/high levels of the respective WSS metrics on the subsequent plaque growth rate (estimated mean±SEM) in plaque initiation (T_1-T_2) and plaque progression (T_2-T_3). Important to note: for the AD pigs, the T_2-T_3 data are derived from 3 (instead of 5) pigs (n=1240 sectors), which means that the analysis of a difference in the relation between T_1-T_2 and T_2-T_3 ($^{\$}$) could only be performed in these 3 animals. *p<0.05 compared to the low tertile; $^{\#}$p<0.05 compared to the mid tertile; $^{\$}$p<0.05 compared to T_1-T_2 in the same tertile (statistics: linear mixed effects model). TAWSS=time-averaged WSS; OSI=oscillatory shear index; RRT=relative-residence time; CFI=cross-flow index; transWSS=transverse WSS.

RESULTS

Of the ten pigs, one pig died during feeding, a day after the invasive imaging procedure at T_2, due to a presumed myocardial infarction. One pig had to be sacrificed between T_2 and T_3 because of suffering from thrombosis in the leg. Data of these pigs have been included in the analysis, although imaging information at T_3 is missing. For analysis of the relation between T_1 WSS metrics and eventual plaque composition, T_2 was considered as T_{last} for these two pigs. For the other pigs, T_3 equalled T_{last}. In total, 30 vessels relating to 3648 3mm/45° sectors were analysed.

Advanced-diseased and mildly-diseased pigs

Although all pigs had the same mutation and were fed the same diet, 5 of the 10 pigs developed large, lumen intruding coronary plaques (plaque burden (PB) >40%) (advanced-diseased pigs (ADs)) within 9 months, while the other 5 pigs only developed limited atherosclerosis (PB<40%) within 12 months follow-up (mildly-diseased pigs, MDs)). The two groups of pigs showed no difference in weight (MDs: 91 kg (80-94) vs. ADs 82 kg (68-94) (p=0.33)) and in cholesterol, LDL, HDL levels (10.4 mmol/L (9.2-12.1) vs. 10.5 mmol/L (9.8-18.3) (p=0.54); 2.8 mmol/L (2.5-4.2) vs. 3.0 mmol/L (2.3-3.5) (p=0.79); 8.5 mmol/L (7.1-9.8) vs. 9.2 mmol/L (8.1-16.6) (p=0.33) in MD versus AD respectively). Because of the large difference in plaque development, the subsequent results will be presented separately for both groups.

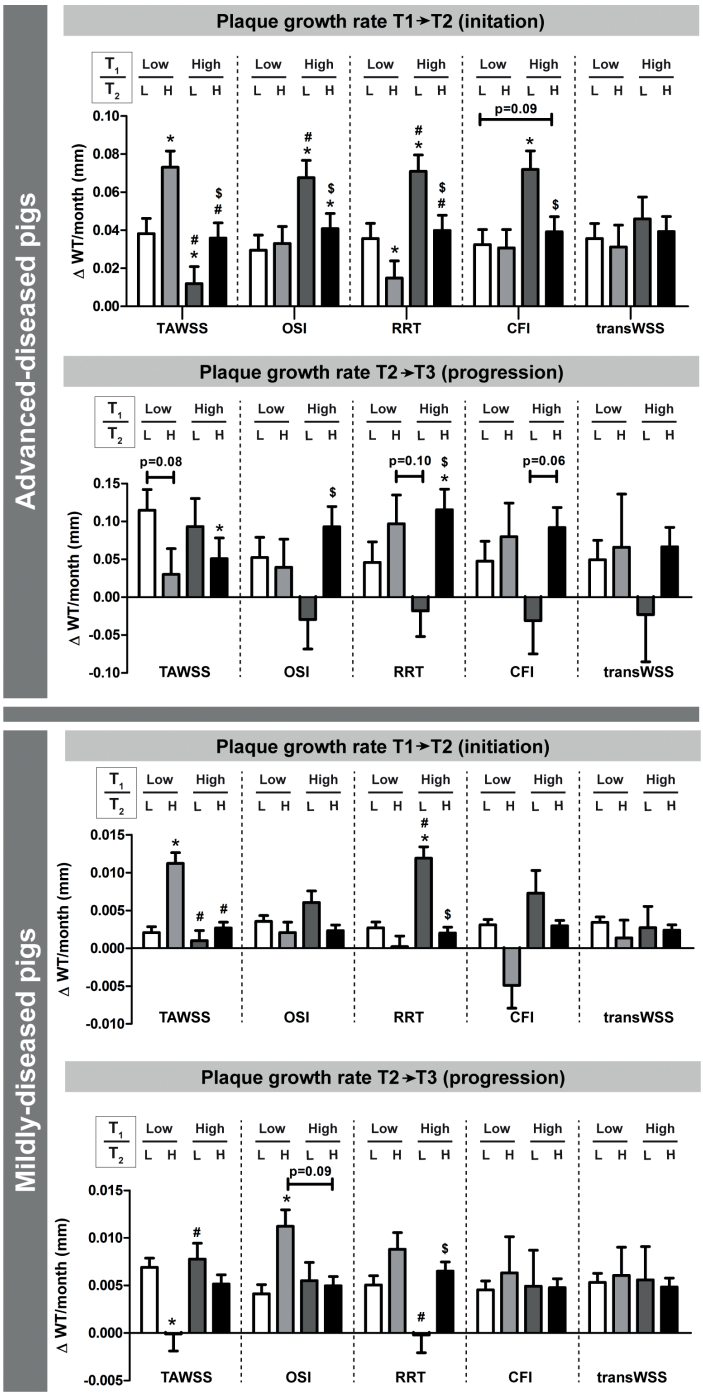

Figure 5.2: The long-term effect of sustained or changed levels of (multidirectional) wall shear stress (WSS) on the plaque growth rate in advanced-diseased and mildly-diseased pigs.

Figure 5.2: Continued: The plaque growth rate during plaque initiation (T_1-T_2) and plaque progression (T_2-T_3) in regions with either sustained low (L), low turning to high (H), high turning to low, or sustained high WSS between T_1 and T_2. Analysis is depicted for all WSS metrics (time-averaged WSS (TAWSS); oscillatory shear index (OSI); relative-residence time (RRT); cross-flow index (CFI); transverse WSS (transWSS)). Number of analysed sectors: for AD pigs T_1-T_2: n=1893 and T_2-T_3: n=1240; for MD pigs: n=1755. *p<0.05 compared to sustained low; $^{\#}$p<0.05 compared to low (T_1)/high (T_2); $^{\$}$p<0.05 compared to high (T_1)/low (T_2) (statistics: linear mixed effects model).

Low and multidirectional WSS result in a high coronary plaque growth rate, both in plaque initiation and plaque progression

Overall, the ADs demonstrated a significant increase of the average WT over the three imaging time points (T_1-T_3) (p<0.001), which was less pronounced, but also significant in the MDs (p<0.001) (Figure 5.1C). There was no difference in absolute WSS values between the AD and MD pigs at T_1. At T_2, the OSI, RRT and CFI levels were slightly higher in the MD than in the AD pigs (Table 5.2). In general, the plaque growth rate was higher between T_2-T_3 than between T_1-T_2 for both AD and MD pigs (Figure 5.1D).

In the AD pigs, coronary sectors exposed to low TAWSS or high multidirectional WSS (OSI, RRT, CFI or transWSS) at T_1 exhibited a significantly higher initial plaque growth per month between T_1-T_2 than regions with higher (TAWSS) or lower (multidirectional metrics) WSS levels (p<0.05). The same significant relations were seen for the plaque progression rate (T_2-T_3), except for the transWSS (Figure 5.1D). In the MDs, low TAWSS and high RRT levels were also related to the fastest initial plaque growth (T_1-T_2) and plaque progression (T_2-T_3). High OSI levels promoted plaque progression, but not initiation in the MDs. For CFI and transWSS, no relation with plaque growth was observed in the MDs (Figure 5.1D).

Besides the effect of WSS values at a single time point, we also assessed what the relation was between sustained low or high WSS and the plaque growth rate during plaque initiation and progression. In plaque initiation, in the ADs, the plaque growth rate was highest in regions with initial (T_1) low TAWSS, that over time changed to high TAWSS (at T_2) (ΔWT T_1-T_2: 0.073±0.008 mm/month; n=94, 5%), also compared to regions with persistently low TAWSS (0.038±0.008 mm/month; n=361, 19%) (Figure 5.2). Besides, also regions with initial (T_1) high OSI, RRT or CFI and subsequently (T_2) low multidirectional WSS presented with the highest plaque growth rate. For the MD pigs, similar results were obtained, but only for the TAWSS and RRT. Subsequently, we assessed in these same regions what the plaque progression was between T_2-T_3. Both in the ADs and MDs, in regions with initial low and subsequently high TAWSS, the plaque growth rate between T_2-T_3 was lowest (Figure 5.2). The highest plaque progression rate was observed in regions with low TAWSS at T_2, independent of the T_1 TAWSS levels, but only in the ADs. For the multidirectional WSS metrics, no clear relations were observed

between sustained WSS and the plaque growth rate (T_2-T_3), except for low RRT levels at T_2 which appeared leading in very limited plaque growth.

The positive predictive values (PPV) of the T_1 WSS metrics for plaque presence (WT>0.5mm) at T_{last} in the AD pigs were 50% (low TAWSS), 48% (high OSI), 49% (high RRT), 47% (high CFI) and 43% (high transWSS). In the MD pigs, a predictive value analysis could not be applied since only 6 sectors (of the total of 1755 sectors) presented with a WT >0.5 mm at T_{last}.

The development of OCT lipid-rich plaques and NIRS-positive plaques was most often preceded by low and multidirectional WSS

Analysis of the NIRS signal at T_{last} (Figure 5.3A) showed that the MDs presented with only 6 NIRS-positive sectors from 3 different arteries, while the ADs demonstrated 33 NIRS-positive sectors derived from 6 arteries. The NIRS positive sectors of the ADs were most frequently preceded by low TAWSS ($p=0.10$), or high OSI ($p<0.05$), RRT ($p=0.08$) or CFI ($p<0.05$) at T_1 (Figure 5.3B). Only transWSS showed no relation at all with NIRS-positive plaque development in the ADs.

For the OCT analysis (Figure 5.3A), 2 pullbacks from T_{last} had to be excluded due to bad image quality or technical problems. From the remaining pullbacks at T_{last}, 668 sectors from 14 arteries of the ADs and 66 sectors from 10 arteries of the MDs showed plaque presence. In the ADs the plaque positive sectors were characterized as either a fibrous (n=196), lipid-rich (n=469) or OCT-detected FCA (lipid pool) (n=3) plaque (Figure 5.3C). Since the OCT-FCAs (with lipid-pool) were scarce, no statistical analysis and thus no WSS analysis could be performed on this plaque type. The development of a fibrous plaque showed no relation with T_1 WSS levels in both types of pigs (Figure 5.3D and Figure 5.4). In contrast, the development of OCT lipid-rich plaques was most frequently preceded by low and multidirectional WSS in the ADs ($p<0.05$) (Figure 5.3D). This relation was confirmed for OSI, CFI and transWSS in de MDs, despite the low number of lipid-rich plaques in this group (n=45) (Figure 5.4).

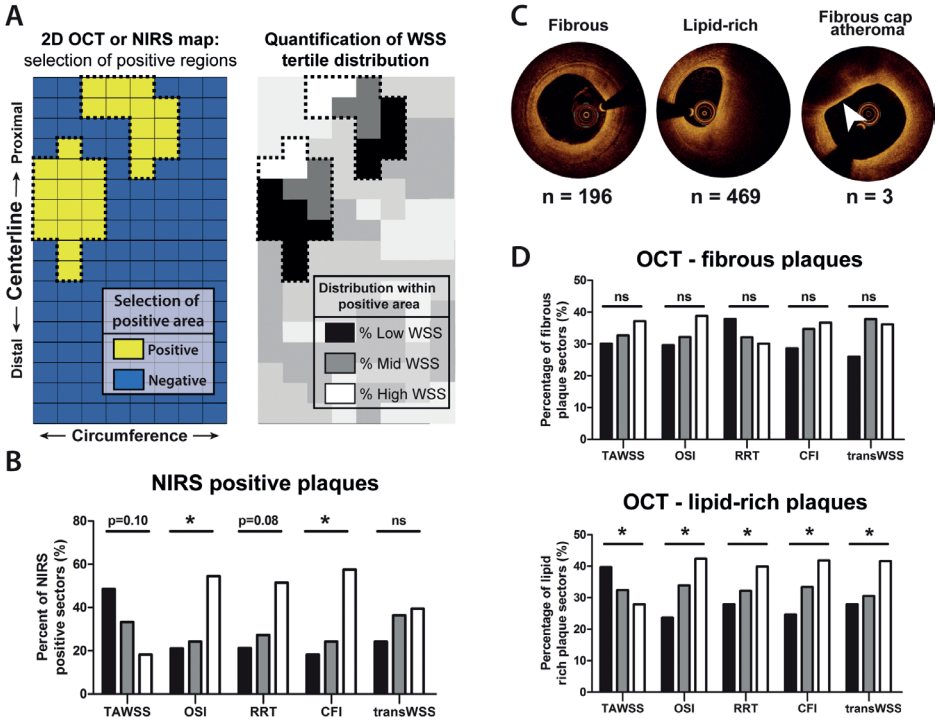

Figure 5.3: Association between T_1 wall shear stress (WSS) levels and final plaque composition detected by OCT and NIRS in advanced-diseased pigs (ADs) at T_{last}. A) OCT and NIRS analysis method: all positive 3mm/45° sectors were selected. Within these positive regions, the percentage of positive sectors that was preceded by one of the WSS tertiles was quantified. **B)** The percentage of NIRS-positive sectors (n=33) that was preceded by low (black bars), mid (grey bars) or high (white bars) levels of the respective T_1 WSS tertiles (time-averaged WSS (TAWSS); oscillatory shear index (OSI); relative-residence time (RRT); cross-flow index (CFI); transverse WSS (transWSS)). *p<0.05 for the overall relations (statistics: chi-square test). **C)** Example images of fibrous, lipid rich and FCA (arrowhead) plaques on OCT. n=number of sectors of ADs presenting with each respective plaque classification at T_{last}. **D)** The percentage of sectors presenting with fibrous or lipid rich plaque that was preceded by low (black bars), mid (grey bars) or high (white bars) levels of the respective WSS metrics. Fibrous plaques displayed no significant relation (p=ns). *p<0.05 for the overall relations (statistics: chi-square test).

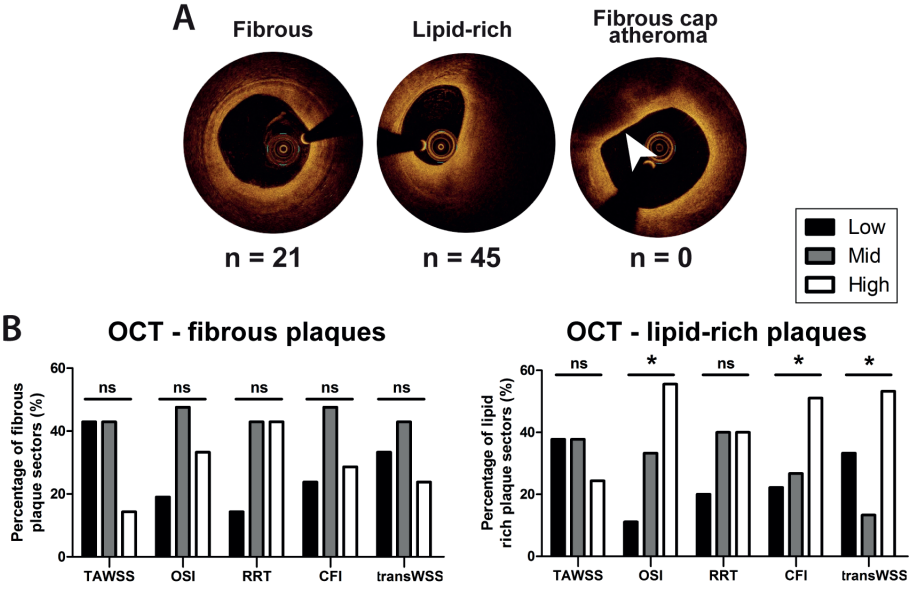

Figure 5.4: Association between T_1 wall shear stress (WSS) levels and OCT-detected plaque composition in mildly-diseased pigs (MDs) at T_{last}. A) Example images of fibrous, lipid rich and FCA (arrowhead) plaques on OCT. n=number of sectors of MDs presenting with each respective plaque classification at T_{last}. **B)** The percentage of sectors presenting with fibrous or lipid-rich plaque that was preceded by low (black bars), mid (grey bars) or high (white bars) levels of the respective WSS metrics. Fibrous plaques displayed no significant relation (p=ns). *p<0.05 for the overall relation (statistics: chi-square test). TAWSS=time-averaged WSS; OSI=oscillatory shear index; RRT=relative-residence time; CFI=cross-flow index; transWSS=transverse WSS.

Low and multidirectional WSS promoted the development of advanced histological plaque types

For a detailed analysis of the association between histological plaque classification, composition and T_1 WSS levels, 190 3mm-segments (15 arteries) from ADs and 145 3mm-segments (13 arteries) derived from MDs could be reliably matched with the invasive imaging data. In the MDs, of all WSS metrics, only TAWSS showed a significant association with histological plaque type, with relatively the most advanced plaques in regions with low TAWSS compared to regions with mid or high TAWSS (p=0.049) (Figure 5.5A and B). In the ADs, this TAWSS relation was more pronounced (p=0.003), and also regions with high OSI and high RRT displayed a more advanced plaque phenotype than regions with lower OSI or RRT levels (p<0.05). For transWSS and CFI, no relation with plaque type was observed (Figure 5.6A and B). The PPVs of the respective WSS metrics

for the presence of an FCA in the ADs were 61% (low TAWSS), 58% (high OSI), 61% (high RRT), 59% (high CFI) and 49% (high transWSS).

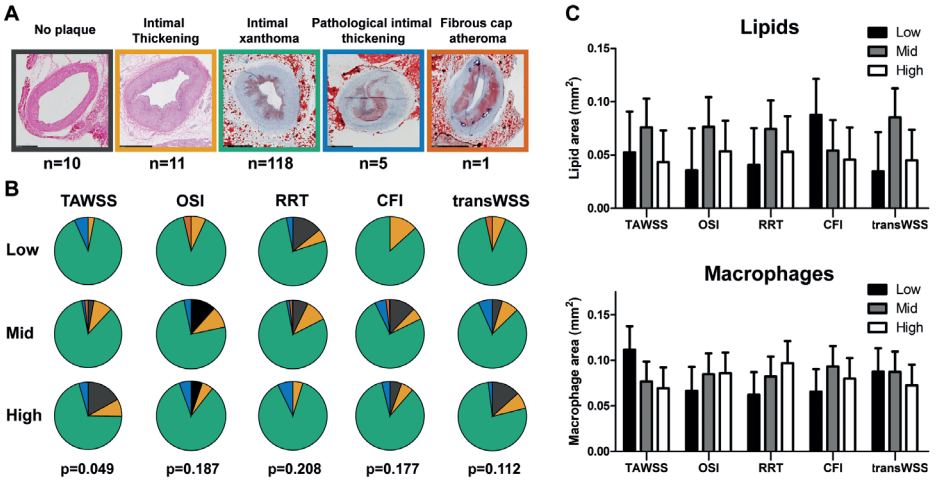

Figure 5.5: Histological plaque composition and the relation with WSS metrics in mildly-diseased pigs. A) Histological examples of plaques according to the revised AHA plaque classification. **B)** Distribution of the plaque types over regions with preceding low, mid or high levels of TAWSS, OSI, RRT, CFI or transWSS. P-value indicated the overall significance (statistics: chi-square test). **C)** The absolute lipid or macrophage area observed in regions with either preceding low (black bars), mid (grey bars) or high (white bars) levels of the respective WSS metrics. No significant relationships were observed (statistics: linear mixed effects model). TAWSS=time-averaged WSS; OSI=oscillatory shear index; RRT=relative-residence time; CFI=cross-flow index; transWSS=transverse WSS.

A more detailed analysis of the plaque composition in the ADs supported these results. We observed that in regions with low (TAWSS) and multidirectional WSS (RRT and CFI), plaques presented with the largest lipid and macrophage area ($p<0.05$) (Figure 5.7A and B). High OSI levels showed a positive trend for increased lipid content. For the necrotic core area, low TAWSS and high RRT levels resulted in twice as large necrotic cores compared to regions with higher TAWSS or lower RRT (Figure 5.7C). TransWSS showed no relation with plaque composition (p=NS). For the MDs, no significant relation was observed between any of the WSS metrics and plaque composition (Figure 5.5C).

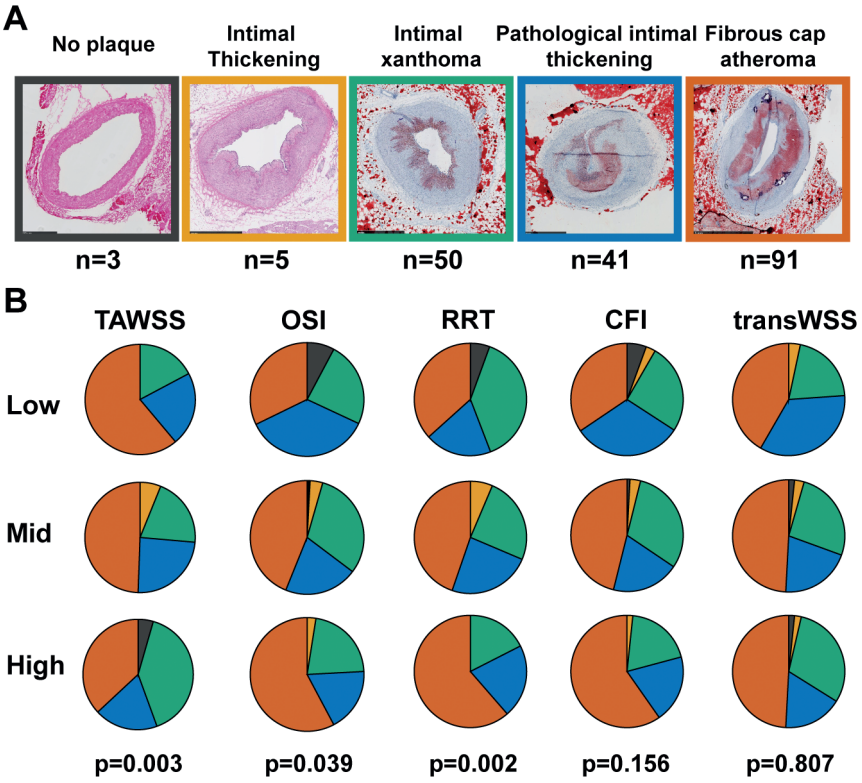

Figure 5.6: Relation between histological plaque classification and T_1 (multidirectional) WSS levels in the advanced-diseased pigs (ADs). A) Histological examples of plaques according to the revised AHA plaque classification. **B)** Distribution of the plaque types over regions with preceding low, mid or high levels of the respective WSS metrics (time-averaged WSS (TAWSS); oscillatory shear index (OSI); relative-residence time (RRT); cross-flow index (CFI); transverse WSS (transWSS)). P-value is for the overall relations (statistics: chi-square test).

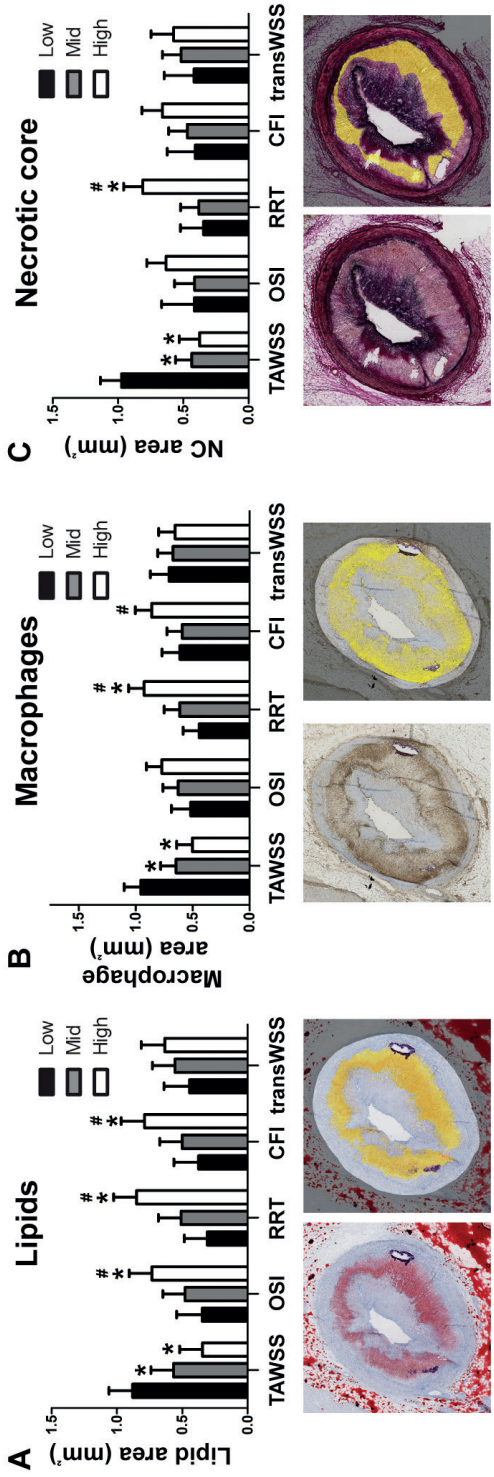

Figure 5.7: The effect of T_1 (multidirectional) wall shear stress (WSS) levels on final histological plaque composition in advanced-diseased pigs (ADs). A-C) The absolute lipid (Oil-red-O staining, red=lipid) (**A**), macrophage (CD68 staining, brown=macrophages) (**B**) or necrotic core (Miller staining, purple=collagen) (**C**) area (example positive staining indicated in yellow) preceded by low, mid or high levels of one of the five WSS metrics (mean±SD) (time-averaged WSS (TAWSS); oscillatory shear index (OSI); relative-residence time (RRT); cross-flow index (CFI); transverse WSS (transWSS)). *p<0.05 vs. low tertile of the respective WSS metric; #p<0.05 vs. mid tertile (statistics: linear mixed effects model).

DISCUSSION

In the present study, we used a serial, multimodality imaging protocol in conjunction with histological analyses to assess the influence of (multidirectional) WSS on the natural initiation and progression of coronary atherosclerotic plaques in adult familial hypercholesterolemia pigs. This study design enabled for the first time a comprehensive comparison of five (multidirectional) wall shear stress metrics. The results of the study demonstrated that: 1) plaque initiation and plaque progression are associated with low TAWSS and high levels of multidirectional WSS, both in mildly-diseased and advanced-diseased pigs, with the most pronounced relations in the latter group; 2) the greatest plaque growth rate was observed in regions with initial low TAWSS, turning into high TAWSS at T_2, while for multidirectional WSS, no clear differences in plaque growth rate were observed between regions with either sustained or changing WSS levels; 3) plaques with a vulnerable composition, as observed in the AD pigs, most often developed in regions with low TAWSS and high levels of OSI, RRT and CFI, while transWSS was not related to plaque composition; 4) all multidirectional WSS metrics, except transWSS, have a good positive predictive value for development of plaque, and an even better predictive value for the development of fibrous cap atheroma.

Relation of low and multidirectional WSS with plaque initiation, progression and composition

In order to discuss our results on the relationship between WSS and plaque initiation and progression, it is vital to recognize the different roles of WSS in the various stages of atherosclerosis[46]. In clinical studies, the presence of larger stenosis degrees leads to local elevation of the WSS. In these advanced disease stages, WSS serves as a marker for the localization of the largest and most vulnerable plaques, as very recently confirmed in a study of Kumar et al.[72], or can function as a predictor for plaque destabilization[74]. Pre-clinical studies, or clinical studies that exclude narrowed arterial regions, are the only way to assess the causal role of WSS in plaque initiation and progression. In this discussion, considering our study design, we focused on the role of (multidirectional) WSS in early disease development.

Since absolute WSS levels are highly dependent on the used methodology, a reliable comparison of the relation between different multidirectional WSS metrics and plaque development is only possible within one study. With our current study, we are the first to assess and compare the effect of five different (multidirectional) WSS metrics on plaque initiation and progression. We confirmed the findings from previous studies[48,93,292] which showed that low TAWSS and high levels of OSI and RRT result in the highest initial plaque growth. We also observed that the same relation holds true

for plaque progression. Both CFI and transWSS showed similar, but less pronounced relations with plaque initiation and progression.

As already described in a study by Koskinas et al.[56], WSS levels change over time. We observed that around 48% of the studied segments exhibited changes in local WSS levels. With regard to plaque initiation, the largest plaque growth was found in sectors with T_1 low TAWSS that changed to higher TAWSS at T_2. This local elevation of TAWSS at T_2 can very well be caused by lumen intrusion of large plaques, which was similarly observed in human advanced disease by Kumar et al.[72]. Interestingly, in these same regions with high TAWSS at T_2, the plaque growth rate during plaque progression between T_2-T_3 was lowest of all analysed sectors. This could indicate that the growth rate of these large plaques tends to decrease when the TAWSS rises. Despite the relatively short time period between T_2-T_3, the significantly highest plaque growth rate from T_2-T_3 was observed in regions with low TAWSS at T_2, independent from the TAWSS levels at T_1. Apparently, when low WSS is present, it triggers plaque growth, confirming the findings by Koskinas et al.[56], until the plaque starts to intrude into the lumen and TAWSS levels elevate. For the multidirectional WSS parameters OSI, RRT and CFI, regions with initial (T_1) high and subsequently (T_2) low levels presented with the highest plaque growth rate. Although never studied before, this could mean that the multidirectionality of WSS reduces upon plaque lumen intrusion. This reduced multidirectionality then results in reduced plaque growth as observed in our plaque progression (T_2-T_3) analysis.

Not only plaque size, but also plaque composition is important for risk-assessment of coronary events[314]. In two human studies with advanced disease, a correlation has been shown between (the development of) a positive NIRS signal (i.e. lipid-rich plaques) and high TAWSS[73,315]. Such a relation has never been described for earlier disease stages. In this study, we demonstrated a trend between NIRS-positive plaques and preceding low TAWSS. Multidirectional WSS metrics showed an even stronger effect, with NIRS-positive plaque development significantly more often preceded by high OSI and CFI levels compared to low multidirectional WSS. However, since the number and size of NIRS-positive regions was limited, our results on the correlation between WSS and NIRS should be interpreted with care.

The observed relation between (multidirectional) WSS and lipid-rich plaques derived from NIRS imaging was confirmed by OCT. Important to notice is that the number of OCT-detected FCAs was much lower compared to our histological findings. Reassessment of the accompanying histological data revealed that many lipid-rich necrotic cores are apparently invisible on OCT, hypothetically because they are ‘shielded’ by a layer of lipids in the cap structure.

Previous pre-clinical studies applied histology to determine the relation between plaque composition and WSS. These studies demonstrated that the development of advanced plaques with lipid and inflammatory cell infiltration was associated with low TAWSS[75,93,292,316]. Furthermore, Pedrigi et al.[75], who used a perivascular cuff to induce atherosclerosis formation, concluded that, besides low WSS, also a variant metric of the transWSS was associated with advanced plaques. In our study, we demonstrated with histology that advanced plaques with a higher lipid and inflammatory cell content and larger necrotic cores developed in regions with low WSS, confirming the results from the previous studies[75,93,292,316]. In contrast to the findings by Pedrigi et al.[75], transWSS was not related to plaque composition. This difference might be related to the use of the perivascular cuff in the study of Pedrigi. The narrowing of the vessel induced by this cuff can result in multidirectional flow patterns that are normally not observed in early disease stages. However, we did show that the other multidirectional metrics OSI, RRT and CFI, were strongly associated with the development of plaques with an advanced and complex composition.

Many of the above-mentioned findings were most pronounced in our advanced-diseased pigs, while in our mildly-diseased pigs, mainly the TAWSS and the RRT were associated with plaque development. The observed differences between MD and AD pigs will be discussed below.

Advanced and mildly-diseased pigs: difference in plaque growth and response to WSS metrics

We observed clear differences in plaque size and growth, but also in the response to WSS between MD and AD animals, despite similar WSS levels and conventional risk factors. The difference in response to WSS between the ADs and MDs indicates that, as commonly accepted, besides WSS, more factors are (synergistically) involved in determining the sensitivity for plaque development. As discovered in a previous study by our group (Chapter 4), a pronounced difference in low-density lipoprotein profile between the ADs and MDs makes the AD pigs much more prone to develop (coronary) atherosclerosis. Recent publications confirm these findings and show that, also in patients, differences in specific lipoprotein profiles can result in inter-individual differences in cardiovascular outcome[287,317]. Since WSS is mainly a factor that triggers the local influx of inflammatory cells and lipids into the vessel wall in an already high-risk systemic environment, differences in systemic risk-factors like the low-density lipoprotein profile might explain why WSS in the MDs is not as strongly associated with plaque growth as in the ADs.

Unfortunately, comparison of these results with other pre-clinical WSS literature is difficult, since animals that present with limited plaque growth are regarded as 'non-responders' and are often not taken into account for analysis. To make an honest assessment of the role of WSS in plaque development, thereby also better mimicking the large variability in disease development observed in human populations, we retained the MD pigs in the analysis.

The predictive value of multidirectional WSS metrics

To enable future application of WSS measurements in the clinic, establishing its positive predictive value for plaque progression is important. The PREDICTION study[69] reported a positive predictive value of low TAWSS of 25% in comparison to 50% in our study. The higher positive predictive value in our study could, at least in part, be explained by the fact that, in contrast to all PREDICTION patients, our animals did not receive statin treatment which is known to induce plaque regression. In stable ACS patients, Rikhtegar et al.[49] reported that multidirectional WSS parameters might be a better predictor for plaque localization at one time point than low TAWSS (low TAWSS: 31%; high OSI: 35%; high RRT: 49%). In our study, where the effect of WSS metrics on plaque development *over time* was assessed, we show that low TAWSS and high RRT are the best predictors, partially contrasting the results of Rikhtegar et al.. Finally, while most studies have evaluated the PPV of WSS for plaque size, we are the first to assess the predictive value of WSS for plaque composition. Interestingly, we observed that WSS might be an even better predictor for the development of FCA than for plaque *size* (PPV of 61% (TAWSS and RRT) versus 50% (TAWSS) and 49% (RRT)). Since this is the first study that enables one-to-one comparison of five different WSS metrics, we can now conclude that, with regard to the predictive value of the WSS metrics for plaque development, the TAWSS remains the strongest predictor. Although multidirectional WSS is significantly involved in the disease process, low TAWSS remains the strongest driving factor of both plaque initiation and progression.

LIMITATIONS

The present study has a number of limitations. First, the number of pigs used in this study was small, and the unexpected split into fast and slow responders further reduced the number of arteries that was available to investigate advanced plaque development. However, multiple sectors within one coronary artery were analysed to capture the local WSS effect. A linear mixed-effects model was applied to correct for remaining dependencies. Using this approach, a statistically significant effect of multidirectional

WSS on plaque development could be identified in both types of pigs. Furthermore, since the absolute levels of OSI, CFI and transWSS were low, the division of the WSS tertiles could be considered as somewhat artificial. Still, we did find significant relations between the relative levels of these metrics and both plaque size and composition.

CONCLUSION

In the present study we combined detailed invasive imaging and histopathology to demonstrate that the highest plaque growth rate was exclusively found at low TAWSS or high multidirectional WSS at both T_1 (for plaque initiation) and T_2 (for plaque progression). Regions with initial low TAWSS which, over time, turned into regions with high TAWSS, demonstrated the overall largest plaque growth. For multidirectional WSS, the largest plaque growth was found in regions with initial high levels of OSI, RRT and CFI that changed into regions with low levels of these parameters. These elevated TAWSS levels and reduced multidirectional WSS levels at T_2 are probably due to the development of lumen-intruding plaques. The development of plaques with an advanced plaque *composition* was also related to low TAWSS and high OSI, RRT or CFI, but not to transWSS. While the predictive values of the individual multidirectional WSS metrics for plaque growth were high, advanced plaque *composition* was even more reliably predicted by (multidirectional) WSS metrics with the TAWSS and RRT being the strongest predictors. The differences between the AD and MD pigs stress the importance of a synergistic effect of systemic risk factors and local shear stress levels. The overall results highlight that, although multidirectional WSS is significantly involved in coronary plaque initiation and progression, low TAWSS remains the best predictive clinical marker for vulnerable disease development.

ACKNOWLEDGEMENTS

We gratefully acknowledge Ilona Krabbendam - Peters, Karen Witberg, Maaike Visser - te Lintel Hekkert, Kim van Gaalen, Jurgen Ligthart and Marcel Dijkshoorn for their expert technical assistance in the animal experiments and data acquisition. Furthermore, we thank Maria Siebes for the lending of the ComboMap device and the accompanying user-advice.

CHAPTER 6

The synergistic effect of NIRS-detected lipid-rich plaque and shear stress on human coronary plaque growth

Annette M. Kok
Eline M.J. Hartman
Ayla Hoogendoorn
Claudio Chiastra
Evelyn Regar
Felix Zijlstra
Frank J.H. Gijsen
Antonius F.W. van der Steen
Joost Daemen
Jolanda J. Wentzel,

Based on:

'The synergistic effect of NIRS-detected lipid-rich plaque and shear stress on human coronary plaque growth',
manuscript in preparation

ABSTRACT

Background

While local wall shear stress (WSS) metrics, local lipid levels (as detected by near-infrared spectroscopy (NIRS)) and systemic lipid levels, have individually been associated with atherosclerotic plaque progression, a possible synergistic effect of these factors remains to be elucidated.

Methods

15 non-culprit arteries from acute coronary syndrome patients were imaged at baseline with coronary computed tomography angiography and NIRS-intravascular ultrasound (NIRS-IVUS), and doppler flow measurements were performed. The NIRS-IVUS imaging was repeated after one year follow up. The arteries were divided into 2291 1.5mm/45° sectors. In each sector, wall thickness at baseline and follow-up was determined, and the following WSS metrics were computed using computational fluid dynamics: time-average wall shear stress (TAWSS), oscillatory shear index, relative residence time (RRT), cross-flow index, and transverse wall shear stress (transWSS). To assess the synergistic effect of circulating lipid levels and shear stress, patients were classified as having 'low' or 'higher' LDL-cholesterol levels based on a median split. Furthermore, each arterial sector was classified for the presence of lipid-rich plaques as NIRS-positive or NIRS-negative.

Results

Plaque progression over a one-year follow-up was not statistically different in patients with low versus high LDL-cholesterol levels (p=0.58), or in sectors that were positive versus negative for NIRS-detected lipid-rich plaque presence (p=0.56). A trend in synergism was observed between high systemic LDL-cholesterol levels and WSS: patients with high LDL-cholesterol levels showed more plaque growth in low TAWSS (p=0.18) and high RRT (p=0.17) compared to patients with low LDL-cholesterol levels. With regard to local lipid levels, sectors presenting with baseline NIRS-detected lipid-rich plaque showed more plaque progression when colocalized with high RRT (p=0.01) or low transWSS (p=0.04), and more plaque regression in sectors additionally exposed to high TAWSS (p=0.03) or high transWSS (p=0.02) compared to NIRS-negative sectors.

Conclusion

This study showed that intravascular lipid-rich plaques (NIRS) and local shear stresses act synergistically in plaque progression or regression in human coronary arteries. This finding suggests that combining local WSS information with knowledge on local plaque composition could improve patient risk assessment.

INTRODUCTION

It is well known that wall shear stress, the frictional force of the blood at the vessel wall, plays an important role in coronary atherosclerotic plaque progression[57]. Endothelial cells are very sensitive to shear stress and at regions of low wall shear stress they express pro-inflammatory genes, whereby creating a pro-atherogenic environment[57,69,318]. Upon plaque growth, lumen narrowing results in increased levels of shear stress and these high shear stress levels have been associated with plaque destabilization and future events[72,319].

Besides wall shear stress, also systemic cholesterol levels have been independently associated with plaque progression[320]. A possible synergistic effect of systemic cholesterol levels and local wall shear stress on early plaque development has been investigated before in a pig study. The results from this study showed that high systemic total cholesterol levels amplified the effect of low shear stress on plaque growth and on plaque destabilization[67]. Not only systemic cholesterol levels, also local plaque lipid-content directly influences plaque growth via activation of endothelial cells and subsequent enhancement of inflammation[11]. Recently, a new intravascular imaging catheter was introduced which allowed simultaneous assessment of the plaque size using intravascular ultrasound (IVUS), as well as of the presence of local lipids with near-infrared spectroscopy (NIRS). Data obtained with this catheter in earlier studies already showed promising results that could potentially contribute to patient risk assessment in clinical practice[40,321–323]. Coronary artery disease patients with a high NIRS-detected lipid core burden index, demonstrated an increased risk of major adverse cardiovascular events[40]. A possible relation between wall shear stress and NIRS-detected lipid-rich plaques was first investigated in a small clinical study with coronary artery disease patients. In this study, they observed that shear stress levels preceding NIRS-detected lipid-rich plaques were different from shear stress levels preceding plaques with a negative NIRS-signal[315]. Whether this relation also effects plaque size has so far not been investigated.

Considering these observations, we hypothesized that in patients with advanced coronary atherosclerosis, combined detection of low wall shear stress regions in arteries with high systemic cholesterol levels, or detection of low shear stress regions colocalized with local lipid-rich plaques, could improve the prediction of plaque progression.

METHODS

Subjects

Hemodynamically stable ACS patients admitted for percutaneous coronary intervention (PCI) were selected for the IMPACT study (imaging and modelling to investigate the mutual relation of plaque growth and biomechanical parameters in human coronary arteries study). The main exclusion criteria included: history of coronary bypass graft, three vessel disease, and renal insufficiency (creatinine clearing <50 ml/min). In the end, 14 patients were enrolled who were treated with a PCI of the culprit vessel(s) according to local treatment standards. Subsequently, at least one, non-treated, coronary segment was imaged according to the IMPACT image acquisition protocol. Written informed consent was obtained from all patients. The study protocol was approved by the local medical ethical committee of the Erasmus MC (MEC 2015-535, NL54519.078.15) and the study was conducted in accordance with the World Medical Association Declaration of Helsinki (64th WMA General Assembly, Fortaleza, Brazil, October 2013) and Medical Research Involving Human Subjects Act (WMO).

Image acquisition protocol

Before the start of the procedure, blood was collected in EDTA and clotting tubes and was send to the Clinical Chemistry lab for analysis of the systemic LDL-cholesterol levels. A non-culprit coronary segment was imaged using angiography and NIRS-IVUS (TVC, InfraReDx (Burlington, Massachusetts, USA)) at index procedure and after one year of follow-up. The target coronary segment contained at least two side branches and was at least 30 mm in length. The side branches were used as matching points for registration of the various imaging modalities. At multiple locations in the imaged region, Doppler-derived blood velocity measurements were performed with a ComboWire (Volcano, Corporation, Rancho Cardova, USA). The location of the ComboWire was documented using angiography. One month after the index procedure, a coronary computed tomography angiography (CCTA) scan was made using the SOMATOM Force (192 slice, 3rd generation, dual-source CT scanner (SOMATOM Force, Siemens AG, Germany)).

IVUS gating and segmentation

IVUS images were ECG-gated by selecting one frame per cardiac cycle in the same diastolic phase (6 frames before the R-peak) using an offline in-house developed algorithm (MATLAB, v. 2015a, Mathworks Inc., Natick, MA, USA). We performed this gating procedure to compensate for changes in lumen diameter caused by cardiac contraction and non-linear catheter movement whereby improving the detection of plaque-induced variations in local lumen area. The IVUS-gating algorithm was validated

using 42 IVUS pull-backs from a pre-clinical study in which the heart rate was ECG-documented during the IVUS pullback. Comparison of the heart rate derived from the IVUS gating algorithm with the ECG heart rate showed a median error in heart rate of <0.5% (0.38% (IQR 0.22–0.70%).

The gated NIRS-IVUS images were segmented by an experienced reader (EH) using QCU-CMS software (Leiden, The Netherlands). In each NIRS-IVUS image, lumen and external elastic membrane (EEM) contours were segmented (Figure 6.1, segmentation). Wall thickness (a measure for plaque presence) was defined as the distance between the EEM and the lumen boundary from the centre point. To assess change in wall thickness, IVUS images from baseline were longitudinally and circumferentially matched with those from follow-up based on the location of side branched. Plaque progression was present if the wall thickness increased more than 0.1 mm.

Sectors in the IVUS pullback with calcifications were excluded from the analysis since the shadow caused by the calcification hampers detection of the EEM and thus the determination of the wall thickness.

CCTA segmentation

Semi-automatic CCTA segmentation of both the artery of interest and all visible side branches was performed by an experienced investigator using graph cuts and robust kernel regression as previously described[310]. From these segmentations, the 3D-centreline of both the main branch and side branches was determined (Figure 6.1, segmentation).

Shear stress analysis

3D reconstruction

A 3D reconstruction of the coronary artery was obtained by fusing information from CCTA and baseline IVUS using in-house developed software (Mevislab (Bremen, Germany)). First, the baseline IVUS images were matched with the CCTA images both in longitudinal and circumferential direction using the location of specific landmarks (side branches or a stent) (Figure 6.1, matching). Subsequently, the IVUS-lumen contours were stacked on the 3D CCTA centreline as previously described[60]. The 3D-matched region based on the IVUS contours will hereafter be referred to as ‘region of interest’ (ROI).

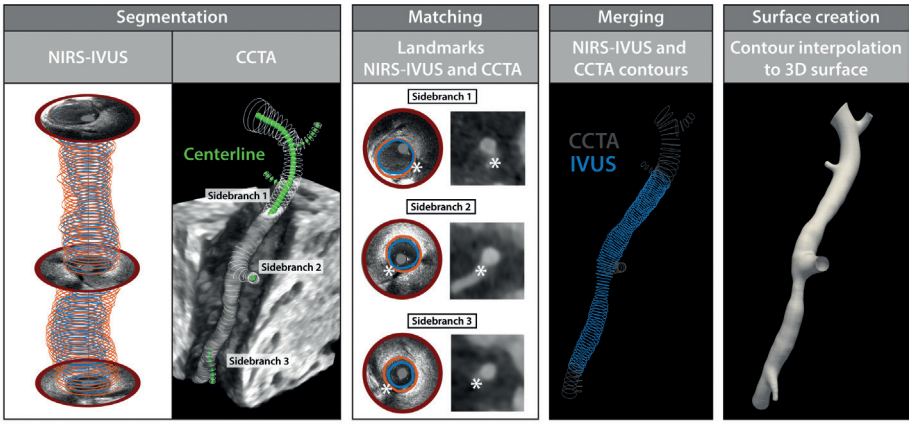

Figure 6.1: An overview of the methodology of image processing, matching and 3D reconstruction. *Segmentation*: in all frames from the gated near-infrared spectroscopy intravascular ultrasound (NIRS-IVUS) images, the lumen (blue) and external elastic membrane (orange) were segmented semi-automatically. Semi-automatic segmentation of the arterial lumen (white contours) was also performed on coronary computed tomography (CCTA) data by which the centrelines of the artery and its side branches were determined (green). ***Matching***: Landmarks (e.g. side branches (white stars)) on the IVUS and CCTA images were used to match the data from both modalities. Subsequently, the IVUS contours could be placed on the CCTA-derived centreline. ***Merging***: the region of interest (ROI)-IVUS contours (blue) were fused with the CCTA contours of the proximal and distal artery outside the ROI and of the side branches (grey). ***Surface creation***: the contours from IVUS and CCTA were interpolated and transformed into a 3D surface.

Next, the segmented lumen volume of the CCTA was corrected to match the segmented lumen volume of the IVUS ROI to compensate for volume differences caused by CT contrast blooming or under-filling[324,325]. Subsequently, the IVUS ROI was merged with the corrected CCTA contours of the side branches and of the proximal and distal parts outside of the ROI (Figure 6.1, merging). All contours were 3D-interpolated, smoothed and transformed to a 3D surface (Figure 6.1, surface creation).

Boundary conditions

Two types of boundary conditions were applied for the 3D computational fluid dynamics (CFD) simulation: 1) flow distribution through the side branches and 2) a time-dependent velocity profile at the inlet. The flow distribution through the side branches was derived from baseline intravascular velocity measurements using an intravascular Doppler wire. An experienced consensus committee (AM, EH, AH, FG, JW) assessed the quality of all velocity measurements by assessing signal intensity, pattern consistency, and similarity in wave-shape in comparison with existing literature[326,327]. Only reliable measurements

were used. As the device measures the local maximum velocity, the velocity values were first converted to the mean velocity by following a previously proposed method[328]. Subsequently, time-averaged flow was calculated by multiplying the local area with the time-averaged mean velocity. The local cross-sectional area was obtained from the 3D vessel reconstruction at the location of the measurement. For regions where no (reliable) velocity measurement was available, a scaling law, as validated by van der Giessen et al.[329], was used to calculate the flow-rate distribution through two daughter branches.

As inlet boundary condition, a time-dependent velocity waveform was applied of which the shape was derived from the most proximal good velocity measurement. In one of the assessed coronary arteries, no reliable velocity measurement was available to determine the time-dependent velocity wave form. In this case a general human velocity waveform was used[326] which was scaled based on the vessel diameter according to a method described in literature by Cutnell et al.[329] to obtain the mean estimated flow-rate.

The vessel lumen was considered as rigid and subjected to no-slip boundary condition. Blood was assumed to behave as shear-thinning fluid and was modelled with the Carreau model[330].

Meshing and Computational Fluid Dynamics solution procedure

Each 3D generated geometry was converted to a tetrahedral mesh in ICEM CFD (v.17.1, ANSYS Inc., Canonsburg, PA, USA) with a 5-prism layer at the boundary to resolve shear stress effects[331]. The mesh size was determined by a mesh independence study (only errors within 1% of shear stress were allowed). A typical mesh consisted of six million elements. Unsteady CFD simulations were performed using Fluent (v.17.1, ANSYS Inc.). All settings regarding the time steps and convergence criteria were determined by a sensitivity analysis (only errors within 1% of wall shear stress were allowed). The solution procedure was carried out following previously described methods[313].

Postprocessing

All parameters of interest (wall thickness at baseline, wall thickness at follow-up and baseline NIRS) were projected onto the 3D geometry at baseline using VMTK (Orobix, Bergamo, Italy) and MATLAB (v. 2015a, Mathworks Inc., Natick, MA, USA) to enable a one-to-one comparison.

To minimize the influence of possible registration mismatch on the final results, the data were averaged over 1.5 mm in the axial direction and over 45° in the circumferential

direction. 1.5 mm was chosen since the registration of baseline and follow up images was estimated to be performed with an accuracy of approximately one image frame (+0.5 mm and -0.5 mm), leading to at least 75% overlap in the worst-case scenario. We chose to average the data within the cross-sections over 45° to capture the heterogeneity in shear stress due to curvature and tortuosity while still ensuring the highest possible overlap between baseline and follow-up registration[77].

Shear stress values were averaged over the cardiac cycle to obtain the time-averaged wall shear stress (TAWSS). The other multidirectional wall shear stress metrics (OSI, RRT, CFI and transWSS (Table 6.1)) were obtained as previously described[313]. Per vessel and per shear stress metric, all analysed 1.5mm/45° sectors were divided in tertiles ('low', 'intermediate' and 'high'). The resulting cut-off values per vessel are described in Table 6.2.

Analysis of local and systemic lipid levels

Using the information derived from plasma, imaging data and shear stress calculations, the synergistic effect of systemic LDL-cholesterol and local plaque lipids (NIRS) with shear stress on plaque growth was investigated.

For the NIRS analysis, each analysed 1.5mm/45° region was classified as NIRS positive (>50% of the region presented with a high probability (>60%) for the presence of lipids) or otherwise as NIRS negative. Besides, to remove the effect of artefacts induced by the presence of the guide wire, all sectors covered (partially) by the guide wire were excluded.

Table 6.1: Overview of the (multidirectional) shear stress metrics

Shear stress metric	Description	References
Time-averaged wall shear stress (TAWSS)	Shear stress averaged over the cardiac cycle	46,47
Oscillatory shear index (OSI)	Ratio between back- and forward going shear stress	48
Relative residence time (RRT)	Relative time that a blood particle resides at a certain location at the vessel wall	49
Transverse wall shear stress (transWSS)	Shear stress vector along the wall, in perpendicular direction to the main flow direction	50
Cross-flow index (CFI)	The transWSS normalized for the wall shear stress	51

Table 6.2: Vessel specific thresholds, based on tertiles

	TAWSS (Pa)		OSI (x10^{-3}) (-)		RRT (Pa^{-1})		CFI (-)		transWSS (Pa)	
Vessel	**Low**	**High**	**Low**	**High**	**Low**	**High**	**Low**	**High**	**Low**	**High**
1	1.34	2.29	0.38	5.59	0.50	0.96	0.03	0.10	0.05	0.10
2	0.79	1.12	0.14	0.69	0.91	1.31	0.02	0.05	0.02	0.04
3	0.27	0.40	0.19	1.44	2.53	3.97	0.02	0.07	0.01	0.02
4	0.31	0.43	0.14	0.68	2.35	3.30	0.02	0.04	0.01	0.02
5	1.30	2.40	0.40	7.96	0.43	1.36	0.03	0.11	0.05	0.10
6	0.51	1.06	1.20	30.82	1.03	2.34	0.05	0.18	0.05	0.10
7	0.84	1.36	0.42	4.56	0.74	1.35	0.04	0.11	0.04	0.10
8	0.38	0.56	0.31	1.10	1.81	2.75	0.03	0.05	0.01	0.02
9	0.37	0.53	0.44	13.23	1.98	3.18	0.03	0.12	0.02	0.04
10	0.69	0.86	0.06	0.23	1.18	1.46	0.01	0.02	0.01	0.02
11	1.31	1.98	0.31	1.25	0.52	0.80	0.03	0.06	0.05	0.08
12	0.33	0.43	0.02	0.17	2.35	3.09	0.01	0.02	0.00	0.01
13	0.55	0.88	0.06	0.57	1.17	1.82	0.01	0.04	0.01	0.02
14	0.55	1.49	1.93	37.55	0.73	2.43	0.06	0.19	0.05	0.08
15	0.99	1.58	0.54	1.89	0.65	1.06	0.04	0.07	0.05	0.08

TAWSS: time-averaged wall shear stress; OSI: oscillatory shear index; RRT: relative-residence time; CFI: cross-flow index; transWSS: transverse wall shear stress

In order to investigate the influence of systemic levels of LDL-cholesterol on shear stress-related plaque growth, the patients were split based on the median LDL-cholesterol level at follow-up into a low (≤1.78 mmol/L) and high (>1.78 mmol/L) LDL-cholesterol group.

Statistical analysis

Normality of the data was tested with a Kolmogorov-Smirnov test. When the data were normally distributed, mean and standard deviation were presented. Otherwise, median and interquartile range were reported. A Wilcoxon-signed ranks test was performed to test the difference between baseline and follow up LDL-cholesterol levels. A linear mixed effect model was used to perform the statistical analysis of the shear stress metrics on plaque progression using the LME4 package in R (version 3.3.2, Vienna, Austria). In this model, clustering of the sectors per vessel was taken into account. The Bonferroni post-hoc test was used to account for multiple-group comparison. Furthermore, to test for synergistic effects between LDL-cholesterol levels and wall shear stress, and

between NIRS-detected local lipids and wall shear stress, the interaction effects were investigated with this model. P<0.05 was considered significant.

RESULTS

In total, 15 coronary arteries from 14 patients were analysed. Patient demographics and clinical characteristics are presented in Table 6.3.

The length of the ROIs in the coronary arteries was 49.5 mm (39.4 – 57.4 mm). In total, 11% (5.8% – 22%) of the data was excluded (due to calcium, artefacts, and guide wire), resulting in 2291 sectors included in the analysis (138 (101 – 190) sectors per artery). 482 sectors displayed plaque progression (delta wall thickness >0.1 mm) and 572 sectors showed stable plaque presence or regression (delta wall thickness ≤0.1 mm). The absolute TAWSS value for all the sectors was 0.80 Pa (0.44 – 1.41 Pa), for OSI $0.6{\cdot}10^{-3}$ ($0.1{\cdot}10^{-3}$ – $3.1{\cdot}10^{-3}$), for RRT 1.33 Pa^{-1} (0.76 – 2.41 Pa^{-1}), for CFI 0.04 (0.02 – 0.08), and for transWSS 0.03 Pa (0.01 – 0.07 Pa).

Table 6.3: Patient demographics and clinical characteristics of the study population at baseline

Number of patients	14
Age (years)	62 (56 - 68)
Male/female ratio (%)	13/1 (92,9%/7,1%)
Body mass index	26 (25 - 30)
LDL-cholesterol (mmol/L)	2.52 (2.23 - 3.01)
Risk factors	
Diabetes mellitus (n (%))	4 (28,6%)
Hypertension (n (%))	4 (28,6%)
Table 6.3: Continued	
Hypercholesterolemia (n (%))	9 (64,3%)
Current smoking (n (%))	4 (28,6%)
Previous smoker (n (%))	4 (28,6%)
Positive family history (n (%))	7 (50%)
Previous stable angina (n (%))	6 (42,9%)
Previous MI (n (%))	3 (21,4%)
Previous PCI (n (%))	4 (28,6%)
Previous statin use (n (%))	9 (64,3%)

Table 6.3: Continued

Indication for coronary angiography	
Unstable angina (n (%))	7 (50%)
NSTEMI (n (%))	6 (42,9%)
STEMI (n (%))	1 (7,1%)
Non-culprit coronary artery	
Left anterior descending (n (%))	6 (35,7%)
Left circumflex (n (%))	4 (28,6%)
Right coronary artery (n (%))	5 (35,7%)

Neither systemic, nor local lipid levels are directly associated with plaque progression

The LDL-cholesterol levels at baseline were 2.5 mmol/L (2.2 - 3.0 mmol/L) and significantly reduced to 1.8 mmol/L (1.5 - 2.6 mmol/L) (p=0.012) at one year follow up, probably due to initiated statin treatment in the statin-naïve patients. Dividing the patients in 'low' and 'higher' systemic LDL-cholesterol groups, we demonstrated that plaque progression did not differ between both groups (p=0.58) (Figure 6.2A).

With regard to the local lipid levels detected by NIRS, a positive NIRS signal was observed in 5.7% (n=130) of the sectors. No significant difference in plaque growth was detected in the NIRS positive sectors versus the NIRS negative sectors (p=0.56) (Figure 6.2B).

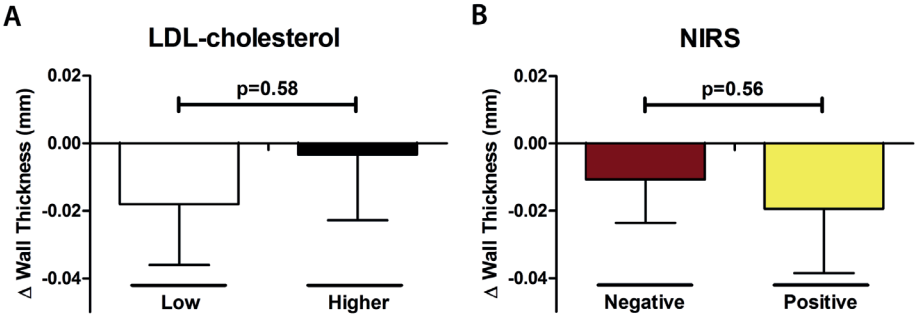

Figure 6.2: Change in coronary wall thickness (mm) after one year follow up in **A)** patients with low LDL-cholesterol levels (white bar) or higher LDL-cholesterol levels (black bar); **B)** NIRS-negative (red bar) and NIRS-positive (yellow bar) regions. Data are represented as mean (SEM).

(Multi)directional wall shear stress is associated with a change in plaque size

Association of the five shear stress metrics with plaque growth demonstrated that change in plaque size over time was associated with TAWSS, RRT, OSI and CFI, but not with transWSS (Figure 6.3). Plaque growth was inversely related to baseline TAWSS, with plaque regression at sectors exposed to high TAWSS (-0.04 ± 0.01 mm). An opposite trend was observed for baseline RRT, with plaque regression in sectors exposed to low RRT (-0.04 ± 0.01) and plaque progression in sectors exposed to high RRT (0.03 ± 0.01 mm). For the OSI and CFI, the decrease in plaque size in regions with low or intermediate OSI or CFI values was higher compared to regions with high OSI or CFI.

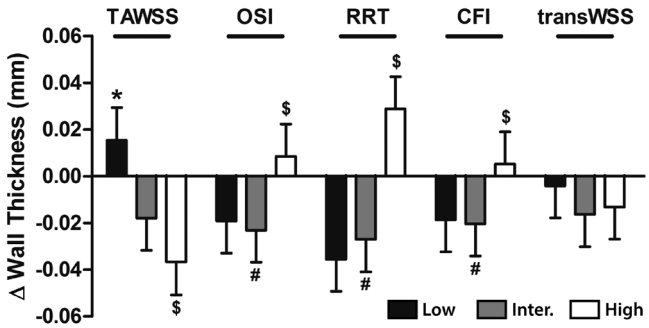

Figure 6.3: Change in wall thickness after one year follow-up for low, intermediate or high levels of the respective shear stress metrics. Time-average wall shear stress (TAWSS), Oscillatory shear index (OSI), Relative residence time (RRT), Cross-flow index (CFI), and Transverse wall shear stress (transWSS). Data represent estimated mean (SEM). p<0.05: *low versus intermediate, #intermediate versus high or $low versus high.

The highest positive predictive values (PPV) for plaque progression were observed for low TAWSS (43%) and high RRT (44%), confirming the relations described above. Interestingly, the PPVs of the other multidirectional shear stress metrics (OSI and CFI), which showed a weaker direct association, was only slightly lower than the PPVs of TAWSS and RRT (Table 6.4).

Systemic LDL-cholesterol levels have a limited influence on the relationship between shear stress and plaque progression

To assess a potential synergistic effect of shear stress and circulating LDL-cholesterol levels on change in plaque size, the relation between shear stress and plaque size change was analysed separately for sectors derived from patients with low versus patients with higher LDL-cholesterol levels. A step-wise relation between TAWSS and

RRT, but not for OSI, CFI and transWSS, and plaque change was observed in both LDL-cholesterol level groups (Figure 6.4). Only in sectors with low TAWSS or high RRT, higher LDL-cholesterol levels augmented the effect of shear stress on plaque change compared to low LDL levels, although this effect did not reach statistical significance (p=0.18 and p=0.17, respectively).

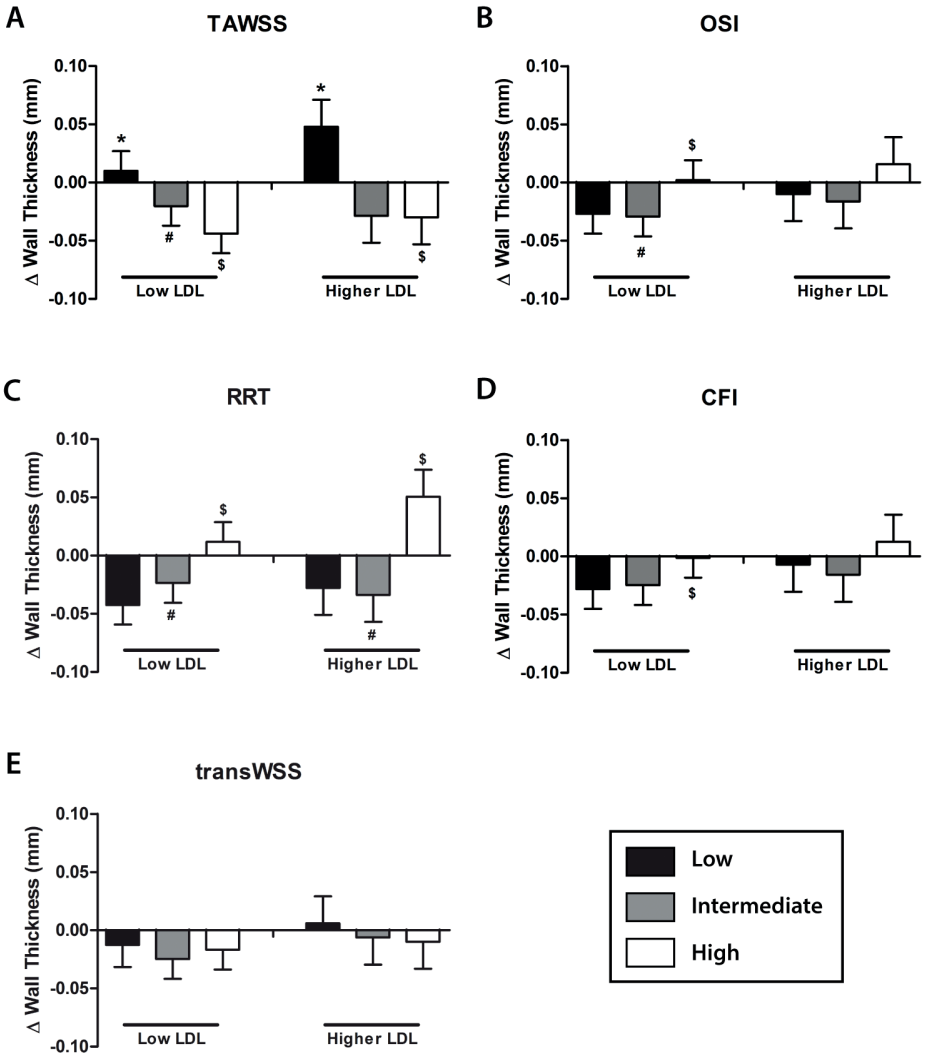

Figure 6.4: Effect of systemic lipid levels on the relation between baseline shear stress levels and change in wall thickness (mm). The data are divided in patients with low (left graphs) versus higher LDL-cholesterol (right graphs) levels. The relation between shear stress and plaque growth is depicted for low (black bars), intermediate (grey bars) and high (white bars) levels of: **A)** time-average wall shear stress (TAWSS), **B)** oscillatory shear index (OSI), **C)** relative residence time (RRT), and **D)** cross-flow index (CFI), **E)** transverse wall shear stress (transWSS). Error bars depict the standard error. $p<0.05$: *low versus intermediate, $^{\#}$intermediate versus high and $^{\$}$low versus high.

NIRS-detected lipid-rich plaques augment the effect of shear stress on plaque progression

In order to investigate the added value of NIRS-information on top of shear stress for the estimation of plaque progression, all sectors were split in NIRS-positive (yellow) and NIRS-negative (red) sectors. For both the NIRS-negative and the NIRS-positive sectors, a stepwise relation was observed between plaque growth and TAWSS, and RRT, similar to TAWSS and RRT alone. The presence of lipids inside the plaque (positive NIRS signal), amplified this stepwise pattern of change in plaque size. Compared to the NIRS-negative sectors, NIRS-positive sectors tended to show more plaque regression ($p = 0.10$) when colocalized with high TAWSS (Figure 6.5A). In comparison with NIRS-negative sectors, the opposite was true for RRT with a trend towards more plaque regression in sectors where low RRT was colocalized with a positive NIRS signals versus a negative NIRS signal ($p=0.06$) (Figure 6.5C). For the transWSS, only in the NIRS positive sectors, an inverse trend with plaque growth was observed ($p=0.06$ of low versus high transWSS). Furthermore, NIRS-positive sectors exposed to high transWSS showed significant plaque regression while high transWSS - NIRS-negative sectors demonstrated no change in plaque size (difference NIRS-positive – NIRS-negative: $p=0.02$) (Figure 6.5E). No effect was observed of NIRS-detected local lipids on the relation between plaque growth and OSI or CFI (Figure 6.5B and D). Although the effect of a positive NIRS-signal on the relationship between shear stress and plaque size change differed per shear stress metric, combining NIRS with shear stress to predict plaque progression slightly improved the predictive value of all shear stress metrics compared to the predictive value of the shear stress metrics alone (Table 6.4).

Table 6.4: Positive predictive value of the individual shear stress parameters for plaque progression (>0.1 mm)

	WSS metric	+ systemic lipids	+ local lipid (NIRS-positive)
Low TAWSS	43%	47%	48%
High OSI	42%	39%	47%
High RRT	44%	47%	49%
High CFI	42%	39%	47%
High transWSS	36%	32%	41%

TAWSS: time-averaged wall shear stress; OSI: oscillatory shear index; RRT: relative-residence time; CFI: cross-flow index; transWSS: transverse wall shear stress

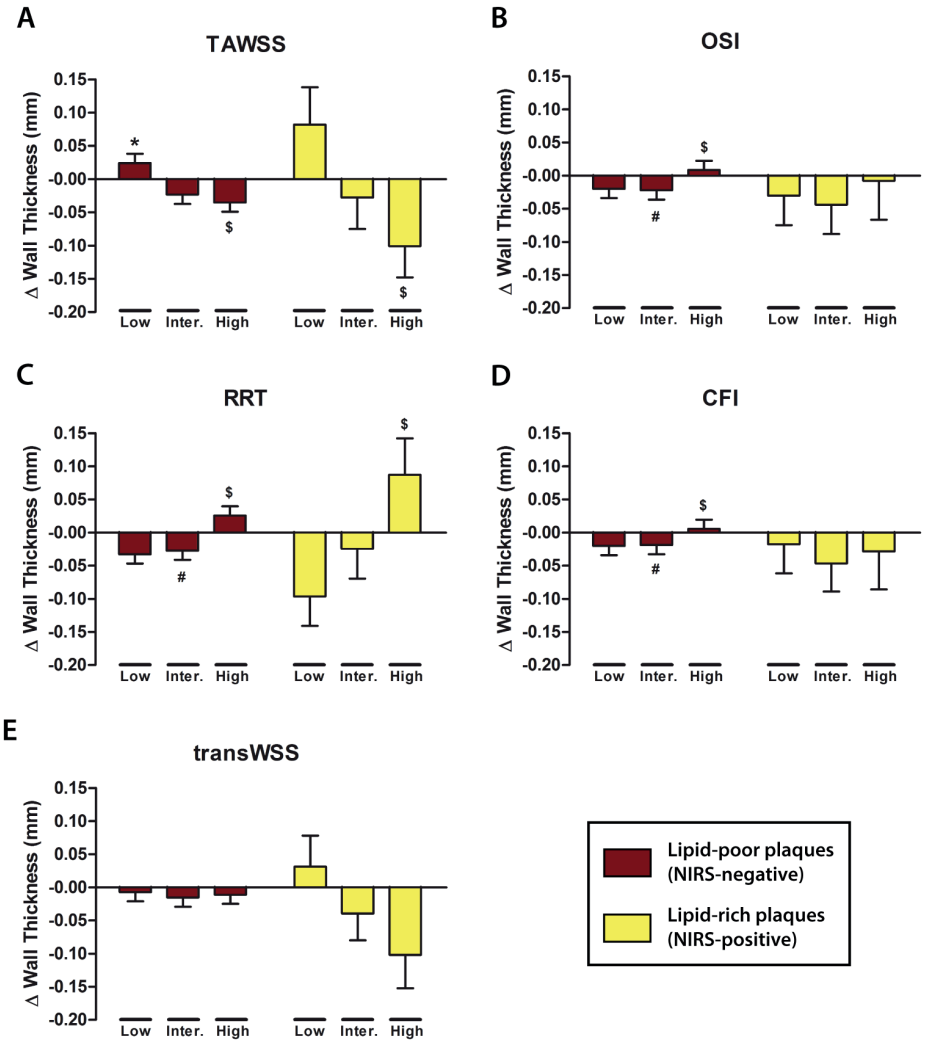

Figure 6.5: The effect of local (NIRS-detected) lipid levels on the relation between shear stress levels and change in wall thickness (mm) after one year follow-up. Data are divided in sectors with positive NIRS signal (yellow bars) or negative NIRS signal (red bars). The relation with plaque growth is depicted for low, intermediate or high levels of: **A)** time-average wall shear stress (TAWSS), **B)** oscillatory shear index (OSI), **C)** relative residence time (RRT), **D)** cross-flow index (CFI), and **E)** transverse wall shear stress (transWSS) co-localized with NIRS negative regions (red) or NIRS positive regions (yellow). Error bars depict the standard error. $p<0.05$: *low versus intermediate, #intermediate versus high and $low versus high.

DISCUSSION

In this natural history study, we investigated the influence of the presence of NIRS-detected lipid-rich plaques at baseline on shear stress related plaque progression in coronary arteries of ACS patients. Since the multi-directionality of shear stress is gaining attention for its involvement in plaque progression, we included four multidirectional wall shear stress parameters in the analysis. The main findings were that: 1) plaque progression over a one year follow up was not statistically different in patients with either low versus higher LDL-cholesterol levels, or in NIRS-positive versus NIRS-negative sectors at baseline, 2) in patients with higher LDL-cholesterol levels at follow-up, the effect of low TAWSS and high RRT on plaque progression was amplified compared to patients with lower LDL-cholesterol levels, 3) NIRS-positive sectors demonstrated more plaque regression in sectors colocalized with high TAWSS, low RRT (both a trend) and high transWSS.

Shear stress computation methodology

In this study, compared to many studies published before, an optimized methodology was used to assess the local shear stress[57,69]. First, we included side branches in the 3D reconstruction of the coronary arteries. Often, side branches are not included in shear stress calculations[69,332,333], which is remarkable since plaques are often formed near side branch regions and side branches affect absolute shear stress values[334]. Sakellarios et al.[335] already demonstrated that improvement of 3D models by incorporating side branches to assess the local shear stress distribution, contributes to a better prediction of shear stress-related plaque progression. Our data confirm this observation with a higher positive predictive value of TAWSS for plaque growth compared to a previous study[69]. Since most of the studies discard side branches, our general shear stress values might be lower than reported before. Despite the fact that the use of side branches in our study inherently leads to lower shear stress levels, interestingly, the absolute TAWSSs in this study were in quite close agreement with most previous reported values of TAWSS [332,336,337], except for the study reported by Samady et al.[57]. Regarding multidirectional wall shear stress, we found lower multidirectionality values for all four metrics compared to the studies described by Kok et al.[338] and Pinho et al.[337]. However, it is difficult to compare the outcomes of studies with our data, since different inflow boundary conditions were used. As a second optimization step, we used Doppler-derived velocity measurements at multiple locations throughout the artery to obtain patient-specific boundary conditions. Interestingly, in comparison with the porcine study described in this thesis (Chapter 5) where similar boundary conditions were used, the multidirectional wall shear stress values were in close agreement.

The relation between shear stress and plaque progression/regression

Using this optimized methodology for shear stress calculation, we observed a negative relation of the TAWSS, and a positive relation of OSI, RRT and CFI with change in wall thickness. We also assessed whether these (multidirectional) wall shear stress metrics could be used to predict plaque progression or plaque regression. In high TAWSS sectors, plaque regression occurred. These results are in line with those reported in previous studies[57]. However, similar as the data described by Kok et al.[338], OSI, CFI, and transWSS could not significantly distinguish plaque progression from regression, which was in our study also the case for low TAWSS. For the RRT, in contrast to the data presented by Kok et al.[338], a positive trend was observed, with significant plaque progression at sectors exposed to high RRT and regression in sectors with low RRT. This difference might again be explained by the use of different boundary conditions, but this latter observation is also in agreement with earlier reports on the positive relationship between high RRT and plaque progression[49].

Synergism between shear stress and systemic or local lipid levels

To assess a possible synergistic role with shear stress levels, we studied the influence of LDL-cholesterol levels on shear stress-related plaque growth. In an earlier publication with an atherosclerotic pig model, high cholesterol levels amplified the shear stress-related plaque progression[67]. This resulted in plaques with high-risk features, such as inflammation, lipid accumulation and plaque progression, especially in the regions exposed to low TAWSS. In our current study, more plaque progression was observed in low TAWSS sectors for patients with higher LDL-cholesterol levels compared to low TAWSS sectors in patients with lower LDL-cholesterol levels, but this difference did not reach statistical significance which is in contrast to the results presented by Koskinas et al.[67]. This could be explained by the fact that Koskinas et al.[67] studied pigs presenting with overall stronger plaque growth. Furthermore, while we assess LDL-cholesterol levels, in the pig-study, total cholesterol levels were used. It is known the LDL-cholesterol/total cholesterol balance is different between pigs and humans[339] and that the balance between LDL-cholesterol and total cholesterol determines the risk of plaque development[340]. Moreover, the patients described in this study were treated with standard statin-therapy which is known to result in overall plaque regression[341]. Maybe more importantly, this statin therapy resulted in overall low LDL-cholesterol levels which means that the absolute difference between the groups with ‘low’ and ‘higher’ LDL-cholesterol level was small.

While we only observed a trend for a synergistic effect of plasma LDL-cholesterol and wall shear stress, we demonstrated a significant synergistic effect of colocalization of NIRS-detected lipid-rich plaques and (multidirectional) shear stress on the change in

plaque size. The presence of NIRS-detected lipid-rich plaque significantly amplified the stepwise relation between RRT or TAWSS, and change in plaque size. For the transWSS, the relationship with change in plaque size was also significantly influenced by colocalization with lipid-rich plaques: plaque regression was amplified in high transWSS regions. This latter observation is however opposite to earlier findings from a preclinical study which showed that high transWSS induces plaque growth[75] instead of regression. In earlier studies on the relation between NIRS-detected lipid-rich plaques and shear stress, only the TAWSS was investigated. In a case report from our group, we described that NIRS-positive sectors were most often exposed to high TAWSS[73]. However, that specific study did not present information on plaque progression over time. Another study that investigated the relation between wall shear stress and plaque lipid content demonstrated higher preceding TAWSS levels in regions that subsequently presented with developing plaque-lipid over a 12-18 months period[315]. Unfortunately, the wall shear stresses in the latter study were assessed with Doppler measurement under the assumption of a parabolic velocity profile and thereby did not take into account local differences in wall shear stress caused by the local geometry. Taking all these results together, we could conclude that in regions with high TAWSS, an increase in NIRS-detected lipid content and a decrease in plaque size can be observed indicting a more unstable plaque phenotype. The effect of TAWSS on plaque size is amplified by the presence of lipid-rich plaques at baseline, as observed in our current study.

LIMITATIONS

Sectors in which visualization of the wall was not possible because of the presence of calcium in the vessel wall were excluded. Since sectors with extensive calcification are in general sectors with very advanced plaque, this exclusion could lead to an overall underestimation bias of wall thickness in the final results. Therefore, the results on plaque growth are only valid for uncalcified sectors.

The number of patients in this sub-study was limited. Therefore, multiple sectors (n=2291) out of the 15 coronary arteries were analysed. Using this approach, we obtained statistical significance, despite the limited number of patients. Besides, this study is an exploratory study and therefore the conclusions should be confirmed in a larger patient cohort.

CONCLUSIONS

With the NIRS-IVUS catheter available in the clinic, lipid-rich regions can be identified locally. This study demonstrated that the presence of local lipids acts in synergy with several (multidirectional) wall shear stress metrics on plaque progression, whereas systemic LDL-cholesterol levels showed to pose only a moderate effect. These conclusions indicate that NIRS-derived information in combination with local shear stress assessment, could help to identify high-risk plaques that will progress, thereby aiding in the identification of regions that need to be treated to prevent future cardiac events.

CHAPTER 7

The atheroprotective nature of helical flow in coronary arteries

Giuseppe De Nisco
Annette M. Kok
Claudio Chiastra
Diego Gallo
Ayla Hoogendoorn
Francesco Migliavacca
Jolanda J. Wentzel
Umberto Morbiducci

Giuseppe De Nisco
Ayla Hoogendoorn
Annette M. Kok
Claudio Chiastra
Diego Gallo
Umberto Morbiducci
Jolanda J. Wentzel

Based on:

'The atheroprotective nature of helical flow in coronary arteries', *Annals of Biomedical Engineering*, 2018

'The impact of helical flow on coronary atherosclerotic plaque progression', *manuscript in preparation*

ABSTRACT

Arterial hemodynamics is markedly characterized by the presence of helical flow patterns. Previous observations suggest that arterial helical blood flow is of physiological significance, and that its quantitative analysis holds promise for clinical applications. In particular, it has been reported that distinguishable helical flow patterns are potentially atheroprotective in the carotid bifurcation as they suppress flow disturbances. In this context, there is a knowledge gap about the physiological significance of helical flow in coronary arteries, a prominent site of atherosclerotic plaque formation. This study aimed to quantitatively assess helical blood flow in coronary arteries, and to investigate its possible associations with vascular geometry, with atherogenic wall shear stress (WSS) phenotypes and with plaque development in a representative sample of 30 swine coronary arteries. This study demonstrates that in coronary arteries: (1) the hemodynamics is characterized by counter-rotating bi-helical flow structures; (2) unfavorable conditions of WSS are strongly and inversely associated with helicity intensity ($r=-0.91$; $p<0.001$), suggesting an atheroprotective role for helical flow in the coronary tree; (3) vascular torsion dictates helical flow features ($r=0.64$; $p<0.001$); (4) the (near-wall) helicity intensity is negatively associated with local plaque development ($p<0.05$). The findings of this work support future studies on the role of helical flow in atherogenesis in coronary arteries.

INTRODUCTION

Early observations using *in vitro* models suggested that arterial hemodynamics is markedly characterized by the presence of helical flow patterns[342–345]. These *in vitro* data were confirmed *in vivo* using several different imaging modalities (as summarized in Table 7.1). As an example, a recent study using Color Duplex scanning observed in a cohort of 42 healthy volunteers that: (1) helical flow was present in 90% of the cases in the common carotid artery and the infrarenal aorta, and in 81% of the cases in the internal carotid artery; (2) 97% of the subjects had multiple helical flow sites[346]. Furthermore, phase contrast magnetic resonance imaging (MRI) has allowed to highlight that the aortic hemodynamics is markedly characterized by the presence of helical flow patterns (Table 7.1). All these observations suggest that helical flow in arteries has a physiological significance, and that its quantitative analysis holds promise for clinical applications[78].

The acknowledgment of a beneficial nature of helical flow in arteries is consistent with the fundamental role recognized for helicity in the organization/stabilization of both laminar and turbulent flows by the fluid mechanics theory[375]. In this regard, the onset of helical blood flow has been explained in terms of energy expenditure, i.e., distinguished helical blood flow patterns might be the consequence of an optimization in physiological transport process in the cardiovascular system, assuring an efficient perfusion as a result[354,356]. Furthermore, the forward-directed rotational fluid motion might stabilize blood flow, thereby minimizing flow disturbances and thus surface exposure to low and oscillatory wall shear stress (WSS), a condition which is known to influence endothelial function[373] creating a pro-atherogenic environment[45]. A first study in *in silico* aorto-coronary bypass models indicated a strong inverse relationship between oscillatory shear stress and the helical flow index[376]. Furthermore, findings in the human carotid bifurcation[79,377] and in the human aorta[378] showed that a high helical flow intensity suppresses flow disturbances, and is thereby potentially protective for atherosclerotic plaque build-up. Moreover, numerical studies suggested that helical flow influences transport and transfer of atherogenic particles to the vessel wall, ultimately contributing to the distribution of atherosclerotic plaques at the luminal surface[80,379]. Only one study by Gallo et al.[380] in carotid arteries described a direct relation between helical flow descriptors and endothelial dysfunction, the very first stage of atherosclerosis development. Until now, there is paucity of studies on the nature of helical blood flow patterns in coronary arteries and whether these patterns directly relate to plaque formation and progression. In this study we (1) assess the quantitative amount of helical blood flow, (2) investigate if correlations exist among helical flow, vascular geometry and descriptors of disturbed shear stress, and 3) explore the association between the helical flow intensity and plaque development in a representative sample of swine-specific computational hemodynamic models of coronary arteries. The study aims at

bridging the gap of knowledge still existing on the atheroprotective nature of helical flow in coronary arteries[381].

Table 7.1: In vivo observations of helical blood flow patterns in arteries, using several imaging modalities.

Arterial Segment	Imaging Technique	Reference
	Aorta	
Thoracic Aorta	Color Doppler Ultrasound	Frazin et al., 1990 [345]
Thoracic Aorta	4D phase contrast MRI	Kilner et al., 1993 [347]
Thoracic Aorta	4D phase contrast MRI	Bogren and Buonocore, 1994 [348]
Thoracic Aorta	4D phase contrast MRI	Bogren et al., 1997 [349]
Thoracic Aorta	4D phase contrast MRI	Houston et al., 2003 [350]
Thoracic Aorta	4D phase contrast MRI	Bogren et al., 2004 [351]
Supra-renal Aorta	MR Angiography	Houston et al., 2004 [350]
Thoracic Aorta	4D phase contrast MRI	Markl et al., 2005 [352]
Thoracic Aorta	4D phase contrast MRI	Hope et al., 2008 [353]
Thoracic Aorta	4D phase contrast MRI	Morbiducci et al., 2009 [354]
Ascending Aorta	4D phase contrast MRI	Hope et al., 2011 [355]
Thoracic Aorta	4D phase contrast MRI	Morbiducci et al., 2011 [356]
Thoracic Aorta	4D phase contrast MRI	Bürk et al., 2012 [357]
Thoracic Aorta	4D phase contrast MRI	Frydrychowicz et al., 2012 [358]
Thoracic Aorta	4D phase contrast MRI	Geiger et al., 2012 [359]
Thoracic Aorta	4D phase contrast MRI	Sigfridsson et al., 2012 [360]
Ascending Aorta	Doppler Ultrasound	Hansen et al., 2016 [361]
Infra-renal Aorta	Color Duplex Scanning	Stonebridge et al., 2016 [346]
Thoracic Aorta	4D phase contrast MRI	Arnold et al., 2017 [362]
Thoracic Aorta	4D phase contrast MRI	Garcia et al., 2017 [363]
	Carotid arteries	
Carotid bifurcation	Ultrasound Duplex Scanning	Ku et al., 1985 [364]
Internal Carotid artery	4D phase contrast MRI	Bammer et al., 2007 [365]
Internal Carotid artery	4D phase contrast MRI	Wetzel et al., 2007 [366]
Internal Carotid artery	4D phase contrast MRI	Markl et al., 2010 [367]
Common Carotid artery	4D phase contrast MRI	Knobloch et al., 2013 [368]
External Carotid artery	4D phase contrast MRI	Knobloch et al., 2013 [368]
Internal Carotid artery	4D phase contrast MRI	Knobloch et al., 2013 [368]
Internal Carotid artery	4D phase contrast MRI	Meckel et al., 2013 [369]
Common Carotid artery	Color Duplex Scanning	Stonebridge et al., 2016 [346]
Internal Carotid artery	Color Duplex Scanning	Stonebridge et al., 2016 [346]

Table 7.1: Continued

Arterial Segment	Imaging Technique	Reference
	Pulmonary arteries	
Right Pulmonary artery	4D phase contrast MRI	Bogren and Buonocore, 1994 [348]
Right Pulmonary artery	4D phase contrast MRI	François et al., 2012 [370]
Main Pulmonary artery	4D phase contrast MRI	Bächler et al., 2013 [371]
Right Pulmonary artery	4D phase contrast MRI	Bächler et al., 2013 [371]
Main Pulmonary artery	4D phase contrast MRI	Schäfer et al., 2017 [372]
Right Pulmonary artery	4D phase contrast MRI	Schäfer et al., 2017 [372]
	Femoral arteries	
Femoral arteries	Color Doppler Ultrasound	Stonebridge et al., 1996 [373]
Femoral arteries	4D phase contrast MRI	Frydrychowicz et al., 2007 [374]
Femoral arteries	Color Duplex Scanning	Stonebridge et al., 2016 [346]
	Iliac arteries	
Iliac arteries	4D phase contrast MRI	Frydrychowicz et al., 2007 [374]
	Intracranial arteries	
Basilar artery	4D phase contrast MRI	Bammer et al., 2007[365]

MATERIALS AND METHODS

Animal Population and Imaging

Ten adult familial hypercholesterolemia Bretoncelles Meishan mini-pigs[150] with a low-density lipoprotein receptor mutation were fed a high fat diet. For each animal model, the right (RCA), the left anterior descending (LAD), and the left circumflex (LCX) coronary artery were imaged at baseline and at 9-13 months follow-up using computed coronary tomography angiography (CCTA) and intravascular ultrasound (IVUS). The IVUS catheter was advanced as far as possible into each coronary artery while still reaching the ostium or a proximal large side branch at the end of the pullback. In each artery, baseline blood flow velocity was measured at several locations with the ComboWire (Volcano Corp., Rancho Cardova, CA, USA). Ethical approval was obtained to perform the pig study (EMCnr. 109-14-10) and the study was performed according to the National Institute of Health guide for the Care and Use of Laboratory animals[280].

IVUS analysis

Since the in vivo IVUS pullbacks were not gated, an off-line ECG gating was performed using an in-house algorithm implemented in MATLAB environment (Mathworks Inc., Natick, MA, USA) to avoid reconstruction artefacts caused by the heartbeat. Specifically, one IVUS frame per cardiac cycle was selected in the same diastolic phase. To quantify plaque development, lumen and vessel wall contours were semi-automatically detected on the IVUS images using QCU-CMS software (version 4.69, Leiden University Medical Centre, LKEB, Division of Image Processing). Wall thickness was assessed by subtracting the distance of the lumen centre to the outer wall contours from the distance to the lumen contour. Plaque development over time was quantified by computing the change in wall thickness between baseline and follow-up. This change in wall thickness was corrected for the number of months between both imaging time points, resulting in a measure of 'Δ wall thickness (ΔWT) per month'.

Geometry Reconstruction

The scheme applied for baseline coronary artery model reconstruction is summarized in Figure 7.1. In short, the IVUS-derived lumen and outer wall contours were stacked upon the 3D CCTA centerline. The matching of IVUS images with CCTA was performed using the side branches as landmarks, as previously reported[60]. Additional luminal regions proximal to the IVUS segment up to the aorta and at least two diameters distal to the IVUS-based models were segmented using the CCTA images. A semi-automatic segmentation method, which uses graph cuts and robust kernel regression, was employed[310]. In the complete CCTA and IVUS regions, all visible side branches were segmented (see Figure 7.1). The CCTA and IVUS lumen contours were merged into a 3D surface using Mevislab. Hereafter a volume preserving Laplacian smoothing filter was applied (10 smoothing iterations, smoothing factor 0.4). To further improve the quality of the 3D reconstruction, in some cases local smoothing was applied at the IVUS-CCTA transitions and at the attachment regions of the side branches. Computational hemodynamics was performed on all models including the side branches. However, data analysis was performed in the IVUS-imaged main branch of the RCA, LAD and LCX segments only. To do that, in the post-processing step, side branches were removed using the open-source Vascular Modeling Toolkit (VMTK, http://www.vmtk.org/).

Morphometric Descriptors

A robust centerline-based analysis of the coronary artery geometry was applied as proposed elsewhere[377]. In short, the average values of curvature ($\bar{\kappa}$) and torsion ($\bar{\tau}$) along the vessel were considered, which are known to have an influence on arterial hemodynamics[377].)

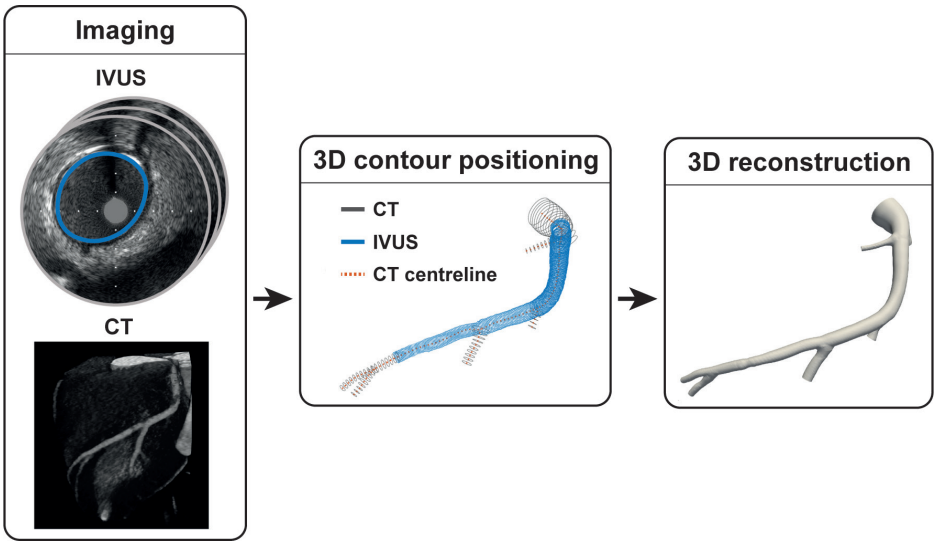

Figure 7.1: Scheme applied for swine coronary artery geometries reconstruction for CT and IVUS images.

Computational Hemodynamics

The governing equations of fluid motion, the Navier-Stokes equations, were numerically solved in their discrete form by applying the finite volume method. To do that, the computational fluid dynamics code Fluent (ANSYS Inc., Canonsburg, PA, USA) was used on fluid domains discretized in ICEM CFD (ANSYS Inc., USA) by means of tetrahedrons (with curvature-based refinement and a 5-layer prism at the lumen). Blood was assumed as an incompressible, homogeneous fluid with density ρ equal to 1060 kg/m^3, and its non-Newtonian behavior was modeled assuming it as a Carreau fluid[382,383]. Arterial walls were assumed to be rigid with no-slip condition. The derivation of boundary conditions from *in vivo* Doppler velocity measurements adopted here represents an accurate method to obtain personalized coronary artery computational models[384]. Technically, in each artery, the instantaneous maximum blood flow velocity was measured at several locations upstream and downstream of each side branch with the ComboWire. At each measurement site, maximum velocity data were used to estimate the flow rate as proposed elsewhere[328]. As condition at the inflow boundary, the most proximal measurement-based flow rate value was prescribed in terms of time-dependent flat velocity profile. At each side branch, a flow ratio was applied as outflow boundary, based on difference between upstream and downstream velocity-based flow rate measurements. In those vessel segments where velocity measurements were inaccurate

or not available, the Huo-Kassab diameter-based scaling law[311] was used to estimate the flow ratio to be prescribed.

Hemodynamic Descriptors

Helical flow in the 30 coronary artery models was characterized at baseline in terms of strength, size and relative rotational direction by applying different helicity-based descriptors. In detail, cycle-average helicity (h_1) and helicity intensity (h_2), signed (h_3) and unsigned helical rotation balance (h_4) were calculated as reported elsewhere[79]. Average helicity descriptors h_1 and h_2 indicate the net amount and the intensity of helical flow, respectively, while the helical rotation balance descriptors measure the prevalence (identified by the sign of descriptor h_3) or only the strength (h_4) of relative rotations of helical flow structures. Besides these whole-volume descriptors, for the helicity intensity h_2, also a near-wall descriptor was assessed by computing h_2 in the outer 10% of the vessel volume.

The luminal distribution of three "established" WSS-based descriptors, namely time-averaged wall shear stress (TAWSS), oscillatory shear index (OSI)[364], and relative residence time (RRT)[385] was computed. Two "emerging" descriptors of WSS multidirectionality were also considered. The first is the transversal WSS (transWSS)[50], defined as the average WSS component acting orthogonal to the time-averaged WSS vector direction, and the second is its normalized version, the Cross-Flow Index (CFI)[51]. As in previous studies[79,386], data from all simulations were pooled to define objective thresholds for 'disturbed shear stress'. From combined data, the lower tertile (i.e., the 33th percentile) for TAWSS, and the upper tertile (i.e., the 66th percentile) for OSI, RRT, transWSS, and CFI were identified. For each model, the percentage of surface area (SA) exposed to OSI, RRT, transWSS, and CFI values belonging to the upper (TAWSS lower) tertile was quantified. These areas were denoted as OSI66, RRT66, transWSS66, CFI66, and TAWSS33, respectively. Intravascular flow was investigated in terms of helical flow amount and topology.

The quantitative analysis, based on the mentioned hemodynamic descriptors, was substantiated by visualizations of near-wall and intravascular quantities. The normalized internal product between local velocity and vorticity vectors, labeled as local normalized helicity (LNH)[376], was used to visualize helical blood flow inside the coronary segments. The LNH allows to visualize left- and right-handed fluid structures in arteries[79,378] and isosurfaces of cycle average LNH values were used throughout the manuscript. Moreover, two more descriptors visualizing WSS multidirectionality were evaluated considering the cycle-average values of the projections of WSS vector respectively along (1) the "axial direction" ($\mathbf{WSS}_{ax}$), identified as the direction of the tangent to the vessel's

centerline, and (2) the secondary direction (**WSS**$_{sc}$), orthogonal to the axial direction and related to secondary flow[387].

Plaque development analysis

The relation between helicity and plaque development was assessed in 15 arteries from all 'advanced-diseased' animals (labelled B, D, G, I and J) which presented with rapid plaque growth resulting in a minimal plaque burden of 40% upon follow-up imaging (as described in Chapter 4 of this thesis).

For analysis of the global effect of helical flow on plaque growth, the whole volume h_2 and *near-wall* h_2 values were associated with the maximal ΔWT per month of each respective artery. The maximal ΔWT per month was taken instead of the mean value to avoid the effect of averaging out the focal atherosclerotic spots with healthy arterial parts.

Besides the global effect of helical flow on plaque development in the artery as a whole, we also aimed to assess whether helicity, like shear stress, has a local effect. Therefore, all arteries were divided in 3mm/45° sectors in an attempt to capture this potential local effect of helicity. Within these sectors, again the h_2 and *near-wall* h_2 values were related to the local plaque growth. For this latter analysis, all data were divided in tertiles (low, mid and high) based on the levels of the two helicity descriptors. These tertiles were determined per individual artery.

Statistical analysis

Bivariate correlations among WSS-based, helicity-based and geometric descriptors were determined in a Matlab environment (The MathWorks Inc., USA) using Spearman rank ordering. Regression analysis was used to identify relationships between each pair of descriptors and reported as Spearman correlation coefficients. The relation between the helicity-based descriptors and plaque development at a local sector level was assessed in IBM SPSS Statistics (version 24.0) with a linear fixed effects model to account for clustering of the analyzed sectors per vessel. Furthermore, the total cholesterol level of the individual pig was applied as confounding factor. Significance was assumed for $p<0.05$.

RESULTS

Helical blood flow patterns occur in most coronary arteries but show large inter-individual differences

Helical blood flow patterns were visualized using the isosurface of cycle-average LNH, with blue and red colors indicating left-handed and right-handed helical flow rotation, respectively (Figure 7.2). Notably, all 30 coronary artery models presented two distinguishable counter-rotating helical flow structures. It can be also appreciated that: (1) in most of the cases, counter-rotating cycle-average helical flow structures are distributed all along the length of the artery; (2) despite inter-individual variations, no marked differences among the coronary artery types is present.

Figure 7.3 shows for 3 different types of coronary arteries from animal model C (see Figure 7.2) the visualizations of the LNH cycle-average isosurfaces, and the maps of the cycle-average secondary (**WSS**$_{sc}$) and axial (**WSS**$_{ax}$) WSS vector projections. As for LNH, also for the **WSS**$_{sc}$ blue and red colors identify the left and right-handed direction, respectively. For **WSS**$_{ax}$ the blue and red colors identify the backward and forward flow direction, respectively. Interestingly, for the LAD and RCA there was a clear match between LNH and **WSS**$_{sc}$ direction of rotation, for the LCX this was less evident.

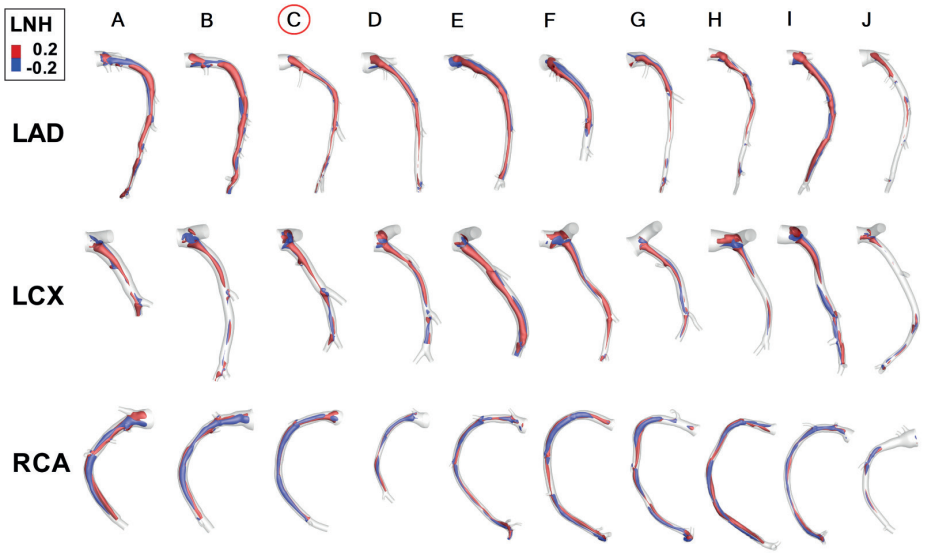

Figure 7.2: Intravascular fluid structures in the 30 coronary arteries. For each case, isosurfaces of cycle-average LNH (LNH= ± 0.2) are presented. Distinguishable left-handed (LNH<0) and right-handed (LNH>0) helical flow structures can be observed in all coronary arteries. Labels from A to J identify the single swine model. For each swine, LAD, LCX and RCA geometries were reconstructed.

Furthermore, Figure 7.3 shows that **WSS**$_{ax}$ is mainly positive, meaning that the WSS vector is predominantly aligned with the forward flow direction. Secondary and axial WSS distributions are presented in Figure 7.4 for all the 30 coronary artery models. The results presented in Figure 7.3 and Figure 7.4 suggested that the bi-helical arrangement of intravascular blood flow delineates the near-wall hemodynamics of coronary arteries.

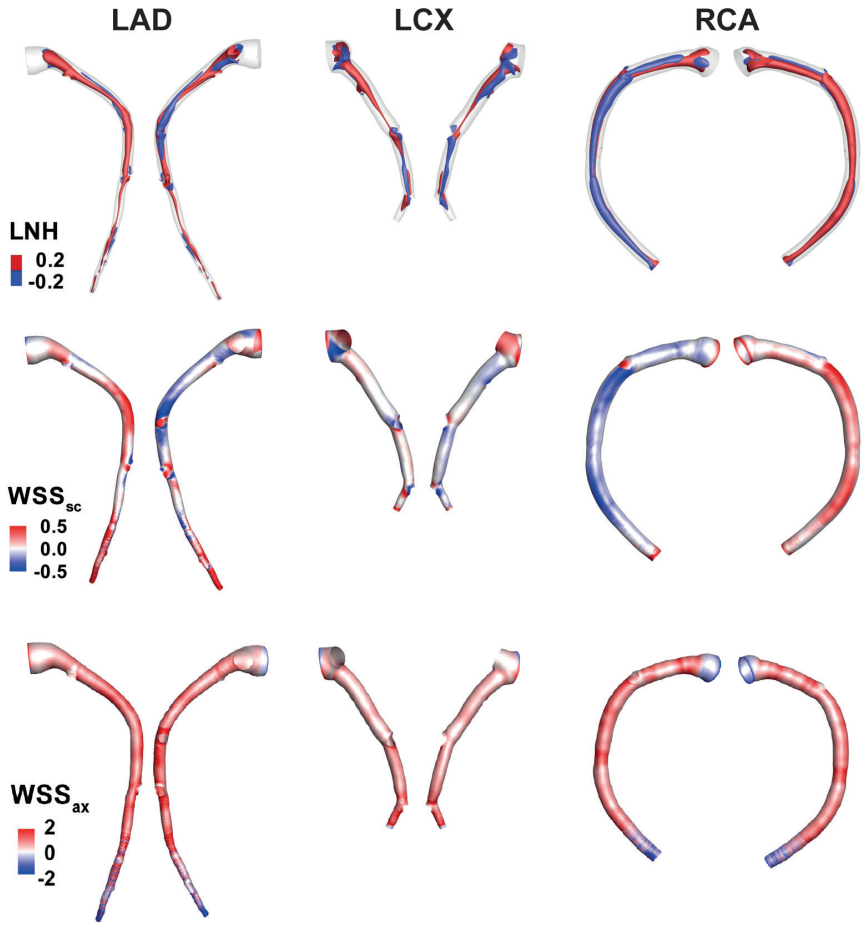

Figure 7.3: Visualization of LNH cycle-average isosurfaces, and of maps of cycle-average secondary (WSS$_{sc}$) and axial (WSS$_{ax}$) WSS vector projections for the three different types of coronary arteries (LAD, LCX, RCA) from the representative animal model C (see Figure 7.2). As for LNH, also for the **WSS**$_{sc}$ blue and red colours identify the left and right-handed direction, respectively. For **WSS**$_{ax}$ the red and blue colours identify the forward and backward flow direction, respectively.

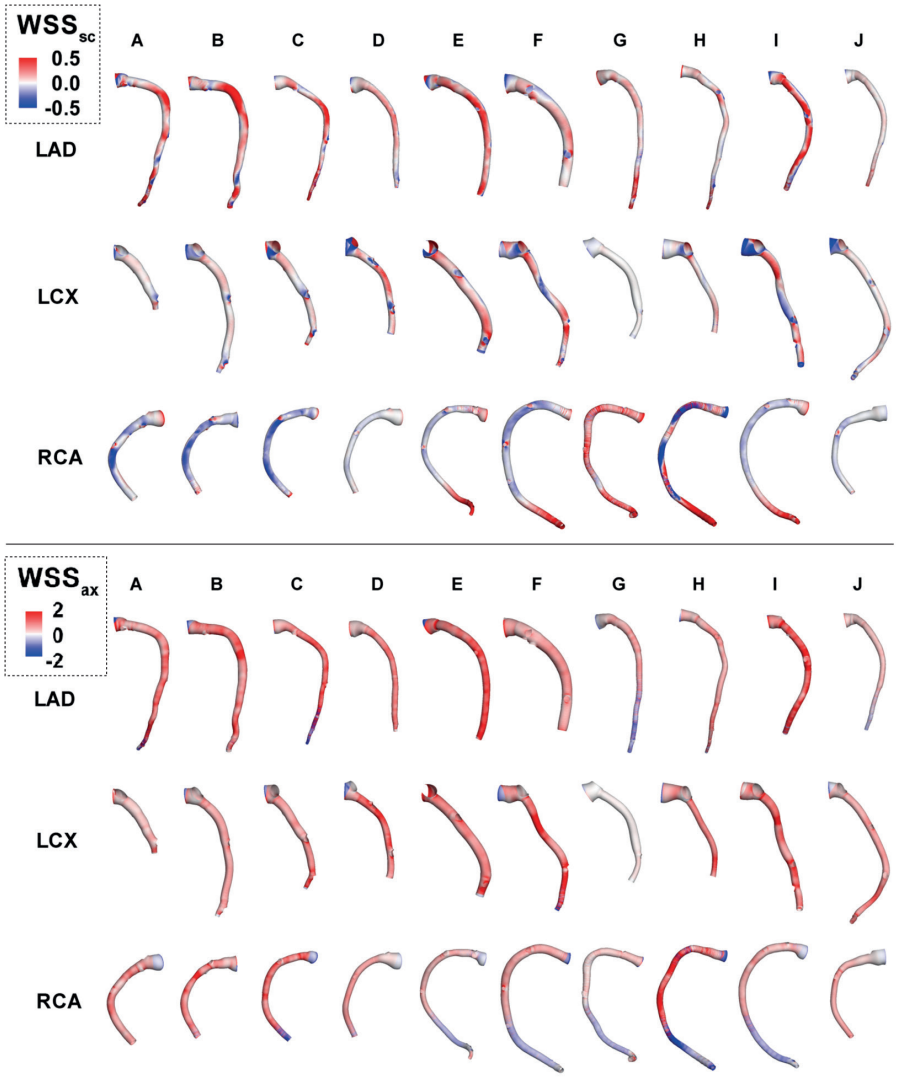

Figure 7.4: Maps of cycle-average secondary (WSS_{sc}) and axial (WSS_{ax}) WSS vector projections for the 30 coronary arteries. **WSS_{sc}** blue and red colours identify the left and right-handed direction, respectively. For **WSS_{ax}** the red and blue colours identify the forward and backward flow direction, respectively.

To complete the intra-individual analysis of representative animal model C, also the luminal distribution of the other computed WSS-based descriptors was presented in Figure 7.5. Notably, OSI, transWSS and CFI values at the luminal surface were low, suggesting that WSS is scarcely multidirectional in the three different types of coronary arteries of animal C. Figure 7.5 highlights that the location of the low WSS regions in the coronary arteries was more focal in the LAD and RCA, but less in the LCX. Moreover,

TAWSS and RRT showed a similar distribution, independent of coronary artery type, which was also the case for CFI and transWSS.

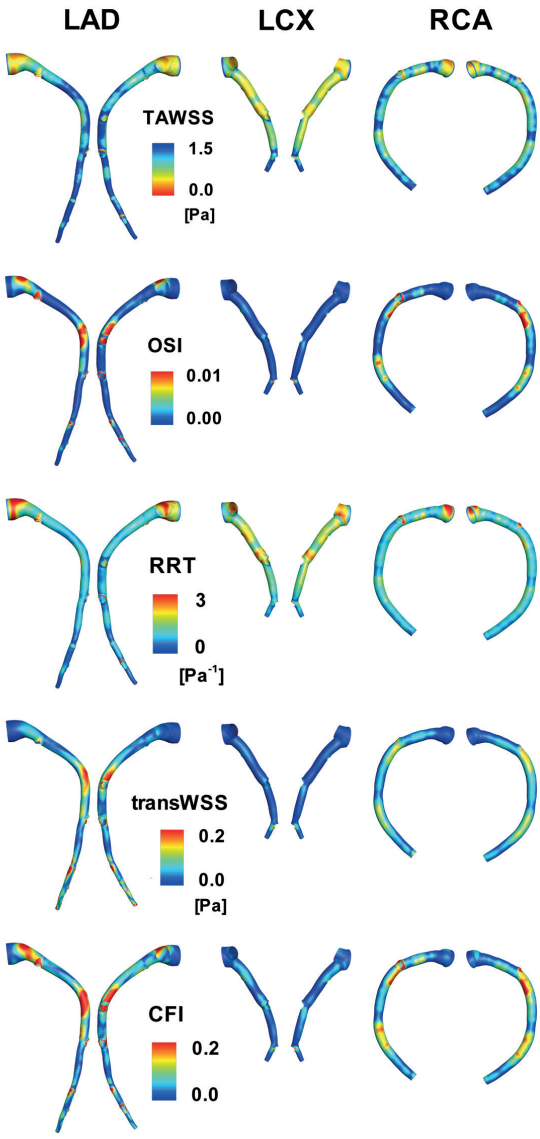

Figure 7.5: WSS-based descriptors distribution at the luminal surface of the three different types of coronary arteries (LAD, LCX, RCA) from the representative animal model C (see Figure 7.2). Red colour highlights those areas exposed to low TAWSS, and high OSI, RRT, transWSS and CFI. The very low values of OSI, transWSS and CFI at the luminal surface suggest that WSS is scarcely multidirectional.

Visualization of SAs exposed to low WSS (TAWSS33) highlights inter-individual variations (Figure 7.6). In some cases, the luminal surface is largely exposed to low WSS (e.g., case J-LDA, case G-LCX, case E-RCA) whereas other arteries are hardly exposed (e.g., case I-LDA, case H-RCA). The distribution of SAs exposed to OSI66, RRT66, transWSS66, CFI66 for all the 30 coronary artery models is presented in Figure 7.7).

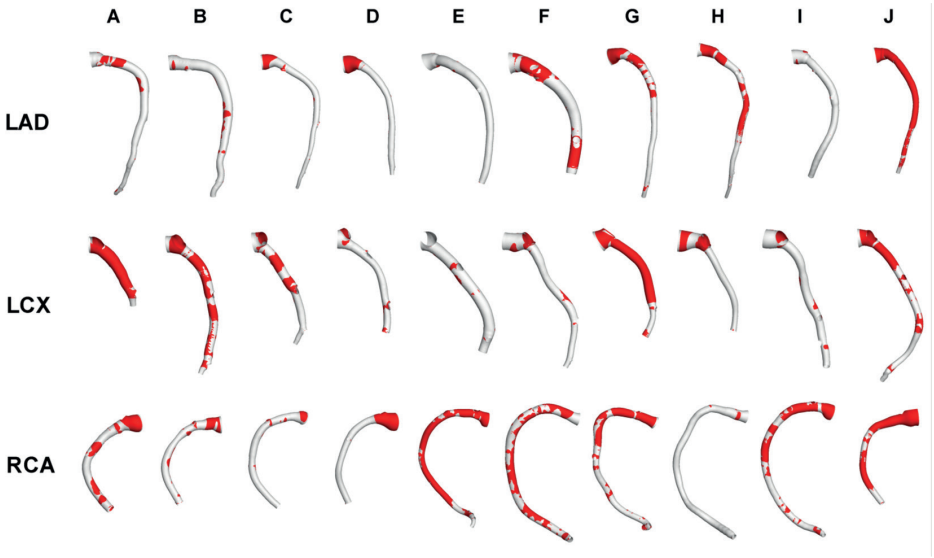

Figure 7.6: Surface areas of the 30 swine coronary artery models exposed to TAWSS33 (red). Labels from A to J identify the single swine model. For each swine, LAD, LCX and RCA geometries were reconstructed. Contour levels for TAWSS33 correspond to lowest tertile value of TAWSS distribution on the combined surface of all models.

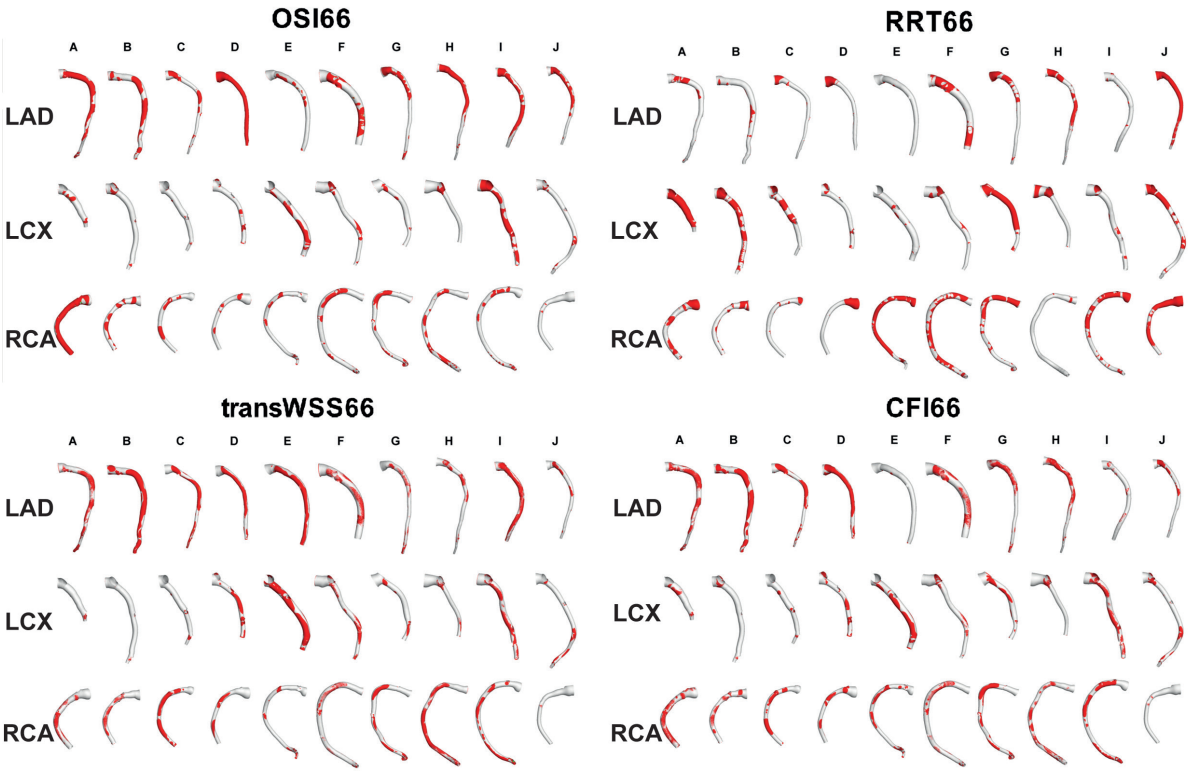

Figure 7.7: Surface areas of the 30 swine coronary artery models exposed to OSI66 (top-left panel), RRT66 (right-left panel), transWSS66 (bottom-left panel) and CFI66 (bottom-right panel). Labels from A to J identify the single swine model. For each swine, LAD, LCX and RCA geometries were reconstructed. Contour levels for OSI66, RRT66, transWSS66, and CFI6 correspond to highest tertile value of OSI, RRT, transWSS, and CFI, distribution on the combined surface of all models, respectively.

WSS descriptors partially relate to vessel geometry

The correlation coefficients between each possible couple of disturbed shear stress and geometry descriptors are summarized in Table 7.2. The WSS-based percentage SAs (exposed to) were significantly correlated to each other, with the sole exception of OSI66 and RRT66.

In this study, RRT66 was considered to be equivalent to TAWSS33. This consideration was based on the strong association that emerged between RRT66 and TAWSS33 (Table 7.2), suggesting that RRT was markedly biased by TAWSS. The definition of RRT as a combination of OSI and TAWSS, and the very low OSI values characterizing the investigated coronary arteries (Figure 7.5), support the observation that RRT66 is a replica of TAWSS33 in the investigated coronary arteries. The significant association between transWSS66 and CFI66 ($r=0.74$, $p<0.001$) emerged as a consequence of the low transWSS values and from their analytical dependence. Interestingly, a significant association was also observed for OSI66 with transWSS66 ($r=0.59$, $p<0.001$) and CFI66 ($r=-0.81$, $p<0.001$). Furthermore, our data showed that larger SAs exposed to low WSS corresponded to smaller SAs exposed to multidirectional WSS, as confirmed by the moderate negative associations of TAWSS33 with OSI66 ($r=-0.37$, $p<0.05$), transWSS66 ($r=-0.84$, $p<0.05$), and CFI66 ($r=-0.39$, $p<0.05$). Low and oscillatory WSS areas were neither correlated to curvature nor to torsion of the artery (Table 7.2). Since transWSS66 ($r=-0.37$, $p<0.05$) and CFI66 ($r=-0.49$, $p<0.05$) were negatively associated with curvature, our data suggest that curvature in coronary arteries serves to suppress WSS multi-directionality.

Table 7.2: Correlation coefficients between each possible couple of disturbed shear stress parameters (% surface area exposed) and geometry (average curvature and torsion) descriptors. Statistically significant values are in bold.

	%OSI66	%RRT66	%transWSS66	%CFI66	$\bar{\kappa}$	$\bar{\tau}$
%TAWSS33	**-0.37***	**1.00‡**	**-0.84***	**-0.39***	0.12	0.12
	%OSI66	-0.34	**0.59‡**	**0.81‡**	-0.28	0.18
		%RRT66	**-0.83‡**	**-0.37***	0.13	0.14
			%transWSS66	**0.74‡**	**-0.37***	-0.05
				%CFI66	**-0.49***	0.13
					$\bar{\kappa}$	0.13

* $P_{value} < 0.05$; † $P_{value} < 0.01$; ‡ $P_{value} < 0.001$

Helicity-based and WSS-based descriptors are associated

Regression analysis revealed significant associations between helicity-based *vs.* WSS-based descriptors (Table 7.3). Notably, h_2 was strongly and negatively associated with TAWSS33 (r=-0.91, p<0.001), indicating that the higher h_2 *is*, the lower the SA of an individual coronary artery exposed to low WSS.

In contrast, positive regression coefficients were found for the significant associations of h_2 with OSI66, CFI66 and transWSS66 (Table 7.3). For clarity, it must be reported here that the threshold values (66th percentile) identified for OSI (0.002), CFI (0.066) and transWSS (0.039 Pa) are very low in the 30 coronary arteries investigated, suggesting that WSS multidirectionality is not a feature marking out their local haemodynamics (Figure 7.5).

Associations with the WSS descriptors were, similar to h_2, although weaker, observed for h_1 (Table 7.3). An explanation for this is that overall, there is a preferential, though sometimes moderate, cycle-average direction of rotation in the observed bi-helical blood flow patterns in the 30 coronary arteries. This is confirmed by the positive sign of average h_3 value and by average h_4 value (h_4 = 0.112).

Table 7.3: Correlation coefficients for percentage luminal surface areas expose to disturbed shear and helicity-based descriptors and for hemodynamic descriptors vs. geometry (average curvature and torsion). Statistically significant values are in bold.

	h_1	h_2	*near-wall* h_2	h_3	h_4
%TAWSS33	**-0.48**†	**-0.91**‡	**-0.60***	-0.05	-0.01
%OSI66	**0.50**†	**0.58**‡	**0.80**‡	**0.39***	0.32
%RRT66	**-0.49***	**-0.90**‡	**-0.60***	-0.03	-0.01
%transWSS66	**0.49**†	**0.86**‡	**0.70**†	0.13	0.13
%CFI66	**0.47**†	**0.51**†	**0.70**†	0.34	0.30
$\bar{\kappa}$	-0.12	-0.22	-0.37	-0.01	0.11
$\bar{\tau}$	**0.49**†	0.09	0.08	**0.64**‡	**0.39***

* P_{value} < 0.05; † P_{value} < 0.01; ‡ P_{value} < 0.001

Regarding geometric attributes, Table 7.3 also shows that neither h_1 nor h_2 and *near-wall* h_2 were associated with curvature. Torsion was found to be positively correlated with helicity h_1 (r=0.49, p<0.01), with signed (h_3) helical rotation balance (r=0.64, p<0.001), and, though weaker, with its unsigned (h_4) version (r=0.49, p<0.05), suggesting an important role of vascular torsion in promoting helical flow in coronary arteries.

The nature of the association of h_2 and *near-wall* h_2 with WSS and geometry can be better appreciated in scatter plots reported in Figure 7.8 and 7.9. It emerges that: (1)

a non-linear decreasing trend relates h_2 and *near-wall* h_2 with TAWSS33 (and RRT66 as well), i.e., the percentage SA exposed to low WSS; (2) an almost (positive) linear trend describes the observed association of h_2, but not of *near-wall* h_2 with transWSS66; (3) trends in the observed associations are not specific for the different types of coronary arteries.

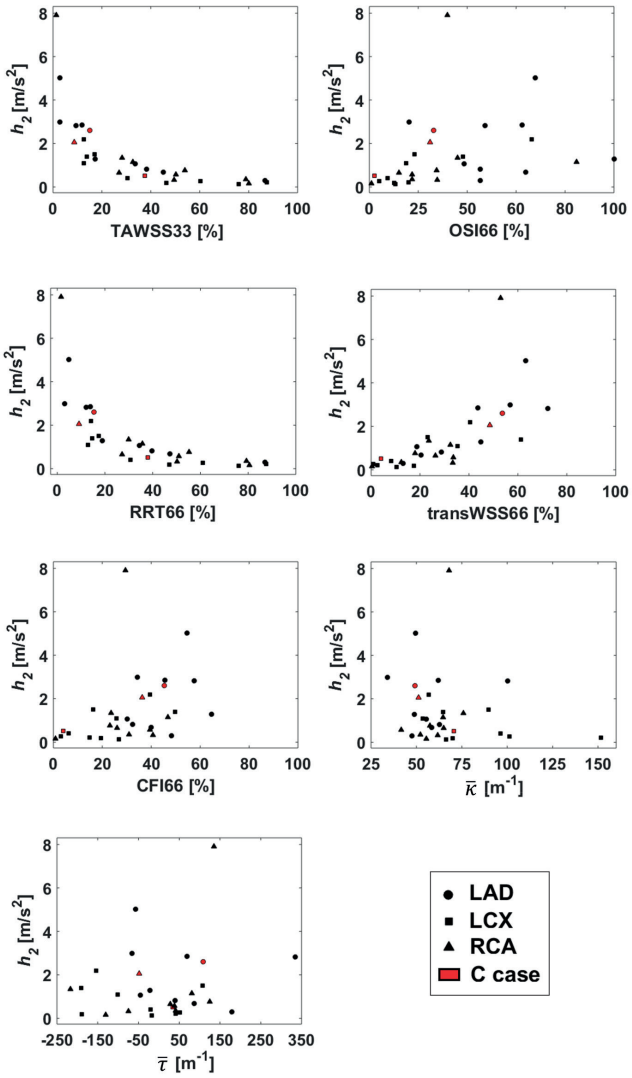

Figure 7.8: Scatter plots of helicity intensity *h2* vs. WSS-based descriptors, and average curvature and values. Red coloured dots indicate case C (Figure 7.2), used as representative example in Figures 7.3 and 7.5.

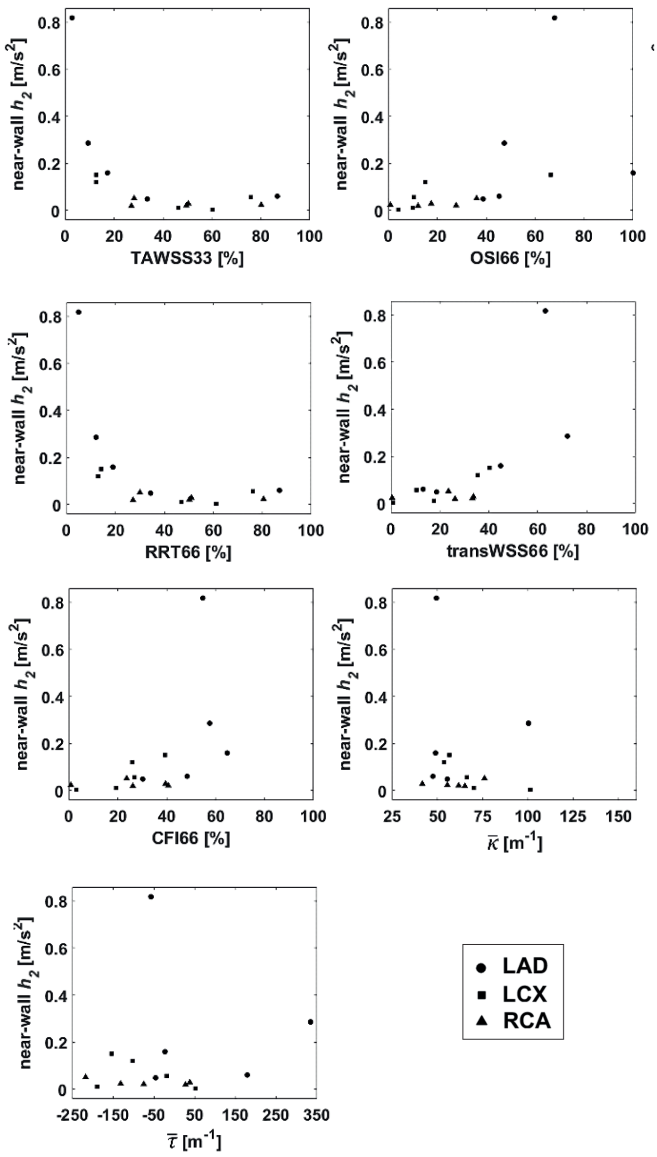

Figure 7.9: Scatter plots of the near-wall helicity intensity *h2* vs. WSS-based descriptors, and average curvature and values. Results are indicated for the LAD, LCX and RCA coronary arteries of the advanced-diseased animals.

The observed associations between helicity-based descriptors and percentage of luminal SAs that, based on thresholds, are subjected to more 'disturbed shear stress' (Table 7.3), are confirmed when considering luminal surface area-averaged values of the WSS-based descriptors. Correlation coefficients for luminal surface area-averaged

values of WSS-based descriptors and helicity-based descriptors are reported in Table 7.4. Results in Table 7.4 confirm the observed associations between helicity-based descriptors and percentage of luminal SAs exposed to "disturbed flow" (Table 7.3). More in detail, h_2 was strongly and positively associated with $\overline{\text{TAWSS}}$ (r=0.92, p<0.001), indicating that the higher the h_2 *is*, the higher is the luminal surface area-averaged value of TAWSS, for an individual coronary artery. Moreover, positive regression coefficients were found for the significant associations of h_2 with $\overline{\text{OSI}}$, $\overline{\text{CFI}}$ and $\overline{\text{transWSS}}$. Associations similar to h_2, although weaker, were observed for h_1 (Table 7.4).

Table 7.4: Correlation coefficients for luminal surface area-averaged values of WSS-based descriptors and helicity-based descriptors. Statistically significant values are in bold.

	h_1	h_2	h_3	h_4
$\overline{\text{TAWSS}}$	**0.54**†	**0.92**‡	0.12	0.05
$\overline{\text{OSI}}$	**0.52**†	**0.57**†	**0.38**†	0.31
RRT	**-0.53**†	**-0.90**‡	-0.12	-0.07
$\overline{\text{transWSS}}$	**0.52**†	**0.86**‡	0.14	0.17
$\overline{\text{CFI}}$	**0.51**†	**0.54**†	0.36	0.32

* $P_{value} < 0.05$; † $P_{value} < 0.01$; ‡ $P_{value} < 0.001$

Local, near-wall helicity intensity is related to atheroprotection

The above described relation between WSS descriptors and helicity indicators indicates a possible atheroprotective role for helicity. To confirm this hypothesis, we assessed the direct association of the helicity descriptor *h2* with subsequent plaque development (i.e. increase in wall thickness). No significant relation was found between h_2 or *near-wall* h_2 and the maximal wall thickness in the artery as a whole (Figure 7.10). For the local analysis however, in regions with a higher *h2* or near-wall *h2*, plaque development was significantly lower than in regions with low *h2*, or mid or low near-wall *h2* levels. This finding indicates that the intensity of local helical flow, both in the whole volume and near the wall, inversely relates to plaque development.

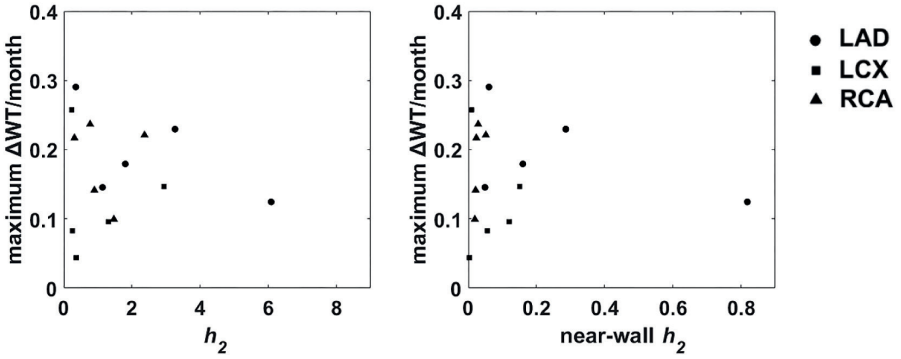

Figure 7.10: Scatter plots of *h2* and near-wall *h2* vs. the maximum plaque growth per month per artery. Results are indicated for the LAD, LCX and RCA coronary arteries of the advanced-diseased animals.

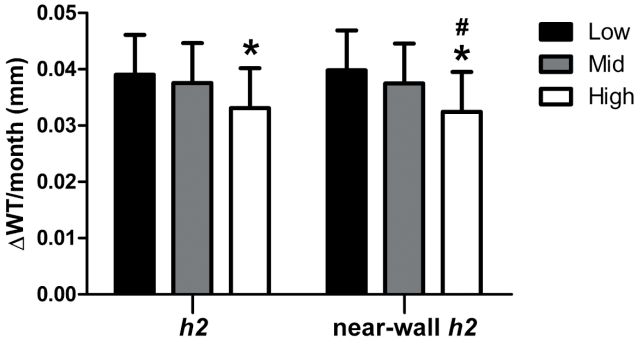

Figure 7.11: Relation between *h2* and near-wall *h2* and plaque development at a local (sector) level. Plaque development is expressed as the change (delta) in wall thickness corrected for the number of months. The data are divided low (black bars), mid (grey bars) and high (white bars) levels of the respective helicity descriptors. *p<0.05 compared to 'low', #p<0.05 compared to 'mid'.

DISCUSSION

In the last decade quantitative approaches have started to be widely applied to investigate the physiological significance of arterial helical flow. However, despite the qualitatively description of a relationship between helical flow and atheroma formation in coronary arteries, only recently a patient-specific computational study on a small dataset (N=3) has suggested a link between helical flow and WSS in human coronary artery segments[382].

Here, the existence of correlations among helical flow, vascular geometry and disturbed shear stress was explored in a representative dataset of 30 swine-specific models of coronary arteries. Among the main findings, it is reported for the first time that distinguishable counter-rotating helical flow patterns were present in all the models under investigation (Figure 7.2). This suggests that helical flow arrangement is a feature characterizing physiological intravascular hemodynamics in coronary arteries. Such arrangement in helical structures characterized by high helicity intensity (h_2) stabilizes blood flow imparting low WSS multidirectionality and minimizing the luminal surface exposed to low WSS, thus indicating that helical flow is instrumental in suppressing flow disturbances in coronary arteries. More in detail, since the rotating direction of helical flow patterns dictates the luminal distribution of $\mathbf{WSS}_{sc}$ (Figures 7.3 and 7.4), it emerges that bi-helical flow patterns could influence endothelial shear stress orientation, in coronary arteries. A preferential direction of rotation of the bi-helical flow structures is promoted by vascular torsion, while vascular curvature moderately suppresses an already scarce multidirectional WSS (Table 7.2). In fact, very low values of OSI, transWSS and CFI were found (Figure 7.5), suggesting a predominant role of low WSS as hemodynamic determinant of plaque formation in coronary arteries. Previous findings support the role of low WSS in promoting endothelial dysfunction[46,66,69,380,388], although the influence of multidirectional shear stress on endothelial function needs to be investigated more in-depth.

In recent years, computational hemodynamics has made a remarkable contribution to highlight the physiological significance of helical blood flow naturally streaming in arteries. In particular, an *in silico* study on a dataset of 50 models of human carotid bifurcations showed that high helicity intensity is instrumental in suppressing flow disturbances, and thereby is potentially atheroprotective[79]. These findings were supported by the observation that helical flow production in the common carotid artery, reinforcing helicity in the carotid bifurcation, provides further contribution to reduce the likelihood of flow disturbances[377]. Similar findings have been reported using computational fluid dynamics in the healthy aorta, suggesting a key role for helical blood flow in (1) reducing luminal areas exposed to low and oscillatory shear

stress,[378] and (2) influencing near-wall transfer of atherogenic particles and oxygen[80,379]. Moreover, computational hemodynamics findings showed that helical blood flow could be posture-dependent[389]. Parallel to basic studies on its physiological significance, the analysis of helical blood flow has been increasingly adopted to better understand how cardiovascular diseases[372,390,391], or ageing[358], alter the arterial flow physics.

All above-mentioned results indicated a hypothetical atheroprotective effect of helical flow. In this study, we have been the first to directly relate helical flow descriptors to plaque development in the coronary arteries. For the artery as a whole, the helicity intensity both in the whole volume and near the wall (h_2 and *near-wall* h_2) did not show a relation with plaque development. This analysis could be hampered by the low number of analyzed arteries and by the fact that there are large regional differences in plaque development throughout the arteries which makes it harder to assess the effect of helicity on plaque development at vessel level. However, when we assessed helicity intensity at a local (sector) level, we observed that regions with high *h2* or *near-wall* h_2 levels were more protected against atherosclerosis formation compared to regions where the *h2* or *near-wall* h_2 descriptor was lower.

Several limitations could weaken the findings of this study. Among them, the assumption of rigid vascular wall might have affected TAWSS estimation. However, studies applying fluid-structure interaction approaches reported that TAWSS spatial distribution is preserved using rigid walls[392]. Moreover, the cardiac-induced motion of coronary arteries was neglected. This idealization was based on previous findings demonstrating that myocardial motion has a minor effect on coronary flow and WSS distribution with respect to the blood pressure pulse[393,394]. Moreover, it can markedly affect instantaneous WSS and OSI wall distribution, with minor effects on TAWSS[395]. Therefore, it is expected to have minor impact on the here reported observations[378]. The relatively modest number (N=30) of coronary artery models investigated could limit the generality of the study. However, the existence of hemodynamic features which are common to all coronary arteries here clearly emerges as the presence of distinguishable helical blood flow patterns, and low WSS multidirectionality. For the plaque development analysis, we only assessed 15 arteries of the most diseased pigs. For the analysis of the relation between helicity and plaque development at vessel level, these modest numbers could limit the possibilities to find statistically significant relations. However, for the local analysis, by dividing all arteries in 3mm/45° sectors, we gained sufficient power to find a relation between helicity and plaque development while we also corrected for the clustering of regions per vessel. Finally, here swine, not human models, have been used to characterize helical flow in coronary haemodynamics and to investigate whether a causal relationship between helical flow and shear stress exists. However, the close similarity between the human and pig coronary anatomy,

in addition to the wide adoption of swine model in studies of coronary disease over the past decades[396], support the translation of the findings of this study to human coronary arteries. Moreover, helical flow features similar to the ones observed here were reported in a small number of image-based computational hemodynamic models of human coronary arteries[382], confirming that swine models are representative of the human coronary circulation.

The findings of this study support the future exploration of the links between the observed helical distribution of fatty and fibrous plaques in coronary artery segments and the hemodynamic factors involved in the local onset and progression of atherosclerosis in the coronary tree. In this sense, the present findings will contribute to answer to the still open questions raised since 60s[342,397–400], regarding the observation of irregular spiral distributions of sclerotic bands in coronary arteries.

CONCLUSION

In conclusion, this study demonstrates that hemodynamics of coronary arteries is characterized by distinguishable and counter-rotating bi-helical flow structures, whose topological features are associated with geometry (in terms of average torsion of the vessel). Remarkably, it emerges that unfavorable conditions of low wall shear stress are strongly and inversely associated with helicity intensity, as already observed in other arterial districts[79]. This finding translated into a negative relation of local (near-wall) helicity intensity with plaque development, demonstrating the atheroprotective nature of helical flow.

Part III

Invasive imaging markers of atherosclerosis

CHAPTER 8

OCT-measured plaque free wall angle is indicative for plaque burden: overcoming the main limitation of OCT?

Ayla Hoogendoorn
Muthukaruppan Gnanadesigan
Guillaume Zahnd
Nienke S. van Ditzhuijzen
Johan C. H. Schuurbiers
Gijs van Soest
Evelyn Regar
Jolanda J. Wentzel

Based on:

'OCT-measured plaque free wall angle is indicative for plaque burden: overcoming the main limitation of OCT?', *International Journal of Cardiovascular Imaging*, 2016

ABSTRACT

Purpose

The aim of this study was to investigate the relationship between the plaque free wall (PFW) measured by optical coherence tomography (OCT) and the plaque burden (PB) measured by intravascular ultrasound (IVUS). We hypothesize that measurement of the PFW could potentially help to estimate the PB, thereby overcoming the limited ability of OCT to visualize the external elastic membrane in the presence of plaque. This could enable selection of the optimal stent-landing zone by OCT, which is traditionally defined by IVUS as a region with a PB<40%.

Methods

PB (IVUS) and PFW angle (OCT and IVUS) were measured in 18 matched IVUS and OCT pullbacks acquired in the same coronary artery. We determined the relationship between OCT measured PFW (PFW_{OCT}) and IVUS PB (PB_{IVUS}) by non-linear regression analysis. An ROC-curve analysis was used to determine the optimal cut-off value of PFW angle for the detection of PB <40%. Sensitivity, specificity, positive predictive value (PPV) and negative predictive value (NPV) were calculated.

Results

There is a significant correlation between PFW_{OCT} and PB_{IVUS} (r^2=0.59). The optimal cut-off value of the PFW_{OCT} for the prediction of a PB_{IVUS} <40% is ≥220° with a PPV of 78% and an NPV of 84%.

Conclusion

This study shows that PFW_{OCT} can be considered as a surrogate marker for PB_{IVUS}, which is currently a common criterion to determine optimal stent-landing zone.

INTRODUCTION

In recent years, intravascular optical coherence tomography (OCT) has emerged as imaging technique for guiding percutaneous coronary intervention (PCI). OCT offers a very high spatial and lateral resolution compared to intravascular ultrasound (IVUS). However, this comes at the expense of penetration depth into the tissue[42]. Based on IVUS studies[401,402], the plaque burden (PB) is a leading criterion for a stent-landing zone, where areas with PB <40%[12] are considered optimal. The ability of OCT to visualize plaque burden is limited by optical attenuation: the signal decreases with depth in tissue. Either a thick layer of fibrous (low-attenuation) plaque or the presence of superficial lipids or dense macrophage accumulations (high-attenuation)[403], may obscure the visibility of the media behind the plaque. This potentially limits the use of OCT to guide stent implantation when it comes to the selection of the optimal stent landing zones within the target artery. More recently, in addition to low plaque burden, the absence of lipid/necrotic core within the landing zone has been advocated as a decision criterion which can very reliably be identified by OCT, in contrast to IVUS[404].

In a previous study[405], we demonstrated a strong inverse linear relationship between PB and the plaque free wall (PFW) angle using IVUS imaging (PB_{IVUS} and PFW_{IVUS}). In the present study we hypothesize that the angle of the PFW measured in OCT (PFW_{OCT}) can likewise reflect the PB. Second, we postulate that regions with a PB <40% can be selected for finding an optimal stent-landing zone. When the PFW angle is small (<180°), it might be instantly clear that disease is present with a PB >40%, thus forming a suboptimal stent-landing zone. Similarly, sections with a large PFW angle >270° can be easily and reliably identified by OCT as optimal stent-landing zones with a PB <40%. However, in the intermediate region between 180°-270° PFW, the interpretation might be more ambiguous. The aim of this study was to investigate the relationship between PFW_{OCT} and $IVUS_{PB}$ and establish the utility (expressed in predictive values for PB <40%) of this relationship to detect PB <40% for selection of the optimal stent landing zone by OCT.

MATERIALS AND METHODS

Study population

To study the predictive value of the PFW_{OCT} for determination of the PB, we performed a retrospective observational study. NIRS-IVUS (TVC, InfraRedx, Burlington, Massachusetts, USA) and OCT (St. Jude Medical Inc., St. Paul, MN, USA) pullbacks of the same ROI were used from 18 left anterior descending (LAD) coronary arteries of 18 patients with stable or unstable coronary syndrome included in the OC3T study (Erasmus MC, Rotterdam). Informed consent was obtained from all individual participants included in the study. All procedures performed in this study involving human participants were in accordance with the ethical standards of the institutional research committee and with the 1964 Helsinki declaration and its later amendments.

The NIRS-IVUS images were acquired using a commercially available hybrid optical/ultrasound catheter with an automated pullback (pullback speed 0.5 mm/sec and 16 frames per second). The OCT images were obtained with C7-XR/Illumien and Dragonfly catheter. Automated OCT pullback (pullback speed 20 mm/s) was performed during simultaneous iso-osmolar X-ray contrast medium (Visipaque 320, GE Healthcare, Buckinghamshire, U.K.) delivery through the guide catheter, using a power injector (Medrad ProVis, Bayer HealthCare LLC, NJ, U.S.A; typical flush rate: 3.0 ml/s).

Analysis

The OCT and IVUS pullbacks were matched by overlaying the frames with the same side branches. The remainder of the frames was linearly interpolated in between the side branches. Matched NIRS-IVUS and OCT images were analysed every millimetre over a ROI of the most proximal 20 mm of a pullback. On the IVUS images, the external elastic lamina (vessel area=VA) and lumen area (LA) contours were drawn using QCU-CMS software (version 4.69, Leiden University Medical Centre, LKEB, Division of Image Processing). These contours were used for the calculation of the plaque area (PA=VA-LA) and subsequently the PB (PA/VA*100%). PFW angle was defined from the centre of the lumen as the arc of the cross-section with a visible, healthy wall having an intima-media thickness of less than 0.5 mm in both imaging modalities. In total, 360 frames were analysed on both the IVUS and OCT images. The frame data were averaged over 3 mm sections to increase robustness and to compensate for imprecise matching. Images that showed a side branch either on IVUS or OCT, with the wall out of view, or a bad flush, were excluded. This resulted in 106 matched IVUS and OCT 3mm sections suitable for analysis. A total of 10 out of the 18 pullbacks of OCT and IVUS were analysed by two independent expert observers for assessment of the reproducibility.

Statistics

Statistical analysis was performed using SPSS software (version 21.0, SPSS Inc., Chicago, IL, USA). Findings were regarded significant when $p < 0.05$. The reproducibility of all PFW and PB measurements was assessed by performing an inter-observer agreement analysis to calculate the intraclass correlation coefficient.

Both a linear and a non-linear model were used to assess the relation between $PFW_{IVUS/OCT}$ and PB_{IVUS}. The non-linear model was defined as follows:

$$PB_{IVUS} = a \times PFW + b \qquad \text{for } PFW \leq \frac{(e-b)}{(a-d)};$$

$$PB_{IVUS} = d \times PFW + e \qquad \text{for } PFW > \frac{(e-b)}{(a-d)};$$

and was computed for both PFW_{OCT} and PFW_{IVUS}. For the non-linear regression analysis, the following starting parameters were chosen: a=0; b=55; d=-0.2; e=100. We denote the crossover value between both linear regimes as PFW_C = (e-b)/(a-d), resulting from the regression.

To test whether the slope of the relationship between PFW_{OCT} vs PB_{IVUS} and PFW_{IVUS} vs PB_{IVUS} was similar, implying that with PFW_{OCT} and PFW_{IVUS} the same PB is predicted, a student's t-test for two independent samples was used. An ROC-curve analysis was performed to find the optimal cut-off value of PFW_{OCT} to predict a PB_{IVUS} <40%. Based on the optimal cut-off value, the sensitivity, specificity, positive predictive value (PPV) and negative predictive value (NPV) of PFW_{OCT} for prediction of PB_{IVUS} <40% were calculated.

8

RESULTS

Relation between PFW and PB in IVUS

PFW_{IVUS} and PB_{IVUS} were significantly, inversely related ($r^2 = 0.78$) which confirmed the findings of our previous publication[405]. However, a closer fit to the model was found by applying a non-linear regression line ($r^2 = 0.82$) (Figure 8.1A), with $PFW_C = 182°$.

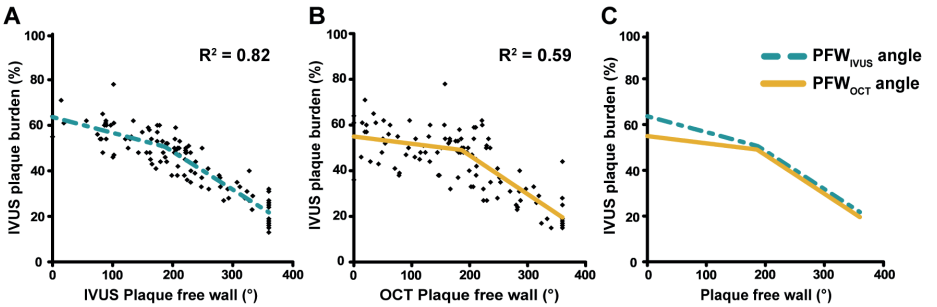

Figure 8.1: Relationship between the plaque free wall (PFW) angle and plaque burden (PB). A) The PFW_{IVUS} measured shows a strong inverse, non-linear correlation with the PB_{IVUS} with a crossover point PFW_C = 182° PFW. Final parameters: a=-0.069; b=63.59; d=-0.163; e=80.74. B) A similar relationship is seen for the PFW_{OCT} angle with the PB_{IVUS} with a crossover point PFW_C = 186°. Final parameters: a=-0.032; b=54.98; d=-0.169; e=80.59. C) Overlay of regression lines of A) and B). PFW_{OCT} and PFW_{IVUS} perform equally well in predicting PB in regions with a PFW angle >186°. In the more diseased regions, the predictive value of the PFW_{OCT} angle is reduced compared to IVUS.

Predictive value of PFW_{OCT}

To assess whether the PFW_{OCT} could serve as a surrogate marker for PB_{IVUS}, the PFW_{OCT} values were plotted against the PB_{IVUS} values. Again, a non-linear regression relationship proved significant (r^2 = 0.59) (Figure 8.1B) with PFW_C = 186°. Interestingly, both IVUS and OCT showed the same slope (student's t-test for inequality of slopes; p=NS) to predict PB for PFW ≥186°. For PFW <186°, PFW_{OCT} had no clear relationship with the PB, contrasting the PFW_{IVUS} which still showed a weak relationship with the PB (Figure 8.1C).

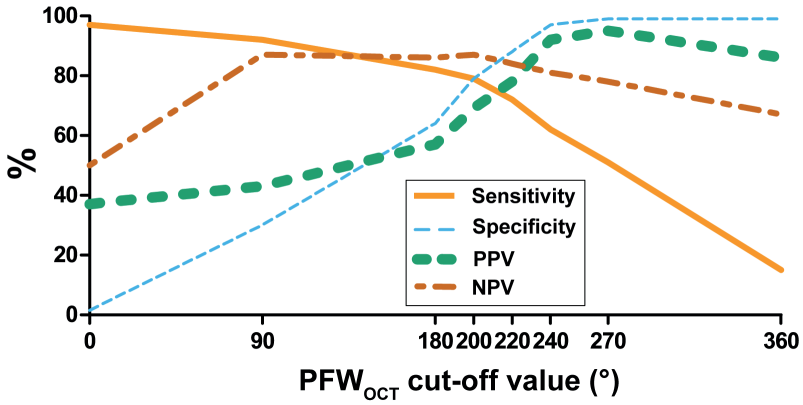

Figure 8.2: Sensitivity, specificity, PPV and NPV values for different PFW angle cut-off points to predict a PB <40%. The optimal cut-off point is set at 220° PFW.

To find the optimal cut-off value of the PFW_{OCT} to predict a PB_{IVUS} <40%, an ROC-curve analysis was performed. Optimization of sensitivity, specificity, PPV and NPV resulted in a PFW_{OCT} cut-off value of ≥220° (Figure 8.2). With this cut-off value, an optimal stent-landing zone (PB <40%) could be predicted correctly in 78% of the cases (PPV) (Figure 8.3). Just as important, the NPV was 84%, meaning that if the PFW angle is <220°, PB >40% and thus a suboptimal stent-landing zone in 84% of the cases. This high negative predictive value will largely prevent stenting too far into a healthy vessel region (PB <40%).

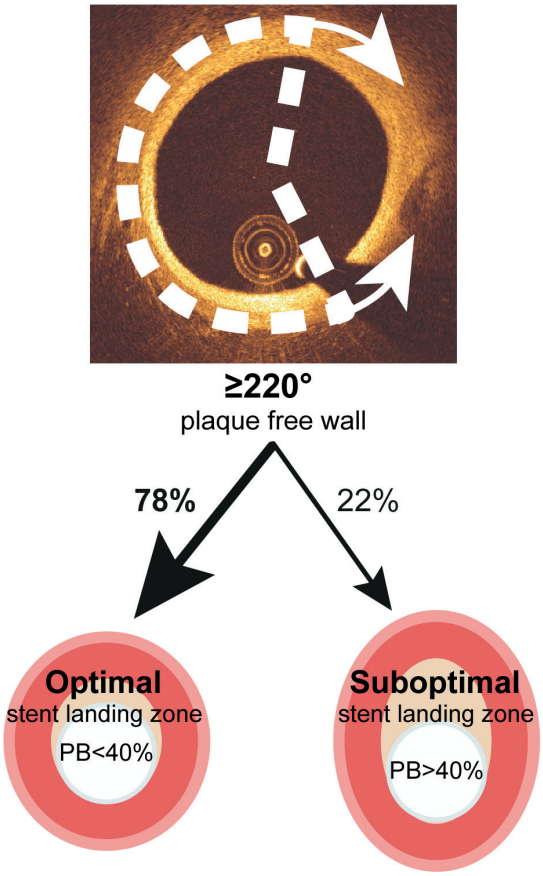

Figure 8.3: Clinical application of PFW_{OCT} angle detection. When a PFW_{OCT} of ≥220° is detected, in 78% of the cases this indicates the presence of a PB<40%, forming an optimal stent landing zone.

As an angle of 220 degrees might be difficult to judge by simple eyeballing in the cathlab, we investigated the predictive value of a PFW >180 degrees for PB <40%. Despite the strong relationship between PFW_{OCT} and PB_{IVUS}, regions with a PFW angle >180° can be

regarded as an optimal stent landing zone with a PB <40% in only 57% of the cases. So, in 43% of the cases, the disease is more severe with a PB >40%, even with only half of the circumference being occupied by plaque.

Reproducibility

Inter-observer agreement analyses of the PFW measurements were performed in 189 OCT and 177 IVUS frames and showed high intraclass correlation coefficients of respectively 0.956 (95% CI: 0.941 - 0.967) and 0.912 (95% CI: 0.884 – 0.934). The intraclass correlation coefficient of the PB_{IVUS} measurements was equally high at 0.886 (95% CI: 0.847 – 0.915).

DISCUSSION

This study shows for the first time that PFW_{OCT} can be considered as a surrogate marker for PB, which is currently a common criterion to determine stent-landing zone. In regions with a PFW angle >186^{o}, the PFW_{OCT} has the same predictive value compared to PFW_{IVUS}. The optimized cut-off value to predict optimal stent landing zone (PB<40%) is ≥220^{o} PFW_{OCT}.

There is a precarious balance between adequate lesion coverage and using too long stents. When the edge of the stent lands in a plaque area, it poses a risk on plaque disruption and edge dissections on a short-term and in-stent restenosis on a long-term[406]. On the other hand, placing longer stents might prove technically more challenging and might increase the risk on in-stent restenosis and stent thrombosis, even in drug eluting stents[407–409]. For this reason, determining an optimal stent-landing zone is critical for the prevention of future stent-related adverse events.

An optimal stent-landing zone is a region without lipids and a PB <40%. In contrast to IVUS, OCT is capable of detecting lipids, but the limited penetration depth hampers PB measurements. OCT can however reliably detect the healthy vessel wall. Therefore, we aimed to investigate if the presence of a normal wall is helpful to predict PB by OCT. This study showed that a measurement of the PFW angle provides a reliable estimate of the PB, without the need to fully visualize the outer wall of the vessel. Together with the fact that OCT is one of the most reliable techniques to structurally assess the presence of a lipid rich plaque, determining the stent-landing zone by OCT becomes even more feasible[410,411].

The detection of the PFW in OCT can be influenced by the composition of the intima. Plaque components like a lipid/necrotic core and sites of inflammatory activity cause

high attenuation and may obscure the vessel wall layers, even in a relatively thin intima. Plaque-free regions (IMT<0.5mm) with a superficial layer of macrophages or foam cells (intimal xanthoma) can appear as regions with plaque, since the healthy 3-layered structure of the vessel is not visible. This leads to underestimation of the PFW angle and thus overestimation of the plaque burden. The confounding effect of vessel wall composition may explain why the association between PFW_{OCT} and PB almost vanishes in the more diseased sections. We observe a similar trend in the relation between PFW_{IVUS} and PB, although the detection of the PFW by IVUS is usually not affected by attenuation-inducing plaque components. This might indicate a possible biological phenomenon. In the initial stages of plaque growth, the asymmetric plaque growth results in a simultaneously decreasing PFW angle and increasing PB. Apparently in later stages, the plaque growth becomes more symmetrical, decreasing the PFW angle with only a limited increase in PB and thus weakening the relationship. This explanation should be supported by serial imaging studies.

PCI procedures are always guided by angiography to determine catheter position and lumen narrowing. Currently, it is challenging to identify segments seen on OCT with the corresponding location on angiography which could lead to wrong sizing and positioning of the stent. The recently introduced on-line co-registration of OCT and angiography[412] could greatly increase the utility of OCT and thereby the application of our findings in the clinical work flow. The most predictive cut-off angle of 220° PFW is hard to determine by eye. This might limit direct clinical application of our findings. New software for the automatic detection of the three wall layers and the determination of the PFW angle is under development in our university.

LIMITATIONS

Some limitations in our study should be taken into account. Despite the use of side branches for optimal matching of OCT and IVUS pullbacks, errors in matching can occur due to intrinsic differences between the two techniques. These include, amongst others, pull back speed, lateral resolution and frame rate. To minimize the impact of these mismatches on the accuracy of the results, the measurements were averaged over a region of 3mm, which is a larger than the maximum expected longitudinal mismatch.

Only a limited number of matched pullbacks were available for analysis. Since we analysed the IVUS images per cross-section and not longitudinally, we regarded the 7 data points per pull-back as separate observations. However, these results should still be interpreted as being a proof-of-principle study. We do not expect that our conclusion would be much different with a larger dataset.

CONCLUSION

In conclusion, this study shows that PFW_{OCT} is a good predictor for the PB in the regions with a PFW angle >186° and gives more insight in the general interpretation of PFW_{OCT} angles. After further clinical validation, this new plaque burden estimation based on OCT could help to identify the optimal landing zone.

CHAPTER 9

Colocalization of intracoronary lipid-rich plaques and calcifications – an integrated NIRS-IVUS analysis

Eline M.J. Hartman
Ayla Hoogendoorn
Ali C. Akyildiz
Anne-Sophie Schuurman
Antonius F.W. van der Steen
Eric Boersma
Jolanda J. Wentzel
Joost Daemen

Based on:

'Colocalization of intracoronary lipid-rich plaques and calcifications – an integrated NIRS-IVUS analysis', *under review at JACC: Cardiovascular Imaging*

ABSTRACT

Background

While the presence of lipid pools in coronary plaques is known as a risk factor for plaque rupture and future events, local calcification of the plaque affects mechanical plaque stability. Little is known about the colocalization of calcium and lipid pools in these plaques. The aim of the present study was to assess to what degree lipid pools and calcifications colocalize in patients with coronary artery disease (CAD) using a combined catheter with near-infrared spectroscopy and intravascular ultrasound (NIRS-IVUS).

Methods

Non-culprit coronary arteries were imaged using NIRS-IVUS and analysed at a level of one frame per millimetre. For each of these frames, the presence of calcium and lipids was assessed and analysed for every degree in circumference. The lipid core burden index (LCBI) and an IVUS-derived calcium score were calculated. Data from the two plaque components were subsequently combined to assess the colocalization at 3 levels: vessel, 4 mm segment and frame.

Results

A total of 154 vessels from 139 patients (9811 frames) from the IBIS-3 study were analysed. At vessel level, the correlation between LCBI and the IVUS-derived calcium score was weak. For the 4 mm segment analysis, LCBI scores were subdivided into 3 different groups: lipid-free (LCBI 0), low-lipid (LCBI 1-250) and high-lipid (LCBI >250). The calcium score differed significantly between these groups, where segments with a high LCBI also had a high calcium score. At frame level, in calcified frames, NIRS-positive frames (LCBI>0) had a significantly larger calcium angle (median 71°; IQR:42-100) than NIRS-negative frames (median 46°; IQR:25-75) ($p < 0.001$).

Conclusions

Both the segment and frame-level analyses showed that high LCBI scores coincided with high calcium scores, implying frequent colocalization of potentially stabilizing calcification and destabilizing lipid pools in atherosclerotic coronary arteries.

INTRODUCTION

Atherosclerosis is the underlying disease of multiple leading causes of morbidity and mortality worldwide[20]. More specifically, several morphometric plaque features showed to substantially increase the risk of future cardiovascular events. The presence of lipids inside the plaque has been strongly associated with plaque vulnerability and destabilization[31]. When detected by near-infrared spectroscopy (NIRS) and quantified as a lipid core burden index (LCBI), local plaque-lipid showed to be a predictor of major adverse cardiovascular events in patients with coronary artery disease[40,322,413,414].

A second plaque component that has been linked to outcome is calcium. The multi-slice computed tomography (MSCT) coronary calcium score proved effective in the prediction of future cardiac events[415]. Conversely, at a local level, the role of calcium in plaque stability is more complex. While calcium by itself adds to the total atherosclerotic burden and is a characteristic of advanced disease, depending on its size and location within the plaque, calcium might also have a plaque stabilizing effect[416,417].

At present, little is known about the prevalence of colocalization of calcifications and lipid-rich plaques (LRP), and whether this colocalization assessment can improve future risk prediction. Intravascular ultrasound (IVUS) enables reliable detection of plaque size and has a high sensitivity to detect coronary calcification[418]. The aim of this study was to investigate the incidence of the co-localization of a positive NIRS signal and the presence of calcium in coronary arteries of coronary artery disease (CAD) patients, by using the near-infrared spectroscopy – intravascular ultrasound (NIRS-IVUS) catheter.

METHODS

All patients from the prospective IBIS3 study of whom a combined NIRS-IVUS (TVC, InfraRedx, Burlington, Massachusetts, USA) pullback was available were included. The design of the IBIS3 study has been described in great detail elsewhere[414]. In brief, IBIS3 was a prospective investigator-initiated, single-centre study in which NIRS-IVUS assessment of a proximal segment of a non-culprit coronary artery was performed to evaluate the effect of rosuvastatin on necrotic core volume in patients with stable or acute coronary syndrome (ACS). NIRS-IVUS imaging was performed in non-culprit vessels using a motorized pullback at a speed of 0.5 mm/sec. The study was performed in accordance with the declaration of Helsinki. All patients provided written informed consent for their participation in the study.

Image analysis for lipid and calcium

For every millimetre of each NIRS-IVUS pullback, one cross-sectional frame was analysed. Regions that were previously stented were excluded from the analysis. Frames with non-uniform rotational distortion (NURD) imaging artefacts were excluded from the analysis to avoid matching errors between the IVUS and NIRS signal[419]. Calcium in the acquired imaging data was defined as a high intensity signal (bright on the image) with a low intensity region (dark shadow) behind it[35]. The minimal measurable and validated calcium angle on IVUS was set at 15°[418]. Calcium angles were manually indicated using QCU-CMS software (version 4.69, Leiden University Medical Centre, LKEB, Division of Image Processing, Leiden) by two independent expert reviewers (E.H. and A.H.), blinded to the NIRS signal during analysis. The protractor originated in the centre of the catheter to analyse the calcification from the same angle as the NIRS detection. An interobserver analysis between the two readers was performed on a subset of 10 arteries using Cohen's Kappa statistics. Values above 0,8 were considered as good agreement.

The NIRS data was analysed based on the color-coded ring that is projected around the IVUS image in each frame. The 128-color scale from red to yellow represent the probability of the presence of lipids, with red as the lowest and yellow as the highest probability. With in-house developed software (MATLAB, v. 2017b, Mathworks Inc., Natick, MA, USA) the probability of the NIRS signal for lipid content was assessed for each 1° in circumference as a continuous number on the NIRS-IVUS image. Every degree with a lipid probability > 0.6 was scored as NIRS positive[38].

For the integrative analyses, 2D maps for the presence and location of both calcium and a positive NIRS signal were generated (Figure 9.1). The latter is comparable to the NIRS-

data display known as the chemogram[38]. By comparing the 2D maps, the colocalization of NIRS signal and calcium was assessed at vessel, 4 mm segment and frame level.

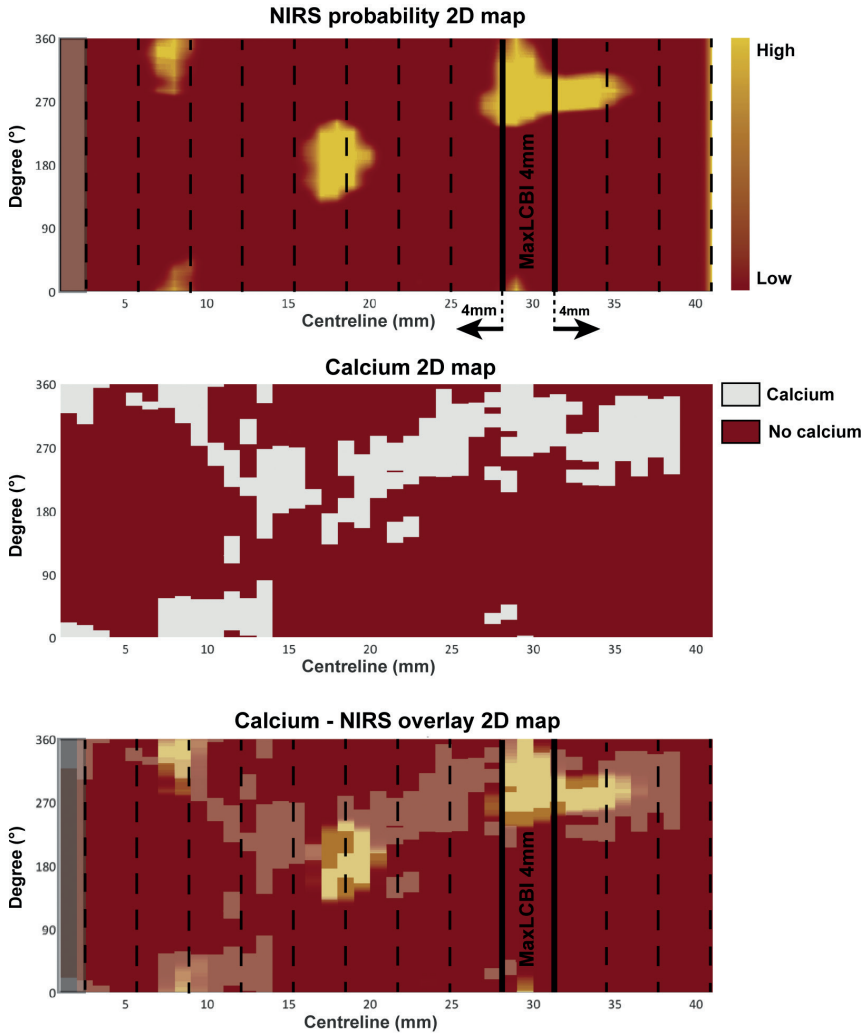

Figure 9.1: 2D maps of NIRS, calcium and overlap. 2D maps of coronary vessel as if the vessel is cut open along the longitudinal axis. The X-axis is the longitudinal length of the pullback with a sample size of 1 frame every millimetre. The Y-axis the circumference of the vessel. **A)** 2D maps with the NIRS probability (chemogram). Red is low probability, yellow is high probability. MaxLCBI4mm is indicated between continues lines. From this Max LCBI4mm region, the vessel is divided in 4mm segments (dashed lines) in proximal and distal direction (as indicated by the arrows). **B)** 2D map with the presence of calcium. White is calcified, red is non calcified. **C)** Overlay of calcium 2D map (A) and NIRS 2D map (B).

Lipid core burden index (LCBI) (area positive for NIRS signal / total area*1000) was determined for the whole vessel. By using a sliding window of 4 mm, the LCBI was calculated for all different 4 mm segments in the vessel (LCBI4: (4 mm LCBI)/total area*1000)[40,413,420]. Furthermore, the MaxLCBI4mm was defined as the 4mm with the highest LCBI within a pullback. From the location of the MaxLCBI4mm, the artery was both proximally and distally divided in consecutive segments of 4 mm. The residual proximal and distal segments smaller than 4 mm were discarded (Figure 9.1). A similar methodology was used to calculate the IVUS-based calcium score (area calcium positive/ total area*1000) for vessel and the before-defined 4 mm segments. Consequently, every segment with an LCBI score had a corresponding calcium score. Previously, 4 mm segments with LCBI scores higher than 250 and 400 were considered as high-risk plaques. Therefore, a subsequent analysis was performed using these cut-off values to select low and high-risk plaques[41,421]. For this analysis, LCBI scores were subdivided into 3 different groups: lipid-free (LCBI 0), low-lipid (LCBI 1-250/400) and high-lipid (LCBI >250/400).

At a frame level, each frame was individually scored with a calcium score and a LCBI score (0-1000). In a separate frame level analysis, the calcifications were subdivided based on their size. Calcifications covering less than 90 degrees (score<250) of the circumferences of the frame were classified as 'spotty'. Calcifications covering over 90 degrees (score>250) were labelled as 'large calcifications'[422].

Statistical analysis

Normality of the distribution of continuous data was tested with the Kolmogorov-Smirnov test. For normally distributed continuous variables, mean and standard deviations (mean ± SD) were calculated. For non-normally-distributed continuous variables, median and inter quartile range (IQR) were calculated. Categorical variables were reported as frequencies (%). The non-normally distributed continuous variables were tested with a Kruskal Wallis or Mann Whitney U-test. Categorical variables were tested with a Chi-Square test. Spearmans' rho correlation was used for testing the correlation of continuous non-normally distributed variables.

All tests were 2-tailed and a p value <0.05 was considered significant. SPSS statistics version 21 for Windows (IBM Corp, Armonk, New York) was used for statistical analysis.

RESULTS

A total of 154 vessels from 139 patients (9811 frames) were analysed with a mean pullback length per artery of 63±19 mm. Baseline characteristics are presented in Table

9.1. The mean age of the patients was 61±10 years and 81% of the patients were men. ACS was the presenting symptom in 40% of the patients and a PCI was performed in 88.2% of the patients. The distribution of the analysed coronary vessels was LAD 43%, LCX 31% and RCA 27%. For the inter observer analysis, both observers segmented the calcium angle in a subset of 810 IVUS frames derived from multiple different pullbacks. The analysis demonstrated a good agreement between the observers, with an average interclass correlation coefficient of 0.957 (95%CI: 0.944-0.968).

Table 9.1: Baseline characteristics

Clinical characteristics	**N = 139 patients**
Age, years	60.9 ± 9.3
Men, n (%)	112 (80.6)
Diabetes Mellitus, n (%)	29 (20.9)
Hypertension, n (%)	95 (68.3)
Dyslipidaemia, n (%)	86 (61.9)
Current smoking, n (%)	34 (24.5)
Positive family history, n (%)	67 (48.2)
Previous myocardial infarction, n (%)	40 (28.8)
Previous percutaneous coronary intervention, n (%)	50 (36.0)
Previous coronary artery bypass graft, n (%)	1 (0.7)
Previous cerebrovascular accident, n (%)	13 (9.4)
History of peripheral artery disease, n (%)	14 (10.1)
History of renal impairment, n (%)	9 (6.5)
History of heart failure, n (%)	0 (0.0)
Procedural characteristics	
Indication for coronary angiography	
Acute MI, n (%)	15 (10.8)
Unstable angina, n (%)	41 (29.5)
Stable angina, n (%)	83 (59.7)
PCI performed, n (%)	121 (87.1)
Coronary artery disease	
No significant stenosis, n (%)	7 (5.0)
1-vessel disease, n (%)	74 (53.2)
2-vessel disease, n (%)	48 (34.5)
3-vessel disease, n (%)	10 (7.2)
Invasive Imaging characteristics	
Imaged study vessel	

Table 9.1: Continued

Left anterior descending, n (%)	66(42.8)
Left circumflex, n (%)	47(30.5)
Right coronary artery, n (%)	41(26.7)
Average pullback length, mm (SD)	63±19
Total LCBI vessel (IQR)	23(6-44)
Total Ca score vessel (IQR)	30(7-63)
MaxLCBI4mm (IQR)	246(92-345)
MaxCa4mm (IQR)	181(60-265)

SD: standard deviation; LCBI: lipid core burden index; IQR: inter-quartile range.

Vessel-level analysis

A number of vessels in this study was not affected by atherosclerosis, no presence of calcium or NIRS detectable lipids, which caused a skewed distribution of calcium and LCBI scores. This resulted in a total vessel calcium score ranging from 0 to 309 with a median value of 30 (IQR: 7-63). The total vessel LCBI ranged from 0 to 175 with a median of 23 (IQR: 6-44). The median MaxLCBI4mm was 246 (IQR:92-345). The correlation of the absolute LCBI and calcium score at vessel-level was weak (Spearman's ρ=0.215, p=0.007).

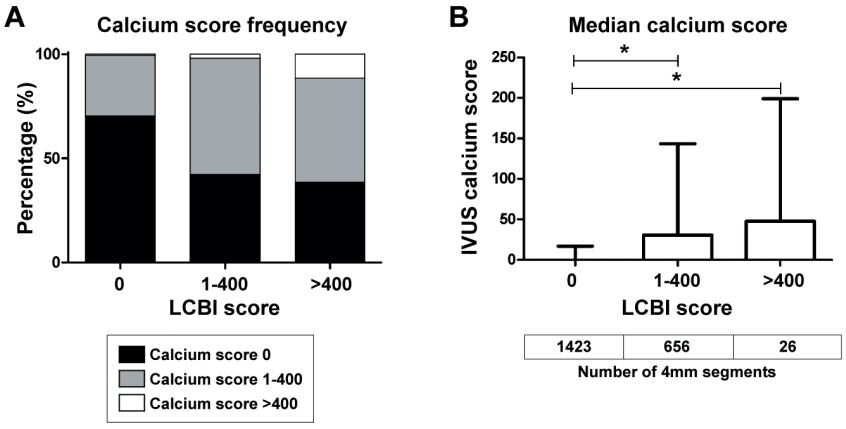

Figure 9.2: Frequency and median calcium score in subgroups with 400 LCBI cut-of-value. A) Frequency of calcium score subgroups of all 4 mm segments divided in subgroups categorized based on an LCBI cut-of-value of 400. **B)** The median (IQR) calcium score of all the 4 mm segments in the LCBI400 score subgroups. *p<0.05.

4mm segment level analysis

The direct correlation between the size of the calcium4mm score and the LCBI4mm score was weak (Spearman's ρ=0.317; p<0.001). When only taking the segments with

calcification into account, the median calcium score in segments with a positive LCBI score (116; IQR: 51-215) was higher than the one in segments with an LCBI score of 0 (60 IQR: 28-125) (p<0.001).

Using an LCBI of 400 as threshold, of all analysed 4-mm-segments (n=2107), 26 (1.2%) segments demonstrated a high LCBI score (>400) and 658 (31%) segments presented with an LCBI between 1-400. The calcium score of segments with a LCBI>400 (48; IQR:0-196) was not significantly different from the calcium score of segments with a LCBI 1-400 (30; IQR:0-144) (p=0.48). However, compared to the segments with an LCBI of 0 (calcium score median: 0; IQR:0-17), both groups (LCBI >400 and LCBI 1-400) showed a higher calcium score (p<0.001) (Figure 9.2).

When using an LCBI of 250 as a threshold, the median calcium score of all groups (LCBI 0, LCBI 1-250, LCBI >250) differed significantly, showing that regions with a higher LCBI also demonstrate a higher calcium score (Figure 9.3).

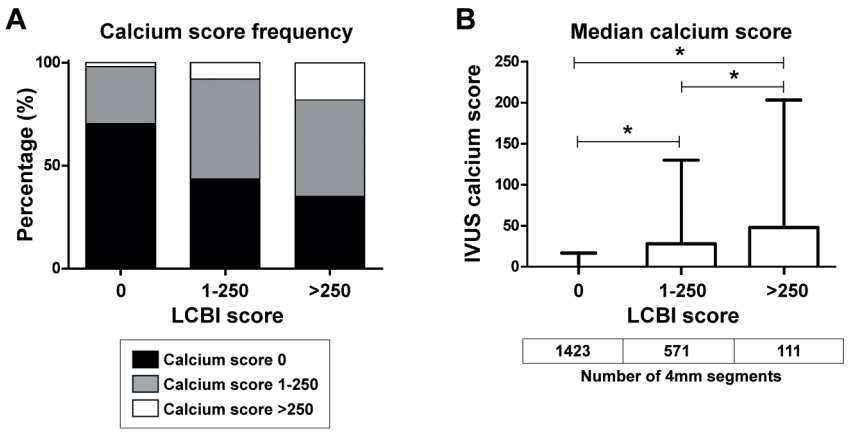

Figure 9.3: Frequency and median calcium score in subgroups with 250 LCBI cut-of-value. A Frequency of calcium score subgroups of all 4 mm segments divided in subgroups categorized based on an LCBI cut-of-value of 250. **B)** The median (IQR) calcium score of all the 4 mm segments of the LCBI250 score subgroups. *p<0.05.

Frame-level analysis

Calcifications and a NIRS positive signal were present in 25.2% and 21.7% of the frames respectively. A total of 9.3% of all frames showed both a NIRS positive signal and calcifications.

In frames with a positive NIRS signal, the median frame LCBI score was 164 (IQR: 83-269). The median calcium score in frames with calcification was 150 (IQR: 81-242). In

the calcified NIRS positive frames, the calcium angle was significantly larger (197; IQR: 117-278) than the one in the calcified NIRS negative frames (128; IQR: 69-208) (p <0.001).

Of the calcified NIRS positive frames, 33% presented with large calcifications and 77% with spotty calcifications while of calcified NIRS negative frames, 16% of the frames had large calcifications and 84% spotty calcifications(p<0.001).

DISCUSSION

To the best of our knowledge, this study describes for the first time the colocalization of lipids and calcium in atherosclerotic coronary arteries using NIRS-IVUS. We were able to demonstrate a significant correlation between the presence of lipids and calcium with significantly higher calcium scores in segments and frames with a higher LCBI.

Colocalization of lipids and calcifications in NIRS- IVUS.

The calcification process in atherosclerotic plaques is driven by inflammation[423]. Multiple histological studies showed that calcifications are often present around inflamed regions with lipid-rich necrotic cores[20,416]. The colocalization of calcification and a positive NIRS signal could confirm an advanced plaque phenotype.

In this study of non-culprit vessels, we found a large range in both the calcium and LCBI scores, as well as in colocalization. However, segments with an LCBI score>250 demonstrated higher calcium scores than segments with LCBI scores <250. The discrepancies that were found in colocalization of the two plaque components could be explained by both a biological and a technical phenomenon. From a biological perspective, it could be that the NIRS-positive segments with calcification are in a different stage of atherosclerosis as compared to NIRS-positive segments without calcification. The occurrence of segments with extensive calcifications but no positive NIRS signal may be explained by the development of calcifications in necrotic cores[424], whereby calcifications replace the lipid rich content and reducing the positive NIRS signal.

From a more technical perspective, NIRS uses near-infrared light with the capability to penetrate through calcium[38]. The technique, as validated by Garner et al. in 2008 was optimized to detect lipid-core plaque and is optimized for plaques that are classified as fibro-atheroma and are larger than 60°, more than 200 µm thick and with a mean fibrous cap thinner than 450 µm[38]. This definition corresponds to an LCBI score of 167 in a single frame. The smallest detectable calcium angle in IVUS is 15 degrees[418], which corresponds to a calcium score of 24 (15°/360° *1000) in a single frame. The large

number of 4mm segments (423) with a low calcium score (1-125) and absence of lipids (low LCVI score), could partially be explained by the fact that the atherosclerotic plaques in these frames did not meet the minimal detection criteria of NIRS and could thus not be detected by the NIRS catheter.

Influence of calcification on image analysis

A number of NIRS studies focused on the correlation between plaque burden and plaque characteristics[425,426]. They showed that combining NIRS and plaque burden improves the detectability of a fibro-atheroma. Plaque burden calculation (plaque area/ vessel area *100%) requires an accurate assessment of vessel area. However, in case of large calcifications, acoustic shadowing hampers plaque burden measurement[35]. In the present study 43% of the NIRS positive frames was partially or completely calcified, hence no analysis on plaque burden was performed.

Risk prediction based on plaque composition

Both CT-derived coronary artery calcification score (CAC) and the LCBI have shown to be significant predictors of advanced stages of coronary atherosclerosis and future adverse events[40,415]. However, distinguishing the rupture-prone “vulnerable” plaque from the stable plaque has proven to be complex. The impact of calcium on plaque stability is widely debated. Larger and denser calcifications, that can be detected using (invasive) imaging, may have a mechanically stabilizing effect on the plaque[427].

With regard to the clinical implication of calcifications, Beckman et al.[427] showed in an IVUS study that the total amount of calcium is higher in culprit lesions of stable angina pectoris (SAP) patients than in patients with ACS. Also, the total arc of the calcification is significant higher in SAP lesions, confirming that IVUS-detectable calcium could be indicative for a more stable coronary atherosclerotic plaque[428].

Pu et al.[422] showed that in NIRS-detected LRPs, spotty calcifications were more prevalent than extensive calcifications. This is in accordance with the results of our current study, in which we found overall more spotty (<90°) calcification than large calcification(>90°). Besides, we found that NIRS-positive calcified frames had larger calcification angles than the NIRS negative calcified frames. Combining the size of the calcification and a high LCBI score can potentially improve the detection of the vulnerable plaque.

LIMITATIONS

We opted to only use a subpopulation of the IBIS-3 study in which the combined catheter was used instead of two separate catheters to avoid any matching errors between individual IVUS and NIRS acquisitions. In this sub-group of this single centre retrospective study in non-culprit coronary arteries, only 11 imaged vessel related events were observed after 4 years. Future studies with larger patient cohorts that register clinical outcome data at a coronary segment level are needed to establish the added value of the presence and size of calcifications in NIRS positive plaques as a predictor for plaque vulnerability. As a future perspective for clinical practice, when determining treatment strategy of NIRS-positive vessels, one has to be aware of the frequent colocalization with calcium deposits and their potential role in plaque stability. This type of extended image interpretation might further improve the detection of the vulnerable plaques as well as improve risk-assessment for the patient.

CONCLUSION

Both on a 4mm segment, and frame level, LCBI scores >250 coincided with a higher IVUS detected calcium score which indicates frequent colocalization of calcium and lipid-rich plaques in atherosclerotic coronary arteries. Future outcome studies have to provide more insights into the added predictive value of the coincidence of calcifications on top of NIRS detected lipid rich plaques.

CHAPTER 10

Summary, Discussion and Future perspectives

SUMMARY

Coronary artery disease is predicted to remain the leading cause of death and disability in the world. One of the main pathologies underlying coronary artery disease is coronary atherosclerosis. Growth and rupture of a (vulnerable) coronary atherosclerotic plaque can, gradually or acute, lead to blockage of blood-supply to the cardiac muscle. When this blockage is not adequately and timely resolved, the ensuing permanent damage to the heart muscle (i.e. a myocardial infarction) can result in heart-failure or death. Despite years of research, the exact mechanism by which atherosclerotic plaques develop, destabilize and eventually rupture remains incompletely understood. To promote drug development, to enable (early) risk-prediction for the individual patient, and to improve clinical decision making upon treatment of an acute coronary event, more in-depth knowledge on atherosclerotic disease pathophysiology is needed. In this thesis, (intravascular) imaging, pathobiology and biomechanical modelling as introduced in **Chapter 1** were combined to 1) describe new and existing animal models for atherosclerosis and discuss the role biomechanics play in plaque development in these models; 2) further elucidate the involvement of the biomechanical factors wall shear stress and helical flow in the development of coronary atherosclerotic plaques, and to assess the potential of these biomechanical factors and of specific lipoproteins as new biomarkers for atherosclerotic disease development; 3) extend the interpretation of imaging data derived from two commonly used invasive imaging techniques to improve plaque and patient risk-stratification.

Animal models of atherosclerosis

Research to the pathophysiology of coronary atherosclerosis in humans is challenging. First of all, it takes years to observe significant changes in plaque size and structure. Furthermore, it is not possible to perform extensive, serial invasive imaging experiments, and to collect tissue samples to determine the plaque composition at a cellular level. In contrast, in animal models, disease progression is often faster and it is possible to perform extensive invasive imaging and tissue collection. Therefore, animal models that mimic human coronary artery disease are highly valuable. In **Part I** of this thesis, existing animal models of atherosclerosis were described (**Chapter 2 and 3**) and we discussed the role of biomechanics in the plaque development and destabilization observed in these models.

In **Chapter 2**, a literature overview was given of animal models that present with atherosclerotic plaque rupture. The occurrence of plaque rupture in an animal model of atherosclerosis is often seen as the ultimate proof of the presence of human-like vulnerable plaques. However, we concluded that plaque rupture in the described models

is never observed as a natural event, but only occurs upon severe pharmacological and/or surgical interventions. The fact that we have to resort to active interventions to induce plaque rupture can be explained by distinct differences between humans and most animal models in plaque composition, biological processes and biomechanical factors. These differences directly influence plaque development and rupture. Taking these differences into account, of all described animal models, the atherosclerotic pig model most closely mimics the human plaque biomechanical environment and plaque morphology. However, even in the currently available pig models, there is still a lack of vulnerable and natural plaque rupture observations.

Chapter 3 provided an overview of studies in which surgical manipulation of the blood flow, and thus of wall shear stress, was used to promote the development of advanced atherosclerosis in animal models. Wall shear stress is the frictional force that arises between the flowing blood and the endothelial cells of the vascular wall and is an important factor in atherogenesis. The reviewed studies applied surgical interventions like the construction of an arteriovenous fistula, implantation of vascular grafts, arterial ligations and implantation of perivascular devices to manipulate the shear stress and thereby induce atherosclerosis formation. Many of the described surgical interventions proofed successful in inducing atherosclerosis. However, we warned that these surgical interventions can affect the vessel wall integrity and wall strain, which can in turn influence the investigated association between wall shear stress and atherosclerotic plaque development. The tandem-ligation mouse model was the model in which, compared to the other described models, the investigated disease process was least effected by the used surgical technique. Besides, this model presented with relatively large and complex plaques, yielding this model highly useful for future studies.

Biomarkers of atherosclerosis

In **Part II** of this thesis, the role of wall shear stress, of helical flow and of specific lipoproteins in atherosclerotic disease was investigated. Besides, we assessed whether these factors could also function as biomarkers to improve coronary atherosclerosis risk-assessment. The potential of these biomarkers was assessed both in an atherosclerotic pig model, as well as in human patient cohorts.

From Chapter 2 and 3 we concluded that an animal model that optimally mimics human atherosclerosis, with similar plaque size, composition and biomechanics, did not exist. Therefore, we refined an existing homozygous familial hypercholesterolemic pig model of atherosclerosis by using only adult animals. This adult age improved the capacity of the model to develop more human-like disease. In **Chapter 4** we used multimodality, serial invasive imaging to monitor the coronary plaque growth over time,

and performed histopathological analyses to assess plaque composition in high detail. We observed that half of the pigs allowed for assessment of early plaque development while the other half developed advanced coronary atherosclerotic plaques. In the latter group of pigs, widespread development of large, lumen encroaching plaques with extensive vulnerable features could be observed, a rare feature in comparison to other pig models of coronary artery disease. To uncover a possible cause for the large differences in disease severity observed between both groups of pigs, we performed an extensive lipoprotein analysis. Using sequential density and size-separation of low-density lipoprotein (LDL) in addition to mass spectrometry sphingolipid analyses, we discovered a distinct LDL-profile with 'regular' and 'larger' LDL. In this distinct LDL-profile, the distribution of cholesterol and sphingolipids over both LDL subclasses was directly related to the eventual atherosclerotic disease severity in the pigs. As a first proof-of-concept for clinical application of this finding, we performed the same lipoprotein analysis in the plasma of three homozygous familial hypercholesterolemia patients and discovered a highly comparable LDL-profile with a varying cholesterol distribution. Whether this profile can also be used for patient risk assessment remains to be elucidated.

As described in Chapter 3, biomechanical factors, like wall shear stress, are involved in atherosclerotic plaque development. The role of wall shear stress is however complex, since both low and high wall shear stress have been associated with plaque size and composition changes. Furthermore, many studies do not take into account that the direction of the wall shear stress changes over the cardiac cycle. Therefore, we investigated the role of (multidirectional) wall shear stress in coronary plaque development (**Chapter 5**) using the atherosclerotic adult porcine model described in Chapter 4. The results of this study demonstrate that the highest plaque growth rate was found in regions with low time-averaged wall shear stress or high multidirectional wall shear stress, both during plaque initiation as well as during plaque progression. When assessing wall shear stress changes over time, regions with initial low wall shear stress that that turned into regions of high wall shear stress presented with the largest overall plaque growth. For multidirectional wall shear stress, the largest plaque growth was observed in regions with initial high and subsequently low multidirectionality. Both observations are probably the result of the intrusion of plaque into the lumen which results in lumen narrowing and subsequent changes in wall shear stress levels. Interestingly, in these same regions, upon elevation of wall shear stress or reduction of multidirectional wall shear stress, further plaque growth was reduced in the subsequent period. Besides these observations, we assessed the potential predictive value of the five different walls shear stress metrics for the development of high-risk plaques. Most (multidirectional) wall shear stress metrics were good predictors for subsequent plaque

growth, but even better predicted the development of advanced fibrous cap atheroma plaques. Of the assessed metrics, the time-averaged wall shear stress resulted in the highest positive predictive values. Taken together, the results of this study demonstrated that although multidirectional wall shear stress is significantly involved in coronary plaque initiation and progression, low time-averaged wall shear stress remains the strongest predictor for vulnerable disease development.

In **Chapter 6** a study was described that assessed whether the relation between wall shear stress and plaque development, as observed in the porcine model in Chapter 5, would also hold in patients with coronary artery disease. In acute coronary syndrome patients, wall shear stress and changes in plaque size and composition were monitored using multimodality imaging in a non-culprit artery at baseline, and after one year follow-up. The results showed that plaque progression in humans could best be predicted when combining (multidirectional) wall shear stress information with imaging data on the plaque lipid composition. These findings can potentially contribute to clinical-decision making during intervention procedures in order to prevent future cardiac events.

Multiple imaging studies demonstrated that blood often flows in helical patterns through the arterial system. However, the occurrence of helical flow and the possible relation of helical flow with atherosclerosis development in the coronary arteries had so far not been investigated. In the study described in **Chapter 7** we showed that blood flow in the coronary arteries of our porcine model described in Chapter 4 is characterized by counter-rotating bi-helical flow structures. Helical flow descriptors strongly and inversely correlated with (multidirectional) wall shear stress metrics suggesting an atheroprotective effect of helicity. The significant inverse relation between (near-wall) helical flow intensity and plaque development confirmed this hypothesis. This study showed, for the first time, a direct link between helical flow and protection against atherosclerosis formation.

Invasive imaging markers of atherosclerosis

In **Part III** of this thesis, two studies were described in which we investigated two invasive-imaging derived plaque features: the plaque free wall angle and the local presence of calcifications. More knowledge on these features could help to improve the interpretation of invasive imaging of atherosclerosis whereby the clinical application of single-modality imaging of coronary atherosclerotic plaques can be extended.

Optical coherence tomography (OCT) has emerged as imaging technique for guiding percutaneous coronary interventions. While OCT offers very high-resolution imaging of the vessel wall and has the ability to detect lipids, this comes at a cost of limited

penetration depth. Therefore, the ability of OCT to visualize the external elastic membrane, and thus assess the plaque burden in the presence of plaque, is hampered. This is unfortunate, since plaque burden is an important marker for plaque vulnerability and is also considered a leading criterion for determining the stent-placement location. In **Chapter 8** a study is described in which we assessed whether the plaque free wall angle measured on OCT could serve as a surrogate marker for plaque burden. For this purpose, matched OCT and intravascular ultrasound (IVUS) images of non-culprit arteries from acute coronary syndrome patients were used. With these data, we showed that the plaque-free wall angle on OCT strongly correlated with plaque burden detected on IVUS. Furthermore, we concluded that the cut-off value for an optimal stent-placement zone is an OCT-derived plaque-free wall angle of ≥220°.

Besides plaque burden, also plaque composition is an important factor to consider for patient risk-stratification. Both heavily calcified vessels (as detected by CT imaging) and lipid-rich plaques (detected by near-infrared spectroscopy (NIRS)) have been associated with an increased risk of cardiovascular events. Little was however known on the colocalization of both plaque components. In **Chapter 9**, a study was described in which NIRS-IVUS images of non-culprit arteries of acute-coronary syndrome patients were assessed for the presence of lipid-rich plaques and calcification. These data demonstrated that the absolute calcium and lipid-scores of individual vessels were weakly correlated. However, when local 4 mm segments or individual frames with the highest lipid content were assessed, these regions presented with higher levels of calcification than regions with low lipid-scores. These results imply frequent colocalization of potentially stabilizing calcifications and destabilizing lipid pools in atherosclerotic coronary arteries. Whether these findings can improve clinical decision making will have to be elucidated in a larger clinical study with outcome data.

In the following part of **Chapter 10**, all findings described in this thesis and their potential clinical application and future implications will be discussed.

DISCUSSION AND FUTURE PERSPECTIVES

This thesis aimed to contribute to the current body of evidence on atherosclerotic plaque pathophysiology and clinical cardiovascular risk-assessment. Several new techniques and methodologies were employed, ranging from the use of a new animal model to novel invasive imaging analysis techniques combined with biomechanical modelling approaches. Hereafter, the resulting observations will be discussed and placed in a clinical perspective. Furthermore, future implications are described.

Animal models for coronary artery disease: essential, but still a simplification of human pathophysiology

No animal model can fully mimic human atherosclerotic disease. However, animal models are widely used in atherosclerosis research, not only to study the disease pathophysiology, but also to test and validate new imaging techniques and (pharmaceutical) treatment strategies. Despite the fact that a major part of biomedical research involves animal models, clinical translation of the results derived from these animal models remains challenging. To improve this translational step, the main quest in experimental animal model research is to find the model that best resembles human disease. In **Chapter 2 and 3**, an overview was given of currently used animal models of atherosclerosis with regard to disease biomechanics and plaque rupture risk. In these chapters we concluded that, despite intense efforts to improve the human resemblance of disease development in these models, only a few animal models come close to developing complex, (rupture-prone) vulnerable plaques. This is not only due to inherent differences in the biomechanical environment (**Chapter 2 and 3**), but this is also related to differences in factors like metabolism, genetics, comorbidities, age and disease duration. Changing metabolism and genetics, and inducing comorbidities like diabetes and hypertension are methods that have been applied in many animal models to induce atherosclerosis formation[106,429,430]. A factor that is however often ignored, is the age of animals and thereby also the duration of disease development. Most of the animals used in atherosclerosis studies are very young, while in humans, advanced disease stages, and related complications, only become apparent upon an older age. One of the reasons for this might be that lipid profile, blood pressure, arterial mechanics (including stiffness) and inflammatory status are very different between adolescents and older people[276–278], while these are exactly the factors that have major impact on atherosclerotic disease development.

In **Chapter 2** we concluded that the pig, as a large animal model, best resembles natural human disease biomechanics and vulnerable plaque composition. However, pig models that present with vulnerable, rupturing plaques are still rare. Therefore, in **Chapter 4**, we refined a previously described, very promising porcine model (LDL-receptor mutation, non-inbred)[150] by using only adult animals since, as described above, age is a significant factor in atherosclerotic disease development. Extensive characterisation of coronary atherogenesis in this model revealed the development of advanced fibrous-cap atheroma plaques throughout the coronary arteries, a rare feature in comparison to other pig and animal models (as reviewed in **Chapter 4**). These advanced plaques render this model uniquely suitable to use in testing of new pharmaceutical or interventional therapies. However, advanced disease development was only observed in half of the animals, despite seemingly similar physiological and environmental conditions. This

again demonstrates the occurrence of individual variations in disease development and offers a unique opportunity to discover new genetic or metabolic factors involved in atherosclerosis development (as for example described in the second half of **Chapter 4**).

What characterises vulnerable disease and do we need animal models that perfectly mimic this disease stage?

Although our pig model was successful and presented with one of the most advanced plaque types described in literature, we still did not frequently observe the presence of thin-cap fibroatheroma, the most rupture-prone plaque type. Furthermore, although we witnessed the presence of thrombus material inside plaques at multiple locations, we could not provide hard evidence for the 'holy grail' in animal model research: the occurrence of natural plaque rupture. Considering all differences between humans and animal models, one might question whether we will ever be able to find a true human-disease mimicking animal model with natural 'vulnerable plaque' rupture. Two important questions to consider for a future search to new animals models are: 1) what exactly characterises human vulnerable atherosclerotic disease?; 2) do we actually need an animal model that perfectly mimics this vulnerable disease stage and presents with natural plaque rupture?

Regarding the first question, since the introduction of the term 'vulnerable plaque', identifying this specific plaque type has become the goal of many pre-clinical and clinical studies. Based on histological data, the vulnerable plaque has been named the precursor lesion of acute coronary thrombosis and is officially characterised by a large, lipid-rich necrotic core with an overlying thin fibrous cap <65µm[17]. However, as also posed by Arbab-Zadeh and Fuster[431], the presence of a vulnerable plaque cannot directly be related to acute events. The PROSPECT study already showed that despite frequent occurrence of vulnerable plaques (detected by invasive imaging) in a population, the risk of myocardial infarction, or death related to those plaques, was very low[31]. One of the reasons for this observation might be that many plaque ruptures occur without clinical symptoms[432,433]. Arbab-Zadeh and Fuster[431] argue that we should look more for the vulnerable patient instead of for the vulnerable plaque. Herein, not only local plaque composition should be considered, but also factors that surround the plaque and influence its natural history, like plasma lipid levels, blood pressure, local stresses and strains, etc.. To find better animal models for atherosclerotic disease, we might have to consider, include and/or modify these factors.

The second question in animal model research is: do we actually need an animal model that perfectly mimics human disease and presents with natural plaque rupture? The most straight-forward answer is: this depends on the research question. For studies

of individual genes, proteins or biomechanical stimuli involved in atherogenesis, small animal models, like mice, are most often used. Although these models do not reflect the full human disease complexity, their small size, fast breeding and the fact that it is relatively easy to perform genetic manipulations, makes small animal models very suitable for the study of specific factors in a specific stage of atherosclerosis. Furthermore, the controlled environment of these models makes them ideally suitable for the first tests of new pharmaceutics. When studying specific events, like plaque initiation or rupture, in both small and large animal models, one could also argue that more severe surgical or pharmaceutical interventions (as described in **Chapter 2 and 3**) are allowed as long as you induce your 'target disease-stage'. However, using these methods, one should always keep in mind that findings derived from these studies may not represent the full complexity of human disease.

The closer research gets to clinical application, the more we have to consider increasing the complexity of the employed animal model. For example, for testing new imaging modalities for the identification of different plaque components, animal models that develop more advanced plaques and that are large enough to undergo invasive imaging, will remain extremely valuable. Years of research in large animal models has brought us closer to achieving this goal. However, as mentioned, coronary plaques, even in the best pig models, including our own, do not reach the most advanced vulnerable plaque stages observed in humans.

Future perspectives on animal models for atherosclerosis

Considering the above statements, for future studies in small atherosclerotic animal models we should maybe abandon the search for 'vulnerable' plaques and focus on a specific part of the atherosclerosis pathophysiology that can be mimicked in in these models. For large animal models, further improvement of the resemblance of human disease is much more relevant. Probably the best way to improve existing pig models is by either incorporating more risk factors that represent the human metabolic syndrome, or by simply elongating the follow-up time of the studies. The latter is highly challenging since long study times are costly and inherently time-consuming. To enable long (multiple years) study duration, we should consider to invest in improvement of our large animal model infrastructure. This could comprise setting up dedicated, large, and maybe even internationally coordinated or shared animal research facilities. These facilities would breed, feed and monitor the animals for longer periods of time until atherosclerotic disease has progressed to more clinically relevant stages, after which the animals can be transported to the individual research facilities. This approach would not only save research funds, but it will also improve the consistency in the models and thereby improve translation of the derived results to the clinic.

Biomarkers for atherosclerosis: the potential of wall shear stress and circulating lipoproteins

Since the introduction of percutaneous coronary interventions, the treatment of stenotic or ruptured atherosclerotic plaques, and thus the survival rate and quality of life of cardiovascular patients has improved dramatically[434,435]. However, despite the success of percutaneous coronary intervention procedures, coronary atherosclerosis and a subsequent myocardial infarction remain the leading cause of heart failure[436], and the overall post-myocardial infarction mortality remains high[437]. Therefore, new methods that achieve early identification of high-risk patients may improve prevention of adverse clinical events[438]. Reliable, early prediction of events is however only possible when we improve our understanding of the complex environment in which atherosclerotic plaques develop. In **Chapter 5-7** of this thesis we showed that multidirectional wall shear stress and helical flow play a role in coronary atherosclerosis development. Furthermore, we pointed out the potential of both multidirectional wall shear stress (**Chapter 5-7)** and circulating lipoproteins (**Chapter 4)** as biomarkers for (advanced) atherosclerosis development. Hereafter, these results, and ways to use these data to improve patient risk-assessment, will be discussed.

Improving cardiovascular risk prediction in familial hypercholesterolemia patients by low-density lipoprotein profiling

Improving cardiovascular risk assessment in familial hypercholesterolemia (FH) patients is vital. Since current risk-prediction methods are not sufficient, all diagnosed FH patients are uniformly treated with statins or other lipid-lowering drugs[439]. There are however also patients with a very low risk who might not need this (high-intensity) lipid-lowering treatment[439] which is associated with side-effects like muscle symptoms, or more infrequently, with complete intolerance[440].

The extensive evaluation of atherosclerosis development in the pig model of familial hypercholesterolemia (FH) (**Chapter 4**), revealed a striking difference between pigs sensitive for atherosclerosis development and pigs that were protected. This difference was independent of age, weight, diet, cholesterol levels and inflammatory status. We discovered that the distribution of cholesterol and sphingolipids over two distinct low-density lipoprotein (LDL) subtypes could be used to discriminate the advanced-diseased from the mildly-diseased pigs. Strikingly, statin-treated homozygous FH patients presented with a similar LDL profile. The pronounced differences observed in the cholesterol profile between patients hint to a similar relation with disease severity as seen in our pig study. Future studies will have to shed light on the potential clinical application of this finding.

Future perspectives: LDL profiling as a new biomarker for cardiovascular risk prediction in FH?

These very first results show the high potential of this specific LDL profile as a novel early biomarker for cardiovascular disease prediction in individual familial hypercholesterolemia patients. A larger and longitudinal study in both homozygous FH and heterozygous FH patients that monitors plaque growth or event rate is necessary to further investigate the relation with disease development and the predictive value of this biomarker in a clinical setting. Furthermore, the effect of different mutations and medication use on this specific profile has to be elucidated. Besides the potential of this LDL-profile as a risk-indicator, in-depth analysis of the composition and biological function of the 'larger' and 'regular' LDL subclasses could provide new targets for pharmaceutical intervention.

Wall shear stress and helical flow in atherosclerosis: merely pathophysiological factors or potent biomarkers?

In **Chapter 5-7** we showed that low and multidirectional wall shear stress, as well as low levels of helical flow, could be linked to subsequent atherosclerotic plaque initiation as well as to plaque progression. Besides, in regions of plaque growth, elevation of wall shear stress levels due to lumen intrusion of the plaque appeared to slow down further plaque progression. These observations indicate a mechanistic relation between the investigated haemodynamic factors and plaque initiation and progression. Whether these (changes in) haemodynamic factors can also function as potent risk predictors or biomarkers in a clinical setting remains subject of an active debate.

In **Chapter 5 and 6** we showed that (multidirectional) WSS metrics as individual factors predicted general plaque development with a predictive value between 43% (in ACS patients) and 50% (atherosclerotic pigs). In the pig study, the development of an advanced fibrous cap atheroma could be predicted with an accuracy up to 61% using these individual metrics. Interestingly, despite the much faster plaque growth in the pigs, and the use of statins and the presence of a more advanced disease stage in the patients, the predictive values of WSS for plaque progression were not far apart. In contrast to our hypothesis, the added value of the multidirectional WSS metrics 'oscillatory shear index' and 'cross-flow index' on top of time-averaged WSS only slightly improved the predictive values for plaque development (from 50% to 53% and 52% respectively, unpublished data from our pig study).

Several recent studies combined information on WSS levels with data on circulating biomarkers like lipid levels, or with local plaque characteristics like plaque size and plaque composition to improve the predictive values of the individual WSS metrics.

It is well established that circulating LDL-cholesterol levels are a strong and independent predictor for atherosclerosis development and event risk[441]. Therefore, when assessing the independent effect of WSS and atherosclerosis, correction for cholesterol levels, as we did in **Chapter 5**, could be considered. Besides the role of cholesterol as confounder, we also aimed to investigated whether cholesterol levels would have a synergistic effect in combination with WSS on atherosclerosis development, as was shown before by Koskinas et al.[67] in a pig model. In our patient study, we observed a more pronounced effect of WSS in the presence of higher cholesterol levels, compared to subjects with lower cholesterol, although the differences did not reach statistical significance. This non-significant difference might be caused by the low number of subjects, but it can also be the result of the on average low cholesterol levels due to statin use.

Besides plasma cholesterol levels, also plaque size and plaque composition together with WSS, have been linked to plaque progression, regression and/or destabilization in several clinical studies[69,71,315]. The PREDICTION trial reported an improved predictive value for clinically relevant luminal obstruction treated with PCI from 25% to 41% when plaque burden was added to data on low WSS[69]. Shishikura et al.[315] showed that also the combination of WSS and plaque composition influences disease progression. They concluded that in low WSS regions with lipid-rich plaques (detected by NIRS), the lipid-content regressed, while in high WSS regions, either lipid-rich plaques developed or remained present. In **Chapter 6** we report progression of plaque size in low WSS regions and plaque regression when high WSS was present. The colocalization with NIRS-detected lipid-rich plaques augmented this relation. These findings indicate a synergistic effect between WSS and the lipid composition of the plaque (probably as a general indicator of plaque stability) on subsequent plaque growth. Combining our results with those of Shishikura et al.[315] we could conclude that in regions where low WSS colocalizes with lipid-rich plaques, plaques become larger while lipid-content reduces. In high WSS regions, the opposite occurs with a decrease in plaque size and an increase in lipid content, indicating a more unstable plaque phenotype. These findings were confirmed by VH-IVUS studies of Corban et al.[71] and Samady et al.[442] who observe plaque destabilization (smaller plaques but an increase in virtual-histology-IVUS detected necrotic core content) in regions with high WSS. Besides a synergistic effect of NIRS-detected lipid-rich plaques and WSS on plaque development, we also showed that the predictive values for plaque progression slightly improved when combining NIRS-information and WSS, compared to (multidirectional) WSS alone (from 43% to 48%).

Although predicting plaque growth or vulnerable plaque presence is valuable, the prediction of cardiovascular events should be the ultimate goal. This is especially true since, as mentioned, only a small percentage of vulnerable atherosclerotic plaques result in an acute coronary event[431]. Two clinical studies investigated the predictive

value of WSS for event rate. Interestingly, the results of both studies are in stark contrast to each other. In a sub-study of the PROSPECT, Stone et al.[70] describe a strong association between low WSS and MACE in ACS patients. When they add plaque burden, minimal lumen area and/or the presence of a TCFA to WSS information, the prognostic risk for MACE within 3.4 years follow-up was 52.1%. In contrast, Kumar et al.[72] concluded that high WSS at the proximal side of the lesion was predictive for myocardial infarction occurrence within 3 years in stable coronary artery disease patients with haemodynamically significant lesions. Furthermore, they describe that high WSS had incremental prognostic value over fractional flow reserve measurement. The fact that Kumar et al.[72] assessed vessel-related myocardial infarction in stable patients and Stone et al.[70] assessed general MACE in non-culprit arteries of ACS patients, could partially explain the contrasting results. Furthermore, Stone et al.[70] specifically selected, per patient, the plaque with the lowest WSS, while Kumar et al. assessed the average WSS around every lesion. This difference could also contribute to the contrasting findings. These results again stress that using WSS for clinical risk prediction is not very straight forward and the analysis methodology should be carefully considered.

In **Chapter 7** we showed for the first time that the haemodynamics in the coronary arteries is governed by helical flow patterns and that higher near-wall helical flow intensity suppressed atherosclerotic plaque development. The presence of helical flow in the arterial system has been explained as a phenomenon that optimizes fluid transport, but also minimizes low or multidirectional wall shear stress. This latter hypothesis was confirmed by our results where we showed a strong, inverse relation between helical flow descriptors and shear stress. Helical flow is a phenomenon occurring in the total volume of the artery[78], and the helical flow intensity near the wall, that could be sensed by endothelial cells, is often very low (as observed in Chapter 7). Despite these very small helicity intensity numbers near the wall, the direct relation between near-wall helical flow intensity and plaque development was clearly significant. Whether helical flow could form a surrogate marker for wall shear stress remains to be elucidated.

A last important note to make when comparing all studies on wall shear stress and helicity is that every study uses different computation techniques and different boundary conditions. Since absolute wall shear stress levels are highly dependent on these factors, these absolute values should be interpreted with care[443]. Furthermore, vast ranges of cut-off values for 'low' and 'high' wall shear stress have been described, hampering direct comparison of the results between studies. Some say that wall shear stress has standard absolute ranges to be physiological or pathological. However, in the era of 'personalized medicine' one could also argue that it is more the deviation from a personal 'normal' value that triggers pathological conditions. Since wall shear stress cannot be measured directly, the only way to get closer to solving this debate is

by standardization of the way in which wall shear stress is calculated, and by comparing personalized thresholds to standard thresholds within one study.

Future perspectives: towards clinical application of shear stress and helical flow
Elucidating the relation between WSS metrics, helical flow and plaque development has been, and will remain, essential for our understanding of the pathophysiology of atherosclerotic disease and for finding possible pharmaceutical targets. In this thesis we showed that besides low WSS, also multidirectional WSS is involved in atherosclerosis development. Low time-averaged WSS however remained the best predictor for plaque growth and for development of plaques with a vulnerable composition. Besides WSS, also helical flow showed to act as an atheroprotective factor in the coronary arteries. Larger pre-clinical and clinical studies are necessary to determine the potential additive effect of these hemodynamic metrics for patient risk-assessment.

The direct application of hemodynamic parameters in clinical decision making is however challenging. As described above, general predictive values of WSS for plaque progression and destabilization are relatively low in all clinical studies. The proposed combination of WSS with other geometric values, like plaque burden and plaque composition, will have the highest chance to serve as a predictive clinical tool. However, the current labour-intensive methods and long computational times still needed for WSS calculation complicate direct, on-line assistance during invasive procedures. Furthermore, the most reliable hemodynamic data are currently derived from invasive techniques. Although helical flow can be visualized and quantified directly by non-invasive imaging techniques in larger arteries like the aorta and carotids[354,444] without the time-consuming computational techniques needed for WSS calculations, this direct visualization is not possible in the coronaries due to the limited resolution of the currently available imaging techniques. Improving non-invasive imaging and physiological measurements (e.g. CT or MRI), together with improvement of computational power, will bring WSS and helical flow as biomarkers closer to application in clinical decision making.

Invasive imaging of coronary atherosclerosis: expanding the application of single-modality imaging

Not only the understanding of the complex environment in which an atherosclerotic plaque develops is important, also assessment of the change in plaque composition can improve risk-assessment and choice of treatment strategy. In **Part III** of this thesis we investigated two plaque features derived from invasive imaging that could help to interpret, and thereby extend, the application of single-modality invasive imaging. In **Chapter 8** we concluded that the plaque-free wall angle on an OCT image is a good

surrogate marker for plaque burden, an important plaque feature that cannot be derived from OCT in the case of large or lipid-rich plaques. OCT is currently the best clinically-used imaging technique to assess plaque vulnerability because of its high resolution[445]. Our finding can further extend the use of OCT imaging for the assessment of plaque stability and general patient risk-assessment during OCT-guided stenting procedures, without having to resort to an IVUS imaging catheter. However, accurate visual assessment of plaque free wall angles is difficult. Therefore, automated software to detect the plaque free wall angle, as developed by Zahnd et al.[446], may pave the road for clinical application of this finding.

In **Chapter 9** we demonstrated, by using the combined NIRS-IVUS catheter, that calcifications are often colocalized with NIRS-detected lipid-rich regions, but only at a local level. The total-vessel calcium score, as imaged by computed tomography, has been associated with a greater risk of cardiovascular events[447]. However, whether calcifications are just a marker of advanced disease or whether these are also directly involved in plaque destabilization or rupture at a local level is still subject of active debate[417,448]. The LRP study[41,421] showed an increased risk of MACE with increasing NIRS-detected plaque lipid-content. Although we showed that calcifications were present in these NIRS-detected higher-risk lesions, the biological effect and predictive value of the presence of these local calcifications remain to be elucidated. Automated IVUS-based calcium detection software, that is currently under development[449,450], will contribute to quicker and easier assessment of the local calcium content in a clinical setting.

Future perspectives: from single- to multimodality imaging

In **Chapter 8 and 9** we attempted to extend the application of two commonly used invasive imaging techniques. However, so far, no single imaging technology has been capable of predicting whether a specific plaque will rupture and possibly trigger an acute myocardial infarction in the near future. Even by intelligent and more detailed interpretation of single-modality images as we propose in Chapter 8 and 9, one can only partially overcome the fact that different imaging technologies are only sensitive for specific plaque features[34]. Ideally, multiple different imaging modalities should be used to gain full insight into the complexity and thus vulnerability of a plaque. Using multiple different (invasive) imaging techniques in sequence is however costly, time-consuming, and increases patient burden. Therefore, integration of different structural and molecular imaging techniques into one catheter has been an important subject of research in the past years[268]. Besides the introduction of the NIRS-IVUS catheter, a vast range of bi- or tri-modal catheters are currently under development which include IVUS-OCT catheters[451], near-infrared autofluorescence-OCT[452], near-infrared fluorescence-OCT[453], near-infrared fluorescence-IVUS[454], near-infrared fluorescene-

OCT-IVUS[455], fluorescent lifetime imaging-IVUS[456] and photoacoustics-IVUS[457]. Most of these catheters have proven high potential as research tools, but translation into clinical practice remains a challenging and slow process. Further development of automated image interpretation software that gives the clinician a binary outcome or a probability scale, could support clinical application.

Final conclusions and considerations: a multidisciplinary approach in cardiovascular risk prediction

This thesis in itself already exhibits the multidisciplinary nature of atherosclerosis research. We demonstrated the importance and value of considering both biomechanical and biological factors involved in atherogenesis when using and/or improving animal models for atherosclerosis. Furthermore, we reported that, although imperfect as individual biomarkers, a distinct LDL profile, multidirectional wall shear stress, helicity descriptors and new invasive-imaging metrics could all contribute to improving atherosclerosis-related patient risk-assessment.

There is already a large abundance of scoring systems that are designed to predict the cardiovascular event risk of individuals within the general population[458,459]. Most models, including the widely used Framingham risk score, are based on common predictors like age, blood pressure, smoking and cholesterol levels. There are also many other risk-scores that add life-style factors, plasma markers or imaging data. This wide variety of risk scores, which are unfortunately often not well validated[459], reflects the complex nature of atherosclerotic disease. To better capture this complex nature in a risk score, we have to strive for a more multidisciplinary approach. Instead of a continuous search for new atherosclerotic disease risk-predictors, we should invest in combining and validating all known biomarkers from different fields of research into one scoring system. This multidisciplinary approach will be our best chance to truly improve the risk-assessment for the individual patient.

REFERENCES

1. Roth, G. A. *et al.* Global, Regional, and National Burden of Cardiovascular Diseases for 10 Causes, 1990 to 2015. *J. Am. Coll. Cardiol.* **70**, 1–25 (2017).
2. Leal, J., Luengo-Fernández, R., Gray, A., Petersen, S. & Rayner, M. Economic burden of cardiovascular diseases in the enlarged European Union. *Eur. Heart J.* **27**, 1610–1619 (2006).
3. Anderson, J. L. & Morrow, D. A. Acute Myocardial Infarction. *N. Engl. J. Med.* **376**, 2053–2064 (2017).
4. Harshman, M. Time to take coronary health to heart. *The Columbian* (2012). Available at: http://www.columbian.com/news/2012/feb/13/time-to-take-coronary-health-to-heart/. (Accessed: 16th November 2018)
5. Fishbein, G. A. & Fishbein, M. C. *Arteriosclerosis Rethinking the Current Classification*. *Arch Pathol Lab Med* **133**, (2009).
6. Schwartz, C. J. & Mitchell, J. R. The morphology, terminology and pathogenesis of arterial plaques. *Postgrad. Med. J.* **38**, 25–34 (1962).
7. Rabson, S. M. Arteriosclerosis: Definitions. *Am. J. Clin. Pathol.* **24**, 472–473 (1954).
8. Hadi, H. A. R., Carr, C. S. & Al Suwaidi, J. Endothelial dysfunction: cardiovascular risk factors, therapy, and outcome. *Vasc. Health Risk Manag.* **1**, 183–98 (2005).
9. Davies, P. F. Hemodynamic shear stress and the endothelium in cardiovascular pathophysiology. *Nat. Clin. Pract. Cardiovasc. Med.* **6**, 16–26 (2009).
10. Deanfield, J. E., Halcox, J. P. & Rabelink, T. J. Endothelial Function and Dysfunction. *Circulation* **115**, 1285–1295 (2007).
11. Lusis, A. J. Atherosclerosis. *Nature* **407**, 233–241 (2000).
12. Glagov, S., Weisenberg, E., Zarins, C. K., Stankunavicius, R. & Kolettis, G. J. Compensatory Enlargement of Human Atherosclerotic Coronary Arteries. *N. Engl. J. Med.* **22**, 1371–1375 (1987).
13. Parma, L., Baganha, F., Quax, P. H. A. & de Vries, M. R. Plaque angiogenesis and intraplaque hemorrhage in atherosclerosis. *Eur. J. Pharmacol.* **816**, 107–115 (2017).
14. Van Hinsbergh, V. W. M., Eringa, E. C. & Daemen, M. J. A. P. Neovascularization of the atherosclerotic plaque: interplay between atherosclerotic lesion, adventitia-derived microvessels and perivascular fat. *Curr. Opin. Lipidol.* **26**, 405–11 (2015).
15. Kolodgie, F. D. *et al.* Intraplaque hemorrhage and progression of coronary atheroma. *N. Engl. J. Med.* **349**, 2316–25 (2003).
16. Newby, A. C. Metalloproteinases and vulnerable atherosclerotic plaques. *Trends Cardiovasc. Med.* **17**, 253–8 (2007).

17. Virmani, R., Burke, A. P., Farb, A. & Kolodgie, F. D. Pathology of the vulnerable plaque. *J. Am. Coll. Cardiol.* **47**, C13-8 (2006).

18. Stary, H. C. *et al.* A definition of initial, fatty streak, and intermediate lesions of atherosclerosis. A report from the Committee on Vascular Lesions of the Council on Arteriosclerosis, American Heart Association. *Circulation* **89**, 2462–2478 (1994).

19. Stary, H. C. *et al.* A definition of advanced types of atherosclerotic lesions and a histological classification of atherosclerosis. A report from the Committee on Vascular Lesions of the Council on Arteriosclerosis, American Heart Association. *Circulation* **92**, 1355–74 (1995).

20. Virmani, R., Kolodgie, F. D., Burke, A. P., Farb, A. & Schwartz, S. M. Lessons From Sudden Coronary Death : A Comprehensive Morphological Classification Scheme for Atherosclerotic Lesions. *Arterioscler. Thromb. Vasc. Biol.* **20**, 1262–1275 (2000).

21. Bentzon, J. F., Otsuka, F., Virmani, R. & Falk, E. Mechanisms of Plaque Formation and Rupture. *Circ. Res.* **114**, 1852–1866 (2014).

22. Malinow, M. R. Atherosclerosis: Progression, regression, and resolution. *Am. Heart J.* **108**, 1523–1537 (1984).

23. Brunzell, J. D., Chait, A. & Bierman, E. L. Pathophysiology of lipoprotein transport. *Metabolism* **27**, 1109–1127 (1978).

24. Goldstein, J. L. & Brown, M. S. A Century of Cholesterol and Coronaries: From Plaques to Genes to Statins. *Cell* **161**, 161–172 (2015).

25. Goldstein, L. J. & Brown, S. M. The Low-Density Lipoprotein Pathway and its Relation to Atherosclerosis. *Annu. Rev. Biochem.* **46**, 897–930 (1977).

26. Ference, B. A. *et al.* Low-density lipoproteins cause atherosclerotic cardiovascular disease. 1. Evidence from genetic, epidemiologic, and clinical studies. A consensus statement from the European Atherosclerosis Society Consensus Panel. *Eur. Heart J.* **38**, 2459–2472 (2017).

27. Blum, C. B. *et al.* 2013 ACC/AHA Guideline on the Treatment of Blood Cholesterol to Reduce Atherosclerotic Cardiovascular Risk in Adults. *Am. Hear. Assoc. Task Force Pract. Guidel. Circ.* **129**, 1–45 (2014).

28. Willeit, P. *et al.* Discrimination and Net Reclassification of Cardiovascular Risk With Lipoprotein(a). *J. Am. Coll. Cardiol.* **64**, 851–860 (2014).

29. Kannel, W. B. Range of serum cholesterol values in the population developing coronary artery disease. *Am. J. Cardiol.* **76**, 69C-77C (1995).

30. Krauss, R. M. & Burke, D. J. Identification of multiple subclasses of plasma low density lipoproteins in normal humans. *J. Lipid Res.* **23**, 97–104 (1982).

31. Stone, G. W. *et al.* A prospective natural-history study of coronary atherosclerosis. *N. Engl. J. Med.* **364**, 226–35 (2011).

32. Newby, D. E. Triggering of acute myocardial infarction: beyond the vulnerable plaque. *Heart* **96**, 1247–1251 (2010).

33. Mann, J. M. & Davies, M. J. Vulnerable plaque. Relation of characteristics to degree of stenosis in human coronary arteries. *Circulation* **94**, 928–31 (1996).

34. van Soest, G., Marcu, L., Bouma, B. E. & Regar, E. Intravascular imaging for characterization of coronary atherosclerosis. *Curr. Opin. Biomed. Eng.* **3**, 1–12 (2017).

35. Mintz, G. S. Intravascular Imaging of Coronary Calcification and Its Clinical Implications. *JACC Cardiovasc. Imaging* **8**, 461–471 (2015).

36. Nair, A. *et al.* Coronary plaque classification with intravascular ultrasound radiofrequency data analysis. *Circulation* **106**, 2200–6 (2002).

37. Nissen, S. E. IVUS Virtual Histology: Unvalidated Gimmick or Useful Technique? *J. Am. Coll. Cardiol.* **67**, 1784–1785 (2016).

38. Gardner, C. M. *et al.* Detection of Lipid Core Coronary Plaques in Autopsy Specimens With a Novel Catheter-Based Near-Infrared Spectroscopy System. *JACC Cardiovasc. Imaging* **1**, 638–648 (2008).

39. Waxman, S. *et al.* In Vivo Validation of a Catheter-Based Near-Infrared Spectroscopy System for Detection of Lipid Core Coronary Plaques: Initial Results of the SPECTACL Study. *JACC Cardiovasc. Imaging* **2**, 858–868 (2009).

40. Schuurman, A.-S. *et al.* Near-infrared spectroscopy-derived lipid core burden index predicts adverse cardiovascular outcome in patients with coronary artery disease during long-term follow-up. *Eur. Heart J.* **39**, 295–302 (2018).

41. Waksman, R. *et al.* The Lipid-Rich Plaque Study of vulnerable plaques and vulnerable patients: Study design and rationale. *Am. Heart J.* **192**, 98–104 (2017).

42. Tearney, G. J. *et al.* Consensus standards for acquisition, measurement, and reporting of intravascular optical coherence tomography studies: a report from the International Working Group for Intravascular Optical Coherence Tomography Standardization and Validation. *J. Am. Coll. Cardiol.* **59**, 1058–72 (2012).

43. DeBakey, M. E., Lawrie, G. M. & Glaeser, D. H. Patterns of atherosclerosis and their surgical significance. *Ann. Surg.* **201**, 115–31 (1985).

44. Caro, C. G., Fitz-Gerald, J. M. & Schroter, R. C. Arterial wall shear and distribution of early atheroma in man. *Nature* **223**, 1159–60 (1969).

45. Malek, A. M., Alper, S. L. & Izumo, S. Hemodynamic Shear Stress and Its Role in Atherosclerosis. *JAMA* **282**, 2035 (1999).

46. Wentzel, J. J. *et al.* Endothelial shear stress in the evolution of coronary atherosclerotic plaque and vascular remodelling: Current understanding and remaining questions. *Cardiovasc. Res.* **96**, 234–243 (2012).

47. Cunningham, K. S. & Gotlieb, A. I. The role of shear stress in the pathogenesis of atherosclerosis. *Lab. Invest.* **85**, 9–23 (2005).

48. Peiffer, V., Sherwin, S. J. & Weinberg, P. D. Does low and oscillatory wall shear stress correlate spatially with early atherosclerosis? A systematic review. *Cardiovasc. Res.* **99**, 242–50 (2013).

49. Rikhtegar, F. *et al.* Choosing the optimal wall shear parameter for the prediction of plaque location—A patient-specific computational study in human left coronary arteries. *Atherosclerosis* **221**, 432–437 (2012).

50. Peiffer, V., Sherwin, S. J. & Weinberg, P. D. Computation in the rabbit aorta of a new metric – the transverse wall shear stress – to quantify the multidirectional character of disturbed blood flow. *J. Biomech.* **46**, 2651–2658 (2013).

51. Mohamied, Y., Sherwin, S. J. & Weinberg, P. D. Understanding the fluid mechanics behind transverse wall shear stress. *J. Biomech.* **50**, 102–109 (2017).

52. Warboys, C. M., Amini, N., de Luca, A. & Evans, P. C. The role of blood flow in determining the sites of atherosclerotic plaques. *F1000 Med. Rep.* **3**, 5 (2011).

53. Stone, P. H. *et al.* Effect of endothelial shear stress on the progression of coronary artery disease, vascular remodeling, and in-stent restenosis in humans: in vivo 6-month follow-up study. *Circulation* **108**, 438–44 (2003).

54. Stone, P. H. *et al.* Regions of low endothelial shear stress are the sites where coronary plaque progresses and vascular remodelling occurs in humans: an in vivo serial study. *Eur. Heart J.* **28**, 705–710 (2007).

55. Chatzizisis, Y. S. & Giannoglou, G. D. Importance of local hemodynamic conditions in the atherosclerotic effect of increased heart rate. *J. Am. Coll. Cardiol.* **57**, 2206 (2011).

56. Koskinas, K. C. *et al.* Thin-capped atheromata with reduced collagen content in pigs develop in coronary arterial regions exposed to persistently low endothelial shear stress. *Arterioscler. Thromb. Vasc. Biol.* **33**, 1494–504 (2013).

57. Samady, H. *et al.* Coronary Artery Wall Shear Stress Is Associated With Progression and Transformation of Atherosclerotic Plaque and Arterial Remodeling in Patients With Coronary Artery Disease / Clinical Perspective. *Circulation* **124**, 779–788 (2011).

58. Eshtehardi, P. *et al.* Association of coronary wall shear stress with atherosclerotic plaque burden, composition, and distribution in patients with coronary artery disease. *J. Am. Heart Assoc.* **1**, e002543 (2012).

59. Slager, C. J. *et al.* True 3-dimensional reconstruction of coronary arteries in patients by fusion of angiography and IVUS (ANGUS) and its quantitative validation. *Circulation* **102**, 511–6 (2000).

60. van der Giessen, A. G. *et al.* 3D fusion of intravascular ultrasound and coronary computed tomography for in-vivo wall shear stress analysis: a feasibility study. *Int. J. Cardiovasc. Imaging* **26**, 781–96 (2010).

61. Vardhan, M. *et al.* The importance of side branches in modeling 3D hemodynamics from angiograms for patients with coronary artery disease. *Sci. Rep.* **9**, 8854 (2019).

62. Gijsen, F. J. H. *et al.* 3D reconstruction techniques of human coronary bifurcations for shear stress computations. *J. Biomech.* **47**, 39–43 (2014).

63. Doucette, J. W. *et al.* Validation of a Doppler guide wire for intravascular measurement of coronary artery flow velocity. *Circulation* **85**, 1899–911 (1992).

64. Wellnhofer, E., Finke, W., Bernard, L., Dänschel, W. & Fleck, E. Improved assessment of intravascular Doppler coronary flow velocity profile. *Int. J. Card. Imaging* **13**, 25–34 (1997).

65. Davies, P. F., Civelek, M., Fang, Y. & Fleming, I. The atherosusceptible endothelium: endothelial phenotypes in complex haemodynamic shear stress regions in vivo. *Cardiovasc. Res.* **99**, 315–327 (2013).

66. Chatzizisis, Y. S. *et al.* Prediction of the localization of high-risk coronary atherosclerotic plaques on the basis of low endothelial shear stress-an intravascular ultrasound and histopathology natural history study. *Circulation* **117**, 993–1002 (2008).

67. Koskinas, K. C. *et al.* Synergistic effect of local endothelial shear stress and systemic hypercholesterolemia on coronary atherosclerotic plaque progression and composition in pigs. *Int. J. Cardiol.* **169**, 394–401 (2013).

68. Koskinas, K. C. *et al.* The role of low endothelial shear stress in the conversion of atherosclerotic lesions from stable to unstable plaque. *Curr. Opin. Cardiol.* **24**, 580–590 (2009).

69. Stone, P. H. *et al.* Prediction of progression of coronary artery disease and clinical outcomes using vascular profiling of endothelial shear stress and arterial plaque characteristics: the PREDICTION Study. *Circulation* **126**, 172–81 (2012).

70. Stone, P. H. *et al.* Role of Low Endothelial Shear Stress and Plaque Characteristics in the Prediction of Nonculprit Major Adverse Cardiac Events: The PROSPECT Study. *JACC Cardiovasc. Imaging* **11**, 462–471 (2018).

71. Corban, M. T. *et al.* Combination of plaque burden, wall shear stress, and plaque phenotype has incremental value for prediction of coronary atherosclerotic plaque progression and vulnerability. *Atherosclerosis* **232**, 271–276 (2014).

72. Kumar, A. *et al.* High Coronary Shear Stress in Patients With Coronary Artery Disease Predicts Myocardial Infarction. *J. Am. Coll. Cardiol.* **72**, 1926–1935 (2018).

73. Wentzel, J. J. *et al.* In vivo 3D distribution of lipid-core plaque in human coronary artery as assessed by fusion of near infrared spectroscopy-intravascular ultrasound and multislice computed tomography scan. *Circ. Cardiovasc. Imaging* **3**, e6-7 (2010).

74. Slager, C. J. *et al.* The role of shear stress in the destabilization of vulnerable plaques and related therapeutic implications. *Nat. Clin. Pract. Cardiovasc. Med.* **2**, 456–64 (2005).

75. Pedrigi, R. M. *et al.* Inducing Persistent Flow Disturbances Accelerates Atherogenesis and Promotes Thin Cap Fibroatheroma Development in D374Y-PCSK9 Hypercholesterolemic Minipigs. *Circulation* **132**, 1003–12 (2015).

76. Mohamied, Y. *et al.* Change of Direction in the Biomechanics of Atherosclerosis. *Ann. Biomed. Eng.* **43**, 16–25 (2015).

77. Timmins, L. H. *et al.* Oscillatory wall shear stress is a dominant flow characteristic affecting lesion progression patterns and plaque vulnerability in patients with coronary artery disease. *J. R. Soc. Interface* **14**, (2017).

78. Liu, X., Sun, A., Fan, Y. & Deng, X. Physiological significance of helical flow in the arterial system and its potential clinical applications. *Ann. Biomed. Eng.* **43**, 3–15 (2015).

79. Gallo, D., Steinman, D. A., Bijari, P. B. & Morbiducci, U. Helical flow in carotid bifurcation as surrogate marker of exposure to disturbed shear. *J. Biomech.* **45**, 2398–404 (2012).

80. Liu, X., Fan, Y. & Deng, X. Effect of spiral flow on the transport of oxygen in the aorta: a numerical study. *Ann. Biomed. Eng.* **38**, 917–26 (2010).

81. Jia, H. *et al.* In vivo diagnosis of plaque erosion and calcified nodule in patients with acute coronary syndrome by intravascular optical coherence tomography. *J. Am. Coll. Cardiol.* **62**, 1748–58 (2013).

82. van der Wal, A. C., Becker, A. E., van der Loos, C. M. & Das, P. K. Site of intimal rupture or erosion of thrombosed coronary atherosclerotic plaques is characterized by an inflammatory process irrespective of the dominant plaque morphology. *Circulation* **89**, 36–44 (1994).

83. Farb, A. *et al.* Coronary plaque erosion without rupture into a lipid core. A frequent cause of coronary thrombosis in sudden coronary death. *Circulation* **93**, 1354–63 (1996).

84. Muller, J. E., Tofler, G. H. & Stone, P. H. Circadian variation and triggers of onset of acute cardiovascular disease. *Circulation* **79**, 733–43 (1989).

85. Libby, P. & Pasterkamp, G. Requiem for the 'vulnerable plaque'. *Eur. Heart J.* **36**, 2984–7 (2015).

86. Burke, A. P. *et al.* Coronary risk factors and plaque morphology in men with coronary disease who died suddenly. *N. Engl. J. Med.* **336**, 1276–82 (1997).

87. Davies, M. J. Stability and Instability: Two Faces of Coronary Atherosclerosis: The Paul Dudley White Lecture 1995. *Circulation* **94**, 2013–2020 (1996).

88. Falk, E., Shah, P. K. & Fuster, V. Coronary Plaque Disruption. *Circulation* **92**, 657–671 (1995).

89. Schaar, J. A. *et al.* Terminology for high-risk and vulnerable coronary artery plaques. Report of a meeting on the vulnerable plaque, June 17 and 18, 2003, Santorini, Greece. *Eur. Heart J.* **25**, 1077–82 (2004).

90. Hofman, A. *et al.* The Rotterdam Study: 2012 objectives and design update. *Eur. J. Epidemiol.* **26**, 657–86 (2011).

91. Stary, H. C. Natural History and Histological Classification of Atherosclerotic Lesions : An Update. *Arterioscler. Thromb. Vasc. Biol.* **20**, 1177–1178 (2000).

92. Libby, P. & Hansson, G. K. Inflammation and immunity in diseases of the arterial tree: players and layers. *Circ. Res.* **116**, 307–11 (2015).

93. Koskinas, K. C. *et al.* Natural history of experimental coronary atherosclerosis and vascular remodeling in relation to endothelial shear stress: A serial, in vivo intravascular ultrasound study. *Circulation* **121**, 2092–2101 (2010).

94. Kubo, T. *et al.* The Dynamic Nature of Coronary Artery Lesion Morphology Assessed by Serial Virtual Histology Intravascular Ultrasound Tissue Characterization. *J. Am. Coll. Cardiol.* **55**, 1590–1597 (2010).

95. Lendon, C. L., Davies, M. J., Born, G. V & Richardson, P. D. Atherosclerotic plaque caps are locally weakened when macrophages density is increased. *Atherosclerosis* **87**, 87–90 (1991).

96. Akyildiz, A. C. *et al.* Effects of intima stiffness and plaque morphology on peak cap stress. *Biomed. Eng. Online* **10**, 25 (2011).

97. Ohayon, J. *et al.* Necrotic core thickness and positive arterial remodeling index: emergent biomechanical factors for evaluating the risk of plaque rupture. *Am. J. Physiol. Heart Circ. Physiol.* **295**, H717-27 (2008).

98. Akyildiz, A. C. *et al.* The effects of plaque morphology and material properties on peak cap stress in human coronary arteries. *Comput. Methods Biomech. Biomed. Engin.* **19**, 771–9 (2015).

99. Akyildiz, A. C., Speelman, L. & Gijsen, F. J. H. Mechanical properties of human atherosclerotic intima tissue. *J. Biomech.* **47**, 773–83 (2014).

100. Walsh, M. T. *et al.* Uniaxial tensile testing approaches for characterisation of atherosclerotic plaques. *J. Biomech.* **47**, 793–804 (2014).

101. Holzapfel, G. A., Mulvihill, J. J., Cunnane, E. M. & Walsh, M. T. Computational approaches for analyzing the mechanics of atherosclerotic plaques: a review. *J. Biomech.* **47**, 859–69 (2014).

102. Cheng, G. C., Loree, H. M., Kamm, R. D., Fishbein, M. C. & Lee, R. T. Distribution of circumferential stress in ruptured and stable atherosclerotic lesions. A structural analysis with histopathological correlation. *Circulation* **87**, 1179–87 (1993).

103. Burleigh, M. C. *et al.* Collagen types I and III, collagen content, GAGs and mechanical strength of human atherosclerotic plaque caps: span-wise variations. *Atherosclerosis* **96**, 71–81 (1992).

104. Vengrenyuk, Y., Cardoso, L. & Weinbaum, S. Micro-CT based analysis of a new paradigm for vulnerable plaque rupture: cellular microcalcifications in fibrous caps. *Mol. Cell. Biomech.* **5**, 37–47 (2008).

105. Gijsen, F. J. H. *et al.* Carotid Plaque Morphological Classification Compared With Biomechanical Cap Stress: Implications for a Magnetic Resonance Imaging-Based Assessment. *Stroke.* **46**, 2124–8 (2015).

106. Getz, G. S. & Reardon, C. A. Animal models of atherosclerosis. *Arterioscler. Thromb. Vasc. Biol.* **32**, 1104–15 (2012).

107. Bentzon, J. F. & Falk, E. Atherosclerotic lesions in mouse and man: is it the same disease? *Curr. Opin. Lipidol.* **21**, 434–40 (2010).

108. Miller, N. E. Associations of high-density lipoprotein subclasses and apolipoproteins with ischemic heart disease and coronary atherosclerosis. *Am. Heart J.* **113**, 589–97 (1987).

109. Falk, E. Pathogenesis of atherosclerosis. *J. Am. Coll. Cardiol.* **47**, C7-12 (2006).

110. Jackson, C. L., Bennett, M. R., Biessen, E. A. L., Johnson, J. L. & Krams, R. Assessment of unstable atherosclerosis in mice. *Arterioscler. Thromb. Vasc. Biol.* **27**, 714–20 (2007).

111. Hansson, G. K. & Heistad, D. D. Two views on plaque rupture. *Arterioscler. Thromb. Vasc. Biol.* **27**, 697 (2007).

112. Schwartz, S. M., Galis, Z. S., Rosenfeld, M. E. & Falk, E. Plaque rupture in humans and mice. *Arterioscler. Thromb. Vasc. Biol.* **27**, 705–13 (2007).

113. Bond, A. R. & Jackson, C. L. The fat-fed apolipoprotein E knockout mouse brachiocephalic artery in the study of atherosclerotic plaque rupture. *J. Biomed. Biotechnol.* **ID 379069**, 10 pages (2011).

114. Falk, E., Schwartz, S. M., Galis, Z. S. & Rosenfeld, M. E. Putative murine models of plaque rupture. *Arterioscler. Thromb. Vasc. Biol.* **27**, 969–72 (2007).

115. Jackson, C. L. Defining and defending murine models of plaque rupture. *Arterioscler. Thromb. Vasc. Biol.* **27**, 973–7 (2007).

116. Riou, L. M. *et al.* Effects of mechanical properties and atherosclerotic artery size on biomechanical plaque disruption - Mouse vs. human. *J. Biomech.* **47**, 765–772 (2014).

117. Campbell, I. C. *et al.* Biomechanical modeling and morphology analysis indicates plaque rupture due to mechanical failure unlikely in atherosclerosis-prone mice. *Am. J. Physiol. Heart Circ. Physiol.* **304**, H473-86 (2013).

118. Hayenga, H. N., Trache, a., Trzeciakowski, J. & Humphrey, J. D. Regional atherosclerotic plaque properties in ApoE-/-mice quantified by atomic force, immunofluorescence, and light microscopy. *J. Vasc. Res.* **48**, 495–504 (2011).

119. Tracqui, P. *et al.* Mapping elasticity moduli of atherosclerotic plaque in situ via atomic force microscopy. *J. Struct. Biol.* **174**, 115–123 (2011).

120. Ohayon, J. *et al.* Is arterial wall-strain stiffening an additional process responsible for atherosclerosis in coronary bifurcations?: an in vivo study based on dynamic CT and MRI. *Am. J. Physiol. Heart Circ. Physiol.* **301**, H1097-106 (2011).

121. Cardoso, L., Kelly-Arnold, A., Maldonado, N., Laudier, D. & Weinbaum, S. Effect of tissue properties, shape and orientation of microcalcifications on vulnerable cap stability using different hyperelastic constitutive models. *J. Biomech.* **47**, 870–877 (2014).

122. von der Thüsen, J. H. *et al.* Induction of Atherosclerotic Plaque Rupture in Apolipoprotein E-/- Mice After Adenovirus-Mediated Transfer of p53. *Circulation* **105**, 2064–2070 (2002).

123. Gough, P. J., Gomez, I. G., Wille, P. T. & Raines, E. W. Macrophage expression of active MMP-9 induces acute plaque disruption in apoE-deficient mice. *J. Clin. Invest.* **116**, 59–69 (2006).

124. Ma, T. *et al.* Th17 cells and IL-17 are involved in the disruption of vulnerable plaques triggered by short-term combination stimulation in apolipoprotein E-knockout mice. *Cell. Mol. Immunol.* **10**, 338–48 (2013).

125. Jin, S. *et al.* Endogenous renovascular hypertension combined with low shear stress induces plaque rupture in apolipoprotein E-deficient mice. *Arterioscler. Thromb. Vasc. Biol.* **32**, 2372–9 (2012).

126. Teng, Z., Sadat, U., Brown, A. J. & Gillard, J. H. Plaque hemorrhage in carotid artery disease: Pathogenesis, clinical and biomechanical considerations. *J. Biomech.* **47**, 847–858 (2014).

127. Johnson, J. *et al.* Plaque rupture after short periods of fat feeding in the apolipoprotein E-knockout mouse: model characterization and effects of pravastatin treatment. *Circulation* **111**, 1422–30 (2005).

128. Chen, Y.-C. *et al.* A novel mouse model of atherosclerotic plaque instability for drug testing and mechanistic/therapeutic discoveries using gene and microRNA expression profiling. *Circ. Res.* **113**, 252–65 (2013).

129. Van Herck, J. L. *et al.* Impaired fibrillin-1 function promotes features of plaque instability in apolipoprotein E-deficient mice. *Circulation* **120**, 2478–87 (2009).

130. Van der Donckt, C. *et al.* Elastin fragmentation in atherosclerotic mice leads to intraplaque neovascularization, plaque rupture, myocardial infarction, stroke, and sudden death. *Eur. Heart J.* **36**, 1049–58 (2015).

131. Roche-Molina, M. *et al.* Induction of sustained hypercholesterolemia by single adeno-associated virus-mediated gene transfer of mutant hPCSK9. *Arterioscler. Thromb. Vasc. Biol.* **35**, 50–9 (2015).

132. Booth, R. F. *et al.* Rapid development of atherosclerotic lesions in the rabbit carotid artery induced by perivascular manipulation. *Atherosclerosis* **76**, 257–68 (1989).

133. Campbell, D. J., Day, A. J., Skinner, S. L. & Tume, R. K. The effect of hypertension on the accumulation of lipids and the uptake of (3H)cholesterol by the aorta of normal-fed and cholesterol-fed rabbits. *Atherosclerosis* **18**, 301–19 (1973).

134. Friedman, M. & Byers, S. O. Aortic atherosclerosis intensification in rabbits by prior endothelial denudation. *Arch. Pathol.* **79**, 345–56 (1965).

135. Lehr, H. A. *et al.* Immunopathogenesis of atherosclerosis: endotoxin accelerates atherosclerosis in rabbits on hypercholesterolemic diet. *Circulation* **104**, 914–20 (2001).

136. Yin, W., Yuan, Z., Wang, Z., Yang, B. & Yang, Y. A diet high in saturated fat and sucrose alters glucoregulation and induces aortic fatty streaks in New Zealand White rabbits. *Int. J. Exp. Diabetes Res.* **3**, 179–84 (2002).

137. Constantinides, P. & Chakravarti, R. N. Rabbit arterial thrombosis production by systemic procedures. *Arch. Pathol.* **72**, 197–208 (1961).

138. Johnstone, M. T. *et al.* In vivo magnetic resonance imaging of experimental thrombosis in a rabbit model. *Arterioscler. Thromb. Vasc. Biol.* **21**, 1556–60 (2001).

139. Fang, S.-M., Zhang, Q.-H. & Jiang, Z.-X. Developing a novel rabbit model of atherosclerotic plaque rupture and thrombosis by cold-induced endothelial injury. *J. Biomed. Sci.* **16**, 39 (2009).

140. Fan, J. *et al.* Rabbit models for the study of human atherosclerosis: from pathophysiological mechanisms to translational medicine. *Pharmacol. Ther.* **146**, 104–19 (2015).

141. Shiomi, M. & Fan, J. Unstable coronary plaques and cardiac events in myocardial infarction-prone Watanabe heritable hyperlipidemic rabbits: questions and quandaries. *Curr. Opin. Lipidol.* **19**, 631–6 (2008).

142. Mahley, R. W., Weisgraber, K. H., Innerarity, T., Brewer, H. B. & Assmann, G. Swine lipoproteins and atherosclerosis. Changes in the plasma lipoproteins and apoproteins induced by cholesterol feeding. *Biochemistry* **14**, 2817–23 (1975).

143. Granada, J. F. *et al.* Porcine models of coronary atherosclerosis and vulnerable plaque for imaging and interventional research. *EuroIntervention* **5**, 140–8 (2009).

144. Rapacz, J., Hasler-Rapacz, J., Taylor, K. M., Checovich, W. J. & Attie, A. D. Lipoprotein mutations in pigs are associated with elevated plasma cholesterol and atherosclerosis. *Science* **234**, 1573–7 (1986).

145. Prescott, M. F., McBride, C. H., Hasler-Rapacz, J., Von Linden, J. & Rapacz, J. Development of complex atherosclerotic lesions in pigs with inherited hyper-LDL cholesterolemia bearing mutant alleles for apolipoprotein B. *Am. J. Pathol.* **139**, 139–47 (1991).

146. Thim, T. Human-like atherosclerosis in minipigs: a new model for detection and treatment of vulnerable plaques. *Dan. Med. Bull.* **57**, B4161 (2010).

147. Gerrity, R. G., Natarajan, R., Nadler, J. L. & Kimsey, T. Diabetes-induced accelerated atherosclerosis in swine. *Diabetes* **50**, 1654–65 (2001).

148. Baker, A. B. *et al.* Regulation of heparanase expression in coronary artery disease in diabetic, hyperlipidemic swine. *Atherosclerosis* **213**, 436–42 (2010).

149. Mohler, E. R. *et al.* Site-specific atherogenic gene expression correlates with subsequent variable lesion development in coronary and peripheral vasculature. *Arterioscler. Thromb. Vasc. Biol.* **28**, 850–5 (2008).

150. Thim, T. *et al.* Familial hypercholesterolaemic downsized pig with human-like coronary atherosclerosis: a model for preclinical studies. *EuroIntervention* **6**, 261–268 (2010).

151. Ishii, A. *et al.* Swine model of carotid artery atherosclerosis: experimental induction by surgical partial ligation and dietary hypercholesterolemia. *AJNR. Am. J. Neuroradiol.* **27**, 1893–9 (2006).

152. Shi, Z.-S. *et al.* Vulnerable plaque in a Swine model of carotid atherosclerosis. *AJNR. Am. J. Neuroradiol.* **30**, 469–72 (2009).

153. Jiang, X.-B., Wang, J.-S., Liu, D.-H., Yuan, W.-S. & Shi, Z.-S. Overexpression of matrix metalloproteinase-9 is correlated with carotid intraplaque hemorrhage in a swine model. *J. Neurointerv. Surg.* **5**, 473–7 (2013).

154. Soulez, G. *et al.* Vulnerable carotid atherosclerotic plaque creation in a Swine model: evaluation of stenosis creation using absorbable and permanent suture in a diabetic dyslipidemic model. *J. Vasc. Interv. Radiol.* **23**, 1700-1708.e4 (2012).

155. Al-Mashhadi, R. H. *et al.* Abstract 17809: In Vivo High Resolution Isotropic 3D MRI of Coronary Atherosclerosis in Hypertensive Hypercholesterolemic Minipigs. *Circulation* **130**, A17809- (2014).

156. Asakura, T. & Karino, T. Flow patterns and spatial distribution of atherosclerotic lesions in human coronary arteries. *Circ. Res.* **66**, 1045–1066 (1990).

157. Salzar, R. S., Thubrikart, M. J. & Eppink, R. T. Pressure-induced mechanical stress in the carotid artery bifurcation: a possible correlation to atherosclerosis. *J. Biomech.* **28**, 1333–1340 (1995).

158. Cheng, C. *et al.* Large variations in absolute wall shear stress levels within one species and between species. *Atherosclerosis* **195**, 225–35 (2007).

159. Tzima, E. *et al.* A mechanosensory complex that mediates the endothelial cell response to fluid shear stress. *Nature* **437**, 426–31 (2005).

160. Conway, D. E. & Schwartz, M. A. Flow-dependent cellular mechanotransduction in atherosclerosis. *J. Cell Sci.* **126**, 5101–9 (2013).

161. Van der Heiden, K., Egorova, A. D., Poelmann, R. E., Wentzel, J. J. & Hierck, B. P. Role for primary cilia as flow detectors in the cardiovascular system. *Int. Rev. Cell Mol. Biol.* **290**, 87–119 (2011).

162. Riha, G. M., Lin, P. H., Lumsden, A. B., Yao, Q. & Chen, C. Roles of hemodynamic forces in vascular cell differentiation. *Ann. Biomed. Eng.* **33**, 772–9 (2005).

163. Boon, R. A. & Horrevoets, A. J. G. Key transcriptional regulators of the vasoprotective effects of shear stress. *Hamostaseologie* **29**, 39–40, 41–3 (2009).

164. Dekker, R. J. *et al.* Prolonged fluid shear stress induces a distinct set of endothelial cell genes, most specifically lung Krüppel-like factor (KLF2). *Blood* **100**, 1689–98 (2002).

165. Nayak, L., Lin, Z. & Jain, M. K. 'Go with the flow': how Krüppel-like factor 2 regulates the vasoprotective effects of shear stress. *Antioxid. Redox Signal.* **15**, 1449–1461 (2011).

166. Dekker, R. J. *et al.* KLF2 provokes a gene expression pattern that establishes functional quiescent differentiation of the endothelium. *Blood* **107**, 4354–63 (2006).

167. Boon, R. A. *et al.* KLF2 suppresses TGF-beta signaling in endothelium through induction of Smad7 and inhibition of AP-1. *Arterioscler. Thromb. Vasc. Biol.* **27**, 532–9 (2007).

168. SenBanerjee, S. *et al.* KLF2 Is a novel transcriptional regulator of endothelial proinflammatory activation. *J. Exp. Med.* **199**, 1305–1315 (2004).

169. Lin, Z. *et al.* Kruppel-like factor 2 (KLF2) regulates endothelial thrombotic function. *Circ. Res.* **96**, e48-57 (2005).

170. Kietadisorn, R., Juni, R. P. & Moens, A. L. Tackling endothelial dysfunction by modulating NOS uncoupling: new insights into its pathogenesis and therapeutic possibilities. *Am. J. Physiol. Endocrinol. Metab.* **302**, E481-95 (2012).

171. Landmesser, U. *et al.* Oxidation of tetrahydrobiopterin leads to uncoupling of endothelial cell nitric oxide synthase in hypertension. *J. Clin. Invest.* **111**, 1201–9 (2003).

172. Yamawaki, H., Lehoux, S. & Berk, B. C. Chronic physiological shear stress inhibits tumor necrosis factor-induced proinflammatory responses in rabbit aorta perfused ex vivo. *Circulation* **108**, 1619–1625 (2003).

173. Huang, Y. H., Rönnelid, J. & Frostegård, J. Oxidized LDL induces enhanced antibody formation and MHC class II-dependent IFN-gamma production in lymphocytes from healthy individuals. *Arterioscler. Thromb. Vasc. Biol.* **15**, 1577–83 (1995).

174. Parthasarathy, S., Printz, D. J., Boyd, D., Joy, L. & Steinberg, D. Macrophage oxidation of low density lipoprotein generates a modified form recognized by the scavenger receptor. *Arterioscler. Thromb. Vasc. Biol.* **6**, 505–510 (1986).

175. Glagov, S., Weisenberg, E., Zarins, C. K., Stankunavicius, R. & Kolettis, G. J. Compensatory enlargement of human atherosclerotic coronary arteries. *N. Engl. J. Med.* **316**, 1371–5 (1987).

176. Gijsen, F. J. H. *et al.* Strain distribution over plaques in human coronary arteries relates to shear stress. *Am. J. Physiol. Heart Circ. Physiol.* **295**, H1608–H1614 (2008).

177. Naghavi, M. *et al.* From vulnerable plaque to vulnerable patient: a call for new definitions and risk assessment strategies: Part I. *Circulation* **108**, 1664–72 (2003).

178. Naghavi, M. *et al.* From vulnerable plaque to vulnerable patient: a call for new definitions and risk assessment strategies: Part II. *Circulation* **108**, 1772–8 (2003).

179. Virmani, R., Burke, A. P., Kolodgie, F. D. & Farb, A. Pathology of the thin-cap fibroatheroma: a type of vulnerable plaque. *J. Interv. Cardiol.* **16**, 267–72 (2003).

180. Moreno, P. R. *et al.* Plaque neovascularization is increased in ruptured atherosclerotic lesions of human aorta: implications for plaque vulnerability. *Circulation* **110**, 2032–8 (2004).

181. Moreno, P. R., Purushothaman, K.-R., Sirol, M., Levy, A. P. & Fuster, V. Neovascularization in human atherosclerosis. *Circulation* **113**, 2245–52 (2006).

182. Baun, J. G. *Vascular Ultrasound: Physics, Instrumentation & Hemodynamics*. (ProSono Publishing, 2010).

183. Chiu, J.-J. & Chien, S. Effects of Disturbed Flow on Vascular Endothelium : Pathophysiological Basis and Clinical Perspectives. **91**, 327–387 (2011).

184. Stein, P. D. & Sabbah, H. N. Turbulent blood flow in the ascending aorta of humans with normal and diseased aortic valves. *Circ. Res.* **39**, 58–65 (1976).

185. Kamiya, a & Togawa, T. Adaptive regulation of wall shear stress to flow change in the canine carotid artery. *Am. J. Physiol.* **239**, H14-21 (1980).

186. Castier, Y. *et al.* Characterization of neointima lesions associated with arteriovenous fistulas in a mouse model. *Kidney Int.* **70**, 315–20 (2006).

187. Castier, Y., Brandes, R. P., Leseche, G., Tedgui, A. & Lehoux, S. p47phox-dependent NADPH oxidase regulates flow-induced vascular remodeling. *Circ. Res.* **97**, 533–40 (2005).

188. Zarins, C. K., Zatina, M. A., Giddens, D. P., Ku, D. N. & Glagov, S. Shear stress regulation of artery lumen diameter in experimental atherogenesis. *J. Vasc. Surg.* **5**, 413–420 (1987).

189. Nanjo, H. *et al.* Intermittent short-duration exposure to low wall shear stress induces intimal thickening in arteries exposed to chronic high shear stress. *Exp. Mol. Pathol.* **80**, 38–45 (2006).

190. Sho, M. *et al.* Subnormal shear stress-induced intimal thickening requires medial smooth muscle cell proliferation and migration. *Exp. Mol. Pathol.* **72**, 150–60 (2002).

191. Sho, E. *et al.* Arterial enlargement, tortuosity, and intimal thickening in response to sequential exposure to high and low wall shear stress. *J. Vasc. Surg.* **39**, 601–12 (2004).

192. Zhuang, Y, J., Singh, T. M., Zarins, C. K. & Masuda, H. Sequential Increase and Decrease in Blood Flow Stimulates Progressive Intimal Thickening. *Eur. J. Vasc. Endovasc. Surg.* **16**, 301–310 (1998).

193. Tronc, F. *et al.* Role of NO in Flow-Induced Remodeling of the Rabbit Common Carotid Artery. *Arterioscler. Thromb. Vasc. Biol.* **16**, 1256–1262 (1996).

194. Chen, Y.-S., Lu, M.-J., Huang, H.-S. & Ma, M.-C. Mechanosensitive transient receptor potential vanilloid type 1 channels contribute to vascular remodeling of rat fistula veins. *J. Vasc. Surg.* **52**, 1310–20 (2010).

195. Langer, S. *et al.* Functional and structural response of arterialized femoral veins in a rodent AV fistula model. *Nephrol. Dial. Transplant* **24**, 2201–6 (2009).

196. Manning, E. *et al.* A new arteriovenous fistula model to study the development of neointimal hyperplasia. *J. Vasc. Res.* **49**, 123–31 (2012).

197. Butterfield, A. B. *et al.* Inverse effect of chronically elevated blood flow on atherogenesis in miniature swine. *Atherosclerosis* **26**, 215–224 (1977).

198. Zou, Y. *et al.* Mouse model of venous bypass graft arteriosclerosis. *Am. J. Pathol.* **153**, 1301–10 (1998).

199. Schepers, a *et al.* Inhibition of complement component C3 reduces vein graft atherosclerosis in apolipoprotein E3-Leiden transgenic mice. *Circulation* **114**, 2831–8 (2006).

200. Thim, T. *et al.* Oversized vein grafts develop advanced atherosclerosis in hypercholesterolemic minipigs. *BMC Cardiovasc. Disord.* **12**, 24 (2012).

201. Wexler, B. C. & Saroff, J. Metabolic Changes in Response to Acute Cerebral Ischemia Following Unilateral Carotid Artery Ligation in Arteriosclerotic Versus Nonarteriosclerotic Rats. *Stroke* **1**, 38–51 (1970).

202. Geary, R. L., Kohler, T. R., Vergel, S., Kirkman, T. R. & Clowes, A. W. Time course of flow-induced smooth muscle cell proliferation and intimal thickening in endothelialized baboon vascular grafts. *Circ. Res.* **74**, 14–23 (1994).

203. Kohler, T. R., Kirkman, T. R., Kraiss, L. W., Zierler, B. K. & Clowes, A. W. Increased blood flow inhibits neointimal hyperplasia in endothelialized vascular grafts. *Circ. Res.* **69**, 1557–1565 (1991).

204. Guyton, J. R. & Hartley, C. J. Flow restriction of one carotid artery in juvenile rats inhibits growth of arterial diameter. *Am J Physiol Hear. Circ Physiol* **248**, H540-546 (1985).

205. Kumar, A. & Lindner, V. Remodeling With Neointima Formation in the Mouse Carotid Artery After Cessation of Blood Flow. *Arterioscler. Thromb. Vasc. Biol.* **17**, 2238–2244 (1997).

206. Chang, P. C., Wu, H. L., Lin, H. C., Wang, K. C. & Shi, G. Y. Human plasminogen kringle 1-5 reduces atherosclerosis and neointima formation in mice by suppressing the inflammatory signaling pathway. *J. Thromb. Haemost.* **8**, 194–201 (2010).

207. Lin, W.-L., Chang, C.-F., Shi, C.-S., Shi, G.-Y. & Wu, H.-L. Recombinant lectin-like domain of thrombomodulin suppresses vascular inflammation by reducing leukocyte recruitment via interacting with Lewis Y on endothelial cells. *Arterioscler. Thromb. Vasc. Biol.* **33**, 2366–73 (2013).

208. Kosuge, H. *et al.* Near infrared imaging and photothermal ablation of vascular inflammation using single-walled carbon nanotubes. *J. Am. Heart Assoc.* **1**, e002568 (2012).

209. Conway, R. G. *et al.* Glucose metabolic trapping in mouse arteries: nonradioactive assay of atherosclerotic plaque inflammation applicable to drug discovery. *PLoS One* **7**, e50349 (2012).

210. Dimastromatteo, J. *et al.* In vivo molecular imaging of atherosclerotic lesions in ApoE-/- mice using VCAM-1-specific, 99mTc-labeled peptidic sequences. *J. Nucl. Med.* **54**, 1442–1449 (2013).

211. Ivan, E. Expansive Arterial Remodeling Is Associated With Increased Neointimal Macrophage Foam Cell Content: The Murine Model of Macrophage-Rich Carotid Artery Lesions. *Circulation* **105**, 2686–2691 (2002).

212. Kureha, F. *et al.* Nectin-like molecule-5 regulates intimal thickening after carotid artery ligation in mice. *Arterioscler. Thromb. Vasc. Biol.* **33**, 1206–1211 (2013).

213. Zhou, J. *et al.* Regulation of vascular smooth muscle cell turnover by endothelial cell-secreted microRNA-126: role of shear stress. *Circ. Res.* **113**, 40–51 (2013).

214. Sugimoto, R. *et al.* Enhanced neointimal hyperplasia and carotid artery remodelling in sequestosome 1 deficient mice. *J. Cell. Mol. Med.* **14**, 1546–54 (2010).

215. da Cunha, V. *et al.* Angiotensin II induces histomorphologic features of unstable plaque in a murine model of accelerated atherosclerosis. *J. Vasc. Surg.* **44**, 364–371 (2006).

216. Sasaki, T. *et al.* A simple method of plaque rupture induction in apolipoprotein E-deficient mice. *Arterioscler. Thromb. Vasc. Biol.* **26**, 1304–9 (2006).

217. Aono, J. *et al.* Deletion of the angiotensin II type 1a receptor prevents atherosclerotic plaque rupture in apolipoprotein E-/- mice. *Arterioscler. Thromb. Vasc. Biol.* **32**, 1453–1459 (2012).

218. Nakamura, K. *et al.* Statin prevents plaque disruption in apoE-knockout mouse model through pleiotropic effect on acute inflammation. *Atherosclerosis* **206**, 355–361 (2009).

219. Mondy, J. S. *et al.* Platelet-Derived Growth Factor Ligand and Receptor Expression in Response to Altered Blood Flow In Vivo. *Circ. Res.* **81**, 320–327 (1997).

220. Miyashiro, J. K., Poppa, V. & Berk, B. C. Flow-Induced Vascular Remodeling in the Rat Carotid Artery Diminishes With Age. *Circ. Res.* **81**, 311–319 (1997).

221. Nam, D. *et al.* Partial carotid ligation is a model of acutely induced disturbed flow, leading to rapid endothelial dysfunction and atherosclerosis. *Am. J. Physiol. Heart Circ. Physiol.* **297**, H1535-43 (2009).

222. Langille, B. L. & O'Donnell, F. Reductions in Arterial Diameter Produced by Chronic Decreases in Blood Flow are endothelium-dependent. *Science (80-.).* **231**, 405–407 (1986).

223. Tropea, B. I. *et al.* Hypertension-enhanced monocyte adhesion in experimental atherosclerosis. *J. Vasc. Surg.* **23**, 596–605 (1996).

224. von der Thusen, J. H., van Berkel, T. J. C. & Biessen, E. a. L. Induction of Rapid Atherogenesis by Perivascular Carotid Collar Placement in Apolipoprotein E-Deficient and Low-Density Lipoprotein Receptor-Deficient Mice. *Circulation* **103**, 1164–1170 (2001).

225. Cheng, C. *et al.* Shear stress affects the intracellular distribution of eNOS: direct demonstration by a novel in vivo technique. *Blood* **106**, 3691–8 (2005).

226. Kivelä, A., Hartikainen, J. & Ylä-Herttuala, S. Dotted collar placed around carotid artery induces asymmetric neointimal lesion formation in rabbits without intravascular manipulations. *BMC Cardiovasc. Disord.* **12**, 91 (2012).

227. Langille, B. L., Bendeck, M. P. & Keeley, F. W. Adaptations of carotid arteries of young and mature rabbits to reduced carotid blood flow. *Am. J. Physiol.* **256**, H931-9 (1989).

228. Duran-Prado, M. *et al.* Cortistatin inhibits migration and proliferation of human vascular smooth muscle cells and decreases neointimal formation on carotid artery ligation. *Circ. Res.* **112**, 1444–1455 (2013).

229. Redmond, E. M. *et al.* Inhibition of patched-1 prevents injury-induced neointimal hyperplasia. *Arterioscler. Thromb. Vasc. Biol.* **33**, 1960–4 (2013).

230. Korshunov, V. a & Berk, B. C. Flow-induced vascular remodeling in the mouse: a model for carotid intima-media thickening. *Arterioscler. Thromb. Vasc. Biol.* **23**, 2185–91 (2003).

231. Korshunov, V. a & Berk, B. C. Strain-dependent vascular remodeling: the 'Glagov phenomenon' is genetically determined. *Circulation* **110**, 220–226 (2004).

232. Shin, I. J. *et al.* Characterization of partial ligation-induced carotid atherosclerosis model using dual-modality molecular imaging in ApoE knock-out mice. *PLoS One* **8**, e73451 (2013).

233. Merino, H., Parthasarathy, S. & Singla, D. K. Partial ligation-induced carotid artery occlusion induces leukocyte recruitment and lipid accumulation--a shear stress model of atherosclerosis. *Mol. Cell. Biochem.* **372**, 267–273 (2013).

234. Ni, C.-W. *et al.* Discovery of novel mechanosensitive genes in vivo using mouse carotid artery endothelium exposed to disturbed flow. *Blood* **116**, e66--73 (2010).

235. Dunn, J. *et al.* Flow-dependent epigenetic DNA methylation regulates endothelial gene expression and atherosclerosis. *J. Clin. Invest.* **124**, 3187–99 (2014).

236. Hollander, W., Madoff, I., Paddock, J. & Kirkpatrick, B. Aggravation of atherosclerosis by hypertension in a subhuman primate model with coarctation of the aorta. *Circ. Res.* **38**, 63–72 (1976).

237. Li, Y. *et al.* Remodeling of carotid arteries is associated with increased expression of thrombomodulin in a mouse transverse aortic constriction model. *Thromb. Haemost.* **97**, 658–664 (2007).

238. Lyon, R. T., Runyon-Hass, A., Davis, H. R., Glagov, S. & Zarins, C. K. Protection from atherosclerotic lesion formation by reduction of artery wall motion. *J. Vasc. Surg.* **5**, 59–67 (1987).

239. Prusty, S., Kemper, T., Moss, M. B. & Hollander, W. Occurrence of stroke in a nonhuman primate model of cerebrovascular disease. *Stroke.* **19**, 84–90 (1988).

240. Cozzi, P. J. *et al.* Aortic wall metabolism in relation to susceptibility and resistance to experimental atherosclerosis. *J. Vasc. Surg.* **7**, 706–14 (1988).

241. Baron, B. W., Glagov, S., Giddens, D. P. & Zarins, C. K. Effect of coarctation on matrix content of experimental aortic atherosclerosis: relation to location, plaque size and blood pressure. *Atherosclerosis* **102**, 37–49 (1993).

242. Ding, S. F. *et al.* A causal relationship between shear stress and atherosclerotic lesions in apolipoprotein E knockout mice assessed by ultrasound biomicroscopy. *Am. J. Physiol. Heart Circ. Physiol.* **298**, H2121-9 (2010).

243. Zhang, X., Zhu, X. & Chen, B. Inhibition of collar-induced carotid atherosclerosis by recombinant apoA-I cysteine mutants in apoE-deficient mice. *J. Lipid Res.* **51**, 3434–42 (2010).

244. de Nooijer, R. *et al.* Lesional overexpression of matrix metalloproteinase-9 promotes intraplaque hemorrhage in advanced lesions but not at earlier stages of atherogenesis. *Arterioscler. Thromb. Vasc. Biol.* **26**, 340–6 (2006).

245. Baetta, R. *et al.* Perivascular carotid collar placement induces neointima formation and outward arterial remodeling in mice independent of apolipoprotein E deficiency or Western-type diet feeding. *Atherosclerosis* **195**, e112-24 (2007).

246. de Nooijer, R. *et al.* Overexpression of IL-18 decreases intimal collagen content and promotes a vulnerable plaque phenotype in apolipoprotein-E-deficient mice. *Arterioscler. Thromb. Vasc. Biol.* **24**, 2313–9 (2004).

247. Ling, M.-Y. *et al.* Up-regulated ATP-sensitive potassium channels play a role in increased inflammation and plaque vulnerability in macrophages. *Atherosclerosis* **226**, 348–55 (2013).

248. van Puijvelde, G. H. M. *et al.* Effect of natural killer T cell activation on the initiation of atherosclerosis. *Thromb. Haemost.* **102**, 223–30 (2009).

249. Ni, M., Zhang, M., Ding, S. F., Chen, W. Q. & Zhang, Y. Micro-ultrasound imaging assessment of carotid plaque characteristics in apolipoprotein-E knockout mice. *Atherosclerosis* **197**, 64–71 (2008).

250. Zadelaar, a S. M. *et al.* Increased vulnerability of pre-existing atherosclerosis in ApoE-deficient mice following adenovirus-mediated Fas ligand gene transfer. *Atherosclerosis* **183**, 244–50 (2005).

251. Thim, T. *et al.* Wall shear stress and local plaque development in stenosed carotid arteries of hypercholesterolemic minipigs. *J. Cardiovasc. Dis. Res.* **3**, 76–83 (2012).

252. Cooke, J. P. Flow, NO, and atherogenesis. *Proc. Natl. Acad. Sci. U. S. A.* **100**, 768–70 (2003).

253. Matlung, H. L. *et al.* Transglutaminase activity regulates atherosclerotic plaque composition at locations exposed to oscillatory shear stress. *Atherosclerosis* **224**, 355–62 (2012).

254. Winkel, L. C. J. *et al.* Folate receptor–targeted single-photon emission computed tomography/computed tomography to detect activated macrophages in atherosclerosis: can it distinguish vulnerable from stable atherosclerotic plaques? *Mol. Imaging* **13**, (2014).

255. Cheng, C. *et al.* Atherosclerotic lesion size and vulnerability are determined by patterns of fluid shear stress. *Circulation* **113**, 2744–53 (2006).

256. Cheng, C. *et al.* Shear stress – induced changes in atherosclerotic plaque composition are modulated by chemokines. **117**, (2007).

257. Cheng, C. *et al.* Activation of MMP8 and MMP13 by angiotensin II correlates to severe intra-plaque hemorrhages and collagen breakdown in atherosclerotic lesions with a vulnerable phenotype. *Atherosclerosis* **204**, 26–33 (2009).

258. Segers, D. *et al.* Atherosclerotic Plaque Stability Is Affected by the Chemokine CXCL10 in Both Mice and Humans. *Int. J. Inflam.* **2011**, 936109 (2011).

259. Olivon, V. C. *et al.* Arginase inhibition prevents the low shear stress-induced development of vulnerable atherosclerotic plaques in ApoE-/- mice. *Atherosclerosis* **227**, 236–43 (2013).

260. Shami, A. *et al.* Fibromodulin deficiency reduces low-density lipoprotein accumulation in atherosclerotic plaques in apolipoprotein E-null mice. *Arterioscler. Thromb. Vasc. Biol.* **33**, 354–61 (2013).

261. Debernardi, N. *et al.* Microcalcifications in atherosclerotic lesion of apolipoprotein E-deficient mouse. *Int. J. Exp. Pathol.* **91**, 485–94 (2010).

262. Zhou, Y.-Q., Zhu, S.-N., Foster, F. S., Cybulsky, M. I. & Henkelman, R. M. Aortic regurgitation dramatically alters the distribution of atherosclerotic lesions and enhances atherogenesis in mice. *Arterioscler. Thromb. Vasc. Biol.* **30**, 1181–8 (2010).

263. Hoi, Y., Zhou, Y.-Q., Zhang, X., Henkelman, R. M. & Steinman, D. A. Correlation between local hemodynamics and lesion distribution in a novel aortic regurgitation murine model of atherosclerosis. *Ann. Biomed. Eng.* **39**, 1414–22 (2011).

264. Bomberger, R. A., Zarins, C. K., Taylor, K. E. & Glagov, S. Effect of hypotension on atherogenesis and aortic wall composition. *J. Surg. Res.* **28**, 402–9 (1980).

265. Farb, A. *et al.* Sudden coronary death. Frequency of active coronary lesions, inactive coronary lesions, and myocardial infarction. *Circulation* **92**, 1701–9 (1995).

266. Kolodgie, F. D. *et al.* The thin-cap fibroatheroma: a type of vulnerable plaque: the major precursor lesion to acute coronary syndromes. *Curr. Opin. Cardiol.* **16**, 285–92 (2001).

267. Hamamdzic, D. & Wilensky, R. L. Porcine models of accelerated coronary atherosclerosis: role of diabetes mellitus and hypercholesterolemia. *J. Diabetes Res.* **2013**, 761415 (2013).

268. Bourantas, C. V. *et al.* Hybrid intravascular imaging: recent advances, technical considerations, and current applications in the study of plaque pathophysiology. *Eur. Heart J.* **38**, 400–412 (2017).

269. Neeb, Z. P. *et al.* Metabolic syndrome and coronary artery disease in Ossabaw compared with Yucatan swine. *Comp. Med.* **60**, 300–15 (2010).

270. Patel, D. *et al.* Subsequent development of fibroatheromas with inflamed fibrous caps can be predicted by intracoronary near infrared spectroscopy. *Arterioscler. Thromb. Vasc. Biol.* **33**, 347–53 (2013).

271. Ludvigsen, T. P. *et al.* Göttingen minipig model of diet-induced atherosclerosis: influence of mild streptozotocin-induced diabetes on lesion severity and markers of inflammation evaluated in obese, obese and diabetic, and lean control animals. *J. Transl. Med.* **13**, 312 (2015).

272. van Ditzhuijzen, N. S. *et al.* Serial Coronary Imaging of Early Atherosclerosis Development in Fast-Food-Fed Diabetic and Nondiabetic Swine. *JACC Basic to Transl. Sci.* **1**, 449–460 (2016).

273. Davis, B. T. *et al.* Targeted Disruption of LDLR Causes Hypercholesterolemia and Atherosclerosis in Yucatan Miniature Pigs. *PLoS One* **9**, e93457 (2014).

274. Al-Mashhadi, R. H. *et al.* Familial Hypercholesterolemia and Atherosclerosis in Cloned Minipigs Created by DNA Transposition of a Human PCSK9 Gain-of-Function Mutant. *Sci. Transl. Med.* **5**, 166ra1 (2013).

275. Sharifi, M., Futema, M., Nair, D. & Humphries, S. E. Genetic Architecture of Familial Hypercholesterolaemia. *Curr. Cardiol. Rep.* **19**, 44 (2017).

276. Jani, B. & Rajkumar, C. Ageing and vascular ageing. *Postgrad. Med. J.* **82**, 357–62 (2006).

277. Franklin, S. S. *et al.* Hemodynamic patterns of age-related changes in blood pressure. The Framingham Heart Study. *Circulation* **96**, 308–15 (1997).

278. Okęcka-Szymańska, J., Hübner-Woźniak, E., Piątkowska, I. & Malara, M. Effects of age, gender and physical activity on plasma lipid profile. *Biomed. Hum. Kinet.* **3**, 1–5 (2011).

279. Stone, N. J., Levy, R. I., Fredrickson, D. S. & Verter, J. Coronary artery disease in 116 kindred with familial type II hyperlipoproteinemia. *Circulation* **49**, 476–88 (1974).

280. National Research Council (US) Committee for the Update of the Guide for Care and Use of Laboratory Animals. *Guide for the Care and Use of Laboratory Animals, 8th edition*. *Guide for the Care and Use of Laboratory Animals* (National Academies Press (US), 2011). doi:10.17226/12910

281. Mauriello, A. *et al.* Coronary calcification identifies the vulnerable patient rather than the vulnerable Plaque. *Atherosclerosis* **229**, 124–9 (2013).

282. Yahya, R. *et al.* Lomitapide affects HDL composition and function. *Atherosclerosis* **251**, 15–18 (2016).

283. Proudfoot, J. M. *et al.* HDL is the major lipoprotein carrier of plasma F2-isoprostanes. *J. Lipid Res.* **50**, 716–22 (2009).

284. Versmissen, J. *et al.* Familial hypercholesterolaemia: cholesterol efflux and coronary disease. *Eur. J. Clin. Invest.* **46**, 643–650 (2016).

285. Bandaru, V. V. R. *et al.* ApoE4 disrupts sterol and sphingolipid metabolism in Alzheimer's but not normal brain. *Neurobiol. Aging* **30**, 591–9 (2009).

286. de Wit, N. M. *et al.* Altered Sphingolipid Balance in Capillary Cerebral Amyloid Angiopathy. *J. Alzheimers. Dis.* **60**, 795–807 (2017).

287. Laaksonen, R. *et al.* Plasma ceramides predict cardiovascular death in patients with stable coronary artery disease and acute coronary syndromes beyond LDL-cholesterol. *Eur. Heart J.* **37**, 1967–1976 (2016).

288. Poulsen, C. B. *et al.* Treatment with a human recombinant monoclonal IgG antibody against oxidized LDL in atherosclerosis-prone pigs reduces cathepsin S in coronary lesions. *Int. J. Cardiol.* **215**, 506–15 (2016).

289. Shim, J. *et al.* Apolipoprotein E Deficiency Increases Remnant Lipoproteins and Accelerates Progressive Atherosclerosis, But Not Xanthoma Formation, in Gene-Modified Minipigs. *JACC Basic to Transl. Sci.* **2**, 591–600 (2017).

290. Badin, J. K., Bruning, R. S. & Sturek, M. Effect of metabolic syndrome and aging on Ca2+ dysfunction in coronary smooth muscle and coronary artery disease severity in Ossabaw miniature swine. *Exp. Gerontol.* **108**, 247–255 (2018).

291. Tharp, D. L., Masseau, I., Ivey, J., Laughlin, M. H. & Bowles, D. K. Endurance exercise training does not limit coronary atherosclerosis in familial hypercholesterolemic swine. *Physiol. Rep.* **7**, e14008 (2019).

292. Chatzizisis, Y. S. *et al.* Prediction of the Localization of High-Risk Coronary Atherosclerotic Plaques on the Basis of Low Endothelial Shear Stress: An Intravascular Ultrasound and Histopathology Natural History Study. *Circulation* **117**, 993–1002 (2008).

293. Vieweg, W. V *et al.* Distribution and severity of coronary artery disease in 500 patients with angina pectoris. *Cathet. Cardiovasc. Diagn.* **5**, 319–30 (1979).

294. Wadhera, R. K., Steen, D. L., Khan, I., Giugliano, R. P. & Foody, J. M. A review of low-density lipoprotein cholesterol, treatment strategies, and its impact on cardiovascular disease morbidity and mortality. *J. Clin. Lipidol.* **10**, 472–489 (2016).

295. Berneis, K. K. & Krauss, R. M. Metabolic origins and clinical significance of LDL heterogeneity. *J. Lipid Res.* **43**, 1363–79 (2002).

296. Hoff, H. F. & Morton, R. E. Lipoproteins Containing Apo B Extracted from Human Aortas. Structure and Function. *Ann. N. Y. Acad. Sci.* **454**, 183–194 (1985).

297. Tabas, I. *et al.* Lipoprotein lipase and sphingomyelinase synergistically enhance the association of atherogenic lipoproteins with smooth muscle cells and extracellular matrix. A possible mechanism for low density lipoprotein and lipoprotein(a) retention and macrophage foa. *J. Biol. Chem.* **268**, 20419–32 (1993).

298. Schissel, S. L. *et al.* Rabbit aorta and human atherosclerotic lesions hydrolyze the sphingomyelin of retained low-density lipoprotein. Proposed role for arterial-wall sphingomyelinase in subendothelial retention and aggregation of atherogenic lipoproteins. *J. Clin. Invest.* **98**, 1455–1464 (1996).

299. Oörni, K., Hakala, J. K., Annila, A., Ala-Korpela, M. & Kovanen, P. T. Sphingomyelinase induces aggregation and fusion, but phospholipase A2 only aggregation, of low density lipoprotein (LDL) particles. Two distinct mechanisms leading to increased binding strength of LDL to human aortic proteoglycans. *J. Biol. Chem.* **273**, 29127–34 (1998).

300. Chatterjee, S. B., Dey, S., Shi, W. Y., Thomas, K. & Hutchins, G. M. Accumulation of glycosphingolipids in human atherosclerotic plaque and unaffected aorta tissues. *Glycobiology* **7**, 57–65 (1997).

301. Boyanovsky, B., Karakashian, A., King, K., Giltiay, N. & Nikolova-Karakashian, M. Uptake and metabolism of low density lipoproteins with elevated ceramide content by human microvascular endothelial cells: implications for the regulation of apoptosis. *J. Biol. Chem.* **278**, 26992–9 (2003).

302. Edsfeldt, A. *et al.* Sphingolipids Contribute to Human Atherosclerotic Plaque Inflammation. *Arterioscler. Thromb. Vasc. Biol.* **36**, 1132–1140 (2016).

303. Hartmann, D. *et al.* The equilibrium between long and very long chain ceramides is important for the fate of the cell and can be influenced by co-expression of CerS. *Int. J. Biochem. Cell Biol.* **45**, 1195–1203 (2013).

304. Jiang, X. C. *et al.* Plasma sphingomyelin level as a risk factor for coronary artery disease. *Arterioscler. Thromb. Vasc. Biol.* **20**, 2614–8 (2000).

305. Cheng, J. M. *et al.* Plasma concentrations of molecular lipid species in relation to coronary plaque characteristics and cardiovascular outcome: Results of the ATHEROREMO-IVUS study. *Atherosclerosis* **243**, 560–566 (2015).

306. Havulinna, A. S. *et al.* Circulating Ceramides Predict Cardiovascular Outcomes in the Population-Based FINRISK 2002 Cohort. *Arterioscler. Thromb. Vasc. Biol.* **36**, 2424–2430 (2016).

307. Sharifi, M., Rakhit, R. D., Humphries, S. E. & Nair, D. Cardiovascular risk stratification in familial hypercholesterolaemia. *Heart* **102**, 1003–8 (2016).

308. Mathers, C. D. & Loncar, D. Projections of Global Mortality and Burden of Disease from 2002 to 2030. *PLoS Med.* **3**, e442 (2006).

309. Knight, J. *et al.* Choosing the optimal wall shear parameter for the prediction of plaque location - A patient-specific computational study in human right coronary arteries. *Atherosclerosis* **211**, 445–450 (2010).

310. Schaap, M. *et al.* Coronary lumen segmentation using graph cuts and robust kernel regression. *Inf. Process. Med. Imaging* **21**, 528–39 (2009).

311. Huo, Y. & Kassab, G. S. Intraspecific scaling laws of vascular trees. *J. R. Soc. Interface* **9**, 190–200 (2012).

312. Seo, T., Schachter, L. G. & Barakat, A. I. Computational study of fluid mechanical disturbance induced by endovascular stents. *Ann. Biomed. Eng.* **33**, 444–56 (2005).

313. De Nisco, G. *et al.* The Atheroprotective Nature of Helical Flow in Coronary Arteries. *Ann. Biomed. Eng.* **47**, 425–438 (2018).

314. Garcia-Garcia, H. M. *et al.* Imaging plaques to predict and better manage patients with acute coronary events. *Circ. Res.* **114**, 1904–17 (2014).

315. Shishikura, D. *et al.* The relationship between segmental wall shear stress and lipid core plaque derived from near-infrared spectroscopy. *Atherosclerosis* **275**, 68–73 (2018).

316. Millon, A. *et al.* Low WSS Induces Intimal Thickening, while Large WSS Variation and Inflammation Induce Medial Thinning, in an Animal Model of Atherosclerosis. *PLoS One* **10**, e0141880 (2015).

317. Anroedh, S. *et al.* Plasma concentrations of molecular lipid species predict long-term clinical outcome in coronary artery disease patients. *J. Lipid Res.* **59**, 1729–1737 (2018).

318. Kwak, B. R. *et al.* Biomechanical factors in atherosclerosis: mechanisms and clinical implications. *Eur. Heart J.* **35**, 3013–20, 3020a-3020d (2014).

319. Slager, C. J. *et al.* The role of shear stress in the generation of rupture-prone vulnerable plaques. *Nat. Clin. Pract. Cardiovasc. Med.* **2**, 401–7 (2005).

320. O'Keefe, J. H., Cordain, L., Harris, W. H., Moe, R. M. & Vogel, R. Optimal low-density lipoprotein is 50 to 70 mg/dl: Lower is better and physiologically normal. *J. Am. Coll. Cardiol.* **43**, 2142–2146 (2004).

321. Oemrawsingh, R. M. *et al.* Near-infrared spectroscopy predicts cardiovascular outcome in patients with coronary artery disease. *J. Am. Coll. Cardiol.* **64**, 2510–2518 (2014).

322. Madder, R. D. *et al.* Large lipid-rich coronary plaques detected by near-infrared spectroscopy at non-stented sites in the target artery identify patients likely to experience future major adverse cardiovascular events. *Eur. Heart J. Cardiovasc. Imaging* **17**, 393–9 (2016).

323. Danek, B. A. *et al.* Long-term follow-up after near-infrared spectroscopy coronary imaging: Insights from the lipid cORe plaque association with CLinical events (ORACLE-NIRS) registry. *Cardiovasc. Revasc. Med.* **18**, 177–181 (2017).

324. Stolzmann, P. *et al.* Variability and accuracy of coronary CT angiography including use of iterative reconstruction algorithms for plaque burden assessment as compared with intravascular ultrasound-an ex vivo study. *Eur. Radiol.* **22**, 2067–2075 (2012).

325. Bulant, C. A. *et al.* A head-to-head comparison between CT- and IVUS-derived coronary blood flow models. *J. Biomech.* **51**, 65–76 (2017).

326. Davies, J. E. *et al.* Evidence of a dominant backward-propagating 'suction' wave responsible for diastolic coronary filling in humans, attenuated in left ventricular hypertrophy. *Circulation* **113**, 1768–1778 (2006).

327. Hadjiloizou, N. *et al.* Differences in cardiac microcirculatory wave patterns between the proximal left mainstem and proximal right coronary artery. *AJP Hear. Circ. Physiol.* **295**, H1198–H1205 (2008).

328. Ponzini, R., Vergara, C., Redaelli, A. & Veneziani, A. Reliable CFD-based estimation of flow rate in haemodynamics measures. *Ultrasound Med. Biol.* **32**, 1545–1555 (2006).

329. van der Giessen, A. G. *et al.* The influence of boundary conditions on wall shear stress distribution in patients specific coronary trees. *J. Biomech.* **44**, 1089–1095 (2011).

330. Cutnell, J. D. & Johnson, K. W. *Physics*. (John Wiley & Sons Inc, 2007).

331. Chiastra, C. *et al.* Coronary fractional flow reserve measurements of a stenosed side branch: a computational study investigating the influence of the bifurcation angle. *Biomed. Eng. Online* **15**, 91 (2016).

332. Vergallo, R. *et al.* Endothelial shear stress and coronary plaque characteristics in humans combined frequency-domain optical coherence tomography and computational fluid dynamics study. *Circ. Cardiovasc. Imaging* **7**, 905–911 (2014).

333. Bourantas, C. V *et al.* Angiographic derived endothelial shear stress: a new predictor of atherosclerotic disease progression. *Eur. Hear. J. - Cardiovasc. Imaging* **20**, 314–322 (2019).

334. Li, Y. *et al.* Impact of Side Branch Modeling on Computation of Endothelial Shear Stress in Coronary Artery Disease. *J. Am. Coll. Cardiol.* **66**, 125–135 (2015).

335. Sakellarios, A. *et al.* The effect of coronary bifurcation and blood flow modelling in prediction of atherosclerotic plaque development: a Serial Computed Tomographic Coronary Angiographic study. *EuroIntervention* **13**, 1084–1091 (2017).

336. Doriot, P. *et al.* In-vivo measurements of wall shear stress in human coronary arteries. *Coron. Artery Dis.* **11**, 495–502 (2000).

337. Pinho, N. *et al.* Correlation between geometric parameters of the left coronary artery and hemodynamic descriptors of atherosclerosis: FSI and statistical study. *Med. Biol. Eng. Comput.* **57**, 715–729 (2019).

338. Kok, A. M. *et al.* The Influence of Multidirectional Shear Stress on Plaque Progression and Composition Changes in Human Coronary Arteries. *EuroIntervention* (2019).

339. Yin, W. *et al.* Plasma lipid profiling across species for the identification of optimal animal models of human dyslipidemia. *J. Lipid Res.* **53**, 51–65 (2012).

340. Millán, J. *et al.* Lipoprotein ratios: Physiological significance and clinical usefulness in cardiovascular prevention. *Vasc. Health Risk Manag.* **5**, 757–65 (2009).

341. Hiro, T. *et al.* Effect of Intensive Statin Therapy on Regression of Coronary Atherosclerosis in Patients With Acute Coronary Syndrome. *J. Am. Coll. Cardiol.* **54**, 293–302 (2009).

342. Sabbah, H. N., Walburn, F. J. & Stein, P. D. Patterns of flow in the left coronary artery. *J. Biomech. Eng.* **106**, 272–9 (1984).

343. Karino, T. Microscopic structure of disturbed flows in the arterial and venous systems, and its implication in the localization of vascular diseases. *Int. Angiol.* **5**, 297–313

344. Ku, D. N. & Giddens, D. P. Laser Doppler anemometer measurements of pulsatile flow in a model carotid bifurcation. *J. Biomech.* **20**, 407–21 (1987).

345. Frazin, L. J. *et al.* Functional chiral asymmetry in descending thoracic aorta. *Circulation* **82**, 1985–94 (1990).

346. Stonebridge, P. A., Suttie, S. A., Ross, R. & Dick, J. Spiral Laminar Flow: a Survey of a Three-Dimensional Arterial Flow Pattern in a Group of Volunteers. *Eur. J. Vasc. Endovasc. Surg.* **52**, 674–680 (2016).

347. Kilner, P. J., Yang, G. Z., Mohiaddin, R. H., Firmin, D. N. & Longmore, D. B. Helical and retrograde secondary flow patterns in the aortic arch studied by three-directional magnetic resonance velocity mapping. *Circulation* **88**, 2235–47 (1993).

348. Bogren, H. G. & Buonocore, M. H. Blood flow measurements in the aorta and major arteries with MR velocity mapping. *J. Magn. Reson. Imaging* **4**, 119–30

349. Bogren, H. G. *et al.* Blood flow patterns in the thoracic aorta studied with three-directional MR velocity mapping: the effects of age and coronary artery disease. *J. Magn. Reson. Imaging* **7**, 784–93

350. Houston, J. G. *et al.* Spiral laminar flow in the abdominal aorta: a predictor of renal impairment deterioration in patients with renal artery stenosis? *Nephrol. Dial. Transplant* **19**, 1786–91 (2004).

351. Bogren, H. G., Buonocore, M. H. & Valente, R. J. Four-dimensional magnetic resonance velocity mapping of blood flow patterns in the aorta in patients with atherosclerotic coronary artery disease compared to age-matched normal subjects. *J. Magn. Reson. Imaging* **19**, 417–27 (2004).

352. Markl, M. *et al.* Time-resolved 3-dimensional velocity mapping in the thoracic aorta: visualization of 3-directional blood flow patterns in healthy volunteers and patients. *J. Comput. Assist. Tomogr.* **28**, 459–68

353. Hope, T. A. & Herfkens, R. J. Imaging of the Thoracic Aorta with Time-Resolved Three-Dimensional Phase-Contrast MRI: A Review. *Semin. Thorac. Cardiovasc. Surg.* **20**, 358–364 (2008).

354. Morbiducci, U. *et al.* In vivo quantification of helical blood flow in human aorta by time-resolved three-dimensional cine phase contrast magnetic resonance imaging. *Ann. Biomed. Eng.* **37**, 516–31 (2009).

355. Hope, M. D. *et al.* 4D flow CMR in assessment of valve-related ascending aortic disease. *JACC. Cardiovasc. Imaging* **4**, 781–7 (2011).

356. Morbiducci, U. *et al.* Mechanistic insight into the physiological relevance of helical blood flow in the human aorta: an in vivo study. *Biomech. Model. Mechanobiol.* **10**, 339–55 (2011).

357. Bürk, J. *et al.* Evaluation of 3D blood flow patterns and wall shear stress in the normal and dilated thoracic aorta using flow-sensitive 4D CMR. *J. Cardiovasc. Magn. Reson.* **14**, 84 (2012).

358. Frydrychowicz, A. *et al.* Interdependencies of aortic arch secondary flow patterns, geometry, and age analysed by 4-dimensional phase contrast magnetic resonance imaging at 3 Tesla. *Eur. Radiol.* **22**, 1122–30 (2012).

359. Geiger, J. *et al.* Aortic flow patterns in patients with Marfan syndrome assessed by flow-sensitive four-dimensional MRI. *J. Magn. Reson. Imaging* **35**, 594–600 (2012).

360. Sigfridsson, A., Petersson, S., Carlhäll, C.-J. & Ebbers, T. Four-dimensional flow MRI using spiral acquisition. *Magn. Reson. Med.* **68**, 1065–1073 (2012).

361. Hansen, K. L. *et al.* Analysis of Systolic Backflow and Secondary Helical Blood Flow in the Ascending Aorta Using Vector Flow Imaging. *Ultrasound Med. Biol.* **42**, 899–908 (2016).

362. Arnold, R. *et al.* Magnetic resonance imaging 4-D flow-based analysis of aortic hemodynamics in Turner syndrome. *Pediatr. Radiol.* **47**, 382–390 (2017).

363. Garcia, J., Barker, A. J., Collins, J. D., Carr, J. C. & Markl, M. Volumetric quantification of absolute local normalized helicity in patients with bicuspid aortic valve and aortic dilatation. *Magn. Reson. Med.* **78**, 689–701 (2017).

364. Ku, D. N., Giddens, D. P., Phillips, D. J. & Strandness, D. E. Hemodynamics of the normal human carotid bifurcation: in vitro and in vivo studies. *Ultrasound Med. Biol.* **11**, 13–26 (1985).

365. Bammer, R., Hope, T. A., Aksoy, M. & Alley, M. T. Time-resolved 3D quantitative flow MRI of the major intracranial vessels: Initial experience and comparative evaluation at 1.5T and 3.0T in combination with parallel imaging. *Magn. Reson. Med.* **57**, 127–140 (2007).

366. Wetzel, S. *et al.* In vivo assessment and visualization of intracranial arterial hemodynamics with flow-sensitized 4D MR imaging at 3T. *AJNR. Am. J. Neuroradiol.* **28**, 433–8 (2007).

367. Markl, M. *et al.* In vivo wall shear stress distribution in the carotid artery: effect of bifurcation geometry, internal carotid artery stenosis, and recanalization therapy. *Circ. Cardiovasc. Imaging* **3**, 647–55 (2010).

368. Knobloch, V., Boesiger, P. & Kozerke, S. Sparsity transform k-t principal component analysis for accelerating cine three-dimensional flow measurements. *Magn. Reson. Med.* **70**, 53–63 (2013).

369. Meckel, S. *et al.* Intracranial artery velocity measurement using 4D PC MRI at 3 T: comparison with transcranial ultrasound techniques and 2D PC MRI. *Neuroradiology* **55**, 389–98 (2013).

370. François, C. J. *et al.* 4D cardiovascular magnetic resonance velocity mapping of alterations of right heart flow patterns and main pulmonary artery hemodynamics in tetralogy of Fallot. *J. Cardiovasc. Magn. Reson.* **14**, 16 (2012).

371. Bächler, P. *et al.* Assessment of normal flow patterns in the pulmonary circulation by using 4D magnetic resonance velocity mapping. *Magn. Reson. Imaging* **31**, 178–88 (2013).

372. Schäfer, M. *et al.* Helicity and Vorticity of Pulmonary Arterial Flow in Patients With Pulmonary Hypertension: Quantitative Analysis of Flow Formations. *J. Am. Heart Assoc.* **6**, (2017).

373. Stonebridge, P. A., Hoskins, P. R., Allan, P. L. & Belch, J. F. Spiral laminar flow in vivo. *Clin. Sci. (Lond).* **91**, 17–21 (1996).

374. Frydrychowicz, A. *et al.* Visualization of iliac and proximal femoral artery hemodynamics using time-resolved 3D phase contrast MRI at 3T. *J. Magn. Reson. Imaging* **25**, 1085–92 (2007).

375. Moffatt, H. K. & Tsinober, A. Helicity in Laminar and Turbulent Flow. *Annu. Rev. Fluid Mech.* **24**, 281–312 (1992).

376. Morbiducci, U., Ponzini, R., Grigioni, M. & Redaelli, A. Helical flow as fluid dynamic signature for atherogenesis risk in aortocoronary bypass. A numeric study. *J. Biomech.* **40**, 519–534 (2007).

377. Gallo, D., Steinman, D. A. & Morbiducci, U. An insight into the mechanistic role of the common carotid artery on the hemodynamics at the carotid bifurcation. *Ann. Biomed. Eng.* **43**, 68–81 (2015).

378. Morbiducci, U., Ponzini, R., Gallo, D., Bignardi, C. & Rizzo, G. Inflow boundary conditions for image-based computational hemodynamics: impact of idealized versus measured velocity profiles in the human aorta. *J. Biomech.* **46**, 102–9 (2013).

379. Liu, X. *et al.* A numerical study on the flow of blood and the transport of LDL in the human aorta: the physiological significance of the helical flow in the aortic arch. *Am. J. Physiol. Heart Circ. Physiol.* **297**, H163-70 (2009).

380. Gallo, D. *et al.* Segment-specific associations between local haemodynamic and imaging markers of early atherosclerosis at the carotid artery: an in vivo human study. *J. R. Soc. Interface* **15**, (2018).

381. Morbiducci, U. *et al.* Atherosclerosis at arterial bifurcations: evidence for the role of haemodynamics and geometry. *Thromb. Haemost.* **115**, 484–492 (2016).

382. Vorobtsova, N. *et al.* Effects of Vessel Tortuosity on Coronary Hemodynamics: An Idealized and Patient-Specific Computational Study. *Ann. Biomed. Eng.* **44**, 2228–2239 (2016).

383. Chiastra, C. *et al.* Healthy and diseased coronary bifurcation geometries influence near-wall and intravascular flow: A computational exploration of the hemodynamic risk. *J. Biomech.* **58**, 79–88 (2017).

384. Siebes, M. *et al.* Single-wire pressure and flow velocity measurement to quantify coronary stenosis hemodynamics and effects of percutaneous interventions. *Circulation* **109**, 756–62 (2004).

385. Himburg, H. A. *et al.* Spatial comparison between wall shear stress measures and porcine arterial endothelial permeability. *Am. J. Physiol. Circ. Physiol.* **286**, H1916–H1922 (2004).

386. Gallo, D., Steinman, D. A. & Morbiducci, U. Insights into the co-localization of magnitude-based versus direction-based indicators of disturbed shear at the carotid bifurcation. *J. Biomech.* **49**, 2413–9 (2016).

387. Morbiducci, U. *et al.* A rational approach to defining principal axes of multidirectional wall shear stress in realistic vascular geometries, with application to the study of the influence of helical flow on wall shear stress directionality in aorta. *J. Biomech.* **48**, 899–906 (2015).

388. Siasos, G. *et al.* Local Low Shear Stress and Endothelial Dysfunction in Patients With Nonobstructive Coronary Atherosclerosis. *J. Am. Coll. Cardiol.* **71**, 2092–2102 (2018).

389. Aristokleous, N., Seimenis, I., Georgiou, G. C., Nicolaides, A. & Anayiotos, A. S. The effect of head rotation on the geometry and hemodynamics of healthy vertebral arteries. *Ann. Biomed. Eng.* **43**, 1287–97 (2015).

390. Condemi, F. *et al.* Fluid- and Biomechanical Analysis of Ascending Thoracic Aorta Aneurysm with Concomitant Aortic Insufficiency. *Ann. Biomed. Eng.* **45**, 2921–2932 (2017).

391. Pirola, S. *et al.* Computational study of aortic hemodynamics for patients with an abnormal aortic valve: The importance of secondary flow at the ascending aorta inlet. *APL Bioeng.* **2**, (2018).

392. Malvè, M., García, A., Ohayon, J. & Martínez, M. A. Unsteady blood flow and mass transfer of a human left coronary artery bifurcation: FSI vs. CFD. *Int. Commun. Heat Mass Transf.* **39**, 745–751 (2012).

393. Zeng, D., Ding, Z., Friedman, M. H. & Ethier, C. R. Effects of cardiac motion on right coronary artery hemodynamics. *Ann. Biomed. Eng.* **31**, 420–9 (2003).

394. Theodorakakos, A. *et al.* Simulation of cardiac motion on non-Newtonian, pulsating flow development in the human left anterior descending coronary artery. *Phys. Med. Biol.* **53**, 4875–4892 (2008).

395. Torii, R. *et al.* MR image-based geometric and hemodynamic investigation of the right coronary artery with dynamic vessel motion. *Ann. Biomed. Eng.* **38**, 2606–20 (2010).

396. Winkel, L. C., Hoogendoorn, A., Xing, R., Wentzel, J. J. & Van der Heiden, K. Animal models of surgically manipulated flow velocities to study shear stress-induced atherosclerosis. *Atherosclerosis* **241**, 100–110 (2015).

397. Nakashima, T., Iwanaga, Y. & Nakaura, Y. Pathological study of hypertensive heart. *Acta Pathol. Jpn.* **14**, 129–41 (1964).

398. Nakashima, T. & Tashiro, T. Early morphologic stage of human coronary atherosclerosis. *Kurume Med. J.* **15**, 235–42 (1968).

399. Fox, B. & Seed, W. A. Location of early atheroma in the human coronary arteries. *J. Biomech. Eng.* **103**, 208–12 (1981).

400. Fox, B., James, K., Morgan, B. & Seed, A. Distribution of fatty and fibrous plaques in young human coronary arteries. *Atherosclerosis* **41**, 337–47 (1982).

401. Morino, Y. *et al.* Intravascular ultrasound criteria for determination of optimal longitudinal positioning of sirolimus-eluting stents. *Circ. J.* **74**, 1609–16 (2010).

402. Takahashi, M. *et al.* Impact of the distance from the stent edge to the residual plaque on edge restenosis following everolimus-eluting stent implantation. *PLoS One* **10**, e0121079 (2015).

403. van Soest, G. *et al.* Atherosclerotic tissue characterization in vivo by optical coherence tomography attenuation imaging. *J. Biomed. Opt.* **15**, 011105

404. Gogas, B. D. *et al.* Edge vascular response after percutaneous coronary intervention: an intracoronary ultrasound and optical coherence tomography appraisal: from radioactive platforms to first- and second-generation drug-eluting stents and bioresorbable scaffolds. *JACC. Cardiovasc. Interv.* **6**, 211–21 (2013).

405. Wentzel, J. J. *et al.* Positive remodeling at 3 year follow up is associated with plaque-free coronary wall segment at baseline: a serial IVUS study. *Atherosclerosis* **236**, 82–90 (2014).

406. Costa, M. A. *et al.* Impact of stent deployment procedural factors on long-term effectiveness and safety of sirolimus-eluting stents (final results of the multicenter prospective STLLR trial). *Am. J. Cardiol.* **101**, 1704–11 (2008).

407. Teirstein, P. S. Drug-eluting stent restenosis: an uncommon yet pervasive problem. *Circulation* **122**, 5–7 (2010).

408. Moreno, R. *et al.* Drug-eluting stent thrombosis: results from a pooled analysis including 10 randomized studies. *J. Am. Coll. Cardiol.* **45**, 954–9 (2005).

409. Hoffmann, R. *et al.* Intravascular ultrasound predictors of angiographic restenosis in lesions treated with Palmaz-Schatz stents. *J. Am. Coll. Cardiol.* **31**, 43–9 (1998).

410. Prati, F. *et al.* Clinical Impact of OCT Findings During PCI: The CLI-OPCI II Study. *JACC. Cardiovasc. Imaging* **8**, 1297–305 (2015).

411. Kini, A. S. *et al.* Multimodality Intravascular Imaging to Predict Periprocedural Myocardial Infarction During Percutaneous Coronary Intervention. *JACC. Cardiovasc. Interv.* **8**, 937–45 (2015).

412. Hebsgaard, L. *et al.* Co-registration of optical coherence tomography and X-ray angiography in percutaneous coronary intervention. the Does Optical Coherence Tomography Optimize Revascularization (DOCTOR) fusion study. *Int. J. Cardiol.* **182**, 272–8 (2015).

413. Oemrawsingh, R. M. *et al.* Integrated Biomarker and Imaging Study 3 (IBIS-3) to assess the ability of rosuvastatin to decrease necrotic core in coronary arteries. *EuroIntervention* **12**, 734–739 (2016).

414. Simsek, C. *et al.* The ability of high dose rosuvastatin to improve plaque composition in non-intervened coronary arteries: rationale and design of the Integrated Biomarker and Imaging Study-3 (IBIS-3). *EuroIntervention* **8**, 235–241 (2012).

415. Taylor, A. J. *et al.* Coronary Calcium Independently Predicts Incident Premature Coronary Heart Disease Over Measured Cardiovascular Risk Factors. *J. Am. Coll. Cardiol.* **46**, 807–814 (2005).

416. Barrett, H. E., Van der Heiden, K., Farrell, E., Gijsen, F. J. H. & Akyildiz, A. C. Calcifications in atherosclerotic plaques and impact on plaque biomechanics. *J. Biomech.* **87**, 1–12 (2019).

417. Puchner, S. B. *et al.* Differences in the association of total versus local coronary artery calcium with acute coronary syndrome and culprit lesions in patients with acute chest pain: The coronary calcium paradox. *Atherosclerosis* **274**, 251–257 (2018).

418. Mintz, G. S. *et al.* American College of Cardiology clinical expert consensus document on standards for acquisition, measurement and reporting of intravascular ultrasound studies (ivus): A report of the american college of cardiology task force on clinical expert consensus documents developed in collaboration with the european society of cardiology endorsed by the society of cardiac angiography and interventions. *J. Am. Coll. Cardiol.* **37**, 1478–1492 (2001).

419. Kawase, Y. *et al.* Comparison of nonuniform rotational distortion between mechanical IVUS and OCT using a phantom model. *Ultrasound Med. Biol.* **33**, 67–73 (2007).

420. Kini, A. S. *et al.* Changes in Plaque Lipid Content After Short-Term Intensive Versus Standard Statin Therapy. *J. Am. Coll. Cardiol.* **62**, 21–29 (2013).

421. Waksman, R. Assessment of coronary near-infrared spectroscopy imaging to detect vulnerable plaques and vulnerable patients. *TCT 2018* (2018).

422. Pu, J. *et al.* Insights into echo-attenuated plaques, echolucent plaques, and plaques with spotty calcification: novel findings from comparisons among intravascular ultrasound, near-infrared spectroscopy, and pathological histology in 2,294 human coronary artery segments. *J. Am. Coll. Cardiol.* **63**, 2220–33 (2014).

423. Shanahan, C. M. Inflammation Ushers in Calcification. *Circulation* **116**, 2782–2785 (2007).

424. Nakahara, T. *et al.* Coronary Artery Calcification: From Mechanism to Molecular Imaging. *JACC Cardiovasc. Imaging* **10**, 582–593 (2017).

425. Kang, S.-J. *et al.* Combined IVUS and NIRS Detection of Fibroatheromas. *JACC Cardiovasc. Imaging* **8**, 184–194 (2015).

426. Puri, R. *et al.* Near-Infrared Spectroscopy Enhances Intravascular Ultrasound Assessment of Vulnerable Coronary Plaque: A Combined Pathological and In Vivo Study. *Arterioscler. Thromb. Vasc. Biol.* **35**, 2423–31 (2015).

427. Criqui, M. H. *et al.* Calcium Density of Coronary Artery Plaque and Risk of Incident Cardiovascular Events. *JAMA* **311**, 271 (2014).

428. Beckman, J. A., Ganz, J., Creager, M. A., Ganz, P. & Kinlay, S. Relationship of clinical presentation and calcification of culprit coronary artery stenoses. *Arterioscler. Thromb. Vasc. Biol.* **21**, 1618–22 (2001).

429. Getz, G. S. & Reardon, C. A. Diet and murine atherosclerosis. *Arterioscler. Thromb. Vasc. Biol.* **26**, 242–9 (2006).

430. Varga, O., Harangi, M., Olsson, I. A. S. & Hansen, A. K. Contribution of animal models to the understanding of the metabolic syndrome: a systematic overview. *Obes. Rev.* **11**, 792–807 (2010).

431. Arbab-Zadeh, A. & Fuster, V. The myth of the 'vulnerable plaque': transitioning from a focus on individual lesions to atherosclerotic disease burden for coronary artery disease risk assessment. *J. Am. Coll. Cardiol.* **65**, 846–55 (2015).

432. Takano, M. *et al.* Angioscopic follow-up study of coronary ruptured plaques in nonculprit lesions. *J. Am. Coll. Cardiol.* **45**, 652–658 (2005).

433. Tanaka, A. *et al.* Distribution and Frequency of Thin-Capped Fibroatheromas and Ruptured Plaques in the Entire Culprit Coronary Artery in Patients With Acute Coronary Syndrome as Determined by Optical Coherence Tomography. *Am. J. Cardiol.* **102**, 975–979 (2008).

434. Levine, G. N. *et al.* 2011 ACCF/AHA/SCAI Guideline for Percutaneous Coronary Intervention. *J. Am. Coll. Cardiol.* **58**, e44–e122 (2011).

435. Smilowitz, N. R. & Feit, F. The History of Primary Angioplasty and Stenting for Acute Myocardial Infarction. *Curr. Cardiol. Rep.* **18**, 5 (2016).

436. Roger, V. L. Epidemiology of Heart Failure. *Circ. Res.* **113**, 646–659 (2013).

437. Nichols, M., Townsend, N., Scarborough, P. & Rayner, M. Cardiovascular disease in Europe 2014: epidemiological update. *Eur. Heart J.* **35**, 2950–2959 (2014).

438. Papafaklis, M. I., Mavrogiannis, M. C. & Stone, P. H. Identifying the progression of coronary artery disease: prediction of cardiac events. *Contin. Cardiol. Educ.* **2**, 105–114 (2016).

439. Oosterveer, D. M. *et al.* Clinical and genetic factors influencing cardiovascular risk in patients with familial hypercholesterolemia. *Clin. Lipidol.* **5**, 189–197 (2010).

440. Banach, M. *et al.* Statin intolerance - an attempt at a unified definition. Position paper from an International Lipid Expert Panel. *Arch. Med. Sci.* **11**, 1–23 (2015).

441. Stamler, J., Wentworth, D. & Neaton, J. D. Is relationship between serum cholesterol and risk of premature death from coronary heart disease continuous and graded? Findings in 356,222 primary screenees of the Multiple Risk Factor Intervention Trial (MRFIT). *JAMA* **256**, 2823–8 (1986).

442. Samady, H. *et al.* Coronary Artery Wall Shear Stress Is Associated With Progression and Transformation of Atherosclerotic Plaque and Arterial Remodeling in Patients With Coronary Artery Disease. *Circulation* **124**, 779–788 (2011).

443. Molony, D. S. *et al.* An assessment of intra-patient variability on observed relationships between wall shear stress and plaque progression in coronary arteries. *Biomed. Eng. Online* **14**, (2015).

444. Harloff, A. *et al.* 3D Blood Flow Characteristics in the Carotid Artery Bifurcation Assessed by Flow-Sensitive 4D MRI at 3T. *Magn. Reson. Med.* **61**, 65–74 (2009).

445. Yabushita, H. *et al.* Characterization of Human Atherosclerosis by Optical Coherence Tomography. *Circulation* **106**, 1640–1645 (2002).

446. Zahnd, G. *et al.* Contour segmentation of the intima, media, and adventitia layers in intracoronary OCT images: application to fully automatic detection of healthy wall regions. *Int. J. Comput. Assist. Radiol. Surg.* **12**, 1923–1936 (2017).

447. Greenland, P., Blaha, M. J., Budoff, M. J., Erbel, R. & Watson, K. E. Coronary Calcium Score and Cardiovascular Risk. *J. Am. Coll. Cardiol.* **72**, 434–447 (2018).

448. Korosoglou, G., Giusca, S. & Katus, H. A. The coronary calcium paradox: Yet another step towards the differentiation between stable and rupture-prone coronary plaques? *Atherosclerosis* **274**, 232–234 (2018).

449. Filho, E. dos S. *et al.* Automated Calcification Detection and Quantification in Intravascular Ultrasound Images by Adaptive Thresholding. *World Congr. Med. Phys. Biomed. Eng. 2006* 1421–1425 (2007).

450. Gao, Z. *et al.* Automated Detection Framework of the Calcified Plaque with Acoustic Shadowing in IVUS Images. *PLoS One* **9**, e109997 (2014).

451. Yin, J. *et al.* Integrated intravascular optical coherence tomography ultrasound imaging system. *J. Biomed. Opt.* **15**, (2010).

452. Ughi, G. J. *et al.* Clinical Characterization of Coronary Atherosclerosis With Dual-Modality OCT and Near-Infrared Autofluorescence Imaging. *JACC. Cardiovasc. Imaging* **9**, 1304–1314 (2016).

453. Verjans, J. W. *et al.* Targeted Near-Infrared Fluorescence Imaging of Atherosclerosis. *JACC Cardiovasc. Imaging* **9**, 1087–1095 (2016).

454. Abran, M. *et al.* Validating a bimodal intravascular ultrasound (IVUS) and near-infrared fluorescence (NIRF) catheter for atherosclerotic plaque detection in rabbits. *Biomed. Opt. Express* **6**, 3989 (2015).

455. Li, Y. *et al.* Fully integrated optical coherence tomography, ultrasound, and indocyanine green-based fluorescence tri-modality system for intravascular imaging. *Biomed. Opt. Express* **8**, 1036–1044 (2017).

456. Bec, J. *et al.* Design, construction, and validation of a rotary multifunctional intravascular diagnostic catheter combining multispectral fluorescence lifetime imaging and intravascular ultrasound. *J. Biomed. Opt.* **17**, (2012).

457. Wu, M., van der Steen, A. F. W., Regar, E. & van Soest, G. Emerging Technology Update Intravascular Photoacoustic Imaging of Vulnerable Atherosclerotic Plaque. *Interv. Cardiol.* **11**, 120–123 (2016).

458. Wessler, B. S. *et al.* Clinical Prediction Models for Cardiovascular Disease. *Circ. Cardiovasc. Qual. Outcomes* **8**, 368–375 (2015).

459. Damen, J. A. A. G. *et al.* Prediction models for cardiovascular disease risk in the general population: systematic review. *BMJ* **353**, i2416 (2016).

NEDERLANDSE SAMENVATTING

Ziekte van de kransslagaders van het hart (coronairen) is een van de belangrijkste doodsoorzaken in de Westerse wereld. Het proces dat ten grondslag ligt aan veel coronaire hartziekten is het ontstaan van aderverkalking, ook wel atherosclerose genoemd. Atherosclerose is een ziekte waarbij vetten en ontstekingscellen in de vaatwand ophopen en een 'plaque' vormen. Het groeien en scheuren van een (onstabiele) atherosclerotische plaque kan, geleidelijk of heel acuut, leiden tot een afname of volledige afsluiting van de bloedtoevoer naar de hartspier. Als deze afsluiting niet snel wordt verholpen kan dit leiden tot permanente schade aan de hartspier (een hartinfarct). Een groot hartinfarct kan hartfalen of zelfs de dood tot gevolg hebben. Ondanks jarenlang onderzoek blijft het exacte mechanisme waarmee atherosclerotische plaques ontstaan, onstabieler worden en uiteindelijk scheuren onduidelijk. Om medicatie ontwikkeling te ondersteunen, om vroege risico-inschatting voor een individuele patiënt mogelijk te maken en om klinische beslisvorming te verbeteren, is meer kennis nodig over het ziekteproces. In dit proefschrift zijn invasieve beeldvorming, histopathologische studies en biomechanische modellering van atherosclerose zoals geïntroduceerd in **Hoofdstuk 1** gecombineerd om: 1) bestaande diermodellen voor atherosclerose te beschrijven, en om te bediscussiëren wat de rol is van biomechanische factoren bij het ontstaan van atherosclerose in deze diermodellen; 2) verder te ontrafelen wat de rol is van de biomechanische factoren wandschuifspanning en helixvormige bloedstroming in de ontwikkeling van atherosclerose en om te beoordelen wat de potentie is van deze biomechanische factoren, en van specifieke lipoproteïnen in het bloed, als nieuwe biomarkers voor plaque ontwikkeling; 3) de interpretatie van twee veelgebruikte invasieve beeldvormingstechnieken uit te breiden om zo de behandeling van patiënten en de risico-inschatting op acute cardiovasculaire gebeurtenissen te verbeteren.

Diermodellen voor atherosclerose

In de mens is het uitdagend om het ontstaan en de progressie van coronaire atherosclerose te onderzoeken. Ten eerste kost het jaren om veranderingen in plaque grootte en compositie te kunnen waarnemen. Daarnaast is het vaak niet mogelijk om uitgebreide invasieve beeldvormingsonderzoeken op meerdere momenten over de tijd uit te voeren. Verder kan er geen weefsel verzameld worden om op celniveau de samenstelling van de plaques te bestuderen. In diermodellen gaat de ziekteontwikkeling vaak sneller en is het meestal wel mogelijk om invasieve beeldvorming op meerdere tijdspunten uit te voeren en om weefsel te verzamelen. Om deze redenen zijn diermodellen die het coronaire atherosclerotische ziekteproces van de mens nabootsen

zeer waardevol. In **Deel I** van dit proefschrift beschreven we verschillende bestaande atherosclerotische diermodellen en hebben we bediscussieerd wat de rol is van biomechanica in het ontstaan en destabiliseren van de plaques die ontstaan in deze modellen.

In **Hoofdstuk 2** hebben we een literatuuroverzicht gegeven van diermodellen die ruptuur van een atherosclerotische plaque laten zien. De waarneming van plaque ruptuur in een atherosclerotisch diermodel wordt vaak gezien als het ultieme bewijs van de aanwezigheid van onstabiele plaques die veel overeenkomst vertonen met humane plaques. Hoewel bij mensen plaque ruptuur spontaan voorkomt, concludeerden we in dit hoofdstuk dat de plaque rupturen in de bestudeerde diermodellen nooit ontstonden op een natuurlijke wijze, maar altijd het gevolg waren van ingrijpende farmaceutische of chirurgische interventies. Het feit dat we in diermodellen onze toevlucht moeten nemen tot dit soort interventies om plaque ruptuur te induceren kan verklaard worden door een aantal grote verschillen tussen mensen en de meeste proefdiermodellen. Deze verschillen zitten onder andere in plaque compositie, onderliggende biologische processen en biomechanische factoren welke direct invloed hebben op de plaque ontwikkeling en op het proces van plaque ruptuur. Na vergelijking van de verschillende diermodellen bleek dat atherosclerotische varkens het beste de menselijke plaque samenstelling en de biomechanische omgeving van de plaque kunnen nabootsen. Ondanks het feit dat deze factoren dus goed overeenkomen, werden onstabiele plaques en plaque ruptuur nog nauwelijks geobserveerd in alle bestaande varkens modellen.

In **Hoofdstuk 3** is een overzicht beschreven van studies waarin onderzocht werd of de ontwikkeling van atherosclerose in diermodellen gestimuleerd kan worden door het chirurgisch manipuleren van de bloedstroomsnelheid en daarmee van de wandschuifspanning. Wandschuifspanning is de wrijvingskracht die ontstaat tussen het stromende bloed en de endotheelcellen die de bloedvatwand bedekken. Het is een belangrijke biomechanische factor die betrokken is bij het ontstaan van atherosclerose. De beschreven studies gebruikten chirurgische technieken, zoals het maken van een arterioveneuze fistel, het implanteren van een vasculaire bypass, een arteriële ligatie of het plaatsen van een perivasculair implantaat om de wandschuifspanning te manipuleren en daarmee het ontstaan van atherosclerose te induceren. Veel van de beschreven chirurgische technieken bleken succesvol in het induceren van atherosclerose. We waarschuwden echter dat deze chirurgische manipulaties de integriteit van de vaatwand en de wandspanning verstoren, wat van invloed kan zijn op de onderzochte relatie tussen wandschuifspanning en atherosclerose ontwikkeling. Het tandem-ligatie muismodel was het model waarbij, in vergelijking met de andere beschreven modellen, de gebruikte chirurgische techniek het bestudeerde ziekteproces het minste leek te beïnvloeden. Daarnaast resulteerde het gebruikt van deze chirurgische techniek in

dit model in de ontwikkeling van grote, geavanceerde plaques wat het model zeer bruikbaar maakt voor toekomstige studies.

Biomarkers voor atherosclerose

In **Deel II** van dit proefschrift werd onderzocht wat de bijdrage is van wandschuifspanning, van helixvormige bloedstroming, en van specifieke lipoproteïnen in het bloed aan de ontwikkeling van atherosclerotische plaques. Daarnaast werd gekeken of deze factoren zouden kunnen dienen als biomarkers om de risico-inschatting bij coronaire atherosclerose te verbeteren. De potentie van deze biomarkers werd zowel bestudeerd in een atherosclerotisch diermodel, als in twee patiënten cohorten.

Naar aanleiding van de studies beschreven in Hoofdstuk 2 en 3 concludeerden we dat er geen enkel diermodel bestaat waarin plaques ontstaan met een humane plaque grootte, samenstelling en biomechanische omgeving. Om deze reden hebben we een al bestaand familiair hypercholesterolemisch varkensmodel voor atherosclerose verder verfijnd door alleen volwassen dieren te gebruiken (**Hoofdstuk 4**). De hogere leeftijd van de dieren verbeterde de capaciteit van het model om meer humane plaques te ontwikkelen. De groei van coronaire plaques in dit model hebben we in kaart gebracht met behulp van invasieve beeldvorming op meerdere tijdspunten. Daarnaast werd de resulterende plaque samenstelling in detail bestudeerd met histopathologie. De resultaten lieten zien dat de helft van de varkens alleen vroege, stabiele plaques ontwikkelden. In de andere helft van de varkens ontwikkelden zich, verspreid door het hele coronaire vaatbed, grote, vaatvernauwende plaques die duidelijk kenmerken vertoonden van een onstabiel plaque fenotype. Vergelijkbare plaques worden maar zelden in andere diermodellen aangetroffen wat laat zien dat dit verfijnde model zeer geschikt is voor toekomstige studies. Om de grote verschillen in atherosclerose ontwikkeling tussen de twee groepen varkens te verklaren hebben we een uitgebreide plasma lipoproteïne analyse uitgevoerd. In deze analyse hebben we de lipoproteïne deeltjes opeenvolgend op dichtheid en op grootte gescheiden. Met behulp van deze analyse ontdekten we een specifiek lage-dichtheid lipoproteïne (LDL) profiel met ‘normaal’ en ‘groter’ LDL. De verdeling van cholesterol en sfingolipiden over deze specifieke LDL-subtypen konden we direct relateren aan de ernst van ziekteontwikkeling in de varkens. In een eerste klinische test hebben we dezelfde lipoproteïne analyse uitgevoerd op het plasma van drie homozygoot familiare hypercholesterolemie patiënten. Met behulp van deze analyse ontdekten we dat ook patiënten de twee LDL-subtypen hebben en dat de verdeling van cholesterol over deze subtypen sterk verschilt per patiënt. Deze variëteit in cholesterol LDL-profiel duidt erop dat er mogelijk ook bij patiënten een verband is tussen dit LDL-profiel en de ontwikkeling van hart- en vaatziekten. Toekomstige grotere patiëntenstudies zullen dit verder moeten uitwijzen.

Zoals beschreven in Hoofdstuk 3 zijn biomechanische factoren, zoals de wandschuifspanning, betrokken bij de ontwikkeling van atherosclerotische plaques. De rol die de wandschuifspanning speelt in dit proces is echter complex omdat zowel hoge als lage niveaus van wandschuifspanning in het verleden zijn geassocieerd met plaque groei en met veranderingen in plaque compositie. Daarnaast wordt in veel studies niet meegenomen dat de wandschuifspanning verandert van richting gedurende de hartcyclus. Om meer inzicht te krijgen in deze processen hebben we de rol van multidirectionele wandschuifspanning in de ontwikkeling van coronaire atherosclerotische plaques bestudeerd (**Hoofdstuk 5**). Hierbij hebben we gebruik gemaakt van het atherosclerotische varkensmodel uit Hoofdstuk 4. De resultaten van de studie in Hoofdstuk 5 lieten zien dat plaques het snelst groeiden in gebieden met lage wandschuifspanning (gemiddeld over de hartcyclus), of met hoge multidirectionele wandschuifspanning. Dit verband observeerden we zowel gedurende plaque initiatie als tijdens plaque progressie. Als we naar veranderingen van wandschuifspanning over de tijd keken, zagen we dat de uiteindelijk grootste plaques zich bevonden in regio's waar eerst lage en vervolgens hoge wandschuifspanning werd geobserveerd. Kijkend naar multidirectionele wandschuifspanning bevonden de grootste plaques zich in gebieden met initieel hoge niveaus multidirectionele wandschuifspanning, die vervolgens verlaagden over de tijd. Deze beide observaties zijn waarschijnlijk het gevolg van de groei van de plaques in het lumen van het vat, waardoor het vat vernauwt. Deze vernauwing beïnvloed direct de bloedstroomsnelheid en dus de wandschuifspanning op de locatie van de plaque. In deze zelfde gebieden zagen we dat na de verhoging in wandschuifspanning, de groeisnelheid van de plaques afnam. Naast deze observationele studie hebben we bekeken of wandschuifspanning een goede voorspeller zou kunnen zijn voor het ontstaan van plaques met een hoog risico op scheuring. De verschillende wandschuifspanningsfactoren bleke plaque groei goed te kunnen voorspellen, maar de voorspelling van het ontstaan van een plaque met een hoog-risico compositie was nog beter. Concluderend kunnen we zeggen dat multidirectionele wandschuifspanning betrokken is bij plaque initiatie en progressie. Lage wandschuifspanning (gemiddeld over de hartcyclus) blijft echter de sterkste voorspeller voor de ontwikkeling van plaques met een onstabiel fenotype.

In **Hoofdstuk 6** hebben we bekeken of de relatie tussen multidirectionele wandschuifspanning en plaque groei, zoals waargenomen in het atherosclerotische diermodel in Hoofdstuk 5, ook terug te vinden was in patiënten met coronaire atherosclerose. In deze patiënten hebben we de wandschuifspanning en veranderingen in plaque grootte en compositie in kaart gebracht door gebruik te maken van invasieve beeldvorming op het eerste tijdspunt tijdens een dotterprocedure, en na een jaar. De resultaten lieten zien dat plaque groei in patiënten het beste kon worden voorspeld

als informatie over multidirectionele wandschuifspanning gecombineerd werd met informatie over de lipiden-samenstelling van de plaques. Deze bevindingen kunnen mogelijk bijdragen aan de klinische beslisvorming tijdens interventieprocedures, zodat toekomstige acute coronaire gebeurtenissen beter voorkomen kunnen worden.

Verschillende beeldvormingsstudies hebben laten zien dat bloed in een helixvormig patroon door slagaders stroomt. Of dit helixvormige stromingspatroon ook aanwezig is in coronairen, en of dit stromingspatroon invloed heeft op het ontstaan van atherosclerose was nog niet eerder onderzocht. In de studie beschreven in **Hoofdstuk 7** hebben we aangetoond dat de bloedstroming in coronairen van ons varkensmodel uit Hoofdstuk 4 gekarakteriseerd wordt door tegengesteld draaiende helixvormige stromingsstructuren. De parameters waarmee verschillende karakteristieken van deze helixvormige stroming gekwantificeerd kunnen worden, waren sterk en invers gerelateerd aan (multidirectionele) wandschuifspanningsparameters. Deze relatie weerspiegelde een mogelijk beschermend effect van spiraalvormige bloedstroming tegen atherosclerose. De bevinding dat een hoge intensiteit van spiraalvormige stroming geassocieerd was met een vermindering van de plaque groei bevestigde deze hypothese. Met deze studie hebben we voor het eerst laten zien dat er een relatie bestaat tussen spiraalvormige bloedstroming en bescherming tegen de vorming van coronaire atherosclerose.

Invasieve beeldvormingsmarkers van atherosclerose

In **Deel III** van dit proefschrift zijn twee studies beschreven waarin we twee plaque-kenmerken bestudeerd hebben die gedetecteerd kunnen worden met invasieve beeldvorming: de hoek van de plaque-vrije wand en de lokale aanwezigheid van calcificaties. Meer kennis over deze plaquekenmerken zou kunnen bijdragen aan het beter interpreteren van invasieve beelden van de plaques, waarmee ook de toepassingen van deze invasieve beeldvormingstechnieken verder zou kunnen worden uitgebreid.

Optische Coherentie Tomografie (OCT) is een belangrijke beeldvormingstechniek voor het begeleiden van stent-plaatsingsprocedures. Hoewel OCT zeer hoog-resolutie beelden oplevert en lipiden in de vaatwand kan detecteren, heeft deze techniek een gelimiteerde penetratiediepte. Hierdoor is de capaciteit van OCT om de buitenwand van het vat, en daarmee de grootte van een plaque te detecteren, beperkt. Dit is een groot nadeel omdat de grootte van de plaque een belangrijke graadmeter is voor plaque stabiliteit en voor het bepalen van de plaatsingslocatie van een stent. In **Hoofdstuk 8** hebben we geanalyseerd of de hoek van de plaque-vrije wand kon dienen als surrogaatmarker voor de grootte van de plaque. Gekoppelde OCT en intravasculaire

ultrageluid (IVUS) beelden van patiënten met coronaire atherosclerose werden gebruikt om te laten zien dat de hoek van de plaque-vrije wand op OCT een sterke relatie had met de plaque grootte gedetecteerd op IVUS. Daarnaast konden we laten zien dat, voor een optimale plaatsingslocatie van een stent, de afkapwaarde van de OCT-gedetecteerde plaque-vrije wand een hoek is van ≥220°.

Naast de grootte van de plaque, is ook de plaque compositie van belang voor het inschatten van het risico van een individuele patiënt. Zowel sterk verkalkte vaten (zoals gedetecteerd met CT-beeldvorming) als lipide-rijke vaten (zoals gedetecteerd met infraroodspectroscopie (NIRS)) zijn geassocieerd met acute cardiovasculaire gebeurtenissen. Er was echter nog weinig bekend over hoe vaak deze twee plaque componenten zich tegelijk op dezelfde plaats bevinden. In **Hoofdstuk 9** hebben we NIRS-IVUS-beelden geanalyseerd van patiënten met vergevorderde coronaire atherosclerose. Deze beelden lieten zien dat de totale hoeveelheid calcificaties en de totale hoeveelheid lipiden in een individueel vat zwak met elkaar gecorreleerd waren. Als echter op een meer lokaal niveau gekeken werd, in 4 millimeter regio's of in individuele frames van de invasieve opnames, bleek dat de regio's met de meeste lipiden vaak ook veel calcificaties bevatten. Deze resultaten laten zien dat potentieel stabiliserende calcificaties en destabiliserende lipiden vaak op één locatie voorkomen. Of deze bevindingen behulpzaam kunnen zijn in klinische beslisvorming moet blijken uit toekomstige studies waarin cardiovasculaire events geregistreerd worden.

DANKWOORD / ACKNOWLEDGMENTS

Deze laatste bladzijden zijn er voor de mensen die onmisbaar waren in het tot stand komen van dit proefschrift, maar vooral ook voor diegenen zonder wie de afgelopen vijf jaar een stuk minder leuk zouden zijn geweest. Bijna zes jaar geleden liep ik voor het eerst binnen bij de biomechanica groep om te beginnen aan mijn laatste master stage. Ik werd ontvangen in een warm bad van leuke, geïnteresseerde mensen waarbij ik me meteen thuis voelde. Tijdens deze stage kreeg ik het aanbod om te solliciteren op het ERC-project van Jolanda. Uiteindelijk heb ik maar kort getwijfeld om deze PhD-positie aan te nemen en daar heb ik geen moment spijt van gehad.

Jolanda, het zou gek zijn om dit dankwoord niet met jou te beginnen. Jouw enthousiasme tijdens mijn eerste onofficiële sollicitatiegesprek was aanstekelijk en heeft zeker bijgedragen aan het feit dat ik 'ja' heb gezegd om bij jullie te komen werken. Ik wil je bedanken voor de vele, vele uren overleggen, discussiëren en brainstormen. Hoewel we het lang niet altijd eens waren over hoe we sommige dingen moesten aanpakken en ik soms de advocaat van de duivel speelde, bleef jij altijd het positieve van de situatie inzien. Ik bewonder de manier waarop je altijd weer een nieuwe invalshoek weet te vinden bij het interpreteren van data en je enorme werkethos (al vraag ik me soms af hoe je het volhoudt). Naast deze meer praktische kant ben ik je dankbaar voor de vrijheid die je me altijd hebt gegeven om mijn projecten zelf op te zetten, voor je luisterend oor en voor het altijd klaarstaan om me te helpen als ik tegen organisatorische of politieke problemen aanliep. Veel dank voor alles!

Beste **Ton**, ik bewonder en heb veel geleerd van je no-nonsense en get-to-the-point politiek. Hoewel mijn project niet helemaal in jouw expertise veld lag, wist ik wel dat ik altijd bij je terecht kon met 'politieke' problemen, of simpelweg om de juiste persoon te vinden binnen dat gigantische netwerk van je. In combinatie met Dirk-Jan vormde jij denk ik het optimale promotoren-koppel. **Dirk-Jan**, hoe meer gesprekken ik met je voerde, hoe meer ik onder de indruk raakte van jouw enorme kennis over zo ongeveer ieder cardiovasculair onderwerp dat ik maar kan bedenken. Ik ben ontzettend blij dat je het verzoek accepteerde om mijn tweede promotor te worden. Dit niet alleen vanwege de varkens experimenten die we bij jullie op de afdeling uitvoerden, maar ook vanwege je kennis en kunde in het opzetten van de experimenten en het interpreteren van de resultaten. Hoewel ik bij jou altijd de druk voelde om nog harder te werken, kon ik altijd bij je terecht met vragen over mijn onderzoek, maar ook om discussies te voeren over het vervolg van mijn carrière. Ook veel dank voor het ondersteunen van mijn PostDoc avontuur in Australië!

Beste leden van mijn leescommissie, beste **Prof. Daemen**, **Prof. Zijlstra** en **Dr. Roeters van Lennep** (beste Jeanine), veel dank voor het zitting nemen in mijn commissie en voor het grondig en kritisch lezen van mijn thesis. Beste Prof. Daemen, ik heb veel geleerd van onze discussies tijdens het schrijven van het review over ruptuurmodellen. De vraag 'maar waarom dan?' blijft sindsdien altijd door mijn hoofd spoken. Beste Jeanine, ik ben vereerd dat je in mijn commissie wilde plaatsnemen ondanks dat er maar een (half) hoofdstuk binnen jouw expertisegebied valt. Je bent een groot voorbeeld voor vrouwen in de geneeskunde én wetenschap en ik ben blij dat je als UHD'er in mijn commissie zit!

Dear other committee members, dear **Prof. Muller**, **Prof. Evans**, **Dr. Regar** (dear Evelyn), I feel honoured that you are willing to travel all the way to Rotterdam to form the opposition during my defence. You have been a great inspiration during the conferences we joined in the past and I hope that we will meet again in the future. Dear Evelyn, thank you for all your help with the IMPACT and Plaque-free wall studies.

Naast goede begeleiding zijn directe collega's eigenlijk onmisbaar voor het succesvol doorlopen van een PhD project. Ook ik heb menig rollercoaster van emoties, successen en vooral heel veel wachten doorgemaakt, en het delen van deze ervaringen met kamer/labgenootjes maakte dit allemaal een stukje makkelijker.

Eline, dank dat jij als paranimf naast mij wilt staan. Ik moet toegeven dat ik even de kat uit de boom moest kijken in de eerste periode dat je op het lab kwam en me heb afgevraagd wie deze aanwezige, veel te snel denkende en niet op haar mondje gevallen persoon was. Al snel was ik echter ontzettend gelukkig met jou als project- en kamergenoot. Je hebt de IMPACT-studie een enorme boost gegeven en het samenwerken binnen zowel de patiënten- als de varkensstudie heeft beide projecten veel goed gedaan. We hebben de afgelopen jaren aardig wat wetenschappelijke en persoonlijke ups en downs gedeeld, maar ook ontzettend veel lol gehad. Mijn productiviteit was misschien niet altijd even hoog met jou op de kamer, maar ik had je voor geen goud willen ruilen voor iemand anders.

Lieve **Astrid**, tijdens ons tripje naar San Francisco hebben we elkaar denk ik pas goed leren kennen en hier ben ik nog steeds heel blij om. Dank voor alle gezelligheid, de goede gesprekken en het soms zijn van een duiveltje in een onschuldig ogend persoon. Naast collega's zijn we ondertussen vrienden geworden en ik hoop dat we elkaar in de toekomst nog blijven zien! Alle goeds voor jou, Thomas en Jasmijn!

Om ons team van biomedicus en arts compleet te maken, dank **Annette**, voor de broodnodige technische input en voor de enorme pipeline die je hebt opgezet voor de shear stress berekeningen in de varkens- en patiëntenstudie. Hoewel we elkaar door onze verschillende achtergronden niet altijd helemaal begrepen, zijn we er denk ik toch

in geslaagd het project tot een succes te maken. Ik ben heel blij dat je inmiddels een baan hebt gevonden die erg goed bij je lijkt te passen!

Ilona, een paar zinnen in dit dankwoord gaan nooit genoeg zijn om je te bedanken voor alle idiote dingen die je voor ons project hebt gedaan: voor iedere OK dag stond de wekker om half 4 ’s ochtends; op onze knieën kruipen door de hokken; de zware beesten vanuit de meest onmogelijke hoeken tillen; je lange flexibele vriend (en niet te vergeten de stijve vrienden van onze lieve katheter bouwers); en nee, toch nog één extra pullback, en zo kan ik nog wel even doorgaan. Ik heb altijd enorme waardering gehad voor je ongezouten mening en vele malen dank voor het feit dat je altijd klaarstond als het nodig was. Stiekem mis ik onze gezellig klets (/roddel) CT-uurtjes en de toch wel heel gezellige OK dagen nog wel eens. Voor de zojuist genoemde lijst aan activiteiten moet ik nog een onmisbaar persoon bedanken: **Maaike**. Vanaf het opzetten van de ethische commissie toestemming ben je betrokken geweest bij dit project. Ik heb veel bewondering voor je rust en je eindeloze geduld, voor je enorme kennis, kunde en inzicht en ik ben je erg dankbaar voor het feit dat ook jij altijd klaar stond om te helpen. Ik denk dat jij een van de belangrijkste schakels bent in het functioneren van de experimentele cardio afdeling en ik ben enorm blij dat je zoveel hebt geholpen bij dit project.

Karen, ook veel dank aan jou voor je hulp bij de varkensexperimenten. Je kennis en kunde over de katheters en katheterisatietechnieken waren onmisbaar. Je no-nonsense mentaliteit paste goed binnen ons team (alleen al omdat het ‘randje’ plaque - dat toch eigenlijk niks voorstelde - op een gegeven moment een begrip is geworden). En dan natuurlijk ook lieve **Jurgen**, ondanks je enorme allergie voor varkens stond je erop bij de eerste experimenten aanwezig te zijn. Al kreeg je na een paar uur bijna geen lucht meer, je weigerde de OK te verlaten. Veel dank voor het overbrengen van al je kennis over het interpreteren van OCT- en IVUS-beelden en voor de heerlijke verhalen waardoor de gesprekken met jou altijd langer duurden dan gepland.

Dennis en **Vincent**, niet alleen zorgde jullie strakke organisatie ervoor dat mijn varkentjes op en top verzorgd werden en was het altijd weer gezellig als we beneden kwamen, daarnaast waren jullie zo gek om me meerdere malen uit de brand te helpen met de idioot vroege CT-experimenten (zelfs ondanks de vele malen verplicht douchen per dag). Ik ben jullie veel dank verschuldigd, net als aan alle andere mensen beneden in het EDC!

En dan is er nog een lange lijst personen die ook veel bijgedragen hebben voor, tijdens of na de experiment dagen. Allereerst **Dylan**: je begon als student op ons lab en bleef uiteindelijk nog een lange tijd hangen als analist. Wat heb ik hier geluk mee gehad. Niet

alleen heb je op een heel nauwkeurige en gestructureerde manier een ongelooflijke berg coupes gesneden, gekleurd en ingescand, ook was je zo gek om mee te helpen met de CTs, OKs en met het vervolgens verwerken van het weefsel. Daarnaast zullen we de geur van je eiwitshakes en de strak naast elkaar geplaatste pennen op je bureau niet snel vergeten. Vele malen dank voor alle hulp en gezelligheid! En dan de andere belangrijke leden van het A-team (dank Robert voor deze term): de studenten die ik mocht begeleiden. **Channa**, **Jessica**, **Merel**, **Bowen**, **Mees**, **Noah** en **Jaëla**. Ik heb ontzettend veel van jullie geleerd (hopelijk is dat wederzijds), jullie brachten veel gezelligheid in het lab en zonder jullie zou ik de komende 5 jaar nog steeds coupes aan het snijden zijn. Veel dank en het ga jullie goed in jullie vervolgopleidingen/werk! **Kim v. G.**, je hulp met het begeleiden van studenten, het opzetten van de weefselverwerkings- en kleuringsprotocollen, het inbedden, snijden en kleuren en al je andere kennis en kunde op het gebied van histologie waren onmisbaar in mijn project. Daarnaast was het ook gewoon ontzettend gezellig om je in het team en op het lab te hebben! **Sadhana**, in het half jaar dat je Kim hebt vervangen heb je een berg histologisch werk verzet en was je ook gewoon een heel leuk lid van ons lab. Dank! **Liesbeth** en **Robert**, bedankt voor alle technische ondersteuning voor en tijdens de OKs. Als er weer eens iets niet werkte of er iets kapot was kon ik altijd bij jullie terecht voor een snelle oplossing. En Liesbeth, ook dank voor het vele malen helpen met het, al wankelend op de ladders, ophangen van de zeilen tussen de OKs en het afzetten van de gang. **Ruben**, **Metin, Annemarie** en **Geraldine**, bedankt voor het af en toe bijspringen tijdens de OKs!

Voor onze CT-experimenten togen we in de hele vroege uurtjes naar de Radiologie afdeling. **Marcel**, **Adriaan, Koen** en **Maarten**, veel dank voor het opzetten en maken van de CT-scans, veelal buiten jullie werktijden om!

For the use of a ComboMap device we were fortunate enough to get in touch with the group of Maria Siebes in Amsterdam. Dear **Maria**, we are still grateful that we could use your ComboMap device so many times, and that you and Lorena took the time to explain us how to use the device and how to interpret the data. Dear **Lorena**, thank you for all the time you spend on processing our data and on patiently explaining to us how to improve the data acquisition and interpretation. We usually only met for a short time during one of my many trips to Amsterdam, but I really enjoyed our chats. You are a kind and helpful person and I wish you all the best for the future!

Dear **Giuseppe** (Mr. Calculetti, sorry ;-)), thank you for your invaluable help with the CFD calculations and postprocessing of our data. Besides the fact that you worked like crazy during your 3-month visit at our lab, we also really enjoyed your amazingly relaxed and happy company in the room. I still enjoy working with you from a distance and hopefully we get the second helicity paper finished soon! Also a big thanks to our

other Italian friends: **Claudio**, thank you for your help with setting up the entire CFD pipeline and with your critical reviews on the papers. **Umberto**, thank you for sending us Giuseppe, for the long brainstorm sessions we had via Skype and for your patience when trying to explain to us the massively complicated concepts of helical flow. Our collaboration has been very nice and fruitful!

En dan de rest van de Biomechanica groep: **Kim v.d. H**, veel dank voor het bijspringen tijdens de OKs. Daarnaast heb ik veel van je geleerd op schrijf-technisch gebied en kijk ik nog steeds met plezier terug op de vele discussies die we voerden tijdens het schrijven van beide reviews. Voor een kritische (/recalcitrante) blik op onze data kon ik altijd bij je terecht, **Frank**. Je bent een meester in presenteren en uitleggen en ik ben je dankbaar voor je vele minicursussen vloeistofdynamica en de basisprincipes van CFD. Ook jouw get-to-the-point mentaliteit, met name met schrijven, heeft me veel geholpen. **Suze-Anne**, je bescheidenheid siert je, maar is totaal onnodig: je bent onmisbaar geworden in ons project. Je gestructureerde manier van werken, het feit dat je zelfs de meest ingewikkelde codes aan me probeerde uit te leggen, en je zeer kritische blik op alles, hebben ons hele project in korte tijd een enorme boost gegeven. Daarnaast ben je ook gewoon een ongelooflijk lief en leuk persoon. Dank voor alles! **Eric**, dank voor het een flink aantal keren bijspringen voor weefsel/plasma verwerking, zelfs op onze gekke 31 december opofferingsdag. Je zeer duidelijke mening over eten en de gezellige spelletjesavonden zal ik niet snel vergeten. **Ali**, bedankt voor je hulp bij het NIRS-Ca paper en voor de vele discussies tijdens onze lunchmeetings. Je inzichten hebben me veel geholpen. **Kristina**, ik ga je droge, onbegrijpelijk humor missen en bij deze heb je je zin in mijn dankwoord ;-). Also a big thanks to all my other current group members: **Imane, Hilary and Su**. Thank you for the great times during conferences, game nights and during our daily lunches. I wish you all the best with your future careers!

In de vijf jaar dat ik in deze groep heb gezeten heb ik veel mensen zien komen en gaan. Lieve **Leah**, ik startte als jouw student met het schrijven van een deel van het shear stress review. Uiteindelijk hebben we er een mooi artikel van gemaakt! Buiten deze wetenschappelijke samenwerking ben je ook gewoon een ontzettend lief, geïnteresseerd en hardwerkend persoon. Ondanks de vele emotionele rollercoasters in de tijd dat wij samen op een kamer zaten, herinner ik me vooral veel gezelligheid en goede gesprekken. Ook ons Hannibal diner, het Bollywood filmavondje en je fantastische kookkunsten zal ik niet snel vergeten! Ik ben super blij dat je een baan hebt gevonden die zo goed bij je past. Alle geluk voor jou, Daniël en kleine Ayla in de toekomst! **Ruoyu**, although I won't miss your 1000-year old eggs, I really enjoyed your happy personality in the lab. **Jelle**, dank voor je CFD-uitleg sessies, maar vooral ook voor de vele gezellige borrelavondjes en etentjes die we de afgelopen jaren hebben gehad. **Merih**, you are one of the sweetest persons I know and I would like to thank you for all the 'How to

survive your PhD' advice you gave me at the start of my project. **Harm**, je was een geniaal en fantastisch persoon. Vergeten zal ik je niet, al was het maar dankzij Amélie.

En dan hebben we nog de rest van de BME-familie: **Sophinese**, thank you for always caring and for our sometimes quite interesting discussions (calcium!). Our *in vivo* photoacoustics experiments were a massive struggle, but I'm so happy that you have managed to get a great paper out of it. You are an amazingly intelligent and talented person. I hope you find as much self-confidence as you show kindness to other people. **Inés**, je blije 'bubbly' persoonlijkheid past bij je project (sorry). Onze pitch-spar sessie voor Innovation for Health heeft me enorm geholpen. **Kirby**, dank voor je eeuwige interesse en bezorgdheid, maar stop met 'sorry' zeggen. **Leonardo** and **Tianshi**, we shared interesting and fun times in the surgery room to get your catheter working. During the '5 second' (Tianshi) and '5 minutes' (Leo), we enjoyed our half hour - hour coffee/tea breaks. **Mirjam**, **Joop, Simone, Lana, Jorinde, Shengnan, Nuria, Gonzalo, Reza, Jason** and all the new PhDs and PostDocs I haven't really met during my past year of (social) absence, thank you for the great times during Labuitjes and PhD-drinks! **Gijs**, dank voor je eeuwige kritische blik tijdens de BME-presentaties en voor al je hulp met het schrijven van mijn beursvoorstel. **Sharon**, bedankt voor het regelen van al het papierwerk, declaraties, afspraken, gezellige gesprekken en voor nog veel meer. Frits, heel veel dank voor het ontcijferen/hacken van onze ComboMap data en het vervolgens ook nog maken van een zeer gebruiksvriendelijk tool! **Gerard**, dank voor de ondersteuning tijdens alle computer- en software-gerelateerde problemen. **Hans, Nico, Klazina, Rik, Verya** en **Pieter**, bedankt voor jullie interesse in mijn project en voor de kritische vragen tijdens de BME meetings die me altijd weer een stapje verder hielpen.

Naast de BME kant van de 23^{e} verdieping heb ik ook veel hulp gehad van 'de overkant' wat op een gegeven moment bijna mijn 2^{e} thuis was. **Oana** en **Vincent**, bedankt voor de vele uren discussies tijdens het schrijven van mijn DEC. Ik heb ongelooflijk veel van jullie geleerd. Niet alleen tijdens het schrijfproces, maar ook tijdens het meekijken met jullie OKs. **Daphne**, bedankt voor de adviezen die ook jij hebt gegeven voor mijn experimenten en tijdens het schrijven van de beursaanvraag voor mijn PostDoc. Je eeuwige enthousiasme is aanstekelijk en je was altijd geïnteresseerd in hoe mijn project ervoor stond (hoewel je wel bijna al mijn presentaties hebt gemist ;-)). **André**, mijn eerste Erasmus MC-ervaring was op jouw project, tijdens mijn bachelor stage. Ik voelde me snel thuis op jullie lab en ik heb in deze korte periode ongelooflijk veel geleerd, zowel op wetenschappelijk als op persoonlijk vlak (incl. een muziekgenre dat ik daarvoor nog maar bar weinig gehoord had). Hoewel onze gesprekken variëren tussen wat ongemakkelijk en gezellig stond je altijd klaar met tips, trucs en de menige levenswijsheden. Dank voor alles! **Monique**, bedankt voor alle hulp met bestelnummers, voor het regelen van afspraken in de onmogelijke agenda van Dirk en voor nog veel

meer. **Maarten, Jens, Jarno, Kelly, Ihsane, Martine, Lau** en **Esther,** dank voor de vele gezellige koffieautomaat gesprekken. **Heleen**, jij was de persoon die mij wees op de vacature van een PhD bij Kim en ik ben je hier nog steeds dankbaar voor. Ik wil je ook graag bedanken voor het managen van het histolab waar we veel gebruik van hebben gemaakt, voor de samenwerking in het opzetten en uitvoeren van onze gezamenlijke experimenten, en voor de tip om contact te zoeken met Monique van de Interne voor de lipoproteïne analyses.

Monique, we kwamen bij jou met een interessante maar onverklaarbare observatie in onze varkensstudie. Je was meteen geïnteresseerd en bood aan om een keer wat lipoproteïne analyses uit te proberen. Vanaf daar ging het balletje rollen. De opvallende verschillen die we zagen tussen beide groepen leidden uiteindelijk tot een heel project en zelfs een succesvolle beursaanvraag. Bedankt voor alle tijd en moeite die je erin hebt gestoken om ons uit te leggen waar we nu eigenlijk naar keken. Ik bewonder je eeuwige positieve blik op resultaten waar ik niets in dacht te zien. 'Strakker opschrijven' zal ik ook niet snel vergeten ;-). **Sandra**, wat was ik blij dat wij elkaar al kenden vanuit de COEUR-commissie. Dit heeft een enorme boost gegeven aan het project. Ik realiseer me dat ik soms ver ging in jullie pushen om de data nog sneller af te leveren, maar je was altijd duidelijk in wat wel en niet ging. Heel erg bedankt voor onze gezellige gesprekken en voor al je hulp! **Leonie**, je bent fantastisch! Je bent een van de meest hardwerkende, georganiseerde en leuke analisten die ik ken en je hebt een enorme berg werk verzet voor dit project naast je al overvolle schema. Heel veel dank! **Frank**, veel dank voor het op korte termijn uitvoeren van de genotyperingen en voor het begeleiden van de studenten! **Kristien**, als MS-expert heb je veel bijgedragen aan het verbeteren van onze metingen. Daarnaast bedankt voor het uitvoeren van de laatste reeks MS-experimenten! **Yanlin** and **Mattia**, thank you for your great contribution in trying to figure out what these weird LDL-subtypes actually do. It was, and is, a difficult project, but you both pushed through!

Tom, we leerden elkaar kennen tijdens mijn eerste Labuitje toen je me meteen al rekruteerde voor de Labuitjes commissie (al moest ik nog wel even aangenomen worden). Sorry, die schapendrijfworkshop heb ook ik er nooit doorheen gekregen… Mede dankzij de vele theedrink-pauzes en treinreisjes tussen Rotterdam en Eindhoven werden we naast collega's ook vrienden. Hoewel we elkaar het afgelopen jaar niet heel veel gesproken hebben, was ieder thee/bier/eet/Guusavondje dat we hadden altijd weer gezellig!

Hoewel ik fantastische collega's heb en had, ben ik ook heel blij met een aantal hele goede vrienden buiten werk.

Bram, Anouk, Tim, Marie, Martijn, Loes, Rob en **Elisabeth**, bedankt voor de gezellige spelletjesdagen en -avonden. Ik kijk uit naar de vele die zullen volgen in de toekomst!

Ruben, dank voor onze mooie geschilderde muurtjes, voor je eindeloze verhalen en voor je vriendschap. En die promotie van je gaat helemaal goedkomen!

Lieve **Sanne** en **Kim**, hoewel er een periode was dat we wat minder contact hadden ben ik ontzettend blij dat we dat de afgelopen jaren weer opgepakt hebben. Heel erg bedankt voor al onze supergezellige etentje/drankje/concertje Mijdrechtdinner-dates en voor alle goede gesprekken!

Lieve **Marloes** en **Ivana**, de fiets-verhuizing van Marloes was denk ik het echte begin van onze vriendschap. We hebben de afgelopen jaren veel lief, leed, etentjes, drankjes en chill-avondjes gedeeld waar ik met ontzettend veel plezier op terug kijk. Hoewel we nu (jammer genoeg) een eindje verder uit elkaar wonen, zien we elkaar gelukkig nog regelmatig en weten we dat we altijd bij elkaar terecht kunnen met eigenlijk alles. Veel dank voor jullie vriendschap en ik hoop dat deze nog vele jaren stand zal houden!

Lieve **Oma (en Opa!) Hoogendoorn** en **Opa en Oma Roskam**, wat prijs ik mezelf gelukkig dat ik jullie heb. Ik heb jullie de afgelopen jaren veel te weinig opgezocht, maar als we langskwamen voelde het bij jullie altijd als thuis. Van een afstandje volgden jullie alles wat ik deed op de voet en werd menige presentatie gedeeld met wie het ook maar wilde horen. Heel erg bedankt voor het zijn van de beste opa's en oma's van de wereld!

Anny, Chris, Laurens en Kelly, bedankt dat jullie me hebben opgenomen in de 'Beeltjes' familie. Qua aanpassing aan de lokale taal hou ik het voorlopig bij 'Hoije' en hoewel bij jullie op bezoek gaan nog steeds een beetje voelt als een mini-vakantie, ben ik me ook steeds meer thuis gaan voelen in het Limburgse land. Ik ben blij dat jullie erbij zullen zijn tijdens mijn verdediging!

Broertje(/Jarmo), ik ben ontzettend blij dat ook jij naast mij wil staan tijdens mijn promotie (al zie ik je ook gewoon graag een keer in een pinguïnpak). We hebben altijd al een goede band gehad en ondanks dat we elkaar niet heel veel zien, weet ik dat ik altijd bij je terecht kan. Ik ben blij dat mijn Vierdaagse-trainingen een mooi excuus vormden om elkaar wat vaker te spreken de afgelopen maanden! Daarnaast ben ik ongelooflijk trots op hoe goed je het doet op werk en op hoeveel plezier je eruit haalt. De komende jaren zie ik je omhoogvliegen op die carrièreladder (CEO?)!. Heel veel geluk voor jou en **Lonneke** in de toekomst!

Lieve **papa** en **mama**, ik weet eigenlijk niet zo heel goed hoe ik jullie in maar een paar zinnen moet bedanken, maar laat ik toch een poging wagen. Ik ben jullie ongelooflijk dankbaar voor het bieden van een warm thuis waar alles bespreekbaar was en is

(o.a. tijdens onze ellenlange natafel sessies), voor de superfijne vakanties, voor jullie eindeloze vertrouwen, voor het stimuleren en ondersteunen van eigenlijk alles wat we maar bedachten, voor het vooral niet laten merken dat jullie wel degelijk bezorgd waren tijdens al mijn buitenland tripjes en voor nog heel veel meer.

Het laatste stukje van dit dankwoord is bestemd voor jou, lieve **Henrik**. We leerden elkaar vlak voor de start van mijn PhD kennen op de meest onwaarschijnlijke plek aan de andere kant van deze aardbol. Ik snap nog steeds niet hoe, maar wat ik wel weet is dat ik ontzettend blij ben dát dit is gebeurd. Tijdens het tegelijk doorlopen van onze promoties heb ik niet alleen de mooie momenten met je kunnen delen en vieren, maar hebben we allebei ook momenten gekend dat het allemaal even niet mee zat. Toch wist je me altijd weer op te vrolijken, gerust te stellen en me het zelfvertrouwen en de ambitie-boost te geven om door te gaan. Dank voor je steun, voor je eeuwige nuchterheid en realisme, voor je droge humor, je acceptatievermogen en je rechtvaardigheidsgevoel, en gewoon voor het zijn wie je bent. Ik kijk enorm uit naar ons avontuur in Australië en naar alle mooie dingen daarna.

Ayla Hoogendoorn
Eindhoven, juli 2019

SCIENTIFIC ACHIEVEMENTS

Peer-reviewed manuscripts

2019 Iskander-Rizk,…, **Hoogendoorn**, et al. 'In-vivo intravascular photoacoustic imaging of plaque lipid in coronary atherosclerosis', *EuroIntervention*.

2018 De Nisco, Kok, Chiastra, Gallo, **Hoogendoorn** et al., 'The Atheroprotective Nature of Helical Flow in Coronary Arteries', *Annals of Biomedical Engineering*.

2017 Zahnd, **Hoogendoorn**, et al., 'Contour segmentation of the intima, media, and adventitia layers in intracoronary OCT images: application to fully automatic detection of healthy wall regions', *International Journal of Computer Assisted Radiology and Surgery*.

2017 Ma, **Hoogendoorn**, et al., 'Automatic Online Layer Separation for Vessel Enhancement in X-ray', *Medical Image Analysis*.

2016 **Hoogendoorn**, et al., 'OCT-measured plaque free wall angle is indicative for plaque burden: overcoming the main limitation of OCT?', *The International Journal of Cardiovascular Imaging*.

2015 Van der Heiden, **Hoogendoorn** et al. (shared first author), 'Animal models for plaque rupture: a biomechanical assessment', *Thrombosis and Haemostasis*.

2015 Winkel, **Hoogendoorn**, et al., 'Animal models of surgically manipulated flow velocity to study shear stress-induced atherosclerosis', *Atherosclerosis*.

2014 Van den Borne, Rygiel, **Hoogendoorn**, et al., 'The CD200-CD200 Receptor Inhibitory Axis Controls Arteriogenesis and Local T Lymphocyte Influx', *PloS One*.

Manuscripts in preparation

Hoogendoorn, et al., 'A familial hypercholesterolemia pig model for advanced coronary atherosclerosis - variation in disease severity related to a distinct LDL profile'. *In rebuttal for ATVB*

Hoogendoorn, et al., 'Multidirectional wall shear stress promotes advanced coronary plaque development – comparing five shear stress metrics'. *In rebuttal for Cardiovascular Research*

Hartman, **Hoogendoorn**, et al. 'Colocalization of intracoronary lipid rich plaques and calcifications – an integrated NIRS-IVUS analysis'. *Under review at JACC: Cardiovascular Imaging*

Kok, Hartman, **Hoogendoorn**, et al., 'The synergistic effect of NIRS-detected lipid-rich plaque and shear stress on human coronary plaque growth'. *In preparation*

De Nisco, **Hoogendoorn**, et al., 'The impact of helical flow on coronary atherosclerotic plaque progression'. *In preparation*

Cecchetti, Wang, **Hoogendoorn**, et al., 'In vitro and in vivo imaging of coronary artery stents with Heartbeat OCT'. *In preparation*

Scientific awards

2019 Nominated for the Young Investigator Award (result will be announced during the congress).
European Society of Cardiology Congress, Paris, France

2019 Upcoming Scientist Award.
Innovation for Health, Rotterdam, The Netherlands

2019 Winner of the abstract presentation contest.
International symposium on Biomechanics in Vascular Biology and Cardiovascular Disease, London, UK

2018 Winner of the abstract presentation contest.
International symposium on Biomechanics in Vascular Biology and Cardiovascular Disease, Atlanta, GA, USA

2017 Winner of the poster presentation contest.
Optics in Cardiology Conference, Rotterdam, The Netherlands

2014 Winner of 'Best popular scientific article'.
PhD training course Vascular Biology, Dutch Heart Foundation

2012 Van Wijck-Stam Caspers Award
Utrecht University, for my internship at Imperial College, London, UK

Grants

2018 Netherlands Heart Institute Fellowship (€45.000) for a PostDoc project on molecular imaging at the University of Adelaide in collaboration with the South Australian Health and Medical Research Institute.

2018 Mrace Erasmus MC grant (€50.000) for a collaboration project with the Internal Medicine department on the relation between a specific lipoprotein profile in familial hypercholesterolemia and the development of cardiovascular disease.

2018 Travel grant from the Erasmus Trustfund.
International symposium on Biomechanics in Vascular Biology and Cardiovascular Disease, Atlanta, GA, USA

2012 Erasmus travel grant from the Erasmus+ programme of the European Union.
Internship at Imperial College, London

PORTFOLIO

Name:	Ayla Hoogendoorn
Department:	Biomedical Engineering, Cardiology
Research School:	COEUR
Promotors:	Prof. A.F.W. van der Steen, PhD
	Prof. D.J.G.M. Duncker, MD, PhD
Supervisor:	J.J. Wentzel, PhD
PhD period:	2014-2019

General courses	**Year**	**ECTS**
Laboratory animal science	2014	0.5
Research Integrity	2015	0.3
Workshop on Photoshop and Illustrator CS6	2016	0.1
Scientific courses		
Vascular Biology Course – Papendal	2014	3.0
COEUR course 'Cardiovascular Imaging and Diagnostics'	2015	1.5
COEUR course 'Arrhythmia Research Methodology	2016	1.5
COEUR course 'Congenital Heart Disease Part I'	2017	0.5
MolMed Translational Imaging Workshop by AMIE	2017	1.4
Scientific seminars (Erasmus MC)		
Salt	2014	0.2
Current Cardiac and Vascular Aging Research at EMC	2014	0.2
Presentation Mr CLEAN study	2014	0.1
Distribution of CGRP and CGRP receptor in the trigeminovascular sytem and CNS	2014	0.1
Imaging of Cardiac Arrythmias	2014	0.2
Arterial Thrombosis in Acute Ischemic Stroke	2014	0.2
Personalized medicine	2015	0.2
Secondary prevention with anti-thrombotics: unrevealing the conundrum of bleeding vs efficacy	2015	0.2
Translational Research	2016	0.2

	Year	ECTS
Discoveries in Atrial Fibrillation Pathophysiology: Implications for AF Therapy	2017	0.4
MRI-based assessment of biomechanical stress and atherosclerosis in carotid arteries (BioStress-project)	2017	0.4
COEUR PhD days (2014-2018)	2014-2018	1.2
BME-lab and Experimental Cardiology lab meetings (8 presentations)	2014-2018	1.6
Scientific seminars (other)		
ICIN Theme Meeting Vascular Medicine	2015	0.2
Medical Delta 10 years	2016	0.2
Young@Heart days Netherlands Heart Institute (2017 and 2018)	2017-2018	0.6
International conferences		
Optics in Cardiology, Rotterdam (poster)	2015	1.2
Biomechanics in Vascular Biology and Cardiovascular Disease symposium, Rotterdam (poster)	2015	1.2
Cardiovascular Conference, Amersfoort (poster)	2015	1.2
Biomechanics in Vascular Biology and Cardiovascular Disease symposium, Atlanta, GA, USA (poster)	2016	1.2
Biomechanics in Vascular Biology and Cardiovascular Disease symposium, Rotterdam (poster)	2017	1.2
Optics in Cardiology, Rotterdam (poster)	2017	1.2
NAVBO Vascular Biology Conference, Pacific Grove, CA, USA (poster)	2017	1.5
Biomechanics in Vascular Biology and Cardiovascular Disease symposium, Atlanta, GA, USA (oral)	2018	1.2
Optics in Cardiology, Zurich, Switzerland (oral)	2018	1.2
Biomechanics in Vascular Biology and Cardiovascular Disease symposium, London, UK (poster)	2019	1.2
Innovation for Health, Rotterdam, The Netherlands (oral)	2019	0.6
European Atherosclerosis Society Conference, Maastricht, The Netherlands (poster and oral)	2019	1.2
Vulnerable Patient Meeting, Stresa, Italy (invited oral)	2019	1.2
Supervision of students		
Bachelor student (4 months)	2016	0.6
4 MLO students (total of 28 months)	2016-2017	4.0
HLO student (6 months)	2016-2017	1.0
Master student (6 months)	2017-2018	1.0

Other activities	**Year**	**ECTS**
COEUR PhD committee	2014-2018	1.0
Erasmus MC PhD committee	2015-2018	0.2
Organisation ExCOEURsion to Philips Healthcare for all COEUR PhD members	2017	0.3
Organization of 'lab-day-out', Department of Biomedical Engineering	2014-2015	0.3
	Total	**38.9**

ABOUT THE AUTHOR

Ayla Hoogendoorn was born on July 16th, 1990 and grew up in Mijdrecht, The Netherlands. In 2008 she graduated from secondary school (Veenlanden College, Mijdrecht). Hereafter, she started her Bachelors in Biomedical Sciences, followed by a Masters in Biology of Disease at the Utrecht University. During her Masters, she undertook an internship at the Biomedical Engineering Department of Imperial College, London where she studied the role of shear stress in atherosclerosis development. She completed both her Bachelor (2011) and Master (2013) degrees *cum laude* (with honours).

In 2014, Ayla joined the Biomechanics group of the Biomedical Engineering Department (Thorax centre, Erasmus MC, Rotterdam, The Netherlands) where she started a PhD project under the supervision of Prof. van der Steen, Prof. Duncker and Dr. Wentzel. Her project focussed on the biomechanical, pathophysiological and invasive-imaging aspects of coronary atherosclerotic disease in both a pre-clinical and a clinical setting. She presented her work at multiple international conferences for which she received prices for 'Best poster presenter' (Optics in Cardiology, 2017) and 'Best abstract presenter' (Biomechanics in Vascular Biology and Cardiovascular Disease symposium, 2018 and 2019). Furthermore, she won the 'Upcoming Scientist Award' at the Innovation for Health conference 2019, and she is currently nominated for the 'Young Investigator Award' at the European Society of Cardiology Conference (September 2019).

Recently, Ayla received a personal fellowship from the Netherlands Heart Institute which enables her to start as a PostDoctoral researcher at The University of Adelaide, in collaboration with the South Australian Health and Medical Research Institute (SAHMRI), Adelaide, Australia from October 2019. During this PostDoctoral period, she will shift her research focus towards invasive and non-invasive molecular imaging of cardiovascular disease.